

# QUARTERLY REPORT of

May 2024 Vol. 65 No. 2

CONTENTS

# RTRI

## PAPERS

Automating Visual Inspection for Underbody Equipment of Railway Vehicles Using On-track Cameras **(R)**

Application of Cylindrical Roller Bearings with Ribs to Gear Units of Railway Vehicles **(R)**

Improvement of Flame Retardancy of Seat Cushion Materials for Railway Vehicles Using Intumescent Flame Retardant **(R)(O)**

Method for Estimating Lateral Carbody Vibration Acceleration used for Safety Evaluation of Railway Vehicles against Crosswind **(R)(T)**

Evaluation Method of Passenger Thermal Comfort Considering Effects of Airflow by Cross-flow Fan in Commuter Vehicles in Summer **(H)**

Wind Tunnel Test Reproducing Track Surface Flow of Passing Shinkansen Trains to Study Ballast Projection and Ballast Screen Lifting **(I)(T)**

Simple Method for Estimating Buckling Temperature of Continuous Welded Rail Considering Lateral Track Irregularities **(I)**

Method for Estimating Bending Stiffness of Concrete Girders during Train Passage Considering Effects of Concrete Cracks and Non-structural Members **(I)**

Crossing Rod Breakage Detection Method Using Surveillance Camera Images **(O)(I)**

Quantitative Evaluation Method of Measures for Prolonging Lifetime of Electronic Signalling Equipment **(I)**

Method for Evaluating Structural Design of Impedance Bond Molded with Resin **(I)**

Typology of Train Evacuations from the Viewpoint of Information Provision and Context **(H)**

## SUMMARIES

Summaries of RTRI REPORT (in Japanese)

- (H)** Human factors
- (I)** Infrastructure
- (O)** Operations
- (R)** Rolling stock
- (T)** Technical system integration and interaction
- (W)** Weather and climate change



**CONTENTS****PAPERS**

- 
- 71 Automating Visual Inspection for Underbody Equipment of Railway Vehicles Using On-track Cameras **(R)**  
.....T.KOJIMA, K.MIYAHARA, A.KAZATO, M.UKAI
- 77 Application of Cylindrical Roller Bearings with Ribs to Gear Units of Railway Vehicles **(R)**  
.....K.TAKAHASHI, D.SUZUKI, S.KIKAWA
- 83 Improvement of Flame Retardancy of Seat Cushion Materials for Railway Vehicles Using Intumescent  
Flame Retardant **(R)** **(O)**  
.....T.TOYOHARA, S.YAMANAKA, M.ITO
- 89 Method for Estimating Lateral Carbody Vibration Acceleration used for Safety Evaluation of Railway  
Vehicles against Crosswind **(R)** **(T)**  
.....H.KANEMOTO, Y.HIBINO
- 97 Evaluation Method of Passenger Thermal Comfort Considering Effects of Airflow by Cross-flow Fan in  
Commuter Vehicles in Summer **(H)**  
.....H.ENDOH, S.YOSHIE, S.ENAMI, F.KIKUCHI, Y.IZUMI, J.NOGUCHI
- 104 Wind Tunnel Test Reproducing Track Surface Flow of Passing Shinkansen Trains to Study Ballast  
Projection and Ballast Screen Lifting **(I)** **(T)**  
.....T.INOUE, T.NAKANO, A.IDO
- 110 Simple Method for Estimating Buckling Temperature of Continuous Welded Rail Considering Lateral  
Track Irregularities **(I)**  
.....D.YAMAOKA, S.TAMAGAWA, Y.NISHINOMIYA
- 117 Method for Estimating Bending Stiffness of Concrete Girders during Train Passage Considering Effects of  
Concrete Cracks and Non-structural Members **(I)**  
.....M.TOKUNAGA, M.IKEDA
- 125 Crossing Rod Breakage Detection Method Using Surveillance Camera Images **(O)** **(I)**  
.....R.KAGEYAMA, N.NAGAMINE
- 131 Quantitative Evaluation Method of Measures for Prolonging Lifetime of Electronic Signalling Equipment  
**(I)**  
.....H.FUJITA, K.TAKASAKI, T.SHINDO, T.KAMIYA
- 138 Method for Evaluating Structural Design of Impedance Bond Molded with Resin **(I)**  
.....S.SHIOMI, T.SHINDO, T.KAMIYA, T.SATO, N.OKO
- 145 Typology of Train Evacuations from the Viewpoint of Information Provision and Context **(H)**  
.....A.SAITO, T.MASUDA, H.SUZUKI, T.TAKAI, K.YAMAUCHI

**SUMMARIES**

- 
- 152 Summaries of RTRI REPORT (in Japanese) **(I)**

- |   |
|---|
| <b>(H)</b> Human factors                                |
| <b>(I)</b> Infrastructure                               |
| <b>(O)</b> Operations                                   |
| <b>(R)</b> Rolling stock                                |
| <b>(T)</b> Technical system integration and interaction |
| <b>(W)</b> Weather and climate change                   |

# Automating Visual Inspection for Underbody Equipment of Railway Vehicles Using On-track Cameras

Takashi KOJIMA

Kohei MIYAHARA

Akihito KAZATO

Vehicle Dynamics Laboratory, Vehicle Technology Division

Masato UKAI

Image Analysis and IT Laboratory, Signalling and Transport Information Technology Division (Former)

*The authors developed an imaging system and a diagnosis algorithm for automating visual inspection of underbody equipment of railway vehicles. The developed system consists of a line scan camera, line lights, a laser Doppler velocimeter and a computer, to scan passing vehicles from the ground. Test results using real vehicles indicate that the system can obtain detailed continuous images of the side of vehicles. The proposed algorithm using template matching and subtraction is designed to be robust against disturbances. The algorithm was tested on images captured under simulated variations in weather and the dirt of underbody equipment. As a result, the algorithm diagnosed, for example, whether the valve was fully open normally with an accuracy of ROC-AUC 0.990.*

**Key words:** vehicle inspection, visual inspection, image analysis, line scan camera, template matching

## 1. Introduction

To ensure that rolling stock remains safe for operation, railway operators have regulations for and carry out inspections of rolling stock. Several types of inspection are defined according to a certain elapsed time or distance traveled. In Japan, one of these inspections is carried out every 2 to 10 days, depending on the type of vehicle and other factors, in a state where the vehicles can be operated as a train. The purpose of these frequent inspections is to check the condition of critical parts by their appearance and sound, as well as check the function of the brakes and other parts of the vehicle. The appearance of these parts is currently checked by human visual inspection. Consequently, automating this visual inspection would save labor. In these visual inspections, most of the visual inspection points outside the vehicle are of underbody equipment. Therefore, in this study, automated image-based inspection methods for visual inspection points of underbody equipment in these inspections were investigated, and an imaging method and an inspection algorithm were developed.

## 2. Development of the vehicle underbody imaging system

### 2.1 Proposal of imaging method

Frequent visual inspection of underbody equipment targets areas which are visible from the side of the vehicle. An efficient way to obtain the images of these inspection areas is to photograph passing vehicles with cameras fixed to the ground. We proposed a continuous imaging method, shown in Fig. 1, using a line scan camera, line lights, a laser Doppler velocimeter, and a computer. The laser Doppler velocimeter measures the speed of a passing vehicle without contact and outputs a pulse every time the vehicle moves a certain distance. The line scan camera captures an image of one vertical line on the side of the vehicle for each pulse received from the velocimeter, and the images are joined laterally to generate a 2D image. The line lights illuminate a line-shaped area to be captured. The computer stores the images received from the camera in storage. These processes produce a continuous image that is unaffected by

changes in vehicle passing speed.

### 2.2 Selection of specifications and positions of imaging devices

To select the specifications and positions of the imaging devices shown in Fig. 1, we carried out tests with these devices to capture real vehicles. In general, the performance of image inspection is highly dependent on lighting conditions. We tested the following three lighting conditions: ‘forward lighting,’ where the lights and the camera axis were almost parallel (Fig. 2 (a)); ‘oblique lighting,’ where the lights were angled horizontally to the camera (Fig. 2 (b)); and ‘bilateral oblique lighting,’ where the light sources were placed on both sides of the camera at a similar angle (Fig. 2 (c)). Figure 3 shows examples of the images captured. In the forward lighting, highlight clipping occurred in areas where the lights were directly

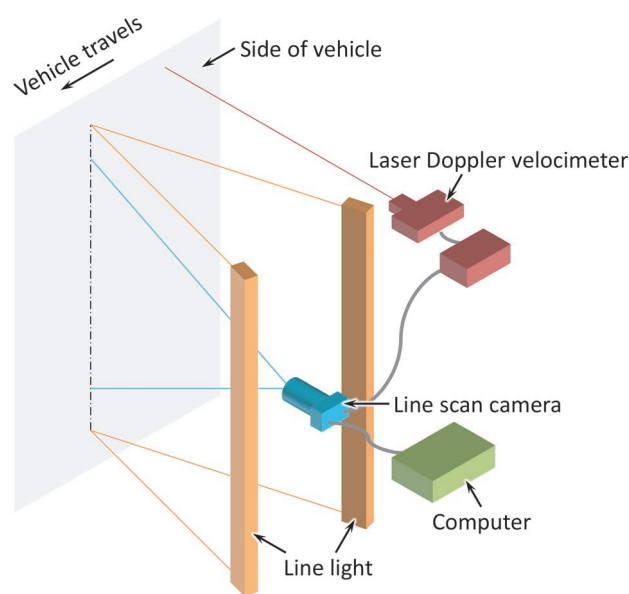


**Fig. 1** Equipment configuration of vehicle continuous imaging method

reflected, as shown in Fig. 3 (a). This was particularly noticeable in vehicles with less soiled underbody equipment surfaces. When the exposure was reduced to prevent the highlight clipping, shadow clipping occurred in other areas. Neither highlight nor shadow clipping can be corrected after shooting. Such clipping may result in the loss of information necessary for visual inspection.

In contrast, the oblique lighting produced almost no highlight clipping, even in vehicles with less soiled underbody equipment surfaces. This is because, with oblique lighting, the camera mainly captures diffuse reflected light. However, close equipment and protruding parts block the light and create shadows, as shown in Fig. 3 (b). Oblique lighting is commonly used to detect minute irregularities such as defects. However, there is a concern that deep objects, such as underbody equipment, may be greatly affected by shadows, making it difficult to inspect the area.

Although the bilateral oblique lighting was inferior to the unilateral oblique lighting in terms of the visibility of minute irregularities, it did not produce the dark shadows that were seen with the unilateral oblique lighting.

From these results, we selected the bilateral oblique light (Fig. 2 (c)) as the most suitable lighting for image inspection of underbody equipment. We also selected the specifications and positions of each imaging device to ensure good imaging.

### 2.3 Prototyping of the imaging system

We designed an enclosure to house the imaging devices in the selected arrangements and built a prototype vehicle underbody imaging system as shown in Fig. 4. The enclosure is splashproof. The enclosure has a window made of a transparent acrylic plate on the side close to the track. In this study, the laser Doppler velocimeter was placed on top of the enclosure. This is because the velocimeter is waterproof and this position facilitates adjustments for each set of test conditions.

### 2.4 Functional verification of the imaging system

The prototype imaging system was temporarily placed in a railway yard to capture the images of real vehicles in operation passing in front of them (Fig. 5). The vehicle passing speed was less

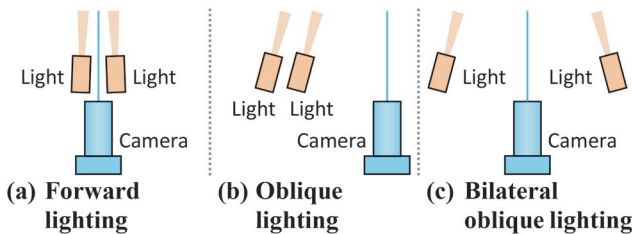


Fig. 2 Lighting conditions (plan view)

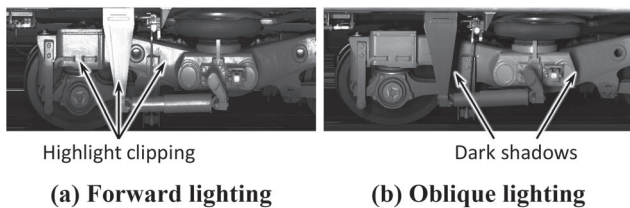


Fig. 3 Comparison of images taken under different lighting

than 25 km/h. A total of 621 cars of several vehicle types were filmed. The weather was sunny. After imaging, we corrected the brightness of the captured images using histogram equalization. Figure 6 shows examples of the corrected images for daytime and nighttime. The test results show that our imaging system can obtain continuous and detailed images of the sides of the underbody equipment independent of sunlight, vehicle passing speed, and vehicle type.

### 3. Examination of inspection algorithms

In recent years, many visual inspection methods using deep learning have been proposed. These methods enable diagnostics that are difficult to achieve with conventional rule-based methods. However, deep learning generally requires a large amount of training data. Depending on its application, it may not be possible to prepare sufficient training data to achieve the required diagnostic performance. On the other hand, our imaging system provides images of objects with an almost constant size or angle, as the line scan camera captures the object images at fixed distances and intervals. It is therefore expected that even rule-based methods will provide sufficient diagnostic performance. In this study, we chose to use a rule-based method. Using some images of a test vehicle with simulated visual anomalies captured in a shed, we proposed a diagnostic algorithm based on template matching and subtraction [1]. In addition, using the captured images of real operational vehicles we developed

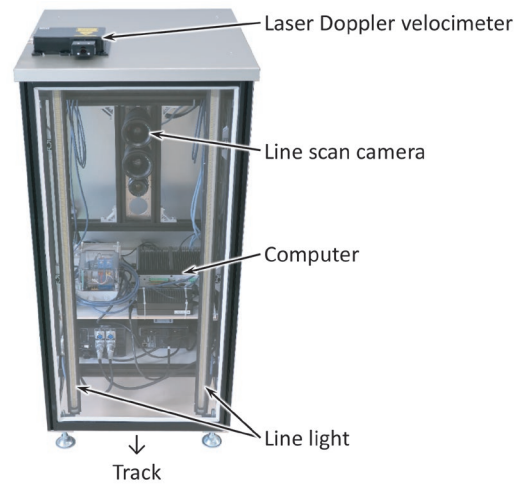


Fig. 4 Prototype vehicle underbody imaging system



Fig. 5 Imaging system placed in a field test

the inspection algorithm shown in Fig. 7. The explanations corresponding to the bracketed numbers in the figures are given below:

- (1) Detects each bogie using template matching from the continuously captured image of the sides of the underbody of a train and recognizes each car from the positions of the detected bogies.
- (2) Recognizes the vehicle number displayed on the body of each vehicle using template matching from the captured image of each recognized vehicle.
- (3) Identifies the vehicle type from the recognized vehicle number and crops the area containing the targeted underbody components, defined by coordinates for each vehicle type.
- (4) Applies template matching on the cropped area, using the pre-prepared image of the component in normal conditions as a template, and detects the exact location of the component.
- (5) Applies histogram equalization to both the cropped component image and the template, calculates the difference in luminance between the two images and applies binarization and denoising. This extracts the areas that differ from the normal as white.
- (6) Calculates the number of white pixels (called the ‘difference pixel count’) and judges it to be normal if the value is smaller than a predefined threshold; otherwise, it is classified as an anomaly.

This paper describes the validation of algorithms (3) to (6).

## 4. Validation and improvement of inspection algorithms

### 4.1 Capturing tests simulating underbody equipment anomalies

To assess anomaly detection performance for different conditions, we carried out tests under several conditions using a test vehicle and the test line of the Railway Technical Research Institute (Fig. 8). We placed our imaging system on the trackside of the test line. The test vehicle drove back and forth on the track in front of the imaging system. The imaging system captured the side of the underbody of the passing vehicle. To simulate anomalies, we mounted several models of underbody equipment components on the side of the underbody of the test vehicle. To include various visual features in the models, we selected the following components and their anomalies as models: air cock valve opening/closing (handle angle), loose/missing hexagonal bolts, bent adjusting rod and pipe, and scratches/dents on flat plates (Fig. 9).

To simulate the normal visual changes in real operation, we set the following conditions: iron oxide powder on the models to simulate surface contamination of underbody equipment and chalk check marks on areas simulating scratches and dents. To simulate weather changes, we set up three conditions: ‘sunny’ with direct sunlight on the component models, ‘cloudy’ without direct sunlight, and ‘rainy’ with no direct sunlight and water droplets on the window of the imaging system (Fig. 10). In addition, we set up ‘dirt’ with soil on the window.

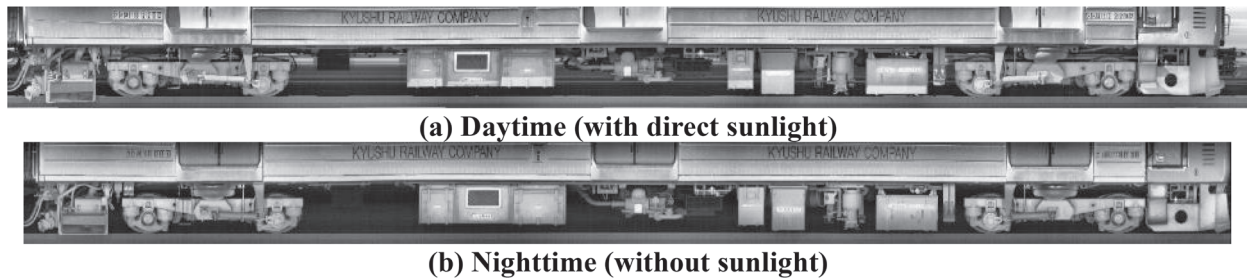


Fig. 6 Captured images with brightness correction

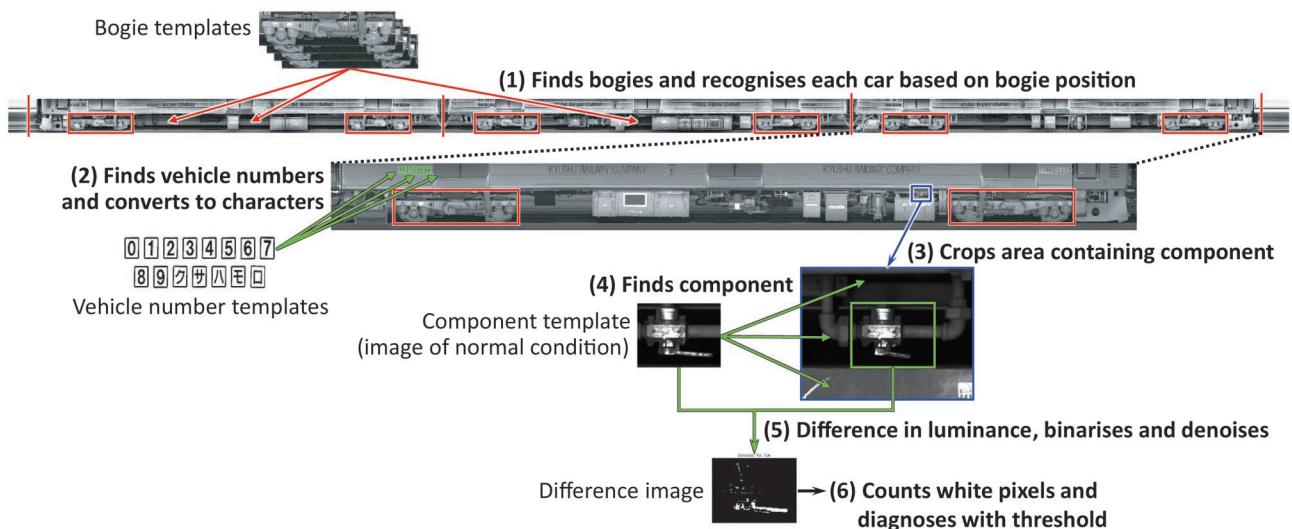


Fig. 7 Proposed inspection algorithm

## 4.2 Algorithm validation

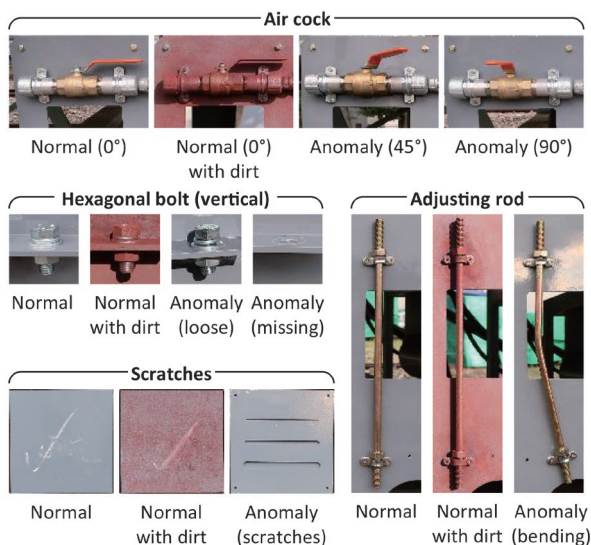
We created templates from images of each component captured in cloudy conditions and applied the proposed algorithm to each captured image. This paper focuses on the results for the air cock valve, which was set with the most anomalous conditions, compared to the other component models.

Figure 11 (a) shows the results for an anomaly (handle angle  $90^\circ$ ) in cloudy conditions. The area of the handle in the difference image is white. The results show that the algorithm adequately detected anomalies in the handle angle, as expected. The difference pixel count is 5,996.

Figure 11 (b) shows the results for a normal condition (handle angle  $0^\circ$ ), where only part of the inspection area was exposed to direct sunlight. Most of the area of the difference image is white. As described in Chapter 3, the algorithm applies brightness correction to the captured images and templates to reduce illumination differences between them. However, when the area exposed to ambient light is part of the image, as in the example shown in Fig. 11 (b), it is difficult to remove the effect of ambient light using brightness correction. This resulted in a large difference between the captured image and the template. The difference pixel count is 46,060, which



**Fig. 8 Image capture test simulating underbody equipment anomalies**



**Fig. 9 Examples of conditions set for underbody component models (photographs taken with a handheld camera)**



**Fig. 10 Rainy condition applied to window of imaging system**

is more than for the anomalous condition (Fig. 11 (a)). Dirt on the components also caused significant differences. The results show that the algorithm needs to adapt to visual changes in appearance other than component anomalies, such as differences in ambient light or dirt on underbody equipment.

## 4.3 Algorithm improvements

We studied ways to reduce the effect of visual changes other than anomalies in underbody equipment and improved the algorithm as follows:

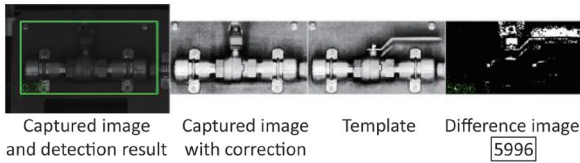
- (1) Use of multiple templates: To reduce the effects of individual differences in the dirt and shape of underbody equipment, several underbody component templates created from different vehicles are used. Template matching is applied using each template to a captured image. The difference between the template with the highest similarity and the captured image is calculated.
- (2) Additional edge detection: To remove differences in illumination and detect differences in component shape, edge detection is used. Edge detection is applied to both the captured image and the template before the component template matching (Chapter 3 (4) and Fig. 7 (4)).
- (3) Limiting the difference evaluation area (masking): To remove differences in illumination, such as in the background of a component, the areas in which the number of difference pixels is calculated are set in the difference image.

The algorithm before the improvement is referred to as the basic algorithm in this paper.

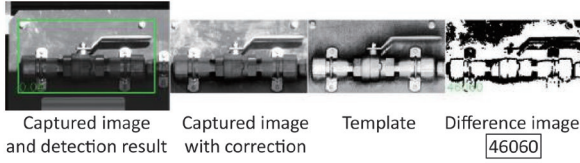
## 4.4 Validation of the improved algorithm

This paper focuses on the results obtained using two templates for cloudy weather with and without dirt and the mask for extracting the range of motion of the handle shown in Fig. 12. Figure 13 shows the results of applying the improved algorithm to the same captured images as in Fig. 11. For the normal condition in sunny weather, most of the area in the difference image by the basic algorithm was white. In contrast, the improved algorithm produced few white areas in the difference image (Fig. 13 (b)). This is because the edge detection removed differences in brightness between the captured image and the template, and the masking removed differences other than the handle. The difference pixel count in the normal condition is 301 pixels, which is less than the 851 pixels in the anomaly condition, as expected.

Figure 14 shows the difference pixel counts calculated by applying the improved algorithm to all captured images except those used as templates. Figure 14 shows a trend towards higher differen-



(a) Cloudy, anomaly condition (90°)



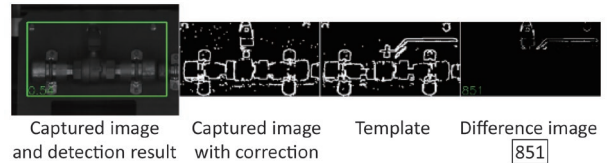
(b) Sunny, normal condition (0°)

**Fig. 11 Results of diagnostic processing of air cock using basic algorithm (Numbers in squares represent differential pixel counts)**

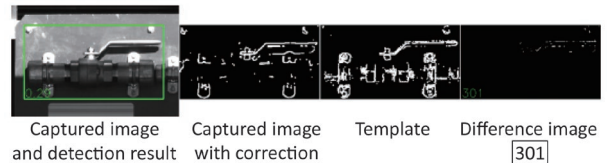


**Fig. 12 Mask image**

tial pixel counts for larger handle angles. In this study, an anomaly is defined as a handle angle of 15° or more. When the threshold is set at 530, the false positive rate (the proportion of normal images incorrectly classified as anomalies) is 1.5% and the true positive rate (the proportion of images showing anomalies correctly classified as anomalies) is 95.9%. To assess the diagnostic performance without determining a threshold value, we used a Receiver Operating Characteristic curve (ROC curve) and an Area Under the Curve (AUC). The ROC curve is calculated and plotted with the false positive rate on the horizontal axis and the true positive rate on the vertical axis, with different thresholds for diagnosing an abnormality. The closer the obtained curve passes to a point with a false positive rate of 0 and a true positive rate of 1, the better the diagnostic performance. The AUC represents the area under the ROC curve that ranges from 0 to 1. The higher the value, the better the diagnosis performance.



(a) Cloudy, anomaly condition (90°)



(b) Sunny, normal condition (0°)

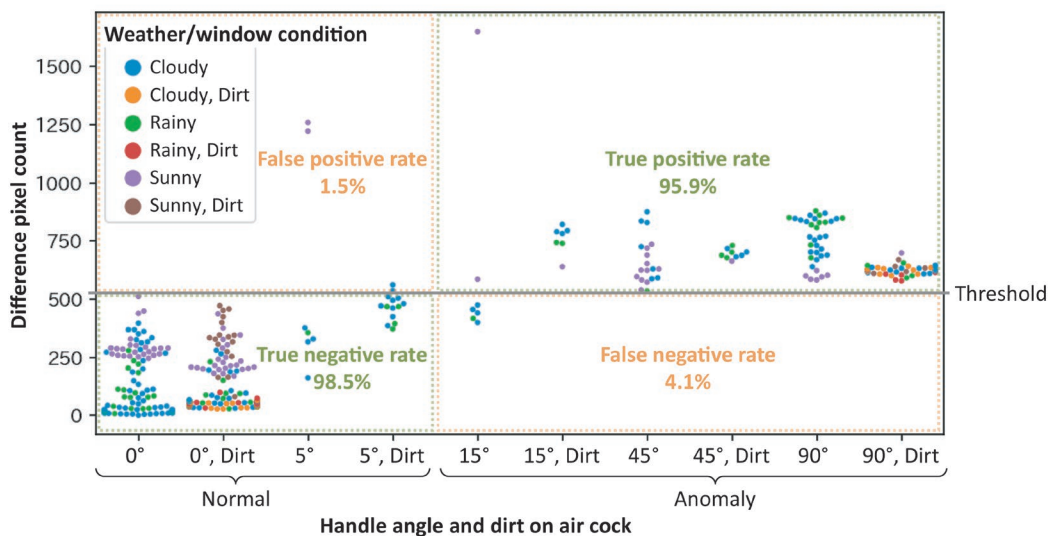
**Fig. 13 Results of diagnostic processing of air cock using improved algorithm (Numbers in squares represent differential pixel counts)**

Figure 15 shows the ROC curves and AUCs calculated from the differential pixel counts. The AUC of the basic algorithm is 0.521, whereas the AUC of the improved algorithm is 0.990. This result shows that the improved algorithm has good discrimination performance.

We applied our algorithm to each underbody component model in various combinations of template, edge detection and masking settings. Table 1 shows the diagnostic processing settings with the highest AUC and the AUC values for each component model. The result shows that the appropriate diagnostic processing settings need to be selected for each component. The results of these tests suggest that although it is difficult to diagnose loose bolts and scratches on plates, our algorithm may be able to diagnose opening/closing of air cock valves, missing hexagonal bolts, and bending of adjusting rods and pipes.

## 5. Conclusions

We studied an automated image-based inspection method for visual inspection points of underbody equipment of rolling stock.



**Fig. 14 Differential pixel counts calculated from each captured image of air cock using improved algorithm**

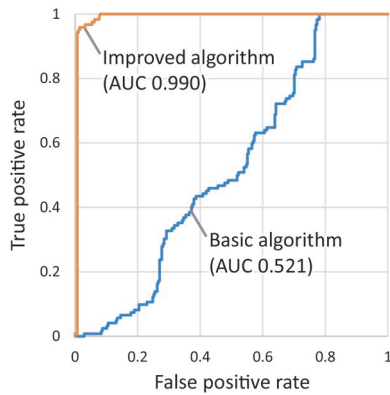


Fig. 15 ROC curves for air cock diagnostics

Table 1 Diagnostic performance of each underbody equipment model

Anomaly	Number of templates	Edge detection	Mask	AUC
Air cock closing	2	With	With	0.990
Missing bolt (vertical)	1	Without	With	0.982
Loose bolt (vertical)	1	Without	With	0.865
Missing bolt (parallel to sleeper)	4	Without	Without	0.985
Loose bolt (parallel to sleeper)	4	With	With	0.909
Adjusting rod bending	2	With	With	0.986
Pipe bending	1	With	With	0.961
Scratch on plate	1	Without	-	0.553

The results are shown below.

- (1) We studied a method for imaging the sides of the underbody of a passing vehicle. We developed an imaging system consisting of a line scan camera, line lights, and a laser Doppler velocimeter. The prototype system was placed in a railway yard and captured images of many vehicles. The result shows that the developed system provides good continuous images.
- (2) We created templates from images of each underbody component taken in normal conditions with our imaging system and proposed an inspection algorithm to detect anomalies

## Authors



Takashi KOJIMA, Ph.D.  
Senior Researcher, Vehicle Dynamics Laboratory, Vehicle Technology Division  
Research Areas: Anomaly Detection, Vehicle Dynamics



Kohei MIYAHARA  
Assistant Senior Researcher, Vehicle Dynamics Laboratory, Vehicle Technology Division  
Research Areas: Vehicle Dynamics, Data Analysis



Akihito KAZATO, Ph.D.  
Chief Researcher, Vehicle Dynamics Laboratory, Vehicle Technology Division  
Research Areas: Carbody Suspension System, Pneumatic Control, Ride Comfort Evaluation



Masato UKAI  
Senior Chief Researcher, Head of Image Analysis and IT Laboratory, Signalling and Transport Information Technology Division (Former)  
Research Areas: Image Processing, Computer Vision

based on the difference in luminance between the templates and the captured images.

- (3) We carried out tests under several weather conditions to capture test vehicles simulating anomalies and contamination of underbody components and applied the proposed algorithm to the captured images. The result shows that when the sunlight and the dirt on underbody equipment differ significantly between the template and the captured image, the luminance difference is significantly affected by them.
- (4) We improved our inspection algorithm using multiple template matching, edge detection and masking. This improvement reduces the effect of luminance differences caused by sunlight and dirt on underbody components. We applied the improved algorithm to the air cock images taken in the tests described in (3). The results show good diagnostic performance with an ROC-AUC of 0.990.

In this study, we evaluated the diagnostic performance for selected underbody component models under simulated environmental conditions. In the future, we will verify the performance with more underbody components. We will install our imaging system in a railway yard for a long period to capture a larger volume of rolling stock in real operation. On this basis, we will evaluate the performance of our system in a real environment.

In addition, we have proposed a generic diagnostic algorithm that is not specific to any particular abnormalities in this study. To detect anomalies that are difficult to detect, we will study diagnostic algorithms according to the characteristics of the anomaly.

## Acknowledgement

The authors would like to express their sincere gratitude to the Kyushu Railway Company and the West Japan Railway Company for their cooperation in the field tests.

## References

- [1] Miyahara, K., Kojima, T., Kazato, A., "Development of anomaly detection method using railway vehicle side images," *STECH 2021*, 2021.

# Application of Cylindrical Roller Bearings with Ribs to Gear Units of Railway Vehicles

Ken TAKAHASHI

Daisuke SUZUKI

Sadayuki KIKAWA

Lubricating Materials Laboratory, Materials Technology Division

*Helical gears are commonly used in the gear units of railway vehicles in Japan, and these gear units use tapered roller bearings. In order to prevent seizure of bearings, this study examined the use of cylindrical roller bearings with ribs that allow a certain degree of axial displacement of inner rings and outer rings. Their performance was compared with conventional tapered roller bearings through various rotating tests. The results of rotation tests using an actual gear unit showed that the temperature rise immediately after the start of rotation and torque of the pinion shaft is lower in the case of cylindrical roller bearings with ribs than with tapered roller bearings.*

**Key words:** machine element, tribology, gear unit, pinion bearing, cylindrical roller bearing with ribs

## 1. Introduction

Tapered roller bearings are commonly used as pinion bearings in the gear units of railway vehicles in combination with helical gears. With tapered roller bearings, it is essential to control the appropriate endplay value (hereafter referred to as EP value) to prevent bearing damage. It is noted that the EP is the total axial clearance of the two bearings supporting the pinion. It has been clarified that the smaller the initial EP value and the lower the atmospheric temperature, the greater the decrease in EP value during rotation and the greater the concern of seizure occurring [1, 2]. In addition, it has also been clarified that an axial load of 150-200 kN acts on the bearing when the EP value decreases and the bearing finally seizes [3].

A possible method to prevent such seizures is the use of cylindrical roller bearings that allow a certain degree of axial displacement of the inner and outer rings. In recent years, there have been examples of structures which combine cylindrical roller bearings and double-helical gears [4, 5]. Unlike single-helical gears, double-helical gears do not generate axial loads due to torque transmission, therefore they have the advantage of reducing the load on the bearings. However, they require high gear manufacturing technology and precision, causing an increase in cost, so it is difficult to apply them to all gear units.

Structures combining single-helical gears and cylindrical roller bearings with ribs on both the inner and outer rings (cylindrical roller bearings with ribs) have also been proposed [6]. In conventional tapered roller bearings, the axial load is partially borne by the rolling contact areas of the bearings. However, in the structure described above, the entire axial load is borne by the sliding contact areas between the roller end faces and ribs on the inner and outer rings. In addition to the difference with axial load, the behavior of the lubricating oil inside the bearing is also thought to differ between these two types of bearing structures. However, there are no examples of studies comparing them, so far. Therefore, in this study, a pinion support structure using cylindrical roller bearings with ribs (prototype structure) was manufactured to compare its performance with that of the conventional structure using tapered roller bearings, in rotation tests [7].

## 2. Pinion support structures and test bearings

### 2.1 Pinion support structures

The structure of a typical railway gear unit is shown in Fig. 1.

The gear unit is mounted on the axle and suspended on the bogie frame by a torque reaction rod. The reduction mechanism of the gear unit consists of two helical gears: a pinion and a gear. The pinion shaft is fitted with pinion bearings on each side of the pinion, supporting the pinion shaft against the gear case. The axle is fitted with gear bearings on each side of the gear, supporting the gear case against the axle. Gear oil is stored in the bottom of the gear case. This oil is splashed onto the bearings and the pinion by the rotation of the gear and lubricates them. The direction of rotation indicated by the arrow CW in Fig. 1 is forward rotation (the pinion shaft rotates clockwise when viewed from the motor side) and the direction of rotation indicated by the arrow CCW is the reverse direction of rotation of CW. The gear oil is applied to the pinion bearings differently in CW and CCW rotation, and the gear oil in the CCW rotation directly lubricates the bearings as the distance from the oil sump is shorter.

The pinion support structures used in the tests are shown in Fig. 2. (a) and (b) in the figure shows a cross-sectional view of a conventional structure with tapered roller bearings and a prototype structure with cylindrical roller bearings with ribs, respectively. The end face of the bearing at the pinion side in the diagram is called the

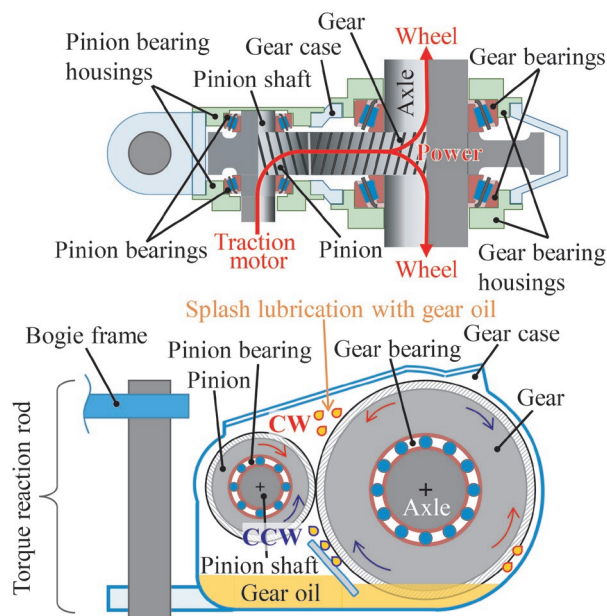


**Fig. 1 Schematic view of gear unit**

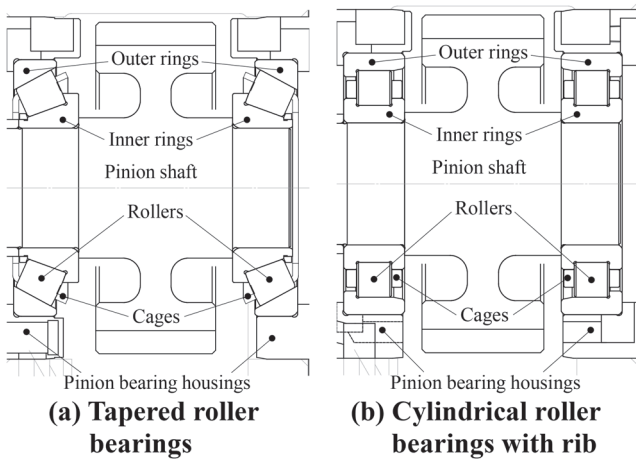


**Fig. 2 Tested pinion support structures**

front face; the opposite end, the back face.

Both of these structures can be interchangeably installed in the test rig described in section 3.1, by changing only the pinion bearing housings and the pinion shaft.

## 2.2 Test bearings

Table 1 shows the specifications of the test pinion bearings. The internal clearances of the bearings are determined by adjusting the thickness of the shims inserted between the pinion bearing housings and the gear case. The displacement that these clearances allow the pinion shaft to move axially is the EP value. In the tapered roller bearings, when the EP value increases, the radial clearances also increase in conjunction with the axial clearances, which may cause a reduction of the fatigue life or an increase in the vibration of the bearings. Therefore, the upper limit of the EP value is relatively small. In the case of cylindrical roller bearings with ribs, on the other hand, since the increase in EP value does not affect the radial clearances, the upper limit of the EP value can be increased.

**Table 1 Tested pinion bearings**

	Tapered roller bearings	Cylindrical roller bearings with ribs
Outside diameter	150 mm	150 mm
Bore diameter	70 mm	70 mm
Width	38 mm	35 mm
Number of rollers	15	13
Basic dynamic load rating	167000 N	158000 N
Maximum design EP value	0.12 mm	0.30 mm

## 3. Rotation test with actual gear case

The pinion support structures described in chapter 2 are mounted on an actual gear unit and subjected to rotating tests to compare their performances. As mentioned in chapter 1, the lower the atmospheric temperature, the greater the concern about bearing seizure: consequently, focus is attached to performance at low temperatures. Although no actual load is applied to the bearings here because the gear unit is rotated almost without the external torque, the aim is to investigate the performance under conditions where the changes in the EP value with temperature and the behavior of the gear oil at low temperatures are equivalent to that of the actual gear unit. First, ro-

tating tests are carried out at an atmospheric temperature of approximately 10°C (rotation test under air-cooled), under conditions that take into account the vehicle running in winter. Next, rotating tests are carried out at -15 to -20°C (warm-up test from low temperature), under conditions that take into account the transient condition of the bearings immediately after vehicle start-up at lower temperatures.

### 3.1 Test rig of actual gear unit

The test rig is shown in Fig. 3. This rig is an actual gear unit in which the pinion shaft is rotated by a motor. The gear case is made of aluminum alloy, the pinion is made of alloy steel and the gear and bearing housings are made of carbon steel. Blowers are installed near the gear case (omitted in the figure).

For the warm-up test from low temperature, no blower is used and the cooling system shown in Fig. 4 is installed around the gear unit. This system cools the gear unit by injecting liquefied carbon dioxide gas into the gear unit in a cold reserving box surrounded by a heat-insulating cover. Although only the lower part of the insulation cover is installed in Fig. 4, it is combined with the upper part during testing and almost completely shields the gear unit except for the axle, pinion shaft and pipe penetrations.

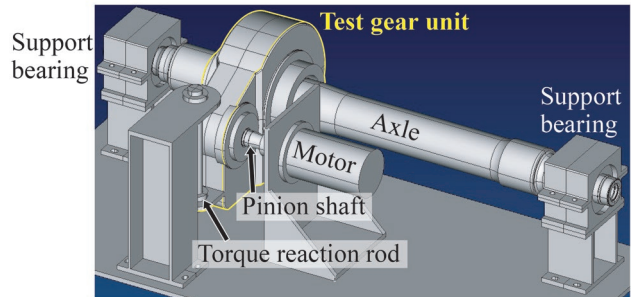


**Fig. 3 Test rig of gear unit**

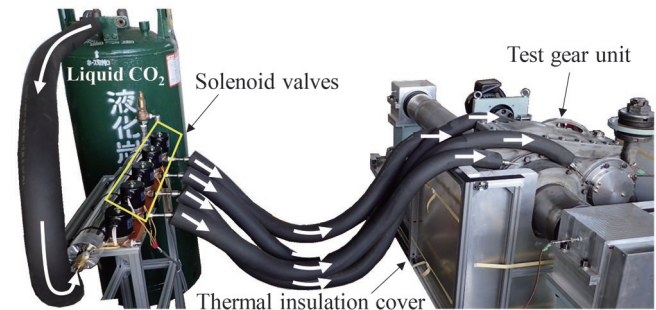


**Fig. 4 Cooling system of test gear unit**

During the rotation test, the temperature of each part of the gear unit and the rotational speed and torque of the pinion shaft (motor) are measured (Fig. 5). Using T-type thermocouples, temperatures are measured on the outer ring surfaces of two pinion bearings, the outer ring surfaces of two gear bearings, the gear case surface, and the gear oil in addition to the atmosphere. The rotational speed of the pinion shaft is measured by a photoelectric rotation detector. The torque of the pinion shaft is calculated from the current value of the motor.

### 3.2 Test conditions and methods

The test conditions are shown in Table 2 and the rotation pattern of the pinion shaft is shown in Fig. 6. In the acceleration zone

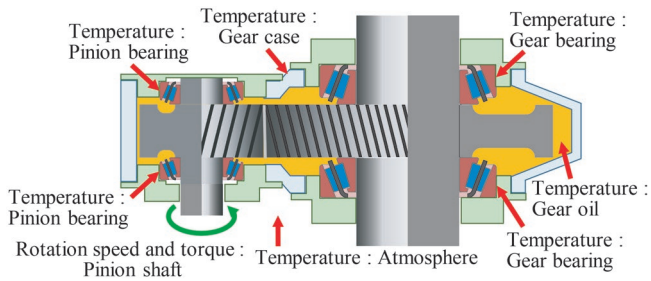


**Fig. 5 Measuring items**

after the start of rotation, the speed of the pinion shaft accelerates to  $6000 \text{ min}^{-1}$  in 315 s. This corresponds to a speed of approximately 320 km/h in a typical high-speed vehicle. The EP value during assembly ( $20^\circ\text{C}$ ) is 0.11 mm for the tapered roller bearings and 0.21 mm for the cylindrical roller bearings with ribs. As mentioned in section 3.1, the atmospheric conditions of the gear unit are air-cooled by blowers ( $10 \text{ m/s}$  at all times during the rotation test) in the rotation tests and cooled by the cooling system (only before the start of rotation) in the warm-up tests from low temperatures. The first part of the rotation pattern is the same in both tests, but in the warm-up tests from low temperatures, the rotation is decelerated from 1800 s after the start of rotation and stopped at 2100 s to complete the test.

**Table 2 Test conditions**

Direction of pinion rotation	Clockwise Counter clockwise (In a view from the motor side)	
Rotation pattern	See Fig. 6	
Lubricants	Oil type	Gear oil (Base oil: Mineral oil)
	Kinematic viscosity	$9.9 \text{ mm}^2/\text{s}$ ( $100^\circ\text{C}$ ) $78.7 \text{ mm}^2/\text{s}$ ( $40^\circ\text{C}$ )
	Viscosity index	105
Oil quantity	2.95 L	

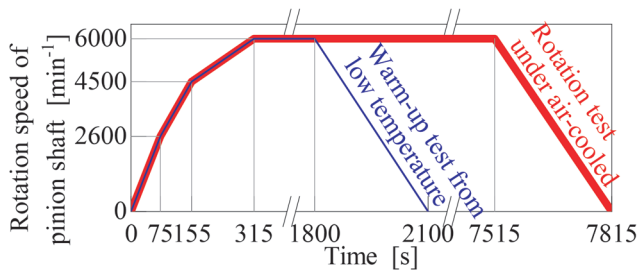


**Fig. 6 Rotation pattern**

### 3.3 Results and discussion

#### 3.3.1 Air-cooled rotation test

The temperatures of the gear unit and the torque of the pinion shaft in the air-cooled rotation tests are shown in Fig. 7. The temperature rise per 10 s of the pinion bearings from the start of rotation to 1800 s is shown in Fig. 8. In Fig. 7 and Fig. 8, (a) shows the results for forward rotation (CW), and (b) shows the results for reversed rotation (CCW). It should be noted that the pinion bearing on the motor side is denoted here as PM and the pinion bearing on the opposite side as PW.

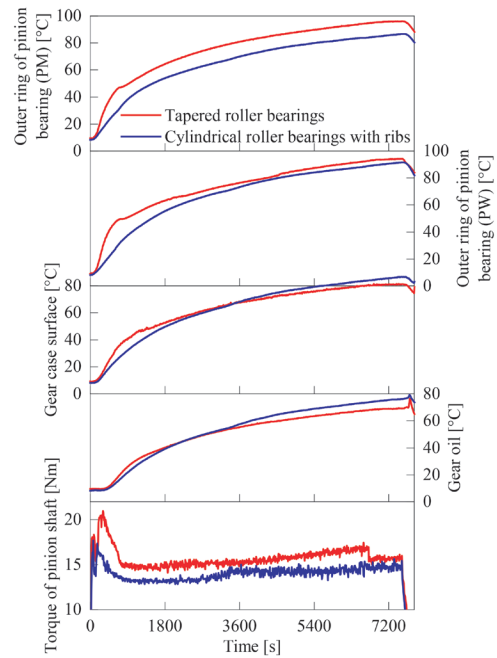


**Fig. 7(a) Temperatures and torque in air-cooled rotation test (CW)**

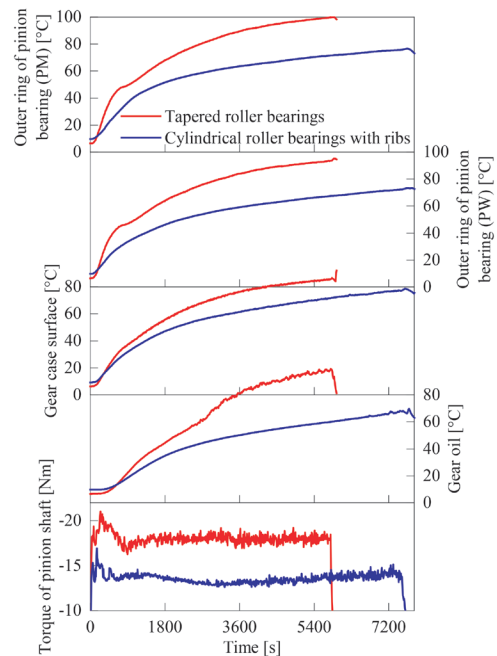


**Fig. 7(b) Temperatures and torque in air-cooled rotation test (CCW)**

Firstly, the results for CW rotation are discussed. Regardless of the PM bearing and PW bearing, the temperature rise during approximately 600 s from the start of rotation is slower for the cylindrical roller bearings with ribs than the tapered roller bearings (Fig. 7(a)). This is thought to be because in the case of the tapered roller bearings, the difference in thermal expansion between the gear case and the pinion shaft reduced the EP value of the original assembly by approximately 0.05-0.06 mm [1, 8]. As the EP value decreases, the load zones of the bearings widen and the heat generated by the rolling viscous resistance inside the bearings increases. On the

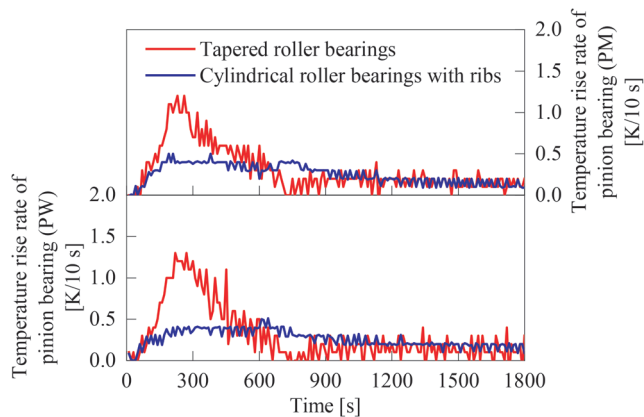


**Fig. 8(a) Temperature rise of pinion bearings in air-cooled rotation test (CW)**

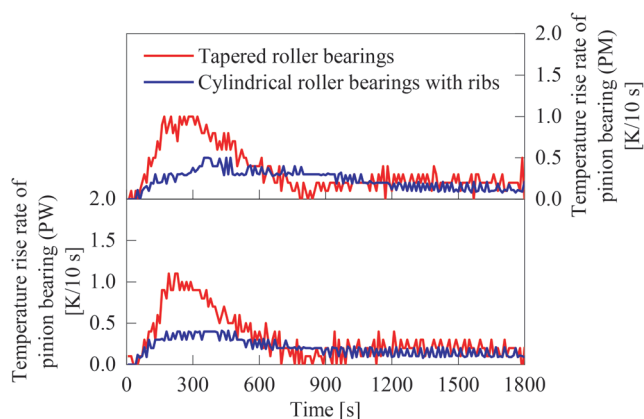


**Fig. 8(b) Temperature rise of pinion bearings in air-cooled rotation test (CCW)**

other hand, the load zones do not change significantly even if the EP value of the cylindrical roller bearings with ribs changes. The maximum temperature rise per 10 s is lower for the cylindrical roller bearings with ribs (PM: 0.5 K/10 s, PW: 0.5 K/10 s) than the tapered roller bearings (PM: 1.2 K/10 s, PW: 1.3 K/10 s) (Fig. 8(a)). Although the temperatures of the gear case and gear oil do not show as clearly as the temperatures of the bearings due to structural differences, the temperature rise during approximately 900 s from the start of rotation is more rapid in the tapered roller bearings. In both structures, the torque of the pinion shaft is high immediately after the start of rotation, but then gradually decreases to approximately 1800 s. The high kinematic viscosity of the gear oil at low temperatures immediately after the start of rotation, causes stirring resistance of the gear oil by the gear, stirring resistance of the gear oil inside the bearings and rolling viscous resistance of the gear oil inside the bearings. The reason for the above-mentioned results is thought to be due to these relatively large resistances. The torque of the cylindrical roller bearings with ribs is lower than that of the tapered roller bearings (Fig. 7(a)). This is thought to be because, as mentioned above, the EP value decreases in the tapered roller bearings due to the difference in thermal expansion between the gear case and the pinion shaft, which widens the load zone of the bearing and increases the rolling viscous resistance inside the bearings.

Secondly, the results for the case of CCW rotation are discussed. The temperature of each part of the gear unit, especially the gear oil, rises rapidly in the tapered roller bearings after about 3000 s from the start of rotation. The test was terminated when the tem-

perature of the gear oil reached 100°C. As shown in Fig. 1, the distance of the gear oil flow path from the oil sump to the bearings is shorter in CCW rotation than in CW rotation. Therefore, when the temperature of the gear oil rises and its kinematic viscosity decreases, more gear oil than in CW rotation splashes directly onto the front face of the bearing. This process explains the above-mentioned temperature rise. In addition, in the tapered roller bearing, the gear oil flows from the rear face to the front face [9], the splashed gear oil flow and the gear oil flow inside the bearing face each other and collide. Therefore, the amount of gear oil retained inside the bearing increases, so that the stirring resistance and rolling viscous resistance increase. This is also considered to be the reason for the temperature rise. The temperature rise of the PM and PW bearings during approximately 600 s from the start of rotation is slower for the cylindrical roller bearings with ribs than the tapered roller bearings (Fig. 7(b)). The maximum temperature rise per 10 s is also lower for the cylindrical roller bearings with ribs (PM: 0.5 K/10 s, PW: 0.4 K/10 s) than for the tapered roller bearings (PM: 1.0 K/10 s, PW: 1.1 K/10 s) (Fig. 8(b)). The torque is also lower for the cylindrical roller bearings with ribs than the tapered roller bearings (Fig. 7(b)). The reasons for the differences due to these structures are all the same as in the forward rotation case above.

### 3.3.2 Warm-up test from low temperature

The temperatures of the gear unit and the torque of the pinion shaft in the warm-up tests from low temperatures are shown in Fig. 9. The temperature rise per 10 s of the pinion bearings is shown in Fig. 10. In Fig. 9 and Fig. 10, (a) shows the results for forward rotation (CW), and (b) shows the results for reverse rotation (CCW).

Firstly, the results for CW rotation are discussed. The temperature rise of the PM and PW bearings during approximately 600 s from the start of rotation is slower for the cylindrical roller bearings with ribs than the tapered roller bearings (Fig. 9(a)). This is because, as described in section 3.3.1, the EP value of the tapered roller bearings decreases due to the difference in thermal expansion between the gear case and the pinion shaft. As a result, there is almost no internal clearance between the bearings, so the heat generated by the rolling viscous resistance inside the bearings increases. On the other hand, for the cylindrical roller bearings with ribs, the heat generated by the bearing does not change significantly unless the EP value falls below 0 mm. The maximum temperature rise per 10 s is lower for the cylindrical roller bearings with ribs (PM: 1.0 K/10 s, PW: 0.9 K/10 s) than the tapered roller bearings (PM: 1.7 K/10 s, PW: 1.5 K/10 s) (Fig. 10(a)). The temperatures of the gear case and gear oil do not show as clear as a difference between the structures of the temperatures of the bearings. However, the temperature rise of the gear case during approximately 600 s from the start of rotation and the temperature rise of the gear oil during approximately 1200 s from the start of rotation are more rapid in the tapered roller bearings. In both structures, the torque of the pinion shaft is high immediately after the start of rotation, but then gradually decreases until approximately 900 s. This is thought to be due to the high kinematic viscosity of the gear oil at low temperatures immediately after the start of rotation. The torque is lower for the cylindrical roller bearings than the tapered roller bearings for most of the duration of the experiment (Fig. 9(a)).

Secondly, the results for the case of CCW rotation are discussed. The temperature rise of the PM and PW bearings during approximately 600 s from the start of rotation is slower for the cylindrical roller bearings with ribs than the tapered roller bearings (Fig. 9(b)). The maximum temperature rise per 10 s is also lower in the case of the cylindrical roller bearings with ribs (PM: 0.7 K/10 s,

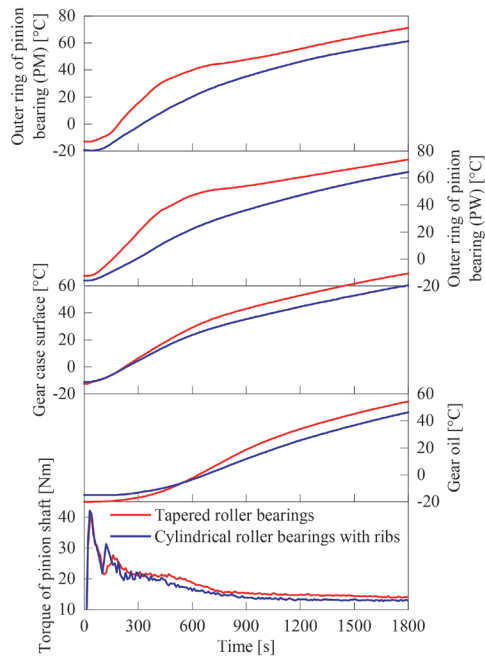


**Fig. 9(a) Temperatures and torque in warm-up test from low temperature (CW)**

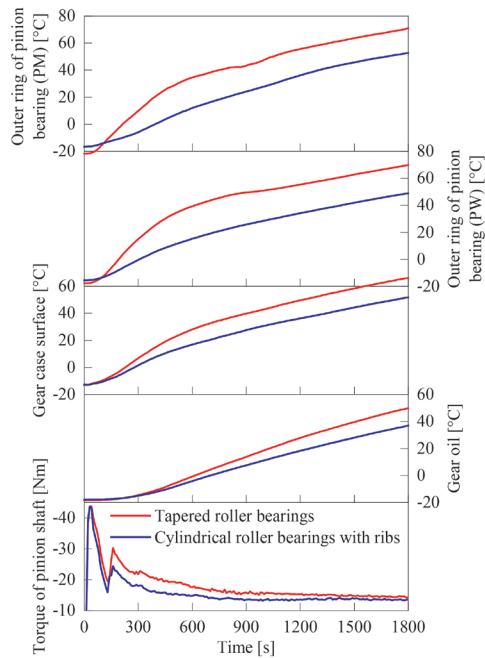


**Fig. 9(b) Temperatures and torque in warm-up test from low temperature (CCW)**

PW: 0.8 K/10 s) than the tapered roller bearings (PM: 1.5 K/10 s, PW: 1.7 K/10 s) (Fig. 10(b)). The torque is also lower in the case of the cylindrical roller bearings with ribs than the tapered roller bearings (Fig. 9(b)).

### 3.3.3 Relationship between gear oil viscosity and torque

The torque is discussed in terms of the kinematic viscosity of the gear oil. The viscosity was obtained from ASTM-Walther equation [10] using the gear oil specifications shown in Table 2. The re-

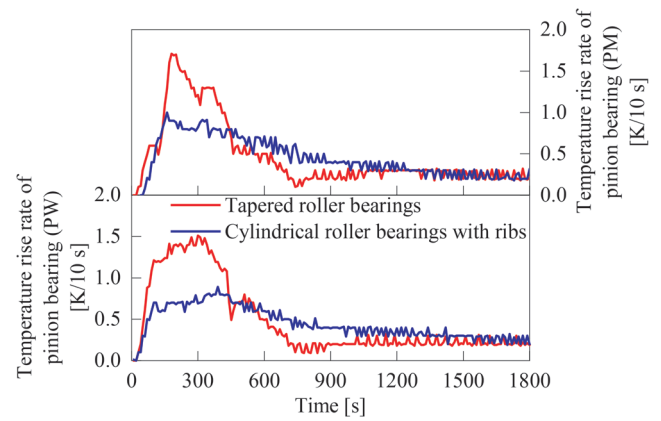


**Fig. 10(a) Temperature rise of pinion bearings in warm-up test from low temperature (CW)**

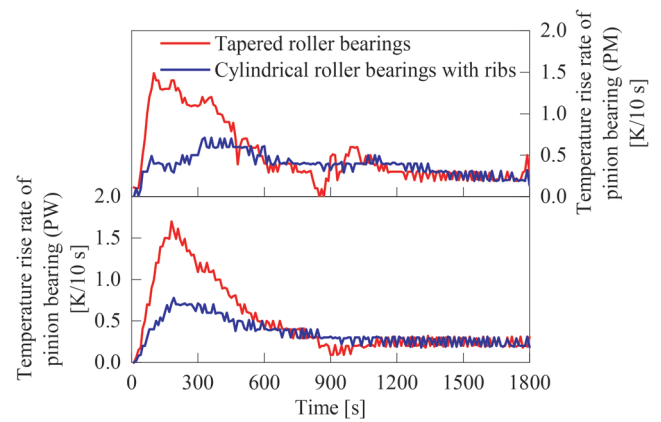


**Fig. 10(b) Temperature rise of pinion bearings in warm-up test from low temperature (CCW)**

lationship between the viscosity and the pinion shaft torque during the rotation test (only at the maximum rotation speed shown in Fig. 6) is shown in Fig. 11. Figure 11 (a) shows the relationship in CW rotation and Fig. 11 (b) in CCW rotation.

From Fig. 11, it is found that, in both directions of rotation, the torque increases with increasing viscosity in the range of viscosity above approximately 100 mm<sup>2</sup>/s. On the other hand, when the viscosity falls below about 100 mm<sup>2</sup>/s, the torque remains unchanged or increases slightly. This is thought to be because the amount of the gear oil supplied into the bearing increases due to the decrease in the viscosity caused by the rise in temperature, which in turn increases the stirring resistance inside the bearing.

The cylindrical roller bearings with ribs exhibit lower torque than the tapered roller bearings for the same viscosity. The reasons for this are that, as mentioned above, the EP value of the tapered roller bearings decreases due to the difference in thermal expansion between the gear case and the pinion shaft. As the EP value decreases, the load zones of the bearings widen and the heat generated by the rolling viscous resistance inside the bearings increases.

## 4. Conclusions

The findings of this study are summarized as follows.

- (1) In the air-cooled rotation tests, it was found that the temperature rise immediately after the start of rotation was lower for the cylindrical roller bearings with ribs than for the tapered roller bear-

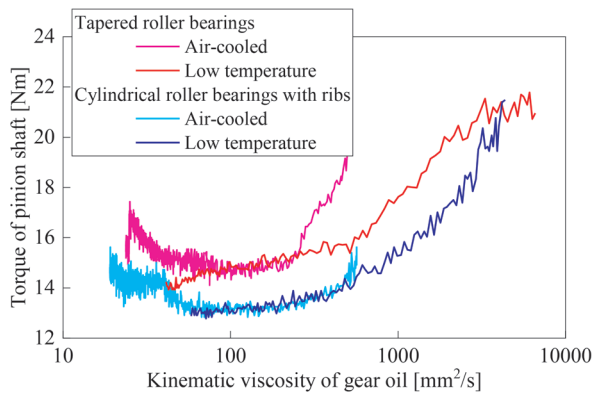


**Fig. 11(a) Relationship between gear oil viscosity and torque (CW)**

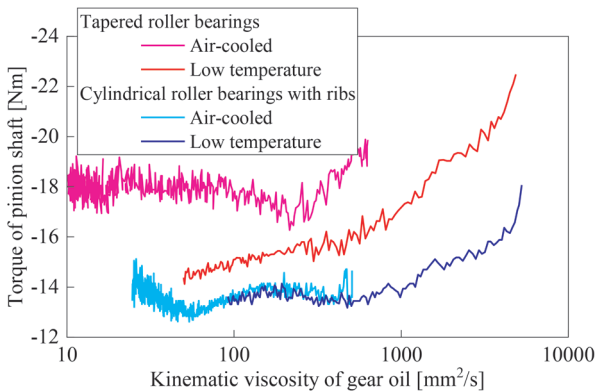


**Fig. 11(b) Relationship between gear oil viscosity and torque (CCW)**

ings in both CW and CCW rotations. Accordingly, the maximum temperature rise per 10 s was 0.4-0.5 K/10 s for the cylindrical roller bearings with ribs, compared with 1.0-1.3 K/10 s for the tapered roller bearings. The torque was also lower for the cylindrical roller bearings with ribs than the tapered roller bearings.

(2) Similar to (1), the temperature rise immediately after the start of rotation was lower for the cylindrical roller bearings with ribs than for the tapered roller bearings in both CW and CCW rotations in the warm-up tests from low temperatures. Accordingly, the maximum temperature rise per 10 s was 0.7-1.0 K/10 s in the

case of the cylindrical roller bearings with ribs, compared with 1.5-1.7 K/10 s for the tapered roller bearings. The torque was also lower for the cylindrical roller bearings with ribs than the tapered roller bearings.

(3) The test results of (1) and (2) were considered in relation to gear oil viscosity, and it was found that the cylindrical roller bearings with ribs exhibited lower torque than the tapered roller bearings at the same gear oil viscosity in both CW and CCW rotations.

## References

- [1] Takahashi, K., Suzuki, D., and Nagatomo, T., "Effects of bearing clearance and atmospheric temperature on performance of pinion bearings of railway vehicles," *JAMDSM*, Vol. 14, No. 4, p. 20-00048, 2020.
- [2] Suzuki, D., Takahashi, K., Okamura, Y., et al., "Load state of tapered roller bearings used for pinion gear of gear units in electric railway vehicle," *Trans JSME*, Vol. 88, No. 910, p. 22-00060, 2022 (in Japanese).
- [3] Nishikawa, T., Suzuki, K., Orito, W., et al., "Product Development of Rolling Bearings for Railway Vehicles," *NTN TECHNICAL REVIEW*, No. 88, pp. 21-26, 2020 (in Japanese).
- [4] Cho, E., Iwanami, K., Goto, K., et al., "Development of Double Helical Gear (Division type Gear) Driving Device for Shinkansen," *Proceedings of the 22th Jointed Railway Technology symposium*, P. 3704, 2015 (in Japanese).
- [5] Kamiya, M., Asano, J., Kanamori, S., et al., "Development of double helical gear for Shinkansen," *Proceedings of the 25th Jointed Railway Technology symposium*, P. 3312, 2018 (in Japanese).
- [6] SKF, *Railway technical handbook*, Vol. 2, p. 48, 2012.
- [7] Takahashi, K., Suzuki, D., and Nagatomo, T., "Effect of bearing types on performance of bearings for gear units of railway vehicles," *Transactions of the JSME*, Vol. 88, No. 911, p. 22-00126, 2022 (in Japanese).
- [8] Takahashi, K., Suzuki, D., and Nagatomo, T., "Investigation of factors affecting the performance of pinion bearing for gear unit of railway vehicle," *Transactions of the JSME*, Vol. 85, No. 876, p. 19-00181, 2019 (in Japanese).
- [9] Omori, T., Okamoto, J., and Wakabayashi, T., "Korogarijikuuke no pompu sayou," *Proceedings of Tribology Conference in Kitakyusyu*, pp. 429-431, 1996 (in Japanese).
- [10] ASTM D2160-92, *Standard Test Method for Thermal Stability of Hydraulic Fluids*, 1992.

## Authors



**Ken TAKAHASHI**, Ph.D.  
Senior Researcher, Lubricating Materials Laboratory, Materials Technology Division  
Research Areas: Tribology, Machine Elements, Rolling Bearings



**Sadayuki KIKAWA**  
Assistant Senior Researcher, Lubricating Materials Laboratory, Materials Technology Division  
Research Areas: Tribology, Lubricants



**Daisuke SUZUKI**, Dr.Eng.  
Assistant Senior Researcher, Lubricating Materials Laboratory, Materials Technology Division  
Research Areas: Tribology, Machine Elements, Rolling Bearings

# Improvement of Flame Retardancy of Seat Cushion Materials for Railway Vehicles Using Intumescent Flame Retardant

Tadashi TOYOHARA

Sho YAMANAKA

Vibration-Isolating Materials Laboratory, Materials Technology Division

Mikiya ITO

Market Planning, Marketing & Business Development Division

*In order to further improve the flame retardancy of seat materials in railway vehicles, the authors investigated the use of new flame-retardants. During the selection phase of flame retardants, their attention was focused on intumescent flame-retardants. Intumescent flame-retardant expands and produces char foam during the burning process, and the produced char foam plays a role as a protective shield against rapid flame spread. Various test pieces using the flame-retardants were prepared to confirm their characteristics. The results of cone calorimeter fire tests found that insertion of a resin containing intumescent flame-retardants into the existing seat cushions can improve flame retardancy.*

**Key words:** train fire, flammability test, materials for railway vehicles, intumescent flame retardant

## 1. Introduction

Safety standards for Japanese railway vehicles are stipulated by the “Ministerial Ordinance Establishing Technical Standards for Railways” and the standards for interpretation of the same, and standards regarding flammability are also determined by the same ministerial ordinance [1].

As a test method for evaluating flammability, a railway vehicle material flammability test (hereinafter referred to as “vehicle material flammability test”) using an alcohol lamp is specified, assuming a small fire source such as a cigarette. The combustibility classification is determined as extremely flame retardant, flame retardant, slow flame, and flammable.

In addition, combustibility classifications are specified according to the area of use, such as wall and ceiling materials being non-combustible, and seating surfaces and flooring materials being flame-retardant.

Vehicle material combustion testing has contributed to ensuring the safety of railway vehicles in Japan against fire.

However, in recent years, there have been cases where materials are loaded with fire sources such as gasoline, which have a higher calorific value than previously expected.

In response to these trends, the Railway Research Institute has conducted cone calorimeter combustion tests on materials for railway vehicles used in Japan under the assumption of a large fire source, and also conducted combustion tests on full-scale express vehicle seats [2]. As a result, it has been confirmed that among the materials used in railway vehicles, seat material burns violently [3].

In addition, the polymer seat materials used for seats, such as cushions, weigh approximately 6 kg [4] per seat, and because they have a relatively large mass, it is thought that their contribution during combustion is also large.

In this study, we therefore decided to use intumescent flame retardants [5] (hereinafter referred to as IFR flame retardants) to further improve the flame retardancy of seat materials for railway vehicles.

We first confirmed the combustion characteristics of the resins containing IFR-based flame retardants (hereinafter referred to as

IFR blended resin) using CCM tests.

Secondly, as a method for applying IFR blended resins to seat materials, we investigated the combustion behavior of the seat when the IFR blended resin is inserted into the seat material.

## 2. Test conditions and Test contents

### 2.1 Overview of CCM tests

The CCM test is a combustion test that assumes a large fire source, and is a test method specified in ISO5660-1.

A feature of the test is that it can quantitatively evaluate the amount of heat generated during combustion and the amount of smoke generated when the test specimen burns by applying radiant heat using a conical heater (Fig. 1).

CCM tests are also carried out as one of a series of evaluation tests for building materials in Japan and for railway vehicles abroad. In 2003 an arson incident occurred in the Daegu Municipality Underground in South Korea. In response to this arson incident, the domestic ministerial ordinance whose interpretation standards were revised in 2004 also introduced a CCM test for ceiling materials of



Fig. 1 Appearance of CCM test

passenger cars such as subways and Shinkansen trains.

## 2.2 Test piece

The specimen dimensions for the CCM test are 100 mm long and 100 mm wide, and actual thickness is 50 mm or less [6]. Therefore, the test pieces in this paper used these dimensions.

### 2.2.1 Resin test piece

In order to compare the combustion characteristics of various flame retardants, test pieces were prepared using IFR compounded resins, and test pieces were also prepared using resins containing magnesium-based flame retardants (hereinafter referred to as Mg-based flame retardants) and bromine-based flame retardants (hereinafter referred to as Br-based flame retardants), which are conventional general-purpose flame retardants. Polypropylene was used as the base resin to be blended. In addition, for comparison, test pieces without flame retardants were also prepared (hereinafter referred to as 0%).

Mg-based flame retardants do not emit toxic gases derived from the flame retardant, but because a large amount of the flame retardant must be added, the physical properties of the resin are reduced and the specific gravity is increased.

Br-based flame retardants can suppress heat generation but generate large amounts of smoke and toxic gases when burned.

IFR flame retardants, however, have the characteristic of suppressing combustion by foaming when the resin burns, providing an insulating effect and preventing gas diffusion (5).

The test pieces of resins containing various flame retardants were rectangular plate-shaped with a thickness of 2 mm.

The flame retardant composition in the test piece was 60% Mg-based flame retardant (hereinafter referred to as Mg60%), 20% Br flame retardant (hereinafter referred to as Br20%), and 8 to 60% IFR (hereinafter referred to as IFR8% to 60%).

Furthermore, IFR30%, IFR40% and IFR60% have been separately tested on vehicle materials and confirmed to be flame retardant.

### 2.2.2 Test piece combining resin and seat material

In order to apply IFR blended resins to seat material, test specimens were prepared using the above-mentioned combination of resin and padding, and the combustion characteristics of the padding used as seat cushioning material were evaluated. Table 1 shows an overview of the conditions for the test pieces prepared, and Fig. 2 shows the appearance of the test pieces.

As shown in Table 1, fillings were inserted into the resin under three conditions A to C. The stuffing used in the test is a commonly used urethane cushioning material that has been certified as flame retardant in vehicle flame tests.

The thickness of the padding as a product is 10 mm, and in real vehicle seats, this product is used in multiple layers. The thickness of the laminated padding varies depending on the car model, but is approximately several tens of millimeters.

In this test, as mentioned above, the standard stipulates that the specimen thickness for the CCM test should be 50 mm or less, so as shown in Table 1, even if a 2 mm thick resin is inserted, the overall thickness must be 50 mm or less.

Therefore, in the CCM test, four pieces of filling were laminated to form a test piece with a thickness of 40 mm. The details of the test conditions are described below.

**Table 1 Summary of test piece conditions**

Cond A		Evaluate differences due to resin size
Cond B		Evaluate differences depending on resin insertion position
Cond C		Evaluate differences depending on type and amount of flame retardant added

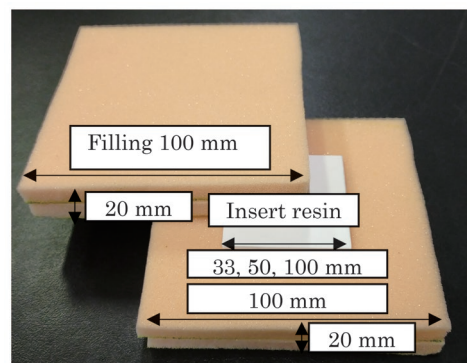


**Fig. 2 Image of test piece**

#### Condition A (size of resin)

The resin inserted in condition A was IFR 60%, which is assumed to have the highest flame retardancy among the resins listed in the previous section, based on the results of vehicle material flame tests. Regarding the dimensions of IFR60% to be inserted, the thickness was 2 mm, and the sizes were 100 mm square, 50 mm square, and 33 mm square. The reason for conducting the tests with different sizes is that the CCM test states that the material is to be designed in the same way as in 100 mm squares, but when the same material is actually applied to the filling, not only the placement over on the entire surface, but also the focused placement in some locations needs to be considered. Therefore, the influence of the amount of insertion was also evaluated.

#### Condition B (position of resin insertion)

In condition B, in order to evaluate the influence of the resin insertion position, the combustion behavior was compared between two conditions: inserting the resin in the middle (20 mm thick part) of the 40 mm thick filling and inserting it at the bottom. The resin to be inserted was the IFR60%, and the resin sizes were 100 mm square and 50 mm square.

#### Condition C (type and composition of resin flame retardant)

In condition C, we evaluated the effects of the type and amount of flame retardant added to the resin as described in Section 2.2.1.

## 2.3 Test method

In the CCM test, the test piece described above was fixed in a stainless steel holder and placed 25 mm directly below the conical heater as shown in Fig. 3. As the test begins, the separator placed between the heater and the test piece that blocks the heat from the heater moves, and the test piece begins to be heated.

At the same time, an electric spark was generated 10 mm above the test piece to ignite the flammable gas generated from the test

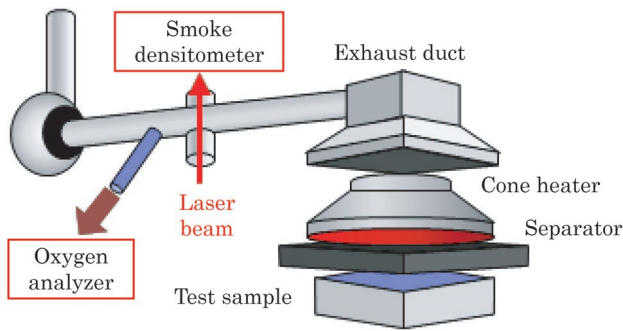
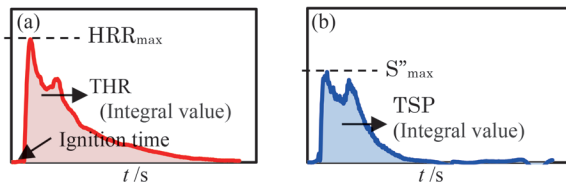


Fig. 3 Overview of CCM fire test



(a) Heat release rate (b) Smoke production rate

Fig. 4 Image of CCM fire test result

piece by heating. The test time was at least 10 minutes after the start of heating, and the test was continued until the specimen was extinguished.

The test was carried out three or more times, and the average of the results was used as the measurement result.

In the European standards for fire protection of railway rolling stock, the combustion test of stuffing specimens is conducted at a radiant heat value of 25 kW/m<sup>2</sup> [7].

In this study, however, the value was set at 50 kW/m<sup>2</sup> in order to grasp the flammability of the stuffing when it burns intensely, assuming a large fire source.

However, even under the same conditions, the variation in ignition time was large, ranging from tens of seconds to several hundred seconds, making accurate evaluation difficult.

The evaluation items in the CCM test were the ignition time, maximum heat release rate (hereinafter referred to as HRR<sub>max</sub>), total heat release value (hereinafter referred to as THR), and maximum smoke production rate (hereinafter referred to as S''<sub>max</sub>) based on the measurement results.

Figure 4 shows an image of the evaluation items obtained from the test results. As shown in Fig. 4(a), the ignition time, HRR<sub>max</sub>, and THR were determined from the measured heat release rate. In addition, with reference to the evaluation time of the CCM test in Ministerial Ordinance (1), the values were evaluated up to 600 seconds.

In this test, the heat generation rate was determined by the oxygen consumption method.

This means that while the calorific value per unit mass of a substance due to combustion varies greatly from substance to substance, if the amount of oxygen consumed in combustion is used as a standard, it is independent of the type of substance and is 13.1 MJ per 1 kg of oxygen. This takes advantage of the fact that it has an almost constant value [8].

The smoke production rate can be measured simultaneously with the above-mentioned heat release rate, and the amount of smoke generated can be determined from the change in the transmittance of the laser light that occurs when the smoke (fine particles) generated as the test piece burns passes through the exhaust duct.

The evaluation item was S''<sub>max</sub> shown in Fig. 4(b).

### 3. Test results

#### 3.1 Test results of resin test pieces

A summary of the test results for the resin test pieces is shown in Table 2. As an example, Fig. 5 shows the test situation for IFR60%.

Focusing on the ignition time, it took about 15 seconds for 0%, while it took 42 seconds for Mg60% and 34 seconds for Br20%, showing a tendency for the ignition time to be slower than for 0%.

On the other hand, the ignition time of the IFR blended resin was 15 to 22 seconds, which was equal to 0% or faster than that of the resins blended with general-purpose flame retardants. This is because the IFR flame retardant is designed to reduce the amount of radiant heat loaded onto the resin and to suppress the spread of combustion by foaming the flame retardant to cover the test piece, although at the first stage accelerating the ignition of the test piece.

Therefore, although the IFR blended resin has a faster ignition time than general-purpose flame retardants, it is considered to have sufficient flame retardancy when judged comprehensively from the results of other evaluation items as described below.

Focusing on HRR<sub>max</sub>, 0% had the highest value of 935 kW/m<sup>2</sup>, resulting in intense combustion. This was followed by IFR8%, Br20%, and IFR15%. In contrast, HRR<sub>max</sub> was significantly reduced at with Mg60% and IFR30% to IFR60%.

In the case of the IFR compound resin, it is thought that the design that suppresses the spread of combustion was effective as described above. In particular, it was confirmed that IFR30% can reduce HRR<sub>max</sub> even though the amount of flame retardant added is less than Mg60%, and is considered to be a highly effective flame retardant.

Focusing on S''<sub>max</sub>, Br20% had the highest value, followed by 0%, IFR8%, and IFR15% at the same level. The reason why Br20% had the highest S''<sub>max</sub> is that this is a characteristic of this flame retardant, but while it can reduce HRR<sub>max</sub>, bromine inhibits the uptake of oxygen during combustion, resulting in incomplete combustion.

Table 2 Test results of resin test pieces

Type of resin	Ignition time	HRR <sub>max</sub>	S'' <sub>max</sub>	THR
	s	kW/m <sup>2</sup>	m <sup>2</sup> /m <sup>2</sup> /s	MJ/m <sup>2</sup>
0%	15	935	11.8	60
Mg60%	42	246	3.4	57
Br20%	34	490	30.3	36
IFR8%	21	498	8.0	66
IFR15%	15	349	6.3	57
IFR30%	22	129	1.8	42
IFR40%	18	103	1.1	37
IFR60%	19	61	1.2	10

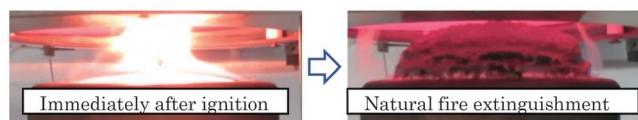


Fig. 5 IFR60% test situation

This is thought to have increased smoke production. On the other hand,  $S''_{max}$  was significantly reduced with Mg60%, IFR30%, IFR40%, and IFR60%. It is thought that  $S''_{max}$  was greatly reduced with the IFR blended resin containing 60% Mg and a large amount of IFR because of the combustion expansion suppression effect, similar to  $HRR_{max}$ .

Focusing on THR, it was high with 0%, Mg60%, and IFR8-15%, and the lowest with IFR60%. This is thought to be because, while 0% and 60% Mg were mostly burned within the evaluation time range of 600 seconds, 20% Br and 30% to 60% IFR continued to burn even after 600 seconds.

The results of the CCM test on the resin test piece showed that, although the effect of IFR60% on ignition time was small, the foaming of the IFR flame retardant exhibited self-extinguishing properties, suppressing not only  $HRR_{max}$  but also the change over time of the heating rate to a greater extent than in other tests. Thus, resins containing more than 30% IFR showed better flame retardancy than resins containing other flame retardants. In particular, when IFR was mixed at 60%, the test specimen self-extinguished rapidly after ignition, and the change in heat release rate over time was suppressed compared to other test specimens, so it is thought to exhibit excellent flame retardancy.

### 3.2 Test results of specimens combining resin and seat material

#### 3.2.1 Condition A (size of resin)

Figure 6 shows the appearance of the test pieces before and after the test under condition A. Table 3 gives a summary of the test results. Note that, hereinafter, the condition where no resin is inserted is referred to as condition X.

As shown by the post-combustion appearance in the bottom row of Fig. 6, black solid residue was observed after combustion when resin was inserted. It was also found that the larger the resin, the larger the residue. This is thought to be because the larger the area of the resin, the more the IFR foams during combustion.

Focusing on the ignition time shown in Table 3, the ignition

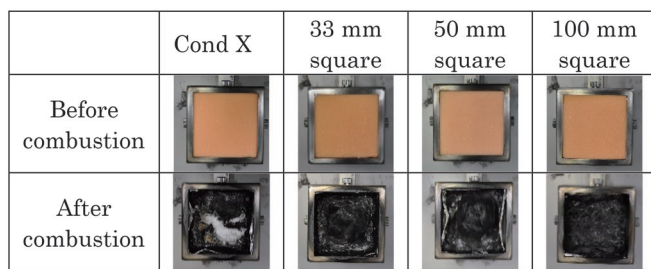


**Fig. 6 Appearance of test piece before and after CCM test under condition A**

**Table 3 Test results under condition A**

Resin size mm	Ignition time s	$HRR_{max}$ kW/m <sup>2</sup>	$S''_{max}$ m <sup>2</sup> /m <sup>2</sup> /s	$THR$ MJ/m <sup>2</sup>
Cond X	6	490	4.4	61
33	5	483	5.4	66
50	5	288	4.3	72
100	6	208	4.0	24

time was approximately the same for all test specimens at 5 to 6 seconds. This is because the filling close to the conical heater ignited first, which means that combustion started at about the same time, rather than due to the influence of the inserted resin.

Focusing on  $HRR_{max}$  condition X without inserting resin was 490 kW/m<sup>2</sup>, while it was almost the same at 483 kW/m<sup>2</sup> when a 33 mm square test piece was inserted. On the other hand, when 50 mm square and 100 mm square test pieces were inserted, the power consumption was 288 kW/m<sup>2</sup> and 208 kW/m<sup>2</sup>, respectively, which was significantly lower than Condition X.

$S''_{max}$  was at the same level in all cases. This is thought to be due to the fact that a certain amount of smoke is generated when the filling material burns, and even if the combustion is suppressed using the IFR blended resin, the maximum value cannot be reduced.

Focusing on THR, when inserting 33 mm square and 50 mm square resins, the larger the resin, the larger the THR. This is thought to be due to an increase in the amount of combustible resin, as IFR60% is composed of 40% resin and 60% IFR flame retardant. It should be noted that the reduction was significant at 100 mm square, but this is thought to be due to combustion being suppressed within the evaluation time of 600 seconds.

#### 3.2.2 Condition B (test results according to different insertion positions)

In order to evaluate the effect of the resin insertion position on the combustion characteristics, Table 4 shows the test results when the resin was inserted in the middle and bottom under the same conditions.

The ignition time was approximately the same at 5 to 6 seconds for all resin conditions and insertion positions. This is considered to be for the same reason as for condition A.

Focusing on  $HRR_{max}$ , it was 490 kW/m<sup>2</sup> for condition X, which is the standard, and was the highest in condition B. On to 50 mm square, the  $HRR_{max}$  when inserted in the middle was about 40% lower than for Condition X, and the  $HRR_{max}$  when inserted at the bottom was about 20% lower than under Condition X. Furthermore, when the dimensions of IFR60% were set to 100 mm square, the  $HRR_{max}$  when inserted in the middle was reduced by about 60% compared to condition X, and the  $HRR_{max}$  when inserted at the bottom was reduced by about 45% compared to condition X. Focusing on  $S''_{max}$ , it was thought that it was about the same in the middle and bottom cases. This is also thought to be due to the fact that a certain amount of smoke is generated when the filling material burns, and even if the combustion was suppressed using the IFR blended resin, the maximum value could not be reduced.

Focusing on THR, when the IFR60% dimension was a 50 mm square, the value was about the same whether the insertion point

**Table 4 Test results under condition B**

Resin	Insertion position	Ignition time s	$HRR_{max}$ kW/m <sup>2</sup>	$S''_{max}$ m <sup>2</sup> /m <sup>2</sup> /s	$THR$ MJ/m <sup>2</sup>
Cond X		6	490	4.4	61
50 mm square IFR 60%	Middle	5	288	4.3	72
	Bottom	6	377	4.3	71
100 mm square IFR 60%	Middle	6	208	2.4	24
	Bottom	5	267	2.4	35

was in the middle or at the bottom, but when it was a 100 mm square, the value was smaller in the middle. In the case of the 50 mm square, the weight of the flammable stuffing and the inserted resin was about the same, and it is thought that all the combustibles burned, resulting in about the same weight. On the other hand, in the case of the 100 mm square, the fire was not extinguished within the evaluation target of 600 seconds and combustion continued, so it is thought that the intermediate condition, where combustion was delayed more, was more effective. As mentioned above, focusing on the  $HRR_{max}$  in this test result, it is considered that inserting the IFR compound resin in the middle rather than at the bottom has a higher flame-retardant effect.

### 3.2.3 Condition C (test results due to different flame retardants)

Based on the results of Condition A and B described above, the size of the resin to be inserted was set to a 50 mm square, the insertion position was set in the middle, and the effects of different flame retardants added to the resin and the amount added were evaluated.

Figure 7 shows the appearance of the test pieces before and after the test under condition C. Table 5 shows the test results.

The post-combustion appearance in the bottom row of Fig. 7 shows that when 60% Mg was inserted, a white solid residue was left after combustion, but under the other conditions, either a black solid residue remained or all of it was combusted. As shown in Table 5, the ignition times were all the same, as under condition A, regardless of the resin inserted in the middle, as the filling in the upper layer affected the ignition time.

Comparing  $HRR_{max}$ , condition X was 490 kW/m<sup>2</sup>, which was about the same as when 60% Mg was inserted. On the other hand, in the case of 0% and 20% Br, values were higher than those under condition X. When the IFR blended resin was inserted,  $HRR_{max}$  was

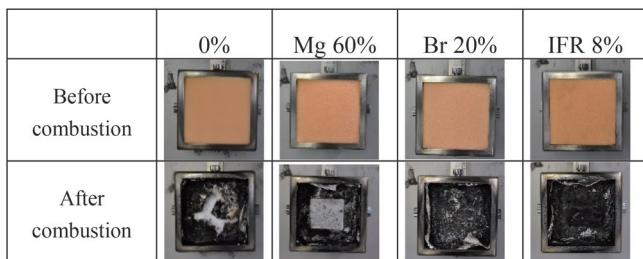


Fig. 7 Appearance before and after test depending on type of flame retardant inserted

Table 5 Test results under condition C

Type of resin	Ignition time	$HRR_{max}$	$S''_{max}$	$THR$
	s	kW/m <sup>2</sup>	m <sup>2</sup> /m <sup>2</sup> /s	MJ/m <sup>2</sup>
Cond X	6	490	4.4	61
0%	5	552	6.2	82
Mg 60%	5	496	4.6	75
Br 20%	5	675	12.9	75
IFR 8%	5	489	6.7	81
IFR 15%	5	439	6.0	80
IFR 30%	5	416	6.1	76
IFR 40%	5	333	5.0	74
IFR 60%	5	288	4.3	72

similar to condition X with IFR 8%, but in the case of IFR 15% to 60%,  $HRR_{max}$  decreased with increasing amount of IFR blends. In particular, when IFR60% was inserted,  $HRR_{max}$  was reduced by about 40% compared to Condition X. Comparing  $S''_{max}$ , it was 4.4 m<sup>2</sup>/m<sup>2</sup>/s for condition X but increased to 12.9 m<sup>2</sup>/m<sup>2</sup>/s when 20% Br was inserted. This is thought to be due to the characteristics of the flame retardant. In addition, there was also a slight increase in the other items, except for IFR 60%.

Comparing THR, the THR increased from 61MJ/m<sup>2</sup> under condition X to 72-82MJ/m<sup>2</sup> in the other conditions when the resin test pieces were inserted.

The THR is thought to have increased because the inserted resin is composed of a flame retardant and resin, and the resin part burned out within the evaluation time of 600 seconds.

Finally, Fig. 8 shows the change in heat release rate over time under condition C. As shown in Fig. 8 (a), although the addition of 60% Mg had the effect of slightly delaying combustion, there was almost no change in the overall combustion behavior. In addition, when 20% Br was inserted, although it had the effect of slightly delaying the initial combustion, the combustion in the latter half was more intense than under condition X. This is thought to be because after the 20% Br flame retardant was consumed, the remaining resin inserted together with the filling combusted violently.

Next, as shown in Fig. 8 (b), the insertion of IFR 8%, had the effect of delaying combustion compared to condition X, but the subsequent combustion behavior was almost at the same level. On the other hand, as the IFR content increases,  $HRR_{max}$  decreases, indicating that the overall combustion can be suppressed. This is thought to be because the IFR of the inserted resin foams formed due to heat generation, covering the resin and the burning filling, thereby blocking oxygen and radiant heat, and suppressing combustion. The fact that the insertions did not burn rapidly but gradually, compared to condition X, suggests that the insertion of IFR blended resin may reduce the overall combustion expansion of the composed stuffing.

From the above results in condition C, it was found that neither inserting resin into the filling like a shield plate nor containing a flame retardant in the inserted resin board is effective in suppressing the combustion of the filling, and that the IFR blended resin is not effective in suppressing combustion of the filling. It has been found that foaming is effective in suppressing the amount of radiant heat that is applied to the entire filling. However, in all cases, the ignition time was approximately 30 seconds after the start of the test. This is because the upper 20 mm of the 40 mm filling has the same composition in all conditions, and this part burned first, so similar results were obtained under all test conditions.

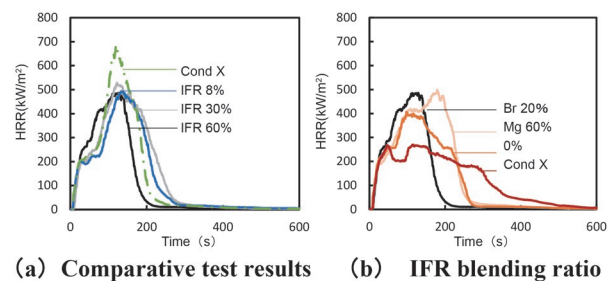


Fig. 8 Change in heat generation rate over time under condition C

#### 4. Summary

In order to further improve the flame retardancy of seating materials for railway vehicles, we focused on IFR flame retardants, which have high flame-retardant properties, and investigated a method of applying IFR blended resin containing the same flame retardants. The combustion characteristics were evaluated using CCM tests under conditions where the IFR blended resins were inserted into seat material. In the CCM tests, for comparison, the test pieces were resins mixed with various flame retardants and inserted into a filling, and the tests were carried out with the parameters of resin size, position of insertion into the fillings, and amount of blended resin. The following results were found.

- (1) In order to compare the combustion performance of various flame retardants including IFR flame retardants, CCM tests were carried out on resins blended with various flame retardants. The result showed that the IFR blended resin exhibits superior flame retardancy compared to general-purpose bromine-based flame retardants and magnesium-based flame retardants.
- (2) Regarding the influence of the size of the IFR blended resin inserted into the filling, it was found that piece size of approximately 50 mm square can suppress combustion, but the suppression effect is greater for larger sizes, such as 100 mm square. It was also found that placing the insert in the middle of the stuffing rather than at the bottom was more effective in suppressing combustion.
- (3) Regarding the influence of the type of flame retardant, it was found that when IFR blended resin was used, the combustion suppression effect was higher than when no resin was inserted or when a general-purpose flame retardant was compounded. This is thought to be due to the fact that the flame retardant foams on ignition, which is a characteristic of IFR, and the surrounding combustion behavior is suppressed.

As described above, it was found that by inserting IFR blended resin into the seat material as a filling, the combustion of the seat material can be suppressed. In the future, a full-scale evaluation will be carried out utilizing the same structure.

#### Authors



**Sho YAMANAKA**  
Researcher, Vibration-Isolating Materials  
Laboratory, Materials Technology Division  
Research Areas: Railway Fire, Polymer  
Sciences



**Tadashi TOYOHARA**  
Researcher, Vibration-Isolating Materials  
Laboratory, Materials Technology Division  
Research Areas: Railway Fire, Polymer  
Sciences

#### Acknowledgment

We would like to express our deepfelt gratitude to ADEKA Co., Ltd. for their cooperation during our joint research and study of resins for this project.

#### References

- [1] Ministry of Land, Infrastructure, Transport and Tourism, “Standards for interpretation of ministerial ordinances establishing technical standards for railways,” Chapter 8, Section 5, Article 83 (in Japanese).
- [2] Yamanaka, S., Toyohara, T., Ito, M., “Combustion Performance of Materials for Railway Rolling Stock under Large Radiation,” *Railway Research Institute Report*, Vol. 32, No. 10, pp. 5-10, 2018 (in Japanese).
- [3] Takano, J., Ishitsuki, M., Yamauchi, Y., Yamanaka, S., Toyohara, T., “Implementation of seat combustion test for railways and reproduction analysis using FDS,” *Proceedings of the 26th Railway Technology Union Symposium (J-RAIL2019)*, No. S-6-4-4, pp. 538-541, 2019 (in Japanese).
- [4] Ministry of Economy, Trade and Industry, Manufacturing Industries Bureau, Textile Division, Teijin Fibers Co., Ltd., “Development of lightweight cushioning materials” evaluation materials: [https://warp.da.ndl.go.jp/info:ndljp/pid/12323307/www.meti.go.jp/policy/tech\\_evaluation/c00/C0000000H20/081110\\_fiber/fiber08-6-4.pdf](https://warp.da.ndl.go.jp/info:ndljp/pid/12323307/www.meti.go.jp/policy/tech_evaluation/c00/C0000000H20/081110_fiber/fiber08-6-4.pdf) (Reference date: January 24, 2023) (in Japanese).
- [5] Yonezawa, Y., *Advances in intumescent flame retardants, The forefront of flame retardants and flame retardant materials*, CMC Publishing, pp. 90-96, 2015 (in Japanese).
- [6] ISO 5660-1:2015/Amd 1:2019, Reaction-to-fire tests — Heat release, smoke production and mass loss rate — Part 1: Heat release rate (cone calorimeter method) and smoke production rate (dynamic measurement) — Amendment 1.
- [7] EN45545-2:2020, Railway applications—Fire protection on railway vehicles part 2: Requirements for fire behavior of materials and components.
- [8] Hugget, C., *Fire and Materials*, No. 4, pp. 61-65, 1980.



**Mikiya ITO, Ph.D.**  
General Manager, Head of Market Planning,  
Marketing & Business Development Division  
Research Areas: Railway Fire, Polymer  
Sciences

# Method for Estimating Lateral Carbody Vibration Acceleration used for Safety Evaluation of Railway Vehicles against Crosswind

Hiroyuki KANEMOTO

Vehicle Mechanics Laboratory, Railway Dynamics Division

Yu HIBINO

Research and Development Promotion Division

*The critical wind speed for overturning is often evaluated using the “RTRI detailed equation.” In the equation, the lateral carbody vibration inertia force is considered to be the exerted force affecting overturning, and the lateral vibration acceleration is assumed from previous running test results. This paper shows that the critical wind speed for overturning can be accurately calculated using simulation results of the lateral vibration acceleration occurring at the center of gravity of a car body under strong crosswinds. In addition, a new method is proposed to estimate the lateral vibration acceleration using track alignment irregularity data.*

**Key words:** crosswind, critical wind speed of overturning, RTRI’s detailed equation, lateral vibration acceleration, vehicle dynamics simulation, alignment

## 1. Introduction

The critical wind speed of overturning is one of indices for the safety evaluation of railway vehicles against crosswinds. The critical wind speed of overturning is defined as the wind speed at which wheel loads on the upwind side become zero, and in Japan, it is often evaluated using the “RTRI detailed equation [1]” based on “Kunieda’s equation [2]” [3, 4].

In the RTRI detailed equation, the following three external forces acting on a running railway vehicle are considered: ① aerodynamic force due to crosswind, ② excess centrifugal force when passing through a curve, and ③ lateral vibration inertia force, as shown in Fig. 1. For ①, it is recommended that the aerodynamic force coefficient be obtained as far as possible by wind tunnel testing [5] and evaluated in accordance with actual conditions. If it is difficult to carry out individual wind tunnel tests, the results of wind tunnel tests [6] combining five different car body shapes and seven different ground structure shapes can also be used. Next, ② can be uniquely obtained once the curve radius, cant, mass of the vehicle, and running speed are determined. On the other hand, ③ can be obtained by multiplying the lateral vibration acceleration of the car

body by the mass of the car body, but the degree of vibration generated varies greatly depending on the track conditions and the running speed, and it can be advantageous or disadvantageous for overturning. The lateral vibration acceleration  $\alpha_y$  m/s<sup>2</sup> is therefore determined by a linear equation for the running speed  $v$  km/h such that it is 0.98 m/s<sup>2</sup> when running at the maximum operating speed  $v_{\max}$  km/h, so that the evaluation is on the safe side.

$$\alpha_y = 0.98 \times v/v_{\max} \quad (1)$$

Equation (1) is an assumption based on the results of previous running tests. It takes into account the condition in which the maximum value of amplitude is added in the overturning direction after excluding high-frequency components above about 2 Hz that do not affect vehicle overturning. Recently, an evaluation method using measured values of lateral vibration acceleration instead of (1) has also been proposed [7] in order to evaluate the critical wind speed for overturning closer to real conditions.

There are some differences between the lateral vibration acceleration that should be used to evaluate the critical wind speed of overturning and the lateral vibration acceleration measured during normal running, as described in the next chapter. However, the effects of these differences on the evaluation of the critical wind speed of overturning have not been discussed much. In this paper, we report on the detailed confirmation of these effects by scaled model experiments and simulations, as well as a relatively simple method for estimating the lateral vibration acceleration from track displacements. This report is an excerpt from [8].

## 2. Difference in lateral vibration acceleration

The following differences exist between the lateral vibration acceleration used in the calculation model of the RTRI detailed equation (Fig. 1) and the lateral vibration acceleration measured on real vehicles.

First, there is a difference in the position at which the lateral vibration acceleration occurs. In the RTRI detailed equation, the point at which the lateral vibration inertia force acts is defined as the center of gravity of the car body, whereas in the real running test, the lateral vibration acceleration was measured on the floor of the car

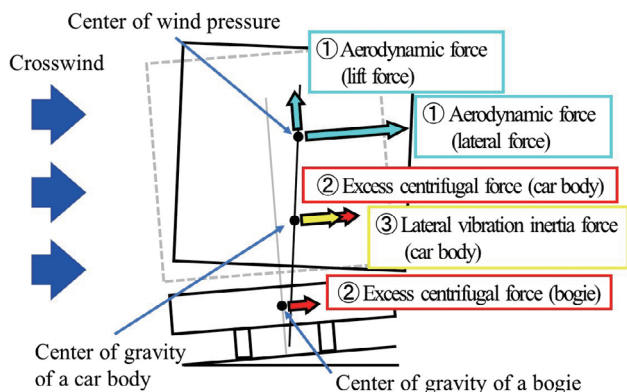


**Fig. 1 Three external forces affecting overturning that are considered when calculating the critical wind speed of overturning**

body. The center of gravity of a general railway vehicle is located slightly higher than the car body floor. Therefore, when roll motion is included in the car body motion, there is a difference between the lateral vibration acceleration at the center of gravity of the body and the lateral vibration acceleration measured at the car body floor.

Secondly, there is a difference in the direction in which the lateral vibration acceleration acts. The RTRI detailed equation defines the lateral vibration inertia force as acting in the direction parallel to the track plane. On the other hand, in running tests, the lateral vibration acceleration is often measured with strain gage accelerometers placed on the floor of the car body. Therefore, when the car body is rolling, the lateral vibration acceleration in the direction rotated by the roll angle is measured, and the gravity acceleration component is superimposed. Therefore, there is a difference between the lateral vibration acceleration that actually occurs at the center of gravity of the car body and the lateral vibration acceleration obtained in running tests.

Finally, there is a difference in the occurrence of lateral vibration acceleration. When determining the critical wind speed of overturning using the RTRI detailed equation, the condition in which the car body is displaced by strong winds and hits the horizontal and vertical stoppers is taken into account. However, since running tests are not carried out under strong winds that would normally result in operating restrictions, hitting the stoppers hardly occurs. Therefore, there is a difference between the lateral vibration acceleration that occurs immediately before overturning, which should be taken into account in the RTRI detailed equation, and the lateral vibration acceleration measured in running tests.

The above differences have not been studied for many years, firstly because the roll angle does not grow significantly while the railway vehicle is running, so the effect on the lateral vibration acceleration is small, and secondly because it is difficult to conduct running tests under strong winds. In order to clarify the influence of the difference between the lateral vibration acceleration measured in running tests and the lateral vibration acceleration defined in the calculation model of the RTRI detailed equation, wind tunnel tests were carried out using a scaled model that can even reproduce overturning phenomena in high winds.

### 3. Scaled model experiments in a wind tunnel

In this chapter, lateral vibration experiments were carried out in a wind tunnel using a 1/10 scale model of a railway vehicle and a comparison was made between the maximum value of lateral vibration acceleration on the car body floor obtained under the same windless conditions and measuring method as in the running test, and the maximum value of lateral vibration acceleration at the car body center of gravity under strong wind (as calculated in the RTRI detailed equation). Also, the correlation between the lateral vibration acceleration and the wheel loads of the upwind side was investigated. Hereafter, the lateral vibration acceleration of the floor of the car body obtained under the same windless conditions and measuring method as in the running test will be referred as “lateral vibration acceleration A (windless, floor)” and the lateral vibration acceleration occurring at the center of gravity of the car body under strong wind (as calculated in the RTRI detailed equation) as “lateral vibration acceleration B (strong wind, center of gravity).” Details and results of the experiments are given below.

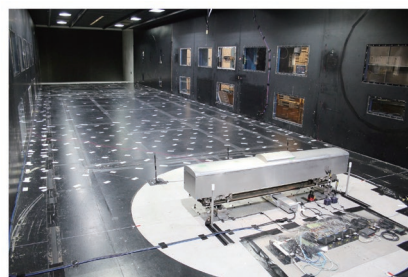


Fig. 2 View of wind tunnel test

#### 3.1 Wind tunnel and scaled model placement

A view of the wind tunnel test is shown in Fig. 2. The wind tunnel tests were carried out in the enclosed section of the large-scale low-noise wind tunnel of the Railway Technical Research Institute. In the test, a 1/10 scaled vehicle model and a vibration table were placed on the turntable on the floor of the enclosed section. The scaled vehicle model was set up so that the wind from the wind tunnel blew perpendicularly to the sides of the car body.

#### 3.2 Scaled model and vibration table

The scaled model was a 1/10 scale model of a commuter train vehicle. The outside body of the model was modeled on a Japanese 103 series car, and the bogies of the model were modeled on bolsterless bogies. The suspensions of the bogies and the stoppers that restrain large displacement of the car body were designed so that the displacement of the car body in response to an external force was similar to that of real railway vehicles, in terms of spring constants and stopper displacements. Specifically, a commuter railway vehicle with a mass of 25 tons was assumed, and the mass of the model was approximately 25 kg, which is the cube of 1/10th of the mass of the vehicle. For the primary and secondary suspension constants, coil springs with values close to the square of 1/10th of the values of general bolsterless bogies were selected. As a result, the lateral vibration acceleration of the scaled model was the same as that of real vehicles, the natural frequency of the scaled model was 3.16 ( $\sqrt{10}$ ) times that of real vehicles, and the wind speed in the wind tunnel was 0.316 ( $1/\sqrt{10}$ ) times the wind speed that real vehicles receive. In this chapter, the values of wind speed, frequency, etc. related to wind tunnel tests were based on the values in the model dimensions.

The vibration table used to vibrate the above scaled model is shown in Fig. 3. A rectangular prismatic part that simulates a rail was attached to the vibration table, and each wheel of the scaled model rode on this dummy rail. A small load cell was placed at the bottom of the dummy rail on which each wheel rode, to measure the wheel load. The vibration table was vibrated by a single-axis actuator with a sinusoidal wave, as shown in the next section.

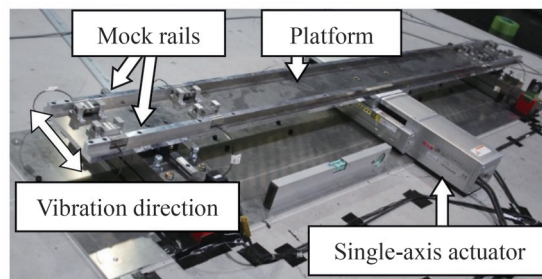


Fig. 3 Wind tunnel test

### 3.3 Test wind speed and vibration conditions

The test wind speeds were set to windless (0 m/s) and strong wind (11 m/s and 12 m/s (34.8 m/s and 37.9 m/s equivalent to a real railway vehicle)). The vibration waveform used to vibrate the vibration table was 20 sinusoidal waves with an amplitude of 1.5 mm. In the vibration experiment, the front and rear bogies of the scaled model were vibrated in the same phase. This situation can be considered similar to that of a real railway vehicle running on a track where there is an alignment with a wavelength that corresponds exactly to the distance between the centers of the vehicle bogies. Therefore, the oscillation frequency was set from 0.6 Hz to 6.0 Hz (equivalent to that of an actual vehicle from 0.2 Hz to 1.9 Hz) in approximately 0.3 Hz increments, assuming that a real vehicle runs on the track at a speed of 10 km/h to 95 km/h in 5 km/h increments.

### 3.4 Measurement details and method of analysis

The measurement details are shown in Fig. 4. First, a strain gage accelerometer was placed on the floor of the scaled model to measure the lateral vibration acceleration  $\alpha_{y1}$  of the car body floor, as in the running test. In order to obtain the lateral vibration acceleration  $\alpha_{yG}$  at the center of gravity of the car body, an accelerometer was also placed on the upper beam inside the scaled model to measure the lateral vibration acceleration  $\alpha_{y2}$  above the car body. The lateral displacements at two points on the side of the car body were measured with laser displacement sensors to determine the roll angle  $\theta$  of the car body. The lateral vibration acceleration  $\alpha_{yG}$  occurring parallel to the track plane at the center of gravity of the car body was determined using the lateral vibration accelerations  $\alpha_{y1}$  and  $\alpha_{y2}$  and the car body roll angle  $\theta$ , assuming that the center of gravity of the car body was at the midpoint between the two accelerometers. The upwind side wheel loads of the scaled model were determined as the average of the four wheel loads on the upwind side obtained from load cells placed beneath the dummy rail supporting the wheels. The sampling frequency for all data recording was 100 Hz.

### 3.5 Experimental results

The maximum lateral vibration acceleration A (windless, floor) in the overturning direction and the maximum lateral vibration acceleration B (strong wind, center of gravity) in the overturning di-

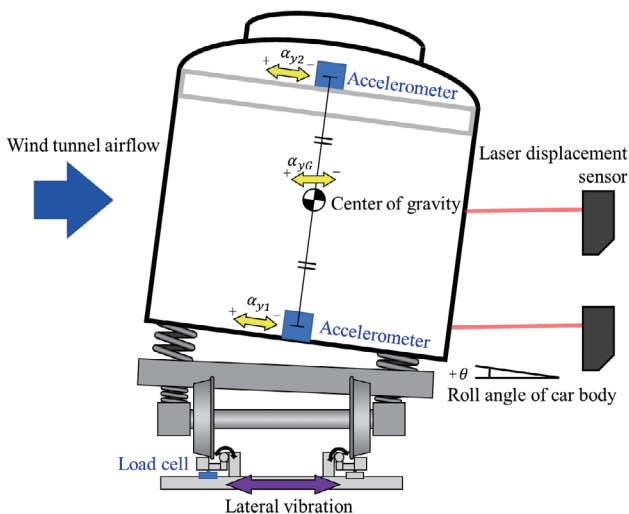


Fig. 4 Measurement details

rection are shown in Fig. 5. The correlation coefficients between the lateral vibration acceleration A and lateral vibration acceleration B and the upwind side wheel load are shown in Fig. 6.

From Fig. 5, the maximum value (red line) of the lateral vibration acceleration A (windless, floor) shows a peak near 2.2 Hz due to the resonance (rolling motion) of the scaled model. At oscillation frequencies above 2.9 Hz, the center of rolling motion of the car body tended to gradually move upwards and the lateral vibration acceleration increased. On the other hand, the maximum values (blue and black lines) of the lateral vibration acceleration B (strong wind, center of gravity) tended to increase with increasing oscillation frequency, although there were no peaks related to resonance because the car body was in constant contact with the lateral and vertical stoppers and there was a large variation due to the effect of turbulence in the rear flow of the vehicle model. Figure 6 shows that the correlation between the lateral vibration acceleration B (strong wind, center of gravity) and the upwind side wheel load is high, with a correlation coefficient of 0.6 or higher over the entire range of oscillation frequencies tested. The correlation coefficient for the test wind speed of 12 m/s was slightly lower than that for the test wind speed of 11 m/s. This is because there was a moment when the upwind wheel load became zero at the test wind speed of 12 m/s, which lowered the correlation coefficient with the lateral vibration acceleration.

From the above, it is considered that the lateral vibration acceleration A (windless, floor) is dominated by the rolling motion of the car body affected by the track alignment, while the lateral vibration acceleration B (strong wind, center of gravity) is dominated by the track alignment since the car body is always in contact with the lateral and vertical stoppers and no rolling motion occurs. Considering that the lateral vibration acceleration B (strong wind, center of gravity) has a higher correlation with the upwind side wheel load, the lateral vibration inertia force (lateral vibration acceleration) used in

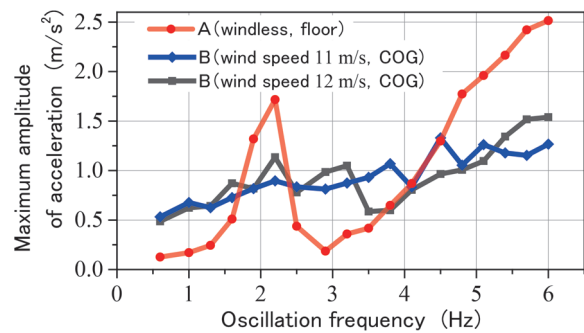


Fig. 5 Maximum lateral vibration acceleration

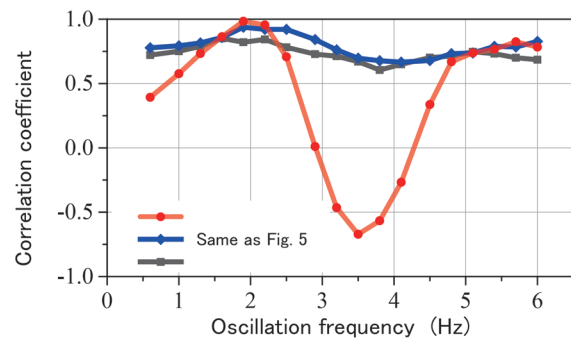


Fig. 6 Correlation coefficients between lateral vibration acceleration and upwind side wheel load

the RTRI detailed equation should use the lateral vibration acceleration that occurs at the center of gravity of the car body under strong wind conditions (as in the calculation model of the RTRI detailed equation), rather than the assumption determined from the results of running tests carried out on real railway vehicles under windless conditions, to determine a more accurate critical wind speed for overturning.

#### 4. Simulation study of lateral vibration acceleration at the center of gravity of a car body under strong winds

From the results of the previous chapter, it was found that when calculating the critical wind speed for overturning using the RTRI detailed equation, a more accurate wind speed can be obtained by using the lateral vibration acceleration that occurs at the center of gravity of the car body under strong winds (as in the calculation model of the RTRI detailed equation). However, it is difficult to carry out running tests in strong winds that could overturn a railway vehicle. In this chapter, the lateral vibration acceleration at the center of gravity of the car body under strong winds is determined by a vehicle motion simulation. We also propose a method for estimating the lateral vibration acceleration from the track alignment.

##### 4.1 Vehicle model

Simpack, a multi-body dynamics analysis software, was used to build a vehicle motion simulation model. The vehicle model is shown in Fig. 7. The dimensions, mass, spring constants, etc. of the vehicle model were assumed to be those of a general commuter train. The bogie is modeled on a recent bolsterless bogie. The model also includes stoppers to suppress large displacements of the car body and other parts. The vehicle consists of rigid elements with 6 degrees of freedom each for 1 car body, 2 bogie frames, 8 axle box supports, and 4 wheel axles, and each rigid element is coupled with a spring and damping system. The lateral force and lift force due to the crosswind (details are given in Section 4.3) were given as the forces acting on the car body. The wheel tread geometry was the JR modified arc wheel profile, and the wheel/rail friction coefficient was set to 0.3.

##### 4.2 Track model

The track model created was a 4000-m straight line. Ten conditions of track alignment irregularities from No. 1 to No. 10 were set on the section from 2500 m to 3500 m. In this report, only alignment irregularities No. 1 to No. 3 are shown in Fig. 8 for reference. Alignments No. 1 to No. 10 are waveforms with a sampling interval of 0.25 m (the restored wavelength band is 5 to 50 m), restored from the actual track alignment data. In order to make both ends of the waveform have a displacement of 0 mm, a linear function was multiplied by 0 at a distance of 2500 m or 3500 m (both ends) and 1 at a distance of 2510 m or 3490 m, 10 m away from both ends, respectively. The track alignment data used are those evaluated as normal or with poor maintenance condition.

##### 4.3 Running speed and aerodynamic conditions

The vehicle running speeds in the simulations were 30, 60, 90, and 120 km/h. Aerodynamic forces were applied to the vehicle model shown in Fig. 7, with lateral and lift forces acting at two locations  $(x, y, z) = (5 \text{ m}, 0 \text{ m}, -2.283 \text{ m})$  and  $(-5 \text{ m}, 0 \text{ m}, -2.283 \text{ m})$  of the car

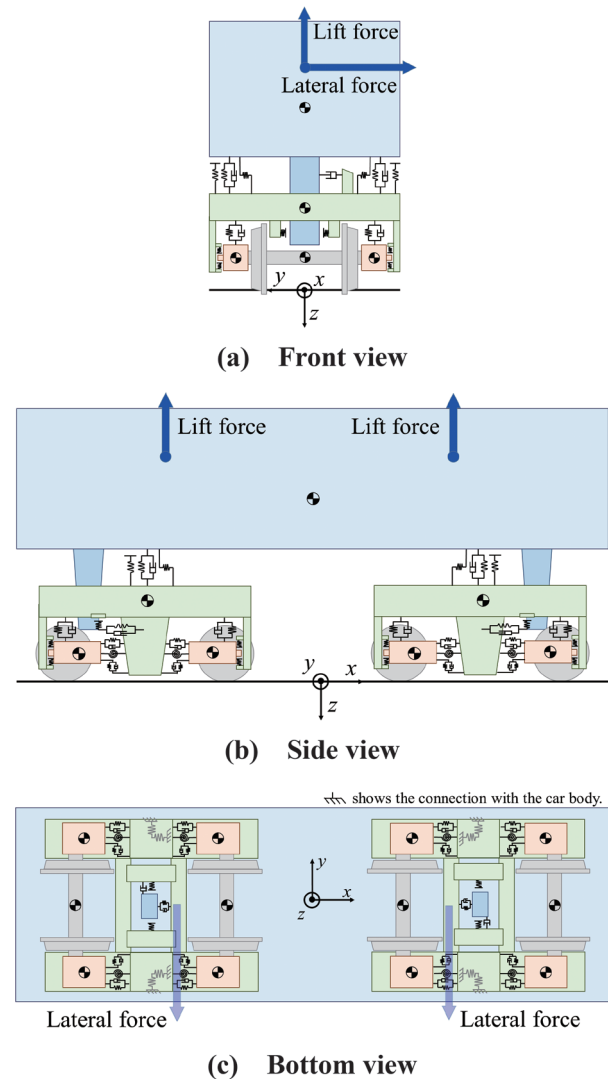


Fig. 7 Outline of vehicle model

body. The value  $z = -2.283 \text{ m}$  indicates the center height of wind pressure from the rail top, a value determined with reference to the results in [6] and assuming a commuter train. The reason why the lateral and lift forces were applied to two separate points of the car body was to allow for extensibility of the model in future studies. The lateral force and lift force were increased slowly from 0 kN/1 location to a maximum lateral force value of 20 kN/1 location and a maximum lift force value of 13 kN/1 location during a half-wave shape (phase  $-\pi/2$  to  $\pi/2$ ) over 70 seconds, and held at their maximum values to avoid transient response in the vehicle. When the maximum values of lateral force and lift force are applied, the car body contacts the vertical and horizontal stoppers, just before it overturns. If the vehicle travels at 120 km/h for 70 seconds, when the lateral force and lift force have reached their maximum values, the vehicle will have traveled approximately 2333 m and will have reached a point ahead of where the track alignment irregularities were set.

##### 4.4 Simulation results

Simulations were carried out under the conditions described in the previous sections to calculate the lateral vibration acceleration that occurs at the center of gravity of the car body under strong

winds. The calculated results were output at a sampling frequency of 50 Hz with positive values in the overturning direction. Examples of the results are shown in Fig. 9. The figure shows the lateral vibration acceleration at the center of gravity of the car body when the

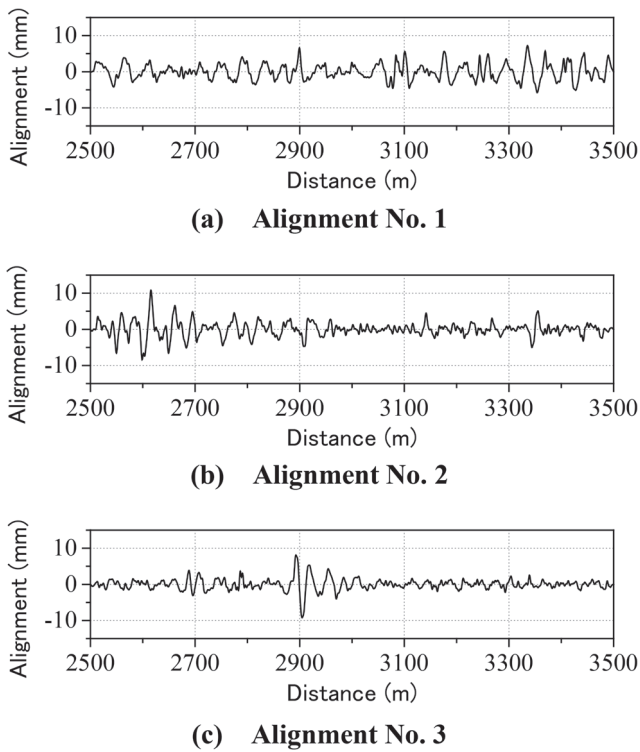


Fig. 8 Alignment irregularities inserted in 2500-3500 m section of 4000 m straight track

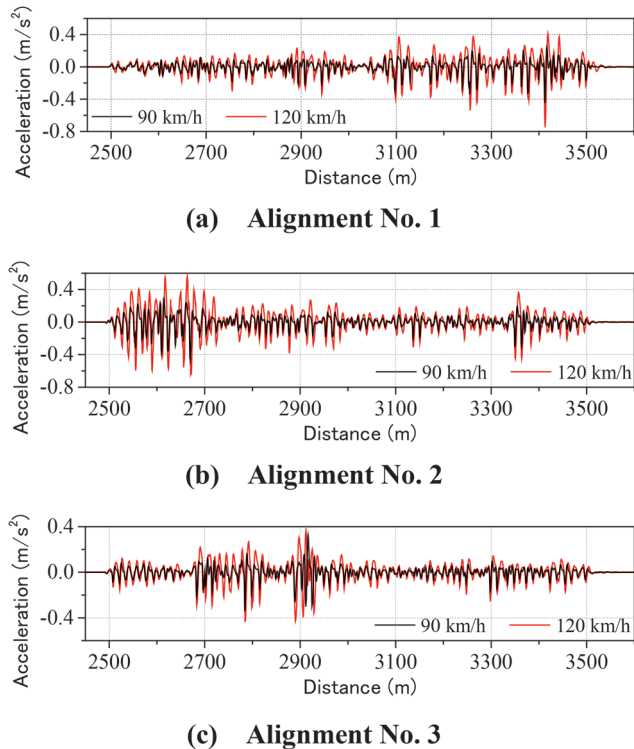


Fig. 9 Examples of simulation results

vehicle traveled through the sections with alignment irregularities No. 1 to No. 3 as shown in Fig. 8 at running speeds of 90 km/h and 120 km/h under strong wind. The calculated results show that the lateral vibration acceleration increased as the running speed increased. The maximum value of lateral vibration acceleration in the overturning direction, when running on a track with a total length of 10 km (1 km × 10 conditions) of track alignment irregularities used in this chapter, was 0.57 m/s<sup>2</sup>, which occurred when running at a speed of 120 km/h on the alignment irregularities No. 2.

The calculated maximum values of lateral vibration acceleration at the center of gravity of the car body are summarized in Fig. 10. This figure shows that the maximum value of the lateral vibration acceleration increases quadratically as the running speed increases. Therefore, the quadratic equation passing through the maximum value of 0.57 m/s<sup>2</sup> at a running speed of 120 km/h is shown by the red line in Fig. 10. Assuming that the maximum lateral vibration acceleration in the overturning direction is  $\alpha_{yG,max}$  (m/s<sup>2</sup>) and the running speed is  $v$  (km/h), this red line becomes (2).

$$\alpha_{yG,max} = 3.93 \times 10^{-5} \times v^2 \quad (2)$$

From Fig. 10, it can be seen that equation (2) almost includes the maximum value of the lateral vibration acceleration. From the above, it is considered that more accurate values can be determined by using (2) in the assumed equation for lateral vibration acceleration in the RTRI detailed equation when calculating the critical wind speed for overturning of a commuter railcar (bolsterless bogie) running on the track assumed in this chapter. However, in this chapter, equation (2) is assumed using track alignment irregularity data for a total length of 10 km. There is room for debate as to how much track alignment irregularity data should be used to create a hypothetical formula that represents the entire length of the line segment, and this is a matter for future study.

#### 4.5 Estimation method of lateral vibration acceleration using track alignment irregularity

This section examines a simpler method for estimating the lateral vibration acceleration at the center of gravity of the car body using track alignment irregularities. First, it is assumed that the railway vehicle is in a state where the car body is displaced by strong winds and in contact with the lateral and vertical stoppers. In this state, as shown in Chapter 3, the car body does not undergo rolling motion due to the secondary spring, etc., but is affected by the track alignment irregularities, causing lateral vibration. Then, for track alignments No. 1 to No. 10 (sampling interval 0.25 m) a two-point average waveform was created by averaging two points 13.75 m apart, which is close to the 13.8 m distance between bogie centers of the vehicle model described in this chapter. This is considered to be

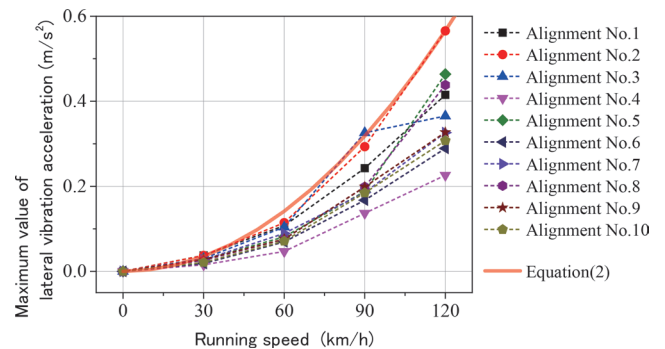


Fig. 10 Maximum value of lateral vibration acceleration occurring at the center of gravity of car body

the lateral displacement that occurs at the center of the car body when the front and rear bogies run along the track alignment. Second-order differentiation of this two-point average waveform yields a value corresponding to the lateral vibration acceleration occurring at the center of gravity of the car body, which is considerably greater than the lateral vibration acceleration determined from the vehicle motion simulation. The reason for this may be that when a railway vehicle runs on a track, it does not follow along the track alignment, but rather absorbs the displacement to some extent through the movement of the bogies and wheel axles.

Therefore, we checked the frequency components in the lateral vibration acceleration (at a running speed of 120 km/h) generated at the center of gravity of the car body calculated from the vehicle motion simulations. The result of the frequency analysis is shown in Fig. 11. This figure shows the results of the frequency analysis of the 10 waveforms of the lateral vibration acceleration generated at the center of gravity of the car body when running at 120 km/h through track alignments No. 1 to No. 10, respectively, and the obtained

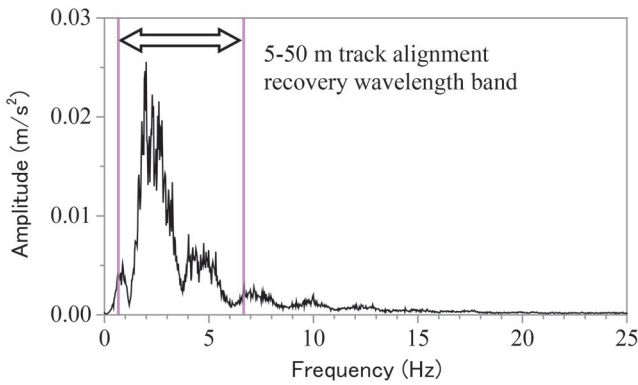
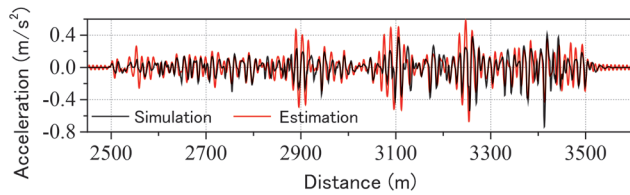
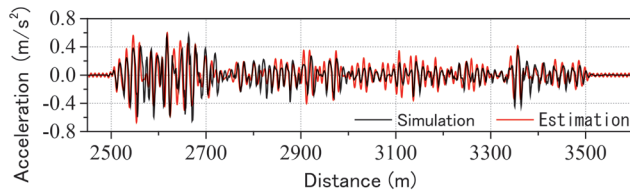


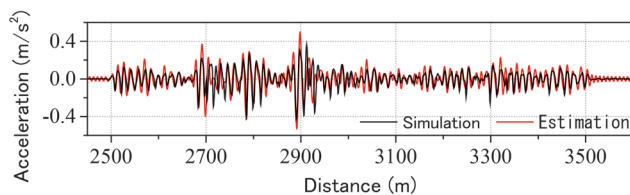
Fig. 11 Frequency analysis result



(a) Alignment No. 1



(b) Alignment No. 2



(c) Alignment No. 3

Fig. 12 Comparison of estimated acceleration

amplitudes are averaged. The frequency band (0.67 to 6.7 Hz) expected to be excited by a railway vehicle traveling at 120 km/h in the 5-50 m track alignment recovery wavelength band used is also described. Figure 11 shows that the frequency component between 1 and 4 Hz is the main component of the lateral vibration acceleration. Therefore, assuming that the vehicle model was running at a speed of 120 km/h, the two-point averaged waveforms of track alignments No. 1 to No. 10 were processed through a low-pass filter (FFT filter) at 4 Hz. The lateral vibration acceleration at the center of gravity of the car body was estimated by second-order differentiation of the two-point averaged waveform through a 4-Hz low-pass filter.

The results obtained are shown in Fig. 12. This figure shows the lateral vibration acceleration estimated from the track alignment irregularities of the track (red line) and the lateral vibration acceleration generated at the center of gravity of the car body (black line) when the railway vehicle runs at 120 km/h under strong winds, as shown in Fig. 9. Figure 12 shows that the appearance trends of the lateral vibration acceleration are almost identical, and that the lateral vibration acceleration estimated from the track alignment (red line) tends to be greater than that at the center of gravity of the car body (black line). Therefore, the method presented in this section for estimating the lateral vibration acceleration at the center of gravity of the car body under strong winds using the track alignment may give a relatively accurate estimation and is on the safe side. However, the lateral vibration acceleration (black line) obtained from the vehicle motion simulation was greater than that estimated in this section (red line) at some points along the 10 km track length used in this report. Although this could be improved by changing the filter, the purpose of this method is to derive an assumed formula for the lateral vibration acceleration in the RTRI detailed equation. It is therefore sufficient if the maximum value of lateral vibration acceleration that may occur during running can be estimated with some accuracy. We plan to verify the accuracy of this method using more track alignment irregularity data in the future.

Finally, the estimated maximum value of the lateral vibration acceleration at the center of gravity of the car body, determined by the method proposed in this section, is  $0.61 \text{ m/s}^2$  at a running speed of 120 km/h. Assuming a quadratic equation as in equation (2), the assumed equation for the lateral vibration acceleration becomes (3):

$$\alpha_{yGmax} = 4.24 \times 10^{-5} \times v^2 \quad (3)$$

It should be noted that the method proposed in this section is based on a commuter railway vehicle (bolsterless bogie, JR modified arc wheel profile), and the filters may differ if the bogie type, bogie dimensions, wheel profile, etc. are significantly different, or if the track alignment appearance tendency, etc. is different.

## 5. Examples of calculations for critical wind speed of overturning

In this chapter, examples of calculations for the critical wind speed for overturning are given using the assumed equations for the current RTRI detailed equation for lateral vibration acceleration and the new method proposed in the previous chapter. For further reference, an assumed equation (1)' based on the actual lateral vibration acceleration data measured on a real vehicle shown in [7] is also shown.

$$\alpha_y = 0.5 \times v/v_{max} \quad (1)'$$

Equation (1)' is a linear expression for the running speed like equation (1), but the maximum value differs from that in (1). The relationship between these lateral vibration accelerations and running speed is shown in Fig. 13. Note that the coefficients of (1)'

based on measured data and (2) and (3) based on track alignment may be different depending on track conditions and vehicle conditions.

The vehicle specifications used in the calculations are assumed values based on relatively light commuter trains of recent years. The aerodynamic force coefficients were calculated based on the results of [6], and the train configuration was the head car of a 103 series in

Japan, a commuter train. The running conditions were a straight line and a running speed 0 to 120 km/h (in 10 km/h increments).

The calculation results of the critical wind speed for overturning for each calculation condition are shown in Fig. 14. This figure shows the vehicle running speed on the horizontal axis and the critical wind speed for overturning on the vertical axis, with the scale on the vertical axis being 2 m/s. Since the vehicle specifications used in the calculations are notional values, the numerical values of the critical wind speed for overturning have no specific meaning, so the numerical values on the vertical axis are omitted. The black line is the assumed lateral vibration acceleration (1) in the current RTRI detailed equation, the gray line is the assumed acceleration (1)' based on measured data, and the red and blue lines are the results using (2) and (3), the new assumed equations proposed in the previous chapter. Figure 14 shows that the critical wind speed for overturning using (2), which is considered to be the most accurate reflecting the real situation, can be taken as a reference, and that the wind speed using (3) can be evaluated to be almost equivalent to that using (2), which is at most 2 m/s higher than the wind speed using (1).

From the above, the lateral vibration acceleration of a car body assumed when calculating the critical wind speed for overturning using the RTRI detailed equation may be selected as appropriate according to the purpose and accuracy. For example, in general evaluation, (1) can continue to be used as it is because it is on a safe side assumption. On the other hand, when conducting evaluations based on the actual situation or when estimating accuracy is required, such as in the consideration of operating regulations, it is conceivable to use the assumed equations based on measured data of lateral vibration acceleration ((1)') or the assumed equations based on track alignment ((2) and (3)).

## 6. Conclusions

This paper examined the lateral vibration acceleration of the car body related to the lateral vibration inertia force, which is one of action forces used in the RTRI detailed equation for evaluating the critical wind speed for overturning of a railway vehicle. The results are summarized as follows.

- 1) Lateral vibration experiments were carried out in a wind tunnel using a 1/10 scale model of a railway vehicle, and a comparison was made between the maximum value of lateral vibration acceleration on the car body floor obtained under the same windless conditions and measuring method as in real running tests and the maximum value of lateral vibration acceleration at the car body center of gravity under strong winds (as calculated in the RTRI detailed equation). The results showed that the calculation results of the RTRI detailed equations had a high correlation with the upwind side wheel loads.
- 2) The lateral vibration acceleration at the center of gravity of the car body under strong winds was calculated by vehicle motion simulation. The lateral vibration acceleration at the center of gravity of the car body increased quadratically with increasing running speed.
- 3) As a simpler method than simulation, a method for estimating the lateral vibration acceleration at the center of gravity of car bodies from track alignment irregularities was studied. Specifically, the lateral vibration acceleration was estimated by second-order differentiation of a two-point average waveform processed through a low-pass filter.
- 4) As a result of estimating the difference in critical wind speeds

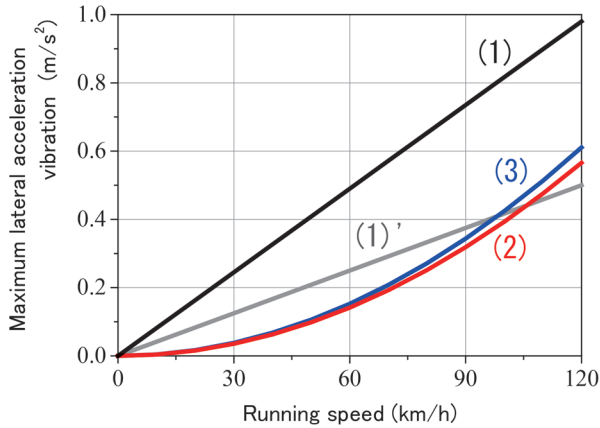
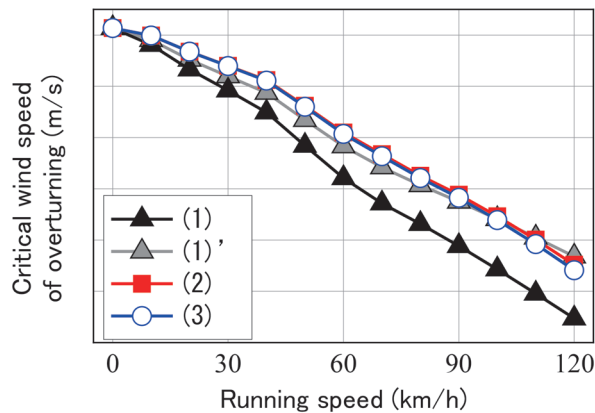
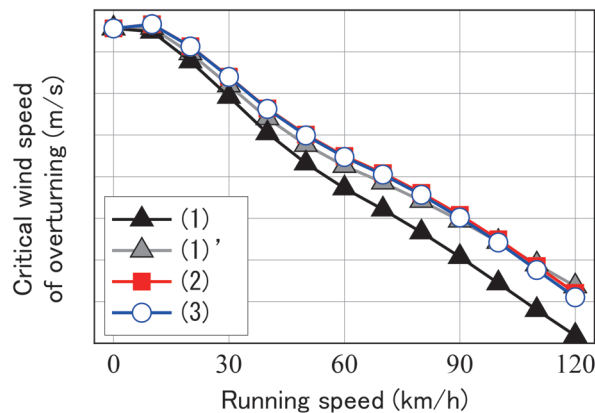


**Fig. 13 Assumed equation for lateral vibration acceleration**



**(a) Head car, double track overhead bridge**



**(b) Head car, embankment**

**Fig. 14 Calculation results of critical wind speed of overturning**

for overturning due to the difference in the assumed equations for lateral vibration acceleration, the critical wind speed for overturning using the assumed equation based on the proposed new method was approximately 2 m/s greater at maximum than that using the current assumed equation.

## References

- [1] Hibino, Y. and Ishida, H., “Static Analysis on Railway Vehicle Overturning under Crosswind,” *RTRI Report*, Vol. 17, No. 4, pp. 39-44, 2003 (in Japanese).
- [2] Kunieda, M., “Theoretical study on the mechanics of overturn of railway rolling stock,” *Railway Technical Research Report*, No. 793, 1972 (in Japanese).
- [3] Aircraft and railway accidents investigation commission, East Japan Railway Company Uetsu Line train derailment accident between Sunagoe station and Kita-Amarume station, *Railway accident investigation report*, RA2008-4, 2008 (in Japanese).
- [4] Nagumo, Y., Ichiki, M. and Misu, Y., “Safety assessment of train operation applying a new method for operation control under strong winds,” *JR EAST Technical Review*, No. 66, pp. 25-33, 2021 (in Japanese).
- [5] Tanemoto, K., Suzuki, M. and Maeda, T., “The Wind Tunnel Tests on Aerodynamic Characteristics of Train/Vehicles Due to Cross Winds,” *RTRI Report*, Vol. 13, No. 12, pp. 47-52, 1999 (in Japanese).
- [6] Tanemoto, K., Suzuki, M., Saitou, H. and Ido, A., “Results of Wind Tunnel Tests for Aerodynamic Coefficients of Railway Vehicles,” *RTRI Report*, Vol. 27, No. 1, pp. 47-50, 2013 (in Japanese).
- [7] Hibino, Y. and Kanemoto, H., “Evaluation of Critical Wind Speed of Overturning Considering Measured Lateral Vibrational Acceleration,” *QR of RTRI*, Vol. 60, No. 4, pp. 243-248, 2019.
- [8] Kanemoto, H., and Hibino, Y., “Estimation method of lateral vibration acceleration of car body used for safety evaluation of railway vehicles against crosswind,” *Transactions of the Japan Society of Mechanical Engineers*, Vol. 89, No. 918, 2023 (in Japanese).

## Authors



*Hiroyuki KANEMOTO*, Ph.D.  
Senior Researcher, Vehicle Mechanics  
Laboratory, Railway Dynamics Division  
Research Areas: Vehicle Dynamics, Cross  
Wind Safety



*Yu HIBINO*, Ph.D.  
Principal Researcher, Research and  
Development Promotion Division  
Research Areas: Vehicle Dynamics, Cross  
Wind Safety

# Evaluation Method of Passenger Thermal Comfort Considering Effects of Airflow by Cross-flow Fan in Commuter Vehicles in Summer

Hiroharu ENDOH

Sachiko YOSHIE

Comfort Science and Engineering Laboratory, Human Science Division

Shota ENAMI

Fumitoshi KIKUCHI

Ergonomics Laboratory, Human Science Division

Yasuhiko IZUMI

Architecture Laboratory, Structures Technology Division (Former)

Jun NOGUCHI

East Japan Railway Company

*The purpose of this study is to propose a method for evaluating passenger thermal comfort in non-steady state thermal environments with airflow by cross-flow fans in commuter trains in summer. The proposed method is composed of a human thermoregulation model applicable to non-steady state thermal environments and a statistical model derived from the results of experiments conducted in commuter trains in summer. To evaluate thermal comfort considering the influence of a cyclic wind from cross-flow fans, the proposed method converts the cyclic wind to a constant wind speed equal to the total amount of heat loss from the whole-body calculated by human thermoregulation model. We applied the proposed method to our previous research and confirmed that the observed data and predictions agree well.*

**Key words:** thermal comfort, cross-flow fan, commuter train, subjective experiment

## 1. Introduction

Almost all commuter trains in Japan are equipped with cross-flow fans in order to circulate the air inside the railway cabin and provide cooling to passengers, especially during the hot and humid summer seasons. Cross-flow fans complement the cooling system to make passengers feel less hot and uncomfortable. Furthermore, various measures have been taken to improve passenger comfort by adjusting airflow from cross-flow fans, such as adjusting the air speed according to the thermal load in the vehicle based on air temperature, humidity, and occupancy rate, detected by on-board sensors [1]. Despite these efforts, there are still many complaints from passengers about the thermal environment on commuter trains. To create a more comfortable in-vehicle thermal environment, accurate and quantitative evaluation of the current in-vehicle thermal environment, including environments with airflow from cross-flow fans, should be conducted from the perspective of passenger comfort and factors that cause discomfort should be identified. However, there are very few studies on passenger thermal comfort in the thermal environment of commuter trains, especially in environments with airflow from cross-flow fans, and no method has been established to quantitatively evaluate passenger comfort in such environments.

This study aims to propose an evaluation method of passenger thermal comfort applicable to environments with airflow from cross-flow fans in commuter trains. This research is based on a method proposed by the authors to evaluate passenger thermal comfort in commuter trains [2] (hereinafter, the proposed method) and investigates the possible application of this method to environments with airflow from cross-flow fans. The prediction accuracy of this method was verified by comparing results from this paper with the results of previous experiments [3, 4] whose data were not used to build the proposed method.

## 2. Method for evaluating passenger thermal comfort

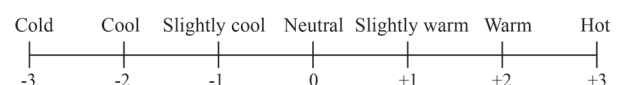
### 2.1 PMV and PPD as thermal indices

There is a long-established body of literature on thermal environment and comfort in the indoor environment field. The ISO 7730 recommends using two indices: PMV (Predicted Mean Vote) to predict the mean hot/cold sensation of a group (hereinafter, mean thermal sensation) and PPD (Predicted Percentage of Dissatisfied) to predict the percentage of people who are dissatisfied with the thermal environment (hereafter, thermal dissatisfaction rate) [5]. PMV predicts mean thermal sensation on a 7-point scale shown in Table 1. First, the thermal load on the human body caused by the surrounding thermal environment is calculated using the thermal equilibrium equation. It is further calculated using a regression equation that links the thermal load to the hot/cold sensation values reported by the participants in the experiment. There are six main factors that affect the thermal load of the human body: air temperature, humidity, radiation temperature, and airflow velocity (air speed) on the environmental side, and metabolic rate and amount of clothing on the human side (hereinafter, six thermal factors). PMV is calculated using all of these factors. PPD is defined by the following formula based on participants' data from the experiment.

$$PPD = 100 - 95 \exp\{-(0.03353PMV^4 + 0.2179PMV^2)\} \quad (1)$$

PMV and PPD are easy to understand because they directly predict the amount of sensation in humans and are currently one of the most

**Table 1 PMV scale**



widely used thermal indices regardless of field.

PMV and PPD are applicable in steady-state thermal environments, such as indoor environments. The relational expression between PMV and PPD shown in (1) is assumed to be true regardless of the season. On the other hand, the thermal environment in commuter trains is a non-steady-state thermal environment with large variations in temperature, humidity, and air speed [2]. In addition, according to a previous research conducted in rail vehicles, the relationship between PMV and the actual percentage of dissatisfied passengers varies with the seasons [6]. In the experiment conducted by the authors in commuter trains during the summer, the maximum prediction error of PPD was as large as 45 pt (pt is the unit for the arithmetic difference between two percentages) under the condition that the temperature in the vehicle increased [2].

## 2.2 Method for evaluating passenger thermal comfort in commuter trains in summer [2]

Figure 1 shows an overview of the proposed method. First, the thermal load the human body receives is calculated by inputting the six thermal factors. Next, mean thermal sensation and thermal dissatisfaction rate are predicted by a regression equation derived from the data of the previous experiments. The process of the prediction follows PMV and PPD. In addition, the proposed method utilizes “the model of the human thermal system that can predict physiological conditions in a non-steady-state thermal environment” and “regression equations based on participants’ data from the experiment in commuter trains conducted during the summer,” which reduces the prediction errors of PMV and PPD.

In the first part, the algorithm of the 65-node thermoregulation-model (hereinafter 65 MN model) developed by Tanabe et al. [7] is used as “the model of the human thermal system that can predict physiological conditions in a non-steady-state thermal environment.” In this model, the human body is divided into 16 parts: head, chest, back, waist, shoulders, arms, hands, thighs, lower legs, and feet (limbs are divided into right and left parts), and each part is further divided into four layers: core, muscle, fat, and skin. The four layers of the same part transfer heat by conduction, while the skin layers on the surface of the human body exchange heat with the surrounding environment through convection, radiation, and evaporation. Heat is also transferred by blood flow between these 64 parts and the 65th part, called the central blood. The thermoregulatory system includes sweating, blood flow regulation, and shivering ther-

mogenesis. These are integrated as a feedback control using the difference between the neutral temperature assumed for each part and the current temperature as a control signal.

In the second part, the following equation, based on the results of the experiment conducted in the summer, is used as the “regression equation based on participants’ data from the experiment in commuter trains conducted during the summer.”

$$DyPMV = c + a_0 \cdot SET^* \quad (2)$$

$$DyPPD_c = \frac{100 \cdot \exp(a_c DyPMV + b_c)}{1 + \exp(a_h DyPMV + b_h) + \exp(a_c DyPMV + b_c)} \quad (3)$$

$$DyPPD_h = \frac{100 \cdot \exp(a_h DyPMV + b_h)}{1 + \exp(a_h DyPMV + b_h) + \exp(a_c DyPMV + b_c)} \quad (4)$$

$$DyPPD = DyPPD_c + DyPPD_h \quad (5)$$

$$[c=-12.3, a_0=0.49, a_c=-1.23, b_c=-3.27, a_h=1.15, b_h=-1.28]$$

SET\* (the New Standard Effective Temperature) in (2) corresponds to the “apparent temperature,” which is defined as the air temperature at 50% relative humidity at which the skin temperature, skin moisture rate, and the amount of body heat dissipation from the skin surface, all calculated with the 65 MN model, are equal to those in the actual thermal environment. DyPMV in (2) is an index that predicts the mean thermal sensation of passengers. The numerical values correspond to the thermal sensation scale used in the experiment described later (see Table 3 presented later). DyPPDc in (3) and DyPPDh in (4) are indices for predicting the proportion of passengers who feel “cold and dissatisfied” and “hot and dissatisfied” with the in-vehicle thermal environment, respectively. DyPPD, obtained by adding the two in (5), is a predicted value of the thermal dissatisfaction rate that includes both heat and cold causes.

The PPD defined by (1) is minimum at the neutral thermal sensation (PMV=0), which is neither hot nor cold, and assumes a symmetrical shape with similar increasing trends on the cold (PMV < 0) and hot (PMV > 0) sides (see Fig. 6 presented later). On the other hand, the proposed method used a multinomial logistic regression model that separated the occurrence of dissatisfied people due to coldness and the occurrence of dissatisfied people due to hotness

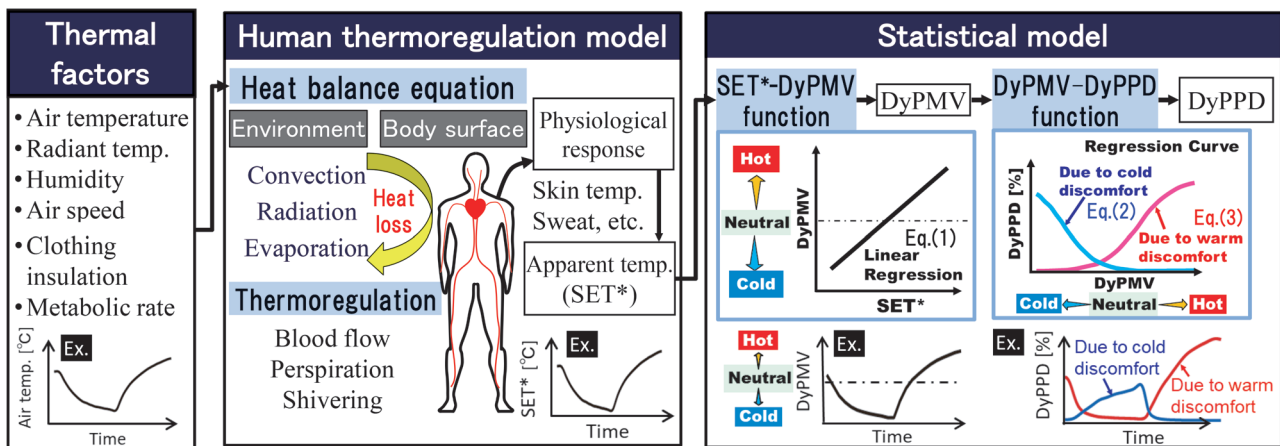


Fig. 1 General description of the evaluation method of passenger thermal comfort applied to a commuter vehicle environment in the summer

((3) and (4)) and obtained a curve shape based on the participants' data from the experiment in the summer (see Fig. 6 presented later). The result shows a relational expression with DyPPD at a minimum around DyPMV of -1 ("slightly cool" on the thermal sensation scale), which is consistent with previous research [6].

The proposed method is more accurate than PPD for predicting passenger thermal comfort in commuter trains in summer, but its applicability to environments with airflow from cross-flow fans has not yet been investigated.

### 2.3 Application of the proposed method to environments with airflow from cross-flow fans [8]

This section describes how the proposed method is applied to environments with airflow from cross-flow fans. When cross-flow fans are on in commuter trains, passengers standing near the cross-flow fans periodically receive fluctuating airflow depending on the fan rotation cycles. Currently, the cross-flow fans complete a cycle approximately every 15 seconds [1]; the thermal sensation of passengers near the cross-flow fans should fluctuate on a cycle of approximately 15 seconds. While this instantaneous change in sensation occurs, passengers may also determine the overall sensation after experiencing the airflow from the cross-flow fans for more than one cycle. Therefore, it is assumed that, after some time has passed after boarding the train, they will decide whether it is a pleasant or unpleasant ride based on their overall sensation. This study, which assumes a condition where passengers receive periodically fluctuating airflow, evaluates their overall thermal sensation and comfort as determined after experiencing the airflow for more than one cycle. To evaluate this overall thermal sensation, the apparent temperature linked to this sensation should be derived.

In the proposed method, when evaluating passenger thermal comfort for environments with airflow from cross-flow fans, the measured fluctuating air speed is converted to a constant air speed for the equivalent amount of body heat dissipation (hereinafter, the converted air speed is referred to as "equivalent air speed in heat loss"). This makes it possible to derive the apparent temperature that is linked to the overall thermal sensation when the periodic fluctuating airflow is experienced for more than one cycle. The conversion of real environmental values based on the equivalent amount of body heat dissipation (equivalence of thermal effects on humans) is consistent with the conventional concept of calculating apparent temperatures. In a real in-vehicle environment, the peak and average values of the air speed of the periodically fluctuating airflow may vary due to various disturbances, even if the intensity of the cross-flow fans is the same. To deal with this, as in the moving average process, the equivalent air speed in heat loss is calculated by cutting out a predetermined interval length (set to 60 seconds in this study), and the process is repeated while moving on the time axis. By repeating this method, we obtain the equivalent air speed in heat loss for all the times to be evaluated.

## 3. Method for verifying the accuracy of the proposed method

### 3.1 Overview of experiments used for verification [3, 4]

The accuracy of the proposed method is tested based on the participants' data from the experiment, which was conducted separately from the derivation of the regression (2) to (4). The outline of these experiments is described below.

### 3.1.1 The time of the experiment, the attributes of participants, and the conditions of congestion

Table 2 shows the time of the experiment, the attributes of participants, and the conditions of congestion. The congestion ratio in Table 2 is defined as 0.35 m<sup>2</sup>/person as 100%. The experiments were conducted in the summer months of 2015 and 2017. All experiments were conducted with commuter trains stationed at the railway operator's depot in the Tokyo metropolitan area. Figure 2 shows an overview of the arrangement of participants and measurement sensors. Experiment 1 was conducted with a congestion ratio below 100% (participants were placed near the cross-flow fans shown in Fig. 2(a)), and Experiment 2 was conducted with a congestion ratio of 120% (about 15 participants were placed in areas 1 and 2 in Fig. 2(b)) and 180% (about 30 participants were placed in area 1 in Fig. 2(b)). Each experiment was conducted under each of the congestion conditions with cross-flow fans turned off (cross-flow fans off) and with cross-flow fans turned on (cross-flow fans on). The air temperature in the vehicle was simulated by manually controlling the air conditioning to create the condition where the temperature rises and falls as observed in the commuter trains [2]. Experiment 2 was conducted over two days with different participants.

Participants moved from a neighboring vehicle to the experimental vehicle 5 to 10 minutes before the start of the evaluation. After the evaluation was completed, the participants sat down and rested in the adjacent vehicle. To ensure that the amount of clothing was consistent across participants, they wore the same clothing except for their underwear. In Experiment 1, the participants wore long-sleeved shirts, short-sleeved underwear, long pants, and socks; in Experiment 2, they wore short-sleeved T-shirts, long pants, and socks. Figure 3 shows the scenes of the experiment. Participants were fully informed of the purpose and content of the experiment; informed consent was obtained.

### 3.1.2 Subjective evaluation method

Participants subjectively evaluated the environment for thermal sensation, sensation of sweating, and level of satisfaction at 1.5-minute intervals in Experiment 1 and at 2-minute intervals in Experiment 2. Table 3 shows examples of subjective evaluation items and their rating scales. For the subjective rating, participants were instructed not to rate factors outside the thermal environment, such as sounds and smells. To evaluate satisfaction, participants were asked to answer whether they were satisfied with the "thermal environment in commuter trains."

### 3.2 Input settings

The inputs to the 65 MN model in the proposed method were as follows: Air temperature and air speed were measured at 0.1 m above the floor and entered for foot and lower leg; measured at 1.1 m above the floor and entered for thighs, waist, arms, and hands; and measured at 1.7 m above the floor and entered for chest, back, shoulders, and head. The air speed was entered after conversion to the equivalent air speed in heat loss for all conditions, regardless of whether the cross-flow fans were on or off. Humidity was measured at 1.1 m above the floor and entered for all 16 parts. The radiation temperature was calculated using Bedford's law (6) shown below and entered for all 16 parts.

$$T_r = T_g + 2.37\sqrt{v}(T_g - T_a) \quad (6)$$

**Table 2** Information of the experiments [8]

Date of experiments	Number		Age Mean (SD)		Congestion ratio [%]
	Male	Female	Male	Female	
[Experiment 1] 3d July 2015	12	11	35.8 (10.7)	30.8 (8.0)	< 100%
[Experiment 2-1] 22th August 2017	15	16	29.4 (9.3)	32.9 (8.7)	120%, 180%
[Experiment 2-2] 28th August 2017	15	16	32.5 (9.5)	33.5 (11.2)	120%, 180%

**Table 3** Examples of subjective evaluation items

Thermal sensation	cold -4	slightly cold -3	cool -2	slightly cool -1	neutral 0	slightly warm +1	warm +2	slightly hot +3	hot +4
Sweat sensation	not feel				slightly feel	feel	very feel		
Degree of satisfaction	"satisfied"			"dissatisfied"		☐Cold   ☐Hot			

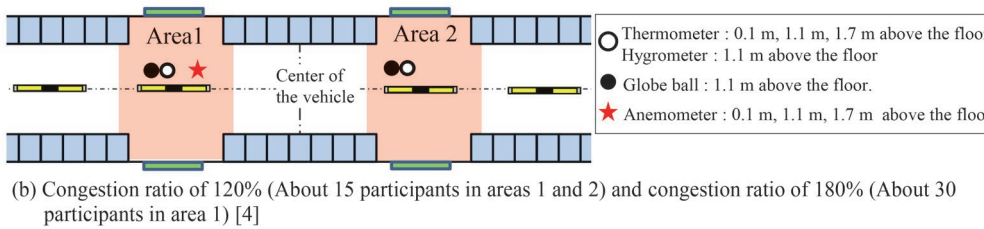
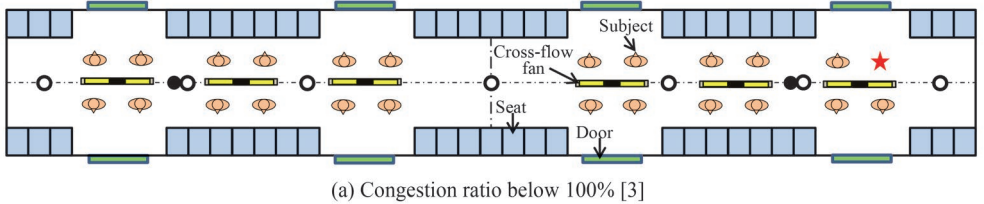


**Fig. 2** Arrangement of participants and measurement sensors in the vehicle



(a) Congestion ratio below 100% [3]



(b) Congestion ratio of 180% [4]

**Fig. 3** Scenes from the experiment

Figure 2 (b) and Fig. 3 (b) are partly modified and reprinted by permission from Springer Nature; Reference 4 © 2019

With  $T_r$ : mean radiation temperature [°C],  $T_g$ : glove temperature at 1.1 m above the floor [°C],  $T_a$ : air temperature at 1.1 m above the floor [°C],  $v$ : air speed at 1.1 m above the floor [m/s], the air speed was applied to (6) after using a 60-second moving average.

The participants' metabolic rates were set to 1.2 met (met is a unit of energy expenditure per unit of body surface area; 1 met = 58.2 W/m<sup>2</sup>), which corresponds to the resting state in the standing position, and the amount of clothing was estimated from the weight of the garment [9]; Experiment 1 was set to 0.59 clo, and experiment 2 was set to 0.45 clo (clo is the unit of thermal resistance of clothing, 1clo = 0.155°C m<sup>2</sup>/W).

PMV and PPD were calculated using the ISO 7730 program. For air temperature and air speed, the mean values measured at 0.1 m, 1.1 m, and 1.7 m above the floor were used as input, and a 60-second moving average was also used for air speed. For the other input items, humidity, radiation temperature, the amount of clothing, and metabolic rate, we used the same input values as in the proposed method described above.

#### 4. Results of applying the proposed method

Figure 4 shows an example of the experimental results of the thermal environment measurement and subjective evaluation under the conditions with a congestion ratio below 100%. In the same figure, the thermal environment measurement results show the equivalent air speed in heat loss, and the subjective evaluation results show PPD, DyPPDc, and DyPPDh.

As shown in Fig. 4, in the temperature rising phase (corresponding to approximately 0 to 15 minutes after the start of the evaluation), the sweat sensation rate and dissatisfaction rate due to

feeling hot are lower in the condition with cross-flow fans on than in the condition with cross-flow fans off; DyPPDh in the time series of predictions by the proposed method captures well this suppression effect of heat discomfort by airflow from cross-flow fans. On the other hand, even when the cross-flow fans are on, the dissatisfaction rate due to feeling hot reaches about 70% at 29°C and 80% humidity (corresponds to approximately 15 to 20 minutes after the start of the evaluation in Fig. 4 (b)); DyPPDh also captures the limitations of the suppression effect of heat discomfort by airflow from cross-flow fans. Then, in the temperature decreasing phase, around the end of the period for evaluating conditions with the cross-flow fans on (corresponds to approximately 30 to 35 minutes after the start of the evaluation in Fig. 4 (b)), the dissatisfaction rate due to coldness tends to increase; DyPPDc captures this trend.

Figure 5 shows the relationship between air temperature/SET\* and mean thermal sensation. The relationship between air temperature and mean thermal sensation is clearly different between the condition with cross-flow fans off and the condition with cross-flow fans on, while the relationship between SET\* and mean thermal sensation is almost the same under both conditions. The correlation coefficient between SET\* and mean thermal sensation ( $r=0.89$ ) was significantly greater than the correlation coefficient between air temperature and mean thermal sensation ( $r=0.65$ ) ( $p<0.01$ ). The SET\* calculated using the proposed method is appropriate as the apparent temperature linked to thermal sensation in environments with variations in temperature and humidity, and environments with airflow from cross-flow fans.

Figure 6 shows the relationship between DyPMV and thermal dissatisfaction rate. There is a tendency for a concave distribution centered around DyPMV=-1; the prediction curves defined by (2)-(4) (DyPPDc/DyPPDh curves) capture the trend well.

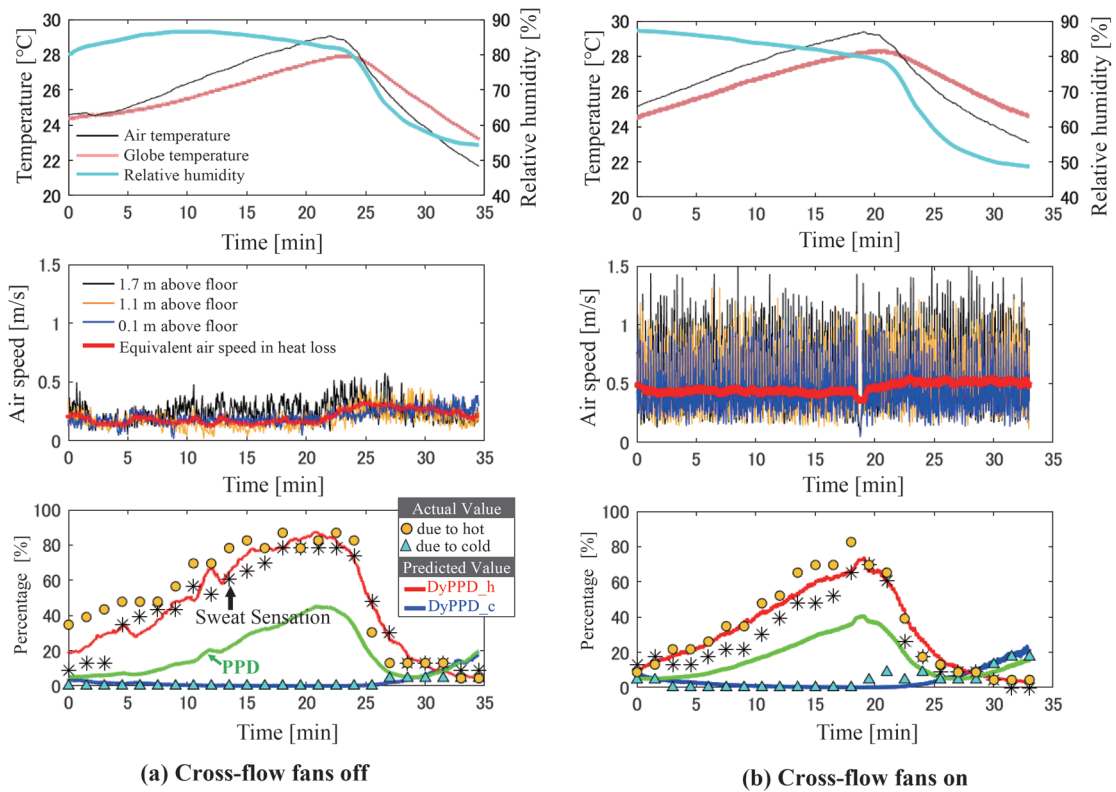


Fig. 4 Examples of results of the thermal environment measurement and subjective evaluation in the experiment (Condition with the congestion ratio below 100%) [8]

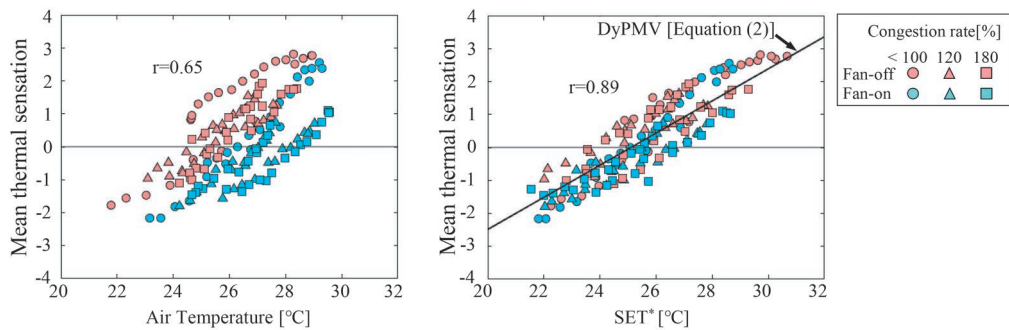


Fig. 5 Relationship between air temperature (left side)/SET\* (right side) and mean thermal sensation [8]

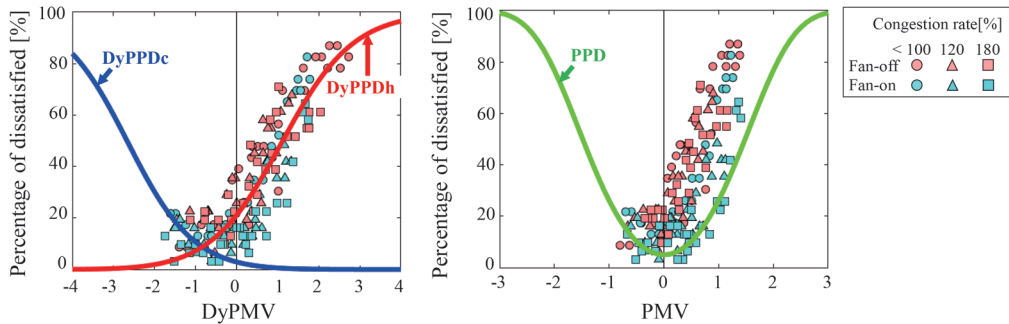


Fig. 6 Relationship between DyPMV (left side)/PMV (right side) and thermal dissatisfaction rate [8]

**Table 4 Mean absolute error of DyPPD and PPD**

Congestion rate	MAE of DyPPD [pt]			MAE of PPD [pt]		
	Fan-off	Fan-on	Total	Fan-off	Fan-on	Total
< 100%	9.4	4.5	7.0	34.0	22.1	28.2
120%	8.2	10.0	9.1	24.6	8.0	16.3
180%	7.3	13.2	10.2	25.4	6.0	15.7
Total	8.3	9.5	8.9	27.7	11.4	19.6

Table 4 shows the mean absolute error of DyPPD. For the condition with cross-flow fans on, the error tended to be larger for the higher congestion ratio condition. However, the mean absolute error for all conditions was within 15 points, and the mean absolute error for all conditions was within 10 pt.

### 5. Accuracy verification of the proposed method and comparison with PMV/PPD

As confirmed in Table 4, the mean absolute error of DyPPD for all conditions combined was 8.9 pt. This is comparable to the mean absolute error of 7.9 pt when the accuracy was verified in a previous study [2]. The participants' data from the experiment used to verify the accuracy were not used to build the regression model of the proposed method. Therefore, the reproducibility of the prediction accuracy of the proposed method is confirmed. The regression model of the proposed method was based on the participants' data from the experiment conducted in early September [2], and the experiments used for verification in this study were conducted in early July and late August. Considering the above, the proposed method should be able to predict and evaluate the thermal comfort of passengers in commuter trains with airflow from cross-flow fans within a mean absolute error of 15 points at least from July to early September. Future work is needed to verify and improve the prediction accuracy for other time periods.

The prediction error of the proposed method was relatively large when the congestion ratio was high and the cross-flow fans were on, and the predicted values tended to be larger than the measured values (see Table 4 and Fig. 6). The main reason for this may be the measurement error of air speed meters installed in congested areas. In conditions with congestion ratios of 120% and 180%, participants standing near the air speed meter may have acted as a wall, slowing the airflow to reach the air speed sensor. This may have resulted in a lower measured air speed than the airflow these participants received. Under the condition with a congestion ratio below 100%, the mean absolute error of the proposed method for the condition with cross-flow fans on was as low as about 5 points. Therefore, if the input accurately captures the air speed around participants, the prediction accuracy will be equivalent to that with the cross-flow fans turned off, even in congested conditions. Future research is needed to determine a more accurate distribution of airflow around passengers during severe congestion.

For comparison with the proposed method, the time series of PPD is shown in Fig. 4. Figure 6 shows the relationship between PMV and thermal dissatisfaction rate, as well as the PMV-PPD curve. Figures 4 and 6 show that PPD tends to underestimate the thermal dissatisfaction rate due to feeling hot and in particular cannot accurately assess the increase in discomfort as the temperature rises. In Japan, which has four seasons, people sweat more in summer than in other seasons due to acclimatization to the heat [10].

While increased sweating helps dissipate body heat and suppresses rises in body temperature, it also increases discomfort because of the moisture on the skin. Since PMV and PPD do not account for changes in sweating function due to heat, the errors tend to be greater in summer. Furthermore, in the condition with cross-flow fans on, the prediction error was small when the congestion ratio was 180%, but large with a congestion ratio below 100%. This is probably due to higher temperatures and humidity in the latter case, which creates a thermal environment more conducive to sweating compared to the former. In summer, the temperature and humidity in commuter trains can reach levels that cause sweating [2]. Therefore, it is inferred that PPD did not meet the requirements as a thermal indicator that matched the passenger experience in commuter trains in summer.

### 6. Summary

This study proposed a method for evaluating passenger thermal comfort in environments with airflow from cross-flow fans in commuter trains. The proposed method is composed of the human thermal system model applicable to non-steady state thermal environments and a statistical model derived from the results of experiments conducted in commuter trains in summer. For periodic fluctuating airflow seen when cross-flow fans are on, it predicts the mean thermal sensation and dissatisfaction rate for a complete cycle by converting it to a constant air speed where the amount of body heat dissipation is the same as when receiving fluctuating airflow. This method was applied to experiments conducted on commuter trains during the summer. The results confirmed that thermal dissatisfaction rates can be predicted with a mean absolute error of about 10 points in a relatively crowded environment where people do not come into contact with each other, regardless of whether the cross-flow fans are on or off.

This method makes it possible to quantitatively predict and evaluate the effect of airflow from cross-flow fans on alleviating heat-related discomfort and the effect of improved/worsened comfort in the thermal environment of commuter trains during the summer. This allows for a better adjustment of the air flow from a point of view of comfort.

### References

- [1] Shiraishi, K. and Sakai, O., "Air conditioning system for advancement of amenity in the train," *Mitsubishi Denki giho*, Vol. 81, No. 10, pp. 681-684, 2007 (in Japanese).
- [2] Endoh, H., Izumi, Y. and Hayashi, N., "Development of a Prediction Method for Thermal Comfort in Commuter Trains in the Summer Season," *Proceedings of the 11th World Congress on Railway Research (WCRR 2016)*, Milano, 2016.
- [3] Endoh, H., Enami, S., Yoshie, S., Izumi, Y., and Hayashi, N., "The effects of wind from cross-flow fans on passengers' thermal comfort in commuter trains," *J-Rail 2016 Proceeding*, S5-1-1, 2016 (in Japanese).
- [4] Endoh, H., Enami, S., Izumi, Y. and Noguchi, J., "Experimental study on the effects of air flow from cross-flow fans on thermal comfort in railway vehicles," *Proceedings of the 20th Congress of the International Ergonomics Association (IEA 2018)*, Springer, pp. 379-388, 2019.
- [5] ISO7730, *Ergonomics of the thermal environment—Analytical determination and interpretation of thermal comfort using cal-*

ulation of the PMV and PPD indices and local thermal comfort criteria, International Standard Organization, 2005.

- [6] Haller, G., "Thermal comfort in rail vehicles," *Climatic Wind Tunnel Vienna*, Rail Tec Arsenal, 2006.
- [7] Tanabe, S., Kobayashi, K., Nakano, J., Ozeki, Y., and Konishi, M., "Evaluation of thermal comfort using combined multi-node thermoregulation (65MN) and radiation models and computational fluid dynamics (CFD)," *Energy and Buildings*, Vol. 34, No. 6, pp. 637-646, 2002.
- [8] Endoh, H., Enami, S., Kikuchi, F., Yoshie, S., Izumi, Y., and Noguchi, J., "Quantitative Evaluation of Effects of Airflow from Cross-flow Fans on Passengers' Thermal Comfort in Commuter Vehicles," *Transactions of the JSME*, Vol. 88, No. 916, DOI: 10.1299/transjsme.22-00171, 2022 (in Japanese).
- [9] Hanada, K., Mihira, K. and Sato, Y., "Studies on the thermal resistance of men's underwear," *Journal of Japan Research Association for Textile End-Uses*, Vol. 24, No. 8, pp. 363-369, 1983 (in Japanese).
- [10] Nakamura, Y. and Okamura, K., "Seasonal variation of sweating responses under identical heat stress," *Applied Human Science*, Vol. 17, No. 5, pp. 167-172, 1998.

## Authors



*Hiroharu ENDOH*  
Senior Chief Researcher, Head of Comfort Science and Engineering Laboratory, Human Science Division  
Research Areas: Thermal Comfort, Ride Comfort, Ergonomics



*Shota ENAMI*  
Assistant Senior Researcher, Ergonomics Laboratory, Human Science Division  
Research Areas: Crashworthiness, Ergonomics



*Fumitoshi KIKUCHI*, Ph.D.  
Senior Researcher, Ergonomics Laboratory, Human Science Division  
Research Areas: Social Psychology, Emotional Psychology



*Sachiko YOSHIE*, Dr.Eng.  
Senior Researcher, Comfort Science and Engineering Laboratory, Human Science Division  
Research Areas: Molecular Biology, Environmental Microbiology



*Yasuhiko IZUMI*, Dr.Eng.  
Senior Chief Researcher, Head of Architecture Laboratory, Structures Technology Division (Former)  
Research Areas: Thermal Comfort, Acoustic Comfort



*Jun NOGUCHI*  
Researcher, East Japan Railway Company  
Research Areas: Ride Comfort

# Wind Tunnel Test Reproducing Track Surface Flow of Passing Shinkansen Trains to Study Ballast Projection and Ballast Screen Lifting

Tatsuya INOUE

Vehicle Aerodynamics Laboratory, Environmental Engineering Division (Former)

Takashi NAKANO

Vehicle Aerodynamics Laboratory, Environmental Engineering Division

Atsushi IDO

Wind Tunnel Technical Center, Research and Development Promotion Division

*Passing Shinkansen trains create track surface flows. Screens are installed on track surfaces to prevent ballast projection due to this flow. However, considering future extensions to high-speed lines and faster Shinkansen running speeds commensurate countermeasures must be developed. Field tests are an effective way to develop such measures, however, conducting research and development using field tests is difficult owing to the risk of ballast projection. This paper therefore describes the development of a wind tunnel test method for flying ballast and ballast screens, and wind tunnel tests to evaluate the possibility of ballast projection and ballast screen lifting.*

**Key words:** wind tunnel test, Shinkansen, track surface flow, ballast, ballast screen, ballast projection

## 1. Introduction

Running Shinkansen trains generate a flow on the track surface (hereinafter referred to as track surface flow) [1][2][3]. Ballast projections caused by this flow can hit underfloor train equipment, causing malfunctions or damage. In addition, the ballast projected on station platforms or along railway lines can harm people. To prevent flying ballast, several countermeasures such as installing a ballast screen to cover the ballast and spraying resin to fix the ballast on the track surface have been implemented [4]. Furthermore, to prevent ballast screens from lifting, they are fastened together using belts or resin joints and fixed to anchors embedded in the tracks outside rails. At present, these countermeasures prevent ballast projection and ballast screens from lifting (hereinafter collectively referred to as trackside equipment). However, considering future extensions to Shinkansen lines, new developments are needed, such as measures to reduce maintenance costs and improve ballast projection prevention. Field tests are an effective way to develop countermeasures, however, field tests are difficult considering cost and the risk of trackside equipment being projected. Therefore, we developed a wind tunnel test method using the Railway Technical Research Institute's large-scale low-noise wind tunnel to study the projection of trackside equipment and develop preventive measures [5][6].

## 2. Development of the wind tunnel test method

### 2.1 Test section arrangement

We used the open test section of RTRI's large-scale low-noise wind tunnel. Figure 1 shows the layout of the test section and a ballast track model. The nozzle dimensions were 5.0 m wide  $\times$  3.0 m high. The ballast track model was placed on a model support table (5.5 m wide  $\times$  7.0 m long). A net was placed downstream of the ballast track model to prevent test pieces from entering the wind duct. A control pitot tube was installed inside the nozzle to measure

the wind velocity in the wind tunnel test.

Figure 2 shows the ballast track model. The ballast was the same as that used on Shinkansen tracks. The rails and sleepers are reproduced by full-size models because the track surface flow is only affected by their shapes on Shinkansen tracks. The rail/sleeper fastening devices were omitted because their influence on track surface flow is negligible. The length of the track was set to 2.7 m considering the limitations on the length of the model support table. The measurement section was the central part of the rail in the flow direction (third section from the upstream in Fig. 2). The height of the ballast surface matched the floor of the nozzle. The depth of the ballast in the measurement section was 195 mm. There were 2 to 3 ballast layers or more in the section.

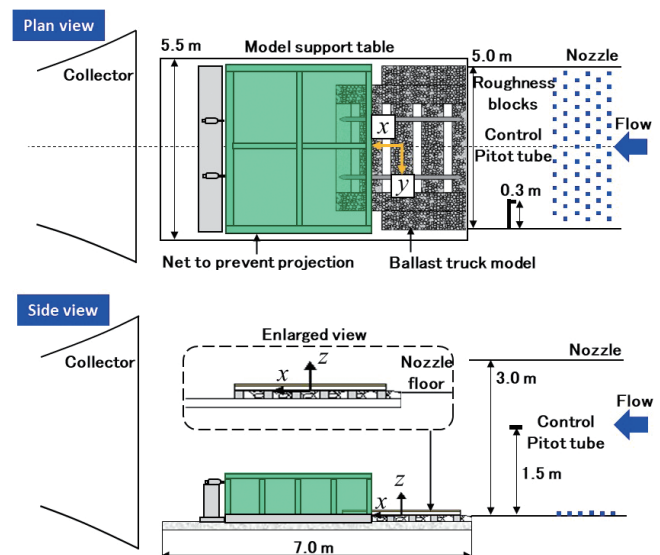


Fig. 1 Wind tunnel and ballast track model

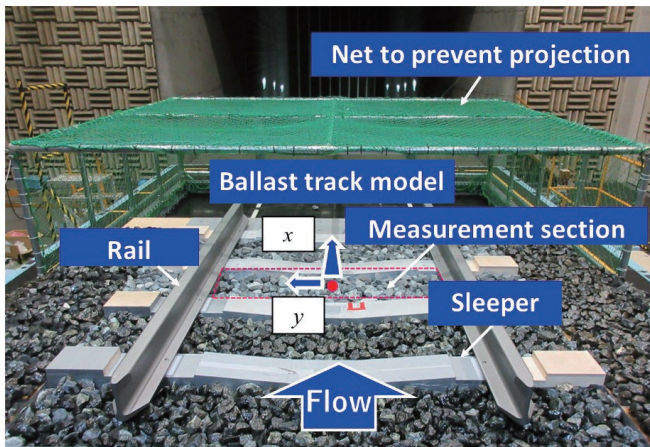


Fig. 2 Ballast track model

## 2.2 Reproduction of wind velocity distribution on the ballast track surface

In the wind tunnel test, roughness blocks were installed on the floor of the nozzle, and the wind velocity distribution on the track surface of a passing the Shinkansen train (16 cars train, train speed: 280 km/h) was reproduced in the measurement section of the ballast track model by adjusting the size, number, and arrangement of the blocks.

Figure 3 shows the measurement of wind velocity distribution above the ballast track surface. A pitot tube was installed on the rail model, and a comb-shaped total pressure tube was installed in the measurement section. The origin was the center of the track surface in the flow and sleeper directions (Fig. 2). The tip of the comb-shaped total pressure tube was installed at  $x = 0$  and  $y = 0$ . The number of comb-shaped pressure tubes were 19, and we measured from 7.5 mm above the track surface to 187.5 mm at a pitch of 10 mm. The total pressure in the comb-shaped total pressure tube and the static pressure in the pitot tube were measured using a multipoint pressure gauge (Digital Sensor Array: DSA-3217, Scani Valve Corp.). The wind velocity at the height of each comb-shaped total pressure tube was calculated from the differential pressure between each total pressure and the static pressure of the pitot tube, that is, the dynamic pressure. Figure 4 shows the wind velocity distribution on the track surface in wind tunnel tests and field tests [1]. By adjusting the installation of the roughness blocks, we approximately matched the wind velocity distribution in the measurement section with the field test results. Then, the wind velocity in the wind tunnel test (the wind velocity of the control pitot tube installed in the nozzle) was 50 m/s. Note that the wind velocity distribution reproduced

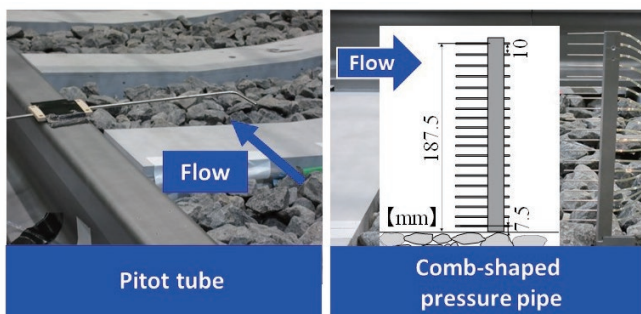


Fig. 3 To measure wind velocity distribution on the track surface

was the time averaged wind velocity when the middle part of the Shinkansen was passing. The turbulence intensity and local flow were not reproduced.

## 2.3 Testing of the wind velocity and train speed

As shown in Fig. 4, the wind velocity of the wind tunnel test was 50 m/s when the wind velocity distribution on the track surface was reproduced on the track model at a train speed of 280 km/h. Assuming that the ratio of the wind velocity in the wind tunnel test to the train speed was constant, it can be converted to the speed of the Shinkansen train by multiplying the wind velocity in the wind tunnel test by 1.56 ( $280/(50 \times 3.6)$ ).

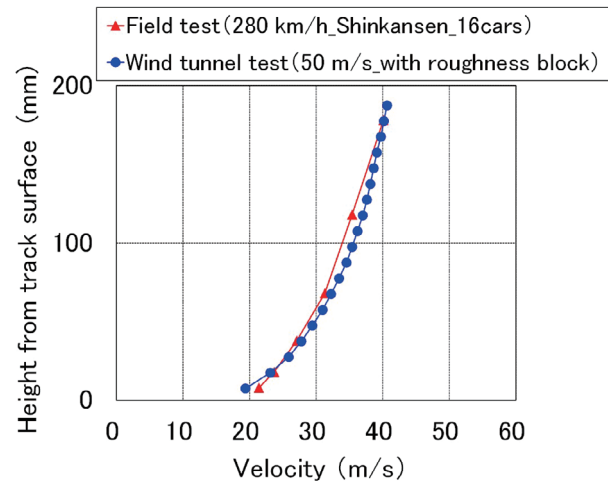


Fig. 4 Time mean flow velocity distribution on the track surface

## 3. Wind tunnel testing on ballast

### 3.1 Ballast model

To prevent ballast projection, several countermeasures such as spraying resin to fix the ballast and installing ballast screens have been implemented, but they have not been applied to all sections of Shinkansen tracks. Therefore, wind tunnel tests were conducted to study ballast projection in sections where no countermeasures have been implemented.

Four types of ballast model were used in the wind tunnel tests in Fig. 5. The “Standard model” represents the commonly observed shape. “Flat model” represented a flat shape, lightweight, with high probability of projection. “Cube model” had a size of 50 mm. “Cube cutout model” was a cube with one beveled bottom corner toward which the flow was directed.

### 3.2 Ballast aerodynamic measurement test

Figure 6 shows the measurement of the aerodynamic force of the ballast. We used the balance (Nissho Denki Co., Ltd. 3-component force balance: LMC-31480) to measure the aerodynamic force acting on the ballast. It was installed at the origin on the horizontal plane (Fig. 2). Generally, six force components acted on the ballast when the reproduced wind of a passing Shinkansen train was applied. Drag force  $D$  (N), lifting force  $L$  (N), and pitching moment  $M$  (Nm) (hereinafter simply referred to as moments) considered to be

	3D-View	Side-View
① Standard model		
② Flat model		
③ Cube model		
④ Cube cutout model		

Fig. 5 Ballast model

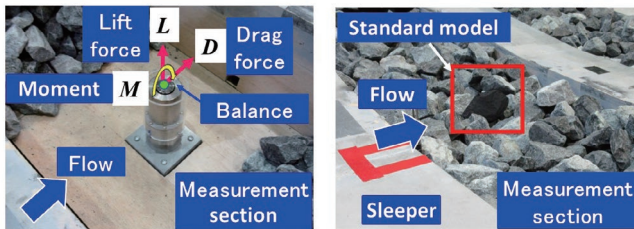


Fig. 6 Measurement of the aerodynamic force applied to the ballast

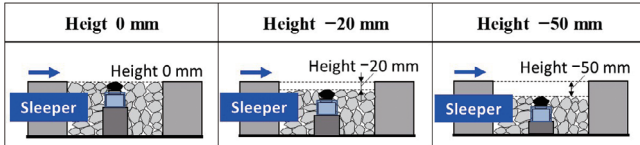


Fig. 7 Ballast height (unit: mm)

the main forces influencing ballast projection. Therefore, we measured these three forces using a balance. As shown in Fig. 7, the installation height of the model was 0 mm when the top of the sleeper and the top of the ballast model were the same height, -20 mm when a ballast screen (20 mm thick) was installed, -50 mm when the ballast between the rails are removed to prevent ballast projection. The wind velocities of the wind tunnel test were 0, 14, 28, 42, and 50 m/s (equivalent to train speeds of 0, 78.4, 156.8, 235.2, and 280.0 km/h). We measured them for 20 s.

Figure 8 shows the aerodynamic force when the ballast height was 0 mm. Regardless of the ballast shape, the aerodynamic forces were exceedingly small in comparison to the actual weight of the ballast (standard: 2.5 N, flat: 1.8 N). When the ballast was installed at a lower height, the forces were even smaller (almost zero), and when the ballast was located on lower height than the top of the sleeper, almost no aerodynamic force was acting on the ballast.

### 3.3 Evaluation of the possibility of ballast projection

To evaluate the possibility of ballast projection when it was located below the track surface (ballast height of 0 mm or less), we calculated the moment around the downstream and lower end of the ballast. In Fig. 9,  $M$ ,  $M_+$  and  $M_-$  are shown in yellow, red, and blue,

respectively. Here,  $l$  (m) is the distance from the center of the ballast model to the downstream end of the ballast model, and  $m$  (kg) is the mass of the actual ballast.  $M_+$  ( $= M + Ll$ ) is the moment due to track surface flow, and  $M_-$  ( $= mgl$ ) is the moment due to self-weight. Whether or not the ballast rotates depends on the maximum value of the moment and the duration of its action; however, here, we calculate the time averaged values of  $M_+$  and  $M_-$ . If the absolute value of  $M_+$  is greater than the absolute value of  $M_-$ , the ballast begins to rotate because of track surface flow. Conversely, if the absolute value of  $M_-$  is greater than the absolute value of  $M_+$ , the ballast does not rotate.

Figure 9 shows the absolute moments ( $M_+$  and  $M_-$ ) related to the standard and flat models at ballast heights of 0 mm, -20 mm, and -50 mm at wind velocity of 50 m/s (equivalent to a train speed of 280 km/h). In both models, the absolute value of  $M_+$  was sufficiently smaller than that of  $M_-$  at all ballast heights. It indicates almost no possibility of the ballast rotating due to track surface flow. Even on actual tracks where Shinkansen trains run at 280 km/h, if the ballast height is 0 mm or less (the top surface of the ballast is lower than the top surface of the sleepers), the possibility of the ballast projection is considered extremely small.

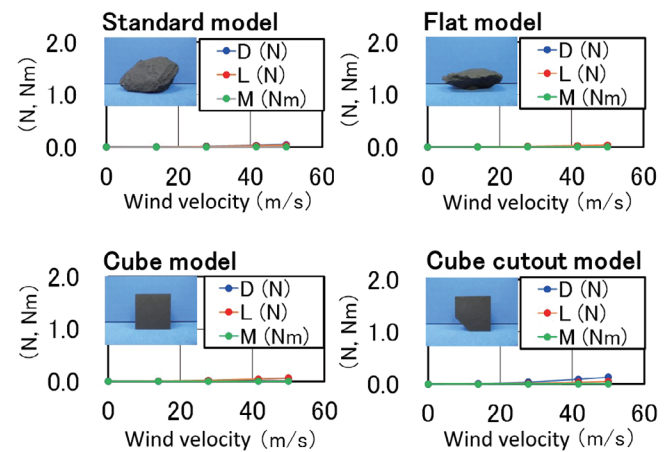


Fig. 8 Aerodynamic force measurement for the ballast (Ballast height is 0 mm)

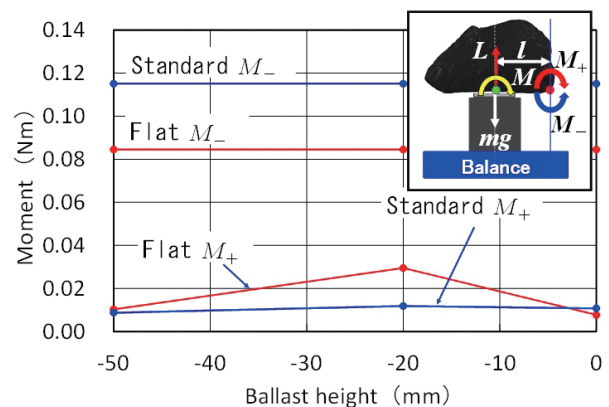


Fig. 9 Evaluation of the possibility of ballast projection

### 3.4 Ballast behavior observation

Using a high-speed camera, we studied the ballast behavior during projection when the wind velocity increased to a maximum

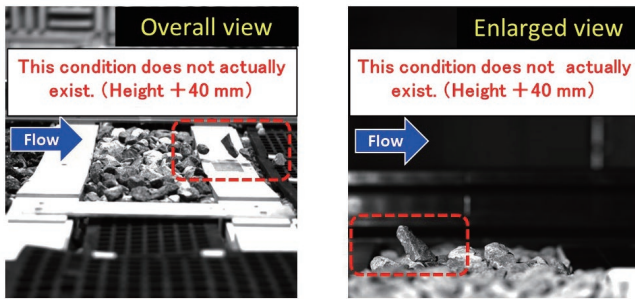


Fig. 10 Ballast behavior

of 72 m/s (equivalent to a train speed of 404 km/h) at a ballast height of +40 mm (Fig. 10). Though these train speed and ballast height do not actually exist, we carried out the tests for this case to study the behavior of the ballast. The following ballast projection behavior was observed: 1) As the wind velocity increases, some unstable ballast begin to sway. 2) If the wind velocity further increases, the ballast begins to roll on the track surface. 3) The ballast rolled on the track surface sometimes sweeps downstream and stops midway, and other times, it is swept downstream by the wind and projected into the air. In addition, we confirmed some flying ballast was blown downstream. We believe that this test method will be extremely effective for observing flying ballast behavior to develop techniques to prevent ballast projection.

#### 4. Wind tunnel tests on ballast screens

##### 4.1 Ballast screen configuration and fixing method

Figure 11 shows the configuration and method for fastening ballast screens (hereinafter simply referred to as screens). Screens are comprised of inner track materials installed between the tracks and outer track materials installed outside the rails. Inner and outer track materials are connected to joints. The inner track material is comprised of one central part installed near the center of the track and two adjacent outer parts; the outer parts and the central part are

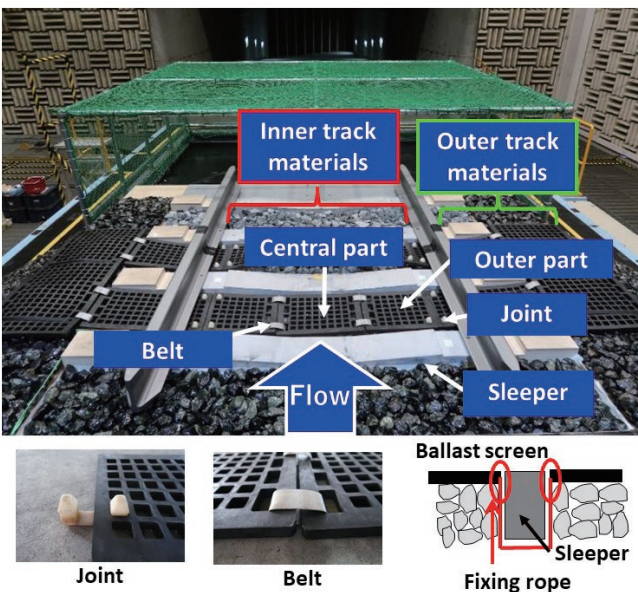


Fig. 11 Ballast screen configuration and fixing method

fastened together with belts. Inner track materials adjacent to each other in the track direction across the sleepers are fastened together with fixing ropes that pass under the sleepers (no fixing ropes were installed in this wind tunnel test). In this way, the screen is firmly fixed to the track surface. However, the fixing ropes require more labor during ballast repairs. Therefore, in this study, to save labor, we conducted wind tunnel tests to study whether the screen would fly away if the fixing ropes were omitted.

##### 4.2 Ballast screen aerodynamic measurement test

The wind velocity on the track surface is the greatest near the center when a Shinkansen train is passing [2]. Thus, we assumed that the aerodynamic force acting on the screen is greatest in the central part, and we measured the aerodynamic force acting on the central part using a balance (6-component force manufactured by Nissho Denki Co., Ltd. LMC-61481.) We measured the aerodynamic force of the ballast screen model with the same shape as the actual screen. When measuring aerodynamic force, the belts connecting the central part were removed so that the aerodynamic force acting on the outer parts would not affect the measurement results. Figure 12 shows the installment of a 20 mm thick screen.

The height from the top of the sleeper to the top of the ballast during the screen test was (0 mm, -20 mm, -50 mm). The maximum angle of the screen was 20°, assuming that the ballast was placed under the screen. The test conditions were determined by combining height (0 mm, -20 mm, -50 mm) and angle (0°, 10°, 15°, 20°). For the evaluation of the aerodynamic forces, we used the drag coefficient  $C_D$ , lift coefficient  $C_L$ , and moment coefficient  $C_M$ , which were made dimensionless by drag force  $D$ , lift force  $L$ , and moment  $M$  using the wind velocity (27.8 m/s). We measured them for 20 s. The results showed that the aerodynamic coefficient acted to the screen increases with increasing height and angle of the screen (Fig. 13).

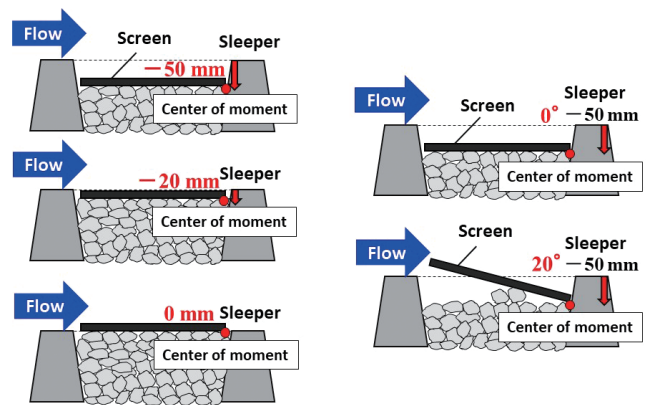


Fig. 12 Ballast screen installation conditions

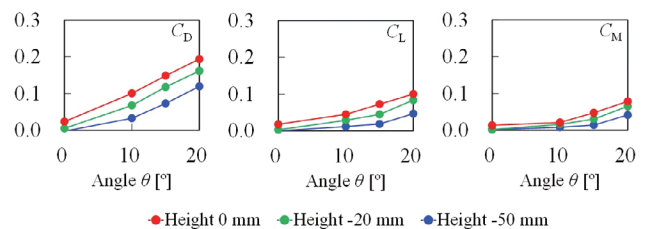


Fig. 13 Aerodynamic coefficient on ballast screen

### 4.3 Evaluation of the possibility of ballast screen projection

In this section, we consider the possibility that the screen (central part) will project without belts, fixing ropes, and joints. The possibility of screen projection was evaluated by the moment applied around the downstream and bottom edge of the screen. Figure 14 schematically shows the moment applied around the downstream side and bottom edges of the screen when the screen is installed.  $M_s$  (Nm) is the moment due to the track surface flow, and  $M_w$  (Nm) is the moment due to the screen's own weight. Here, the rotational stability  $S$  is defined as  $M_s / M_w$ . When the rotational stability  $S$  exceeds 1 ( $M_s$  becomes larger than  $M_w$ ), the screen lifts. Conversely, if the rotational stability  $S$  is less than 1, the screen will not lift. Figure 15 shows the results for  $S$  at wind velocity 53.4 m/s, which is equivalent to a train speed 300 km/h. When the height is 0 mm or -20 mm, and the angle is 20°, the rotational stability  $S$  is 1 or more, and the screen may lift. Therefore, if a fixing rope is not installed and the height or angle is large (height -20 mm or more and angle: 20° or more), there is a possibility that the screen will lift. However, the actual screen installation conditions are -50 mm height and 0° angle, and the results of this test show that the rotational stability  $S$  is almost 0 (Fig. 15). Notably, this wind tunnel test examined the possibility of screen projection, and there is no possibility of it lifting away in reality.

### 4.4 Ballast screen behavior observation

In the wind tunnel tests, we measured the aerodynamic force of the central part of the screen without belts, fixing rope, and joints. Figure 16 shows the screen's lifting behavior when the wind velocity increased to a maximum of 71 m/s (equivalent to a train speed of 399 km/h) at a height of -20 mm and an angle of 20° using a high-speed camera. The behavior of the screen when it lifts is as follows:

1) As the wind velocity increases, the central part gradually begins

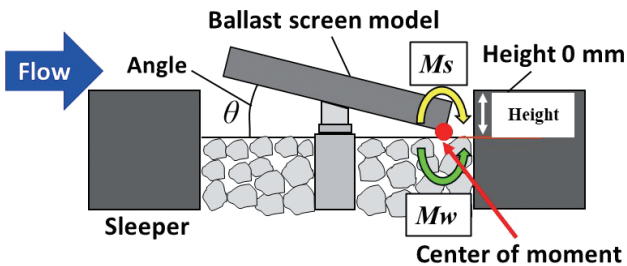


Fig. 14 Screen downstream/bottom moment

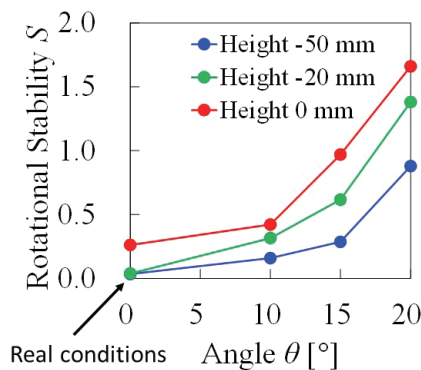


Fig. 15 Evaluation of the possibility of ballast screen projection

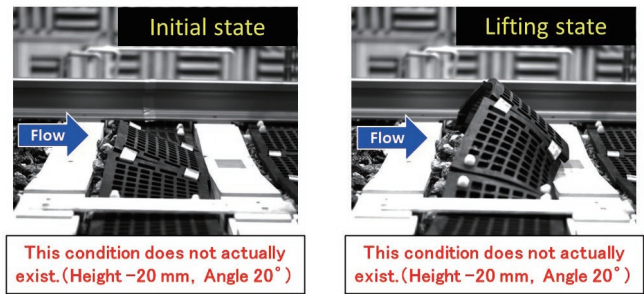


Fig. 16 Ballast screen behavior

to lift. 2) Since the central part and the outer part are connected using belts, the outer part is also pulled up by the central part. 3) After that, the downstream side of the central part also lifts, and the part of the downstream side of the central part covers the sleepers. 4) When the air blower stops, the screen keeps moving downstream. The screens that have moved downstream will not return to their original state. Furthermore, the lifting screens may foul the vehicle and structure gauges. Notably, this test was also conducted to confirm the behavior of the screen in installation conditions of a height of -20 mm and an angle of 20° which do not actually exist.

### 5. Conclusions

We developed a wind tunnel test method that can be used for the development of countermeasures to prevent the projection of trackside equipment considering the future extension of Shinkansen lines and increase in running speed of Shinkansen trains. The developed wind tunnel test method was also used to measure the aerodynamic forces exerted on ballast and ballast screens, and to evaluate the possibility of flying ballast or ballast screens. The results can be summarized as follows:

- (1) We developed a wind tunnel test method that allows the ballast to fly by covering a full-scale ballast track model with a net to prevent damage from projections.
- (2) Roughness blocks were installed on the nozzle floor of the wind tunnel to reproduce the wind velocity distribution on the track surface of a passing Shinkansen train.
- (3) The measurements of aerodynamic forces acting on the ballast showed that when the ballast is installed at a lower height than the sleepers, almost no aerodynamic force is exerted on the ballast.
- (4) The aerodynamic force exerted on the ballast screen was measured at different installation heights and angles to determine the height and angle at which it was likely to lift.
- (5) We clarified the behaviors which lead to ballast projection and lifting of ballast screens.

### References

- [1] Ido, A., "Measurement of Under-floor Air Flow on Board the Train and on the Ground," *RTRI Report*, Vol. 23, No. 7, pp. 39-44, 2009 (in Japanese).
- [2] Yamazaki, N., Kitagawa, T., Uda, T., Nagakura, K., Iwasaki, M. and Wakabayashi, Y., "Evaluation Method for Aerodynamic Noise Generated from the Lower Part of Cars in Consideration of the Characteristics of Under-floor Flows on Shinkansen

- Trains,” *Quarterly Report of RTRI*, Vol. 57, No. 1, pp. 62-68, 2016.
- [3] Premoli, A., Rocchi, D., Somaschini, C. and Tomasini, G., “Ballast flight under high-speed trains: Wind tunnel full-scale experimental tests,” *Journal of Wind Engineering and Industrial Aerodynamics*,” Vol. 145, pp. 351-361, 2015.
- [4] Yoshida, M., Uchida, M., Yaguchi, N. and Mifune, N., “Countermeasures for Ballast-Flying Phenomena Caused by High-Speed Trains,” *RTRI Report*, Vol. 6, No. 6, pp. 27-36, 1992 (in Japanese).
- [5] Inoue, T., Nakano, T. and Ido, A., “Wind Tunnel Test to Reproduce Track Surfaces Flow When Shinkansen Trains Pass for Ballast and Ballast Screen Scattering,” *RTRI Report*, Vol. 37, No. 7, pp. 27-33, 2023 (in Japanese).
- [6] Ido, A., “Transaction of Railway Development in Large-Scale Low-Noise Wind Tunnel,” *RRR*, Vol. 79, No. 3, pp. 4-9, 2022 (in Japanese).

## Authors



*Tatsuya INOUE*, Ph.D.  
Assistant Senior Researcher, Vehicle Aerodynamics Laboratory, Environmental Engineering Division (Former)  
Research Areas: Fluid Engineering of Railway



*Atsushi IDO*, Ph.D.  
Director, Wind Tunnel Technical Center, Research and Development Promotion Division  
Research Areas: Fluid Engineering of Railway



*Takashi NAKANO*  
Researcher, Vehicle Aerodynamics Laboratory, Environmental Engineering Division  
Research Areas: Fluid Engineering of Railway

# Simple Method for Estimating Buckling Temperature of Continuous Welded Rail Considering Lateral Track Irregularities

Daiki YAMAOKA

Shingo TAMAGAWA

Yuki NISHINOMIYA

Track Structure and Components Laboratory, Track Technology Division

*The setting of the control index for buckling of continuous welded rails in Japan is based on the lowest rail temperature increase at which buckling can theoretically occur. However, there is a considerable difference between the index temperature and the buckling temperature at which actual rail buckling occurs. Therefore, the current buckling control index safety margin may be excessive. In order to improve the accuracy of this control index, it is necessary to estimate the buckling temperature affected by lateral track irregularities. This study proposes a method for easily estimating the buckling temperature of continuous welded rails considering lateral track irregularities measured by a track inspection car.*

**Key words:** lateral track irregularities, track inspection car, continuous welded rail, buckling temperature, FEM

## 1. Introduction

On ballasted tracks, the expansion and contraction of continuous welded rails due to temperature changes is restrained by the ballast bed with sleepers and rail fastening systems, creating a rail axial force. In particular, in high temperatures during summer, a compressive force acts on the rails. When the rail axial force reaches the compression limit force, track buckling can occur, pushing out the rails in the lateral direction. It is therefore necessary to manage track conditions appropriately to prevent track buckling in continuous welded rail sections.

Figure 1 shows the relationship between the lateral displacement of rails and the temperature increase in rails from a stress-free temperature, i.e., an equilibrium state of temperature loads and internal forces in the tracks. Here, a stress-free temperature is a temperature at which the rail axial force is zero. As the rail temperature reaches the maximum point A in Fig. 1, the balance state jumps to point B without passing through point C where the balance state is unstable, and lateral rail displacement increases at once. This movement represents the buckling behavior seen on an actual track. Between points OA where lateral rail displacement is very small,  $T_c$  indicates the lower limit of the rail temperature increase at which buckling can theoretically occur, since there is only one balancing point until the rail temperature increase reaches  $T_c$  and snap-through buckling does not occur. Here, it has been pointed out that the rail temperature increase  $T_a$  (hereinafter buckling temperature) decreases with increasing lateral track irregularities [1]. In Japan, the safety margin against track buckling has been evaluated based on  $T_c$  in a way that includes the influence of lateral track irregularities for buckling strength [2].

However, there is quite large temperature difference between the buckling temperature  $T_a$  and  $T_c$ , which means the safety margin against track buckling may be larger than necessary and may not be rational from a maintenance cost perspective. On the other hand, to decrease the safety margin, it is necessary to accurately evaluate the buckling temperature when influenced by lateral track irregularities. A study has been carried out to try to decrease the safety margin by taking into account the temperature difference between the actual buckling temperature and  $T_c$  [3]. However, this study does not sufficiently take into account the complex lateral track irregularities observed in actual tracks.

We therefore carried out a series of analyses that can simulate

track buckling using FEM, to accurately evaluate the buckling temperatures of actual tracks. In these analyses, the lateral curved rail geometry was calculated from actual lateral track irregularities measured by a track inspection car (hereinafter rail geometry). Based on the analysis results, we proposed a simple method for estimating the buckling temperatures of continuous welded rails, considering complex lateral track irregularities of the rails, without conducting FEM analyses that incur large calculation costs [4].

## 2. Basic study on parameters influencing buckling temperature using FEM

### 2.1 Overview of analysis model

We used a nonlinear static analysis tool developed for calculating track buckling [5]. The validation of this analysis tool has been confirmed by comparison of output with the results of a track buckling test on a full-size track [5].

Figure 2 shows the overview of the track buckling analysis model in this study. This model consists of a straight track model with a length of 100 m. It assumes a fixed section of continuous welded rail that does not expand and contract with changing rail temperature: longitudinal displacement ( $x$  axial translation direction) of both ends of the rail is restrained in this model. Rails and

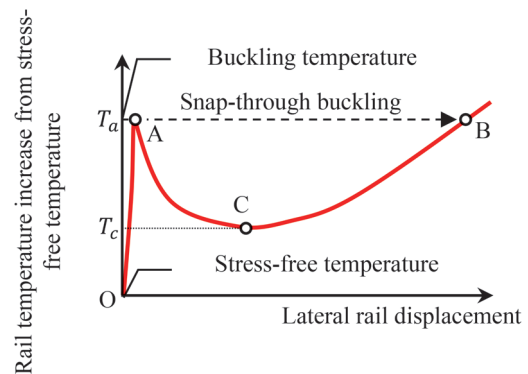


**Fig. 1 Relationship between increase in rail temperature and lateral rail displacement**

sleepers are represented by Euler beam elements. The longitudinal/lateral/rotational resistance properties of rail fastening systems are represented by spring elements connecting nodes of rails and sleepers; the properties of ballast longitudinal resistances and ballast lateral resistances are represented by spring elements connecting nodes of sleeper ends and fixed points. In addition, it is possible to apply nonlinear properties on each spring element.

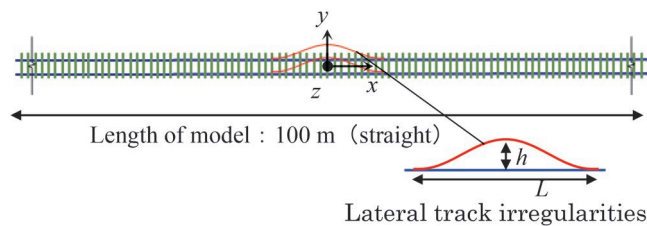
This analysis is based on finite displacement theory and uses the load increment method and the arc-length increment method [6] to solve the balance equation.

## 2.2 Parameters for analysis

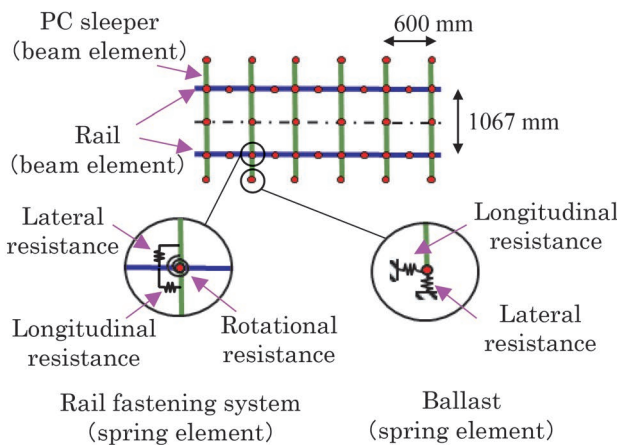
Table 1 shows the parameters of the analysis model. The material properties of the rails and sleepers are 50kgN rail and type-3 PC sleeper, respectively. The resistance of each rail fastening system is the standard value of rail fastening systems for ballast tracks [7, 8]. Ballast longitudinal resistances and ballast lateral resistances are non-linear properties [3]. And the maximum value of ballast lateral resistance (hereinafter maximum ballast lateral resistance) is the value that is generally secured for sections without sharp curves in Japan [9]. And the maximum value of the ballast longitudinal resistance is 1.5 times that of the maximum ballast lateral resistance. In addition, “kN/m/rail” will be used hereafter as the unit of ballast lateral resistance and ballast longitudinal resistance in this paper. This is the value per sleeper converted to the value per 1m of track, and then converted to the value per rail on one side.

In section 2.3.1, the virtual lateral track irregularity expressed in (1) is shown in Fig. 2 (a) and Table 1.

$$y_0 = \frac{h}{2} \left( 1 + \cos \frac{2\pi}{L} x \right), \quad -\frac{L}{2} \leq x \leq \frac{L}{2} \quad (1)$$



(a) Whole of analysis model



(b) Component element of analysis model

Fig. 2 Overview of track buckling model

Where  $y_0$  = lateral track irregularity;  $h$  = wave height of lateral track irregularity; and  $L$  = wavelength of lateral track irregularity.

In addition, this study does not consider rail bending moments and changes in ballast lateral resistance caused by initial lateral track irregularities.

## 2.3 Analysis of the influence of each parameter on buckling temperatures

### 2.3.1 Relationship between each parameter and buckling temperatures

In this section, we carried out buckling analyses in which each resistance of rail fastening systems, ballast longitudinal resistances, ballast lateral resistances, and wave heights of lateral track irregularities were changed. And we summarized the relationship between each parameter and the buckling temperatures. Here, when any parameter was changed, the other parameters were fixed at the standard values shown in Table 1.

Figure 3 shows the relationship between each parameter and the buckling temperatures. First, in Fig. 3 (a) to (c), the buckling temperatures when each resistance of rail fastening systems was varied from 0.5 to 2.0 times the standard values were from 0.99 to 1.06 times the standard value, and notable differences were not confirmed.

Secondly, in Fig. 3 (d), when ballast longitudinal resistance was varied from 0.5 to 2.0 times the standard value, the buckling temperatures matched the standard value. However, as shown in Fig. 3 (e), it was observed that the buckling temperature changed by approximately 13°C per 1 kN/m/rail in response to increase ballast lateral resistance.

Finally, Fig. 3 (f) shows that the buckling temperature decreased non-linearly as the wave height of lateral track irregularities increased, and a decrease of approximately 67°C was observed when the wave height was increased from 4 mm to 20 mm.

### 2.3.2 Influence against buckling temperatures by parameter related with lateral track irregularities

From the parameters that characterize waveforms it is important to identify the governing factors that affect buckling temperatures, to estimate the buckling temperature based on lateral track irregularities measured by inspection car. Prior to the study using the complex lateral track irregularities measured by inspection car, we carried out buckling analyses by varying the types, wave heights, and wavelengths of the lateral track waveforms. We then summarized the relationship between the parameters of lateral track irregularities and the buckling temperatures.

In this section, parametric analyses were carried out on the wavelengths and wave heights of the four types of waveforms conventionally used in theoretical analyses on the buckling strength of track [10], as shown in Fig. 4, as the lateral displacement waveforms. Although the mathematical formulas for each waveform are not described in this paper, the analysis model is the same as in Fig. 2 and the specifications are the values in Table 1.

We carried out the buckling FEM analyses, by changing the wavelength  $L$  of each waveform from 10 m to 20 m, and the wave height  $h$  of each waveform from 4 mm to 20 mm. Here, the range of wavelengths  $L$  is the value taken into consideration for track maintenance [11]; from among the track maintenance standard values used on commercial lines of Japan Railways, the maximum wave height  $h$  20 mm is the value equivalent to the standard value of lat-

**Table 1 Specifications of analysis model (standard values)**

Item	Value	
50kgN Rail	Young's modulus	2.058×10 <sup>5</sup> N/mm <sup>2</sup>
	Poisson ratio	0.3
	Linear expansion coefficient	1.14×10 <sup>-5</sup> /°C
	Cross-sectional area	6.42×10 <sup>3</sup> mm <sup>2</sup>
	Second moment of area (around the z axis)	3.22×10 <sup>6</sup> mm <sup>4</sup>
Type-3 PC sleeper	Young's modulus	2.2×10 <sup>4</sup> N/mm <sup>2</sup>
	Poisson ratio	0.2
	Cross-sectional area	2.84×10 <sup>4</sup> mm <sup>2</sup>
	Second moment of area (around the z axis)	1.14×10 <sup>8</sup> mm <sup>4</sup>
	Length	2000 mm
Rail fastening system	Spring constant of rotational resistance	27.6 kNm/rad
	Spring constant of longitudinal resistance	12 kN/mm
	Spring constant of lateral resistance	43 kN/mm
Ballast lateral resistance	Saturation value $g_0$	4 kN/m/rail
	Calculation formula $g$	$g = g_0 \times v / (v + 1.0)$ $v$ : y direction displacement (mm)
Ballast longitudinal resistance	Saturation value $k_0$	6 kN/m/rail
	Calculation formula $k$	$k = k_0 \times u / (u + 1.0)$ $u$ : x direction displacement (mm)
Lateral track irregularities	Wavelength $L$	10 m
	Wave height $h$	13 mm

eral track irregularities on line sections where the running speed is over 120 km/h.

Figure 5 (a) shows the relationship between the buckling temperatures and the wavelengths when the wave height is 10 mm. It shows that the buckling temperatures increase as the wavelength increases for each waveform. However, the buckling temperatures at the same wavelength are different depending on the waveforms.

Figure 5 (b) shows the relationship between the buckling temperatures and the wave heights when the wavelength is 10 m. It shows that the buckling temperatures decrease as the wave height increases for each waveform. However, the buckling temperatures at the same wave height are difference depending on the waveforms.

It is difficult to estimate buckling temperatures on actual tracks using only the parameters of wavelength or wave height because of the above results and the fact that it is difficult to define the wavelengths and wave heights of actual lateral track irregularities, which have more complex waveforms than the waveforms shown in Fig. 4. Nevertheless, the increase in buckling temperature as the wavelength increases and the wave height decreases, suggests there is a relationship between the curvatures of the waveforms and the buckling temperatures. We therefore summarize this relationship below.

Figure 5 (c) shows the relationship between the buckling temperatures and the maximum curvatures of the waveforms (hereinafter max curvature,  $\kappa_{max}$ ) in the case of wavelengths of 10 m ~ 20 m and wave heights of 4 mm ~ 20 mm. In addition, the curvatures of the waveforms are calculated by (2) ~ (4), which are discretized to be applied to the track inspection data shown in the following section.

$$\kappa = \frac{|y''|}{(1 + y'^2)^{\frac{3}{2}}} \tag{2}$$

$$y'' = \frac{1}{2} \left( \frac{y_0 - y_1}{x_0 - x_1} + \frac{y_1 - y_2}{x_1 - x_2} - \frac{y_2 - y_1}{x_2 - x_1} - \frac{y_1 - y_0}{x_1 - x_0} \right) / (x_1 - x_{-1}) \tag{3}$$

$$y' = \frac{1}{2} \left( \frac{y_{-1} - y_0}{x_{-1} - x_0} + \frac{y_0 - y_1}{x_0 - x_1} - \frac{y_1 - y_2}{x_1 - x_2} \right) \tag{4}$$

Where  $x_i$  = coordinate value of x axial of five consecutive rail nodes including lateral track irregularities ( $i = -2 \sim 2$ );  $y_i$  = coordinate value of y axial of five consecutive rail nodes including lateral track irregularities ( $i = -2 \sim 2$ ).

Figure 5 (c) shows the trend that the buckling temperatures decrease as the maximum curvatures increases for each waveform. And the buckling temperatures of each waveform are approximately the same at each maximum curvature. It is therefore conceivable that the buckling temperatures of actual tracks including complex lateral track irregularities can be estimated by the maximum curvatures of the waveforms.

### 3. Track buckling analyses using measured lateral track irregularities

In this section, based on the results of the basic studies in section 2, we conducted buckling analyses using the lateral track irreg-

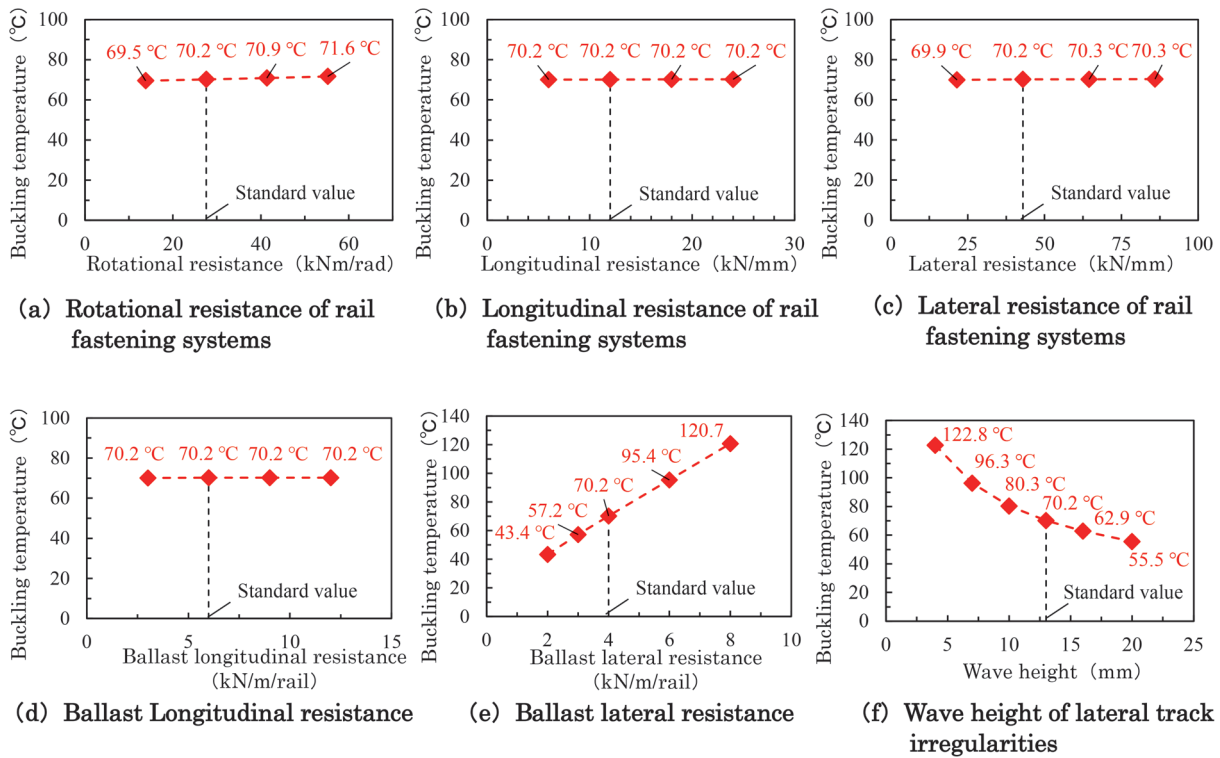


Fig. 3 Relationship between each parameter and buckling temperature

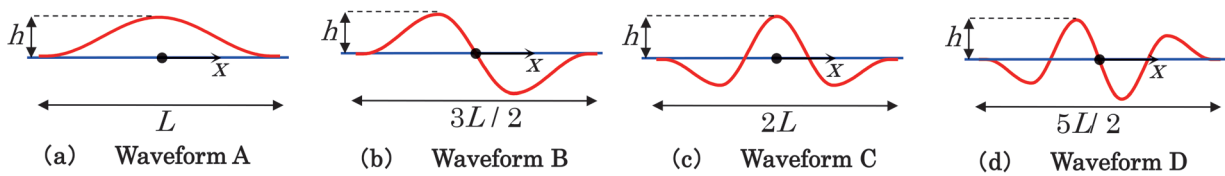


Fig. 4 Lateral track waveform

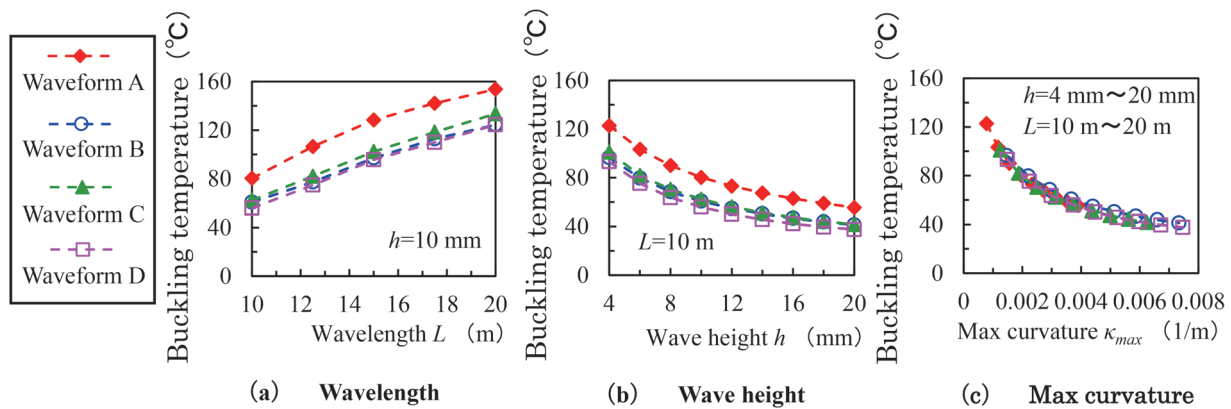


Fig. 5 Relationship between buckling temperature and parameters of lateral track irregularities

ularities measured by a track inspection car, and summarized the relationship between the results of the analysis and the maximum curvature of the lateral track irregularities. We then investigated a simple method that can estimate the buckling temperatures with track inspection data. To focus on the effect of lateral track irregularities on the analysis results, longitudinal level track irregularities, cross level track irregularities and twisting track irregularities are not considered.

### 3.1 Overview of analysis model

The lateral track irregularities used for the analysis model are the data inspected by a 2-bogie type track inspection car using the 2.1 m – 14.4 m asymmetrical chord offset method [12]. Here, the inspected lateral track irregularities are converted to restored waveforms [13] by the digital inverse filter [13]. And these restored waveforms are added to the rail geometry of the analysis models. In

**Table 2 Details of analysis cases**

Basic alignment (curve radius $R$ )	Case number	Basic alignment of actual measurement section
Straight	144	Straight
$R800$ m	28	$R > 800$ m
$R600$ m	61	$400 \text{ m} < R \leq 800$ m
$R400$ m	60	$R \leq 400$ m

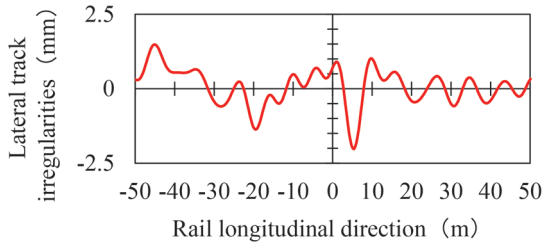


**Fig. 6 Example of restored waveform of lateral track irregularities**

the case of the curved track model, the restored waveforms are added to the circular curved rail geometry of the analysis models. Here, the wavelength bands for generating the restored waveforms were set from 6 m to 45 m, taking into account the application to the inspection data measured using the 10 m chord offset method and the elimination of the effects of curve radius on the amount of chord offset. The 293 analysis cases of straight track and curved track (curve radius  $R$  is 400 m/600 m/800 m) were generated as shown in Table 2. Figure 6 shows the example of the restored waveform of lateral track irregularities on straight track. The size of the analysis models and the parameters other than lateral track irregularities are the same as in Fig. 2 and Table 1.

### 3.2 Setting of control nodes

When conducting analyses using the arc length increment method, it is necessary to select the degree of freedom of the node whose displacement is considered to be relatively larger than that of other nodes in the analysis model, and to track the balance path at the degree of freedom of the node sequentially by convergence calculations. In these analyses, the node whose balance path is tracked is a “control node.” And assuming that a relatively larger displacement is generated in the  $y$  axial translation direction that is equivalent to the buckling direction, we decided to track the balance path of the  $y$  axial translation direction of the control node. In addition, each displacement per convergence calculation step at the degree of freedom of the other nodes can be sought by following the displacement of the control node in the  $y$  axial translation direction.

On the other hand, the lateral track irregularities shown in Fig. 6 are complex, so it is not possible to identify the location at which buckling occurs. Here, in the study of section 2, it is shown that maximum curvatures are related to buckling temperatures. Therefore, in these analyses, predicting that maximum curvatures influence buckling temperatures and buckling locations, we carried out buckling analyses using the rail node corresponding to the location of maximum curvature as the control node. However, in the cases where buckling did not occur at the maximum curvature location, we carried out the analyses by changing the control node until we identified the buckling location. None of the analysis cases

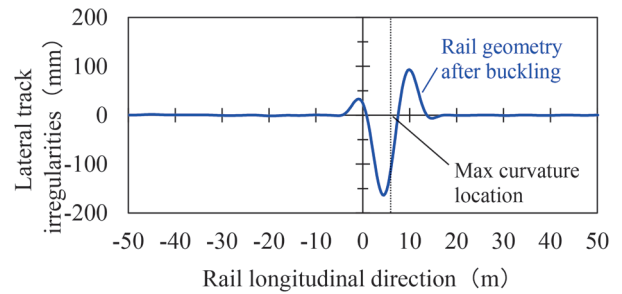


**Fig. 7 The rail geometry after buckling**

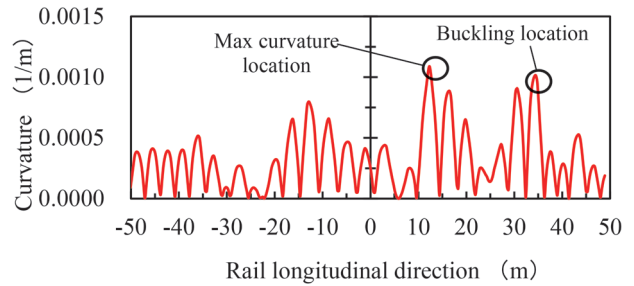


**Fig. 8 Curvature distribution of analysis case where maximum curvature location and buckling location deviate**

shown in Table 2 include cases where the buckling location is within 15 m from both ends of the analysis model due to prior consideration so that the analysis results are not affected by the restraint conditions at both ends of the analysis model.

### 3.3 Analysis results

We carried out buckling analyses of the 293 cases shown in section 3.1. Figure 7 shows an example of the rail geometry after buckling in the analysis case where lateral track irregularities were applied as shown in Fig. 6. It was found that buckling occurred close to the location of maximum curvature. Nevertheless, it was confirmed that there are some cases where the maximum curvature location and the buckling location diverge. However, in these cases, the curvature at the buckling location is nearly equal to the maximum curvature shown in Fig. 8. In this study, the curvatures of rail geometries that are discrete data have been calculated in (2) ~ (4). However, there are various calculation methods for curvatures that are discrete data, and it has been shown that the curvature values are different depending on the calculation methods [14]. That is, if the curvatures of the cases where the maximum curvature location and the buckling location are separated are calculated by methods other than the method shown in this study, there may be a possibility that the maximum curvature location and the buckling location could coincide. However, this study does not provide comparative validation of the accuracy of the degree of agreement between the maximum curvature location and the buckling location. We would like to leave this as an issue for future consideration. In addition, in this study, buckling occurred at the maximum curvature location in 248 out of 293 cases. This means that buckling occurred at the maximum curvature locations in more than 80% of cases.

The relationship between maximum curvatures and buckling temperatures was summarized, as shown in Fig. 9, for the 248 cases where buckling occurred at the maximum curvature location. Figure 9 shows that there is a strong relationship between the maxi-

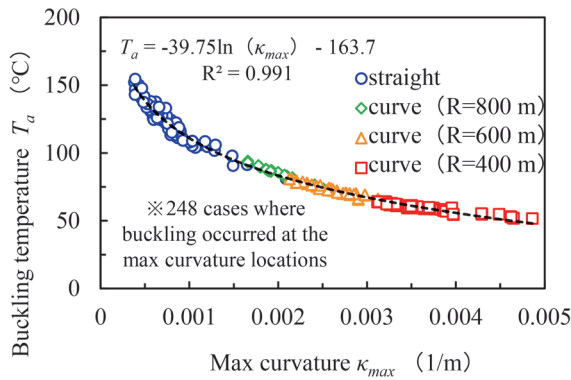


**Fig. 9 Relationship between maximum curvatures and buckling temperatures**

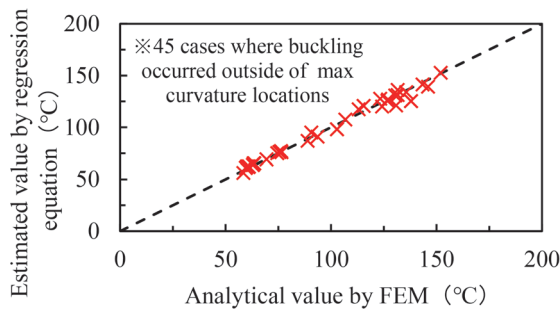


**Fig. 10 Comparison of buckling temperature results**

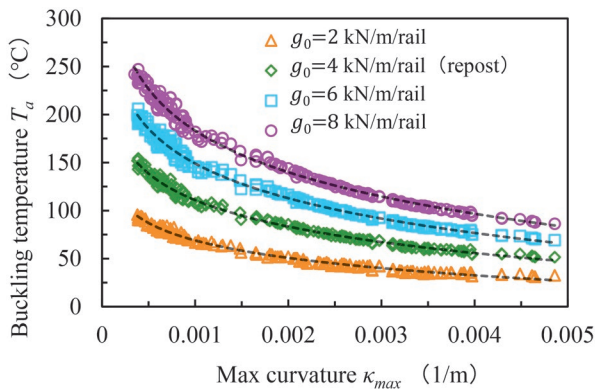


**Fig. 11 Relationship between maximum curvatures and buckling temperatures for each ballast lateral resistance**

maximum curvature and the buckling temperature, as indicated by a logarithmic function with a determination coefficient of approximately 0.99. As for the 45 cases where buckling occurred at a location other than the maximum curvature location, the buckling temperatures were estimated by substituting the maximum curvature for each analysis model into the regression equation shown in Fig. 9, and compared with the FEM analysis values. Figure 10 shows the results of a comparison of buckling temperatures for the 45 cases mentioned above. According to the figure, even when the maximum curvature location and the buckling location do not coincide, it is possible to accurately estimate the buckling temperatures using the maximum curvature as an explanatory variable. This is because, as shown in Fig. 8 above, for each analysis case, the curvature at the buckling location is close to the maximum curvature.

**Table 3 Number of cases buckling occurred at maximum curvature locations**

$g_0$ (kN/m/rail)	The number of cases buckling occurred at max curvature locations (out of 293 cases)
2	258 (88.1%)
6	272 (92.8%)
8	266 (90.8%)

**Table 4 Regression equation coefficient and determination coefficient**

$g_0$ (kN/m/rail)	$a$	$b$	Determination coefficient
2	-26.21	-112.1	0.990
6	-52.14	-211.2	0.990
8	-62.41	-247.9	0.991

(Format of regression equation :  $T_a = a * \ln \kappa_{max} + b$ )

### 3.4 Regression estimation formula for each ballast lateral resistance

A series of analyses were so far carried out with the maximum ballast lateral resistance in the analysis model kept constant at 4 kN/m/rail. On the other hand, the buckling temperatures are also affected by the ballast lateral resistances. Therefore, for all the analysis cases shown in Table 2, the buckling analyses were carried out in the same way when the maximum ballast lateral resistance  $g_0$  was set to 2, 6 and 8 kN/m/rail (other parameters are fixed). The relationship between the maximum curvatures and the buckling temperatures was summarized.

Table 3 shows the number of cases where buckling occurred at the maximum curvature location for each ballast lateral resistance, and Fig. 11 shows the relationship between the maximum curvatures and the buckling temperatures for each ballast lateral resistance. In addition, Table 4 shows the coefficients and the determination coefficients of the regression equation (logarithmic representation) is used as an explanatory variable for each ballast lateral resistance.

Table 3 shows that it is possible to predict the buckling location in more than 88% of the sections even when the ballast lateral resistance is varied. In addition, Table 4 confirms that there is a strong relationship between the maximum curvatures and the buckling temperatures via a logarithmic function with a determination coefficient of approximately 0.99.

From the above, it is thought that even if different ballast lateral resistance is set for each evaluation section, the buckling temperatures can be estimated from the maximum curvature in the evaluation section according to the value of the ballast lateral resistance.

## 4. Conclusion

We carried out a series of buckling analyses using FEM for continuous welded rails on ballasted tracks. We also investigated a method for estimating buckling temperatures more easily than FEM analysis using lateral track irregularities measured by a track inspection car. The main results obtained are as follows.

(1) Buckling analyses were carried out by varying rail fastening system resistance, ballast longitudinal resistance, ballast lateral res-

sistance, and wave height of lateral track irregularities. The results showed that ballast lateral resistance and wave heights of lateral track irregularities have a large influence on buckling temperature, with sharp changes due to changes in wave height.

(2) As a result of parametric analyses that varied the waveforms of the lateral track irregularities, their wave heights, and their wavelengths, it was found that although the relationship between the wavelengths, wave heights, and the buckling temperatures differed for each waveform, the relationship between the maximum curvatures of the waveforms and the buckling temperatures was consistent for each waveform.

(3) As a result of buckling analyses using the restored waveforms of lateral track irregularities measured by a track inspection car as rail geometries (with a circular curve added in the case of a curved track), it was found that there is a strong relationship between the maximum curvatures of the rail geometry and the buckling temperatures, with a determination coefficient of approximately 0.99 in the regression equation using the maximum curvatures as the explanatory variable.

(4) A practical method for easily estimating the buckling temperatures is to calculate the maximum curvatures of the rail geometry based on the lateral track irregularities measured by a track inspection car and use this and the regression formula in (3) above.

In the future, we plan to develop a simple method for estimating buckling temperatures, considering the actual conditions of the track, such as variations in ballast lateral resistance, rail temperature, free-stress temperature, and so on.

## References

- [1] Miyai, T., "Numerical Analysis of Track Buckling by Energy Method," *Railway Technical Research Report*, Issue 1271, 1984 (in Japanese).
- [2] Supervised by Ministry of Land, Infrastructure, Transport and Tourism, *Design Standards for Railway Structures and Commentary (Track Structures)*, Maruzen, pp. 173-186, 2012 (in Japanese).
- [3] Nishinomiya, Y. and Kataoka, H., "Study of the stability of continuous welded rail in consideration of a critical buckling temperature increase," *Journal of Railway Engineering*, JSCE, Issue 20, pp. 9-15, 2016 (in Japanese).
- [4] Tamagawa, S., Yamaoka, D. and Nishinomiya, Y., "Practical method for estimating buckling temperature of continuous welded rails based on lateral track irregularities measured by track inspection car," *Journal of Structural Engineering*, Vol. 69A, pp. 1-10, 2023 (in Japanese).
- [5] Tamagawa, S. and Nishinomiya, Y., "FEM simulation of buckling test of full size track," *Journal of Railway Engineering*, JSCE, Issue 23, pp. 267-274, 2019 (in Japanese).
- [6] Ramm, E., "Strategies for Tracing the Nonlinear Response Near Limit Points," *Nonlinear Finite Element Analysis in Structural Mechanics*, pp. 63-89, 1981.
- [7] Umeda, S. and Kumazaki, H., "Development of Improved Type-5 Rail Fastening Device for Type-3 Prestressed Concrete Tie," *Railway Technical Research Report*, Issue 1332, 1986 (in Japanese).
- [8] Tamagawa, S., Kataoka, H., Nishinomiya, Y. and Kotani, J., "Improvement in Evaluation Method of Lateral Stability of Turnout Connected with Continuous Welded Rail," *RTRI Report*, Vol. 27, No. 4, pp. 11-16, 2013 (in Japanese).
- [9] Ito, M., "Rail neutral temperature of continuous welded rail and ballast lateral resistance," *Shinsenro*, Vol. 50, No. 4, pp. 28-31, 1996 (in Japanese).
- [10] Numata, M., "Buckling Strength of Long Welded Rail," *Railway Technical Research Report*, Issue 721, 1970 (in Japanese).
- [11] Furukawa, A., "Improving ride comfort from the perspective of track maintenance," *RRR*, Vol. 62, No. 12, pp. 10-13, 2005 (in Japanese).
- [12] Takeshita, K., "A Method for Track Irregularity Inspection by Asymmetrical Chord Offset Method," *RTRI Report*, Vol. 4, No. 10, pp. 18-24, 1990 (in Japanese).
- [13] Yoshimura, A., "Study on theoretical foundations to restoring an original waveform of track irregularity and its application," *Proceedings of JSCE*, Vol. 377, pp. 117-126, 1987 (in Japanese).
- [14] Ono, N., and Takiyama, R., "On calculations of curvature of sampled curves," *ITEJ technical report*, Vol. 17, No. 76, pp. 7-14, 1993 (in Japanese).

## Authors



**Daiki YAMAOKA**  
 Researcher, Track Structures and Components Laboratory, Track Technology Division  
 Research Areas: Continuous Welded Rail, Rail Fastening System



**Yuki NISHINOMIYA**, Ph.D.  
 Senior Researcher, Track Structures and Components Laboratory, Track Technology Division  
 Research Areas: Continuous Welded Rail, Railway Vehicle Dynamics Simulation



**Shingo TAMAGAWA**, Ph.D.  
 Senior Researcher, Track Structures and Components Laboratory, Track Technology Division  
 Research Areas: Continuous Welded Rail, Rail Fastening System

# Method for Estimating Bending Stiffness of Concrete Girders during Train Passage Considering Effects of Concrete Cracks and Non-structural Members

Munemasa TOKUNAGA      Manabu IKEDA  
Structural Mechanics Laboratory, Railway Dynamics Division

*This paper presents the results of a study to investigate a method for estimating the stiffness of concrete girders when calculating the dynamic factor and deflection. Based on a fatigue test of concrete members, we proposed an estimation formula which takes into account the reduction in bending stiffness due to crack propagation under cyclic loading. In addition, we quantified the stiffness contribution of each type of non-structural member by means of finite element analysis for various girder structures. Finally, we propose a simple method for estimating the equivalent bending stiffness of girders considering reduction in stiffness due to bending cracks after repetitive loading and the stiffness contribution of non-structural members.*

**Key words:** bending stiffness, concrete girder, concrete cracks, non-structural member, dynamic factor

## 1. Introduction

Increasing train running speeds on high-speed railways and widespread use of low-stiffness girders such as PRC and SRC girders, has led to the observation of a significant number of resonance phenomena on railway bridges due to passing train because of the decrease in bending stiffness caused by bending cracks in the main girders [1].

In order to accurately predict dynamic response amplification due to resonance phenomena at the design stage, it is necessary to appropriately estimate the equivalent stiffness  $EI_{eqr}$  (see Fig. 1) during reloading after cracking of the concrete members due to passing trains. Here, the equivalent stiffness during reloading is calculated based on the cross section that can be assumed to be effective, which differs from the secant stiffness  $EI_e$  after cracking and the stiffness  $EI_{cr}$  based on the crack section theory because the stiffness changes with repeated loading due to train passages. Previous design standards [2] have not provided specific methods for considering decrease in stiffness due to bending crack occurrences in concrete members or the stiffness contribution of non-structural members, as shown in Fig. 2. The stiffness calculated on the basis of entire cross section theory has traditionally been used in design for convenience; however, the scope of its application has not been clarified.

The bending stiffness of girders decreases due to the occurrence of bending cracks in the main girder, whereas it increases considerably due to the contribution of non-structural members installed on the main structure of railway structures such as tracks, noise barriers and bridge railings. The influence of these non-structural members becomes larger when the cross-sectional stiffness of the main girder is relatively small, such as SRC girders or short-span concrete girders. When non-structural members are not considered for the bridges, the natural frequency may be underestimated, and the calculated value of the dynamic factor tends to be larger than the actual bridge measurement. The influence of these non-structural members varies greatly depending on the variety of members in terms of shape, arrangement, etc. Therefore, a method for estimating the bending stiffness of girders, taking into account the non-structural members used in recent railway bridges, is needed so that it can be applied to actual designs.

This paper presents the results of a study on the effects of cracks in concrete members and the contributions of non-structural members such as tracks on the reloaded stiffness of concrete girders

during train passages. Based on the presented results, a method for estimating the equivalent stiffness of concrete girders during reloading is presented. In addition, the scope of application of the conventional entire cross-sectional stiffness has been clarified.

These results have been incorporated into the Design Standards for Railway Structures and Commentary (Concrete Structures) [3], the principle of which is to use the equivalent reloaded stiffness, which takes into account the decrease in stiffness due to bending cracks and the contribution of non-structural members when calculating the dynamic factor and deflection for structural members such as girders during train passage.

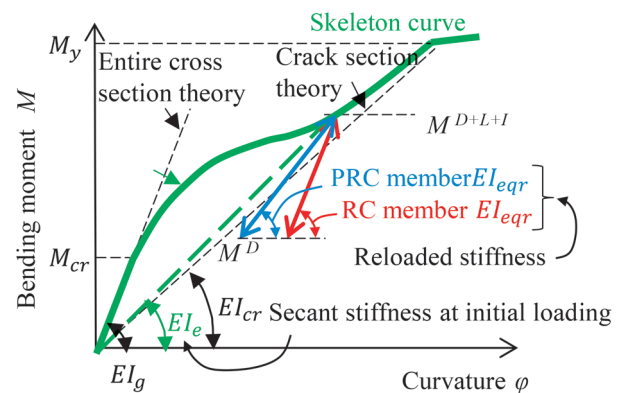


Fig. 1 Reloaded stiffness

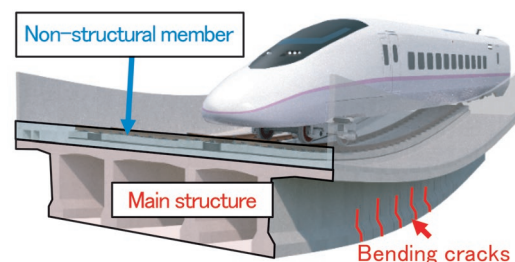


Fig. 2 Factors influencing bending stiffness

**Table 1 List of specimen specification**

Case	Name	PC steel bar			Tensile steel bar			Loading pattern
		Diameter	Prestress (kN)	Prestressing coeff.		Reinforcement ratio	Reinforcement coeff.	
1	RCs	-	-	0	D22	1.0%	0.118	Static loading
2	RCf	-	-	0	D22	1.0%	0.118	Fatigue
3	PRCs	$\phi 17$	165	0.716	D13	0.6%	0.131	Static loading
4	PRCf	$\phi 17$	165	0.716	D13	0.6%	0.131	Fatigue

**2. Reloaded stiffness of concrete members when cracks occur under repeated loading**

**2.1 Experiment method**

Table 1 shows a list of the specifications of the specimen [4]. In this study, the experimental specimen were PRC members and RC members to understand the basic characteristics of the prestress caused by PC tendons. Specifications such as the reinforcing bar ratio of the specimen and the amount of introduced prestress were adjusted to fit within the parameter range of a typical recent railway bridges. The reinforcement ratio includes tensile reinforcing steel bars and PC steel bars. The prestressing coefficient is the ratio of the strength of the PC tendons to the sum of the strengths of the reinforcing bar and the PC tendons, where the larger the value, the greater the implied similarity of PC member behavior. The reinforcing bar coefficient is the ratio of the strength of reinforcing bars and PC tendons based on the compressive strength of the concrete cross section, which was set to be roughly same for all specimens. Two RC member specimens and two PRC member specimens were produced, and a total of four experimental cases were carried out in which the loading patterns were varied in static loading tests and fatigue tests.

The same concrete material was used for the RC and PRC members. The material test results showed that the compressive strength was 47 N/mm<sup>2</sup>, the tensile strength was 3.56 N/mm<sup>2</sup>, and the Young's modulus was 32.2 kN/mm<sup>2</sup>. A highly fluid material was used for the grout of the PRC member, and material test results showed that it had compressive strength of 83.6 N/mm<sup>2</sup>, a tensile strength of 3.57 N/mm<sup>2</sup>, and a Young's modulus of 64.9 kN/mm<sup>2</sup>.

Figure 3 shows an overview of the experiment. As shown in the figure, the purpose of the static loading test was to evaluate the basic hysteresis characteristics of the member. The load was applied in increments of 20 kN by load control until the tensile reinforcing bar yielded, and after the yield, the load was applied in increments of 2 mm by displacement control. In the static loading test, the number of repetitions at each load level was three. The applied load was maintained at approximately 5 kN even when the load was unloaded for the sake of specimen stability. In the fatigue test, the load was dynamically applied, and the excitation frequency was 5 Hz, with a lower limit load of 50 kN assuming a reinforcing steel stress equivalent to the dead load of actual bridges (approximately 100 MPa), and an upper limit load of 70, 120, 170 and 200 kN. The number of repetitions at each load level was 2 million.

**2.2 Experiment result**

Figure 4 shows the relationship between load and displacement obtained from static loading tests and fatigue tests. The fatigue test results show the relationship when the number of repetitions is 1, 10<sup>2</sup>, 10<sup>3</sup>, 10<sup>4</sup>, 10<sup>5</sup>, 10<sup>6</sup>, and 2×10<sup>6</sup>. From the static loading test shown by the gray line, the skeleton curve where cracks occur and the stiff-

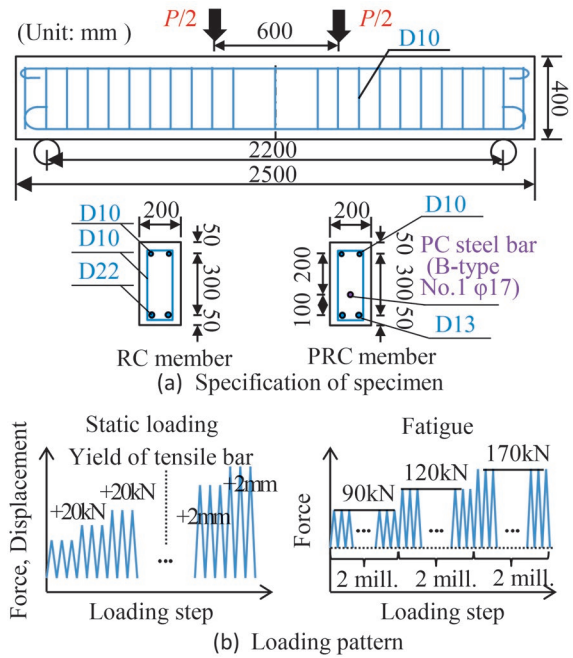


**Fig. 3 Overview of experiment**

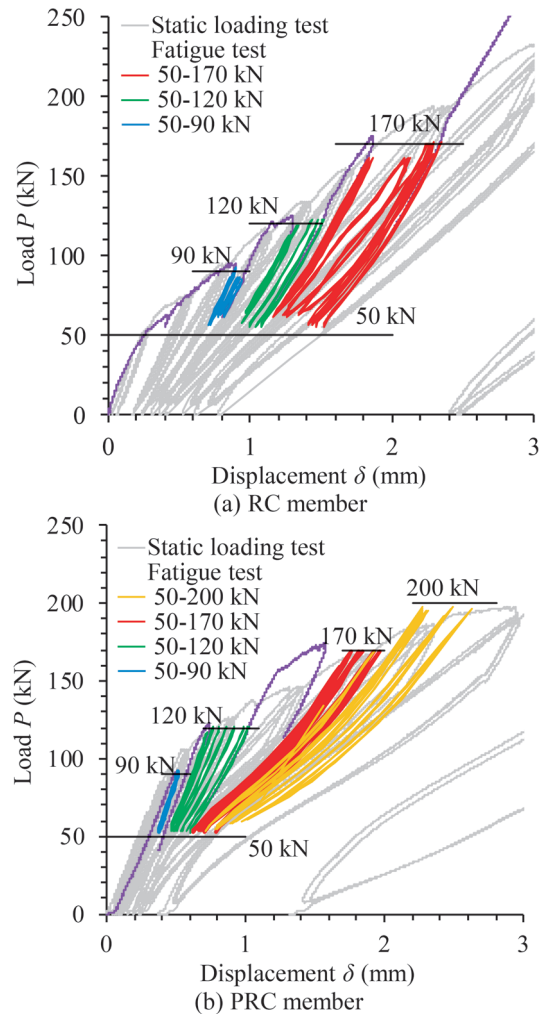


**Fig. 4 Relationship between load and displacement**

ness decreases (about 50 kN or more for RC members, about 90 kN or more for PRC members) implies that the slope of the load-displacement relationship during reloading and reloaded decreases as the load increases. From this, it can be seen that the stiffness during reloading is smaller than the stiffness in the elastic state before cracking. It can be seen that the residual displacement of RC members after unloading grows as the load increases, compared to PRC members. Compared to RC members, PRC members demonstrate the hysteresis characteristics of pointing closer to origin in the unloading stage, resulting in smaller residual displacement with a tendency to lose stiffness in the unloading stage. In other words, it can be said that the prestress introduced to reduce the crack width results in a decrease in the stiffness of the entire beam system.

The reloaded stiffness  $K_{egr}$ , which is the stiffness when the maximum load point and minimum load point of the loop in the load-displacement relationship during repeated loading in fatigue tests are connected by a straight line, is focused. Fatigue tests show that in the case of RC members, 2 million repeated loadings decrease  $K_{egr}$  by approximately 11% at 50-90 kN, 6% at 50-120 kN and 16% at 50-170 kN compared to the stiffness at initial loading for each load amplitude. In the case of PRC members, the repeated loadings decrease  $K_{egr}$  by about 10% at 50-90 kN, about 33% at 50-120 kN, and about 20% at 50-170 kN, which indicates that the decrease of PRC member is larger than that of RC members. These results imply that the stiffness of PRC members decreases, and the dynamic response tends to increase due to repeated loads caused by train passage.

Figure 5 shows the relationship between the fluctuation range of the effective moment of inertia  $I_{egr}$  in the reloading stage and the load level (load converted into bending moment).  $I_{egr}$  is calculated by dividing the stiffness during reloading by the Young's modulus of the concrete. The figure shows  $I_{egr}$  during reloading, which is nondimensionalized using the moment of inertia  $I_g$  of the entire cross-section theory (Bernoulli-Euler hypothesis) and the moment of inertia  $I_{cr}$  based on crack cross-section theory.

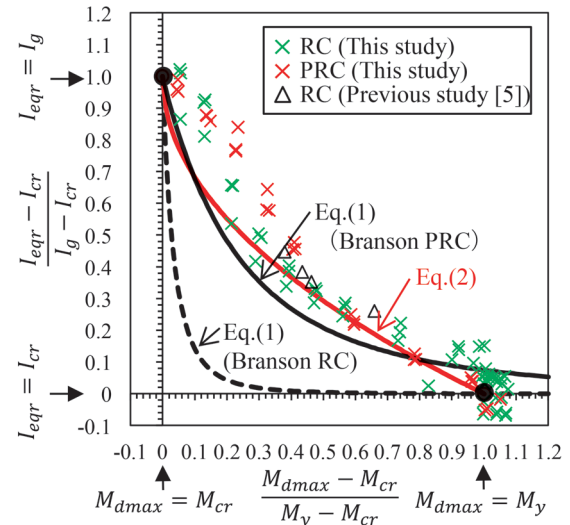
Figure 5(a) shows the results obtained from static loading tests of RC members and PRC members. The figure indicates that in the region close to the cracking moment  $M_{cr}$ ,  $I_{egr}$  gets closer to the moment of inertia  $I_g$  based on entire cross section theory, while it asymptotically approaches the moment of inertia  $I_{cr}$  based on crack cross-section theory as the bending moment response value  $M_{dmax}$  increases and approaches the yield moment  $M_y$ . It can be confirmed that the experimental results of both RC members and PRC members are distributed on a unique curve by nondimensionalizing both the horizontal and vertical axes by the formula in the figure. Rewriting Branson's rule [2] and [6] results in the equation (1):

$$\frac{I_{egr}}{I_g} = \frac{I_{cr}}{I_g} + \left(1 - \frac{I_{cr}}{I_g}\right) \left(\frac{M_{cr}}{M_{dmax}}\right)^3 \quad (1)$$

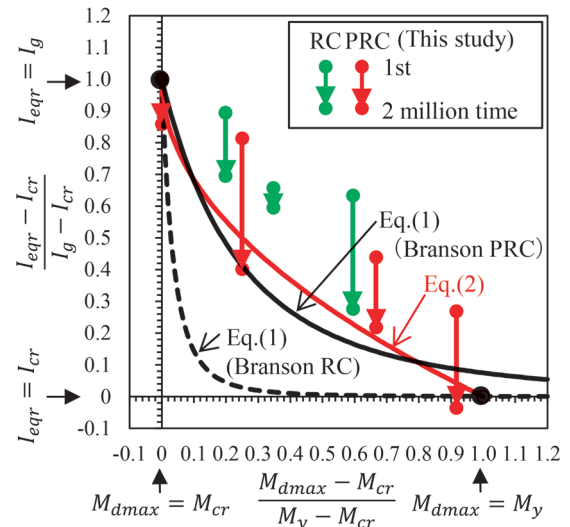
Where,  $M_{cr}$  is the bending moment when the bending crack occurs ( $\gamma_c=1.0, \gamma_b=1.0$ ) and  $M_{dmax}$  is the assumed response value of the bending moment.

Although equation (1) is consistent for PRC members, it gives an underestimate for RC members. Note that Branson's rule calculates the decrease in stiffness due to cracking during monotonous loading and does not take into account the effects of repeated loading during reloading state.

Figure 5(b) shows the results obtained from the fatigue tests of RC members and PRC members. The fatigue test results show that the stiffness at the first reloading for each load level tends to be larger than the static load test results. This is thought to be because the reloaded stiffness depends not only on the maximum load but



(a) Static loading test



(b) Fatigue test

**Fig. 5 Relationship between effective moment of inertia during reloading and load**

also on the lower limit of the load amplitude (dead load). In addition, the reloaded stiffness decreases through 2 million repeated loadings.

Based on the above loading experimental results, equation (2) is proposed as an estimation formula for the reloaded stiffness of concrete beam members.

$$\frac{I_{egr}}{I_g} = \frac{I_{cr}}{I_g} + \left(1 - \frac{I_{cr}}{I_g}\right) \left(1 - \sqrt{\frac{M_{dmax} - M_{cr}}{M_y - M_{cr}}}\right) \quad (2)$$

Where,  $M_y$  is the yield bending moment ( $\gamma_c=1.0, \gamma_b=1.0$ ). As can be seen from the fatigue test results, the reloaded stiffness during train passage changes depending on the number of repetitions; however, equation (2) was set so that the results of the 2 millionth fatigue test could be evaluated on the safe side in most cases, assuming that it would be used in design. Equation (2) shown in Fig. 5 can accurately express the tendency for  $I_{egr}$  to decrease as the load level increases, giving an evaluation slightly below the average of the test results.

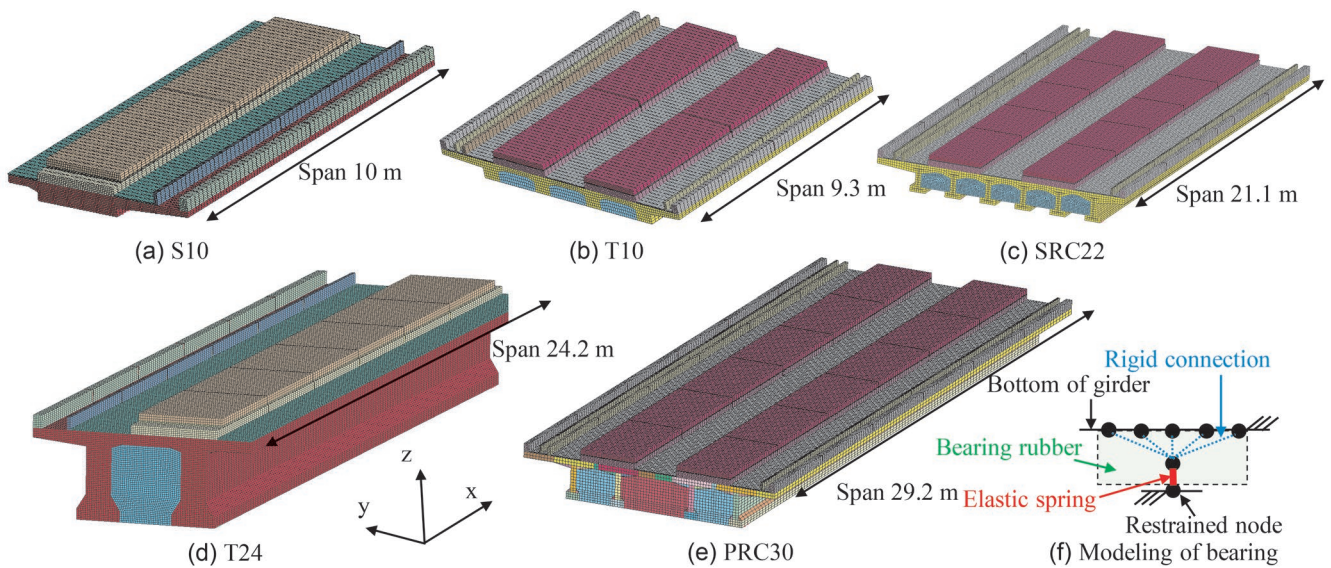


Fig. 6 Analysis model of 3D FEM

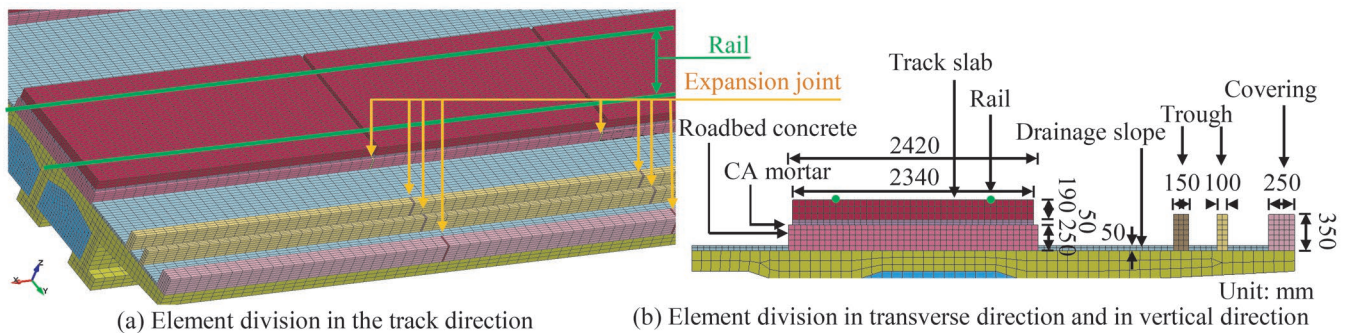


Fig. 7 Dimension and mesh division of non-structural member

### 3. Effect of non-structural members on effective stiffness of main girder

#### 3.1 Analysis method

A three-dimensional finite element method (3D FEM) was carried out to investigate the effect of non-structural members on effective stiffness of main girders.

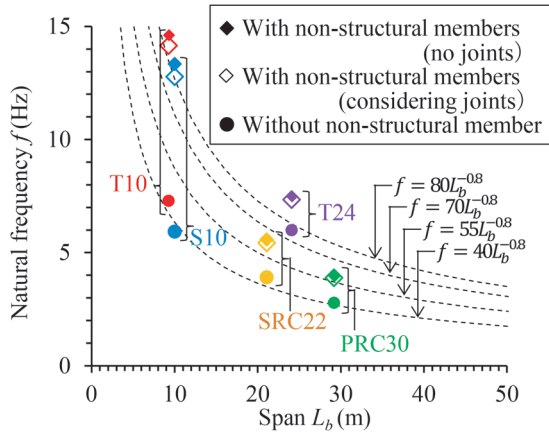
Figure 6 shows an overview of the analysis model of 3D FEM [7]. Five types of concrete girders from Shinkansen concrete girders, namely RC single plate girders with a span of 10.0 m (hereinafter referred to as “S10”), RCT type girders with spans of 9.3 m and 24.1 m (hereinafter referred to as “T10” and “T24”), composite girders with a span of 21.1 m (hereinafter referred to as “SRC22”) and PRCT girders with a span of 29.2 m (hereinafter referred to as “PRC30”) were subjected to 3D FEM. The eigenvalue analyses were performed to evaluate their first-order natural frequencies (vertical bending). The non-structural members targeted were roadbed concrete, cement asphalt (CA) mortar, track slabs, rails, troughs, drainage slope concrete, and RC bridge railings, assuming common concrete girders in recent years. S10 is the standard design used on the Tokaido Shinkansen, T24 on the Tohoku Shinkansen (between Omiya and Morioka), and T10, SRC22, and PRC30 on the Hokuriku Shinkansen (between Karuizawa and Nagano).

Figure 7 shows the non-structural members which are based on

standard values for Shinkansen line sections in recent years. Expansion joints are installed with non-structural members for the purpose of suppressing initial concrete cracks due to differences in construction stage. Although their location is sometimes specified at the design stage, it is often determined at the construction stage, so that even if girders are designed using the same standard design, the layout of expansion joints may differ. Taking into consideration expansion joints in the roadbed concrete, trough, covering, and RC bridge railings, the joint spacing was set as 5 m, and the joint length in the track direction was set as 30 mm, as general values.

#### 3.2 Analysis result

Figure 8 shows the relationship between the natural frequency  $f$  and the span  $L_b$  obtained by eigenvalue analyses. Focusing on the first bending mode of the entire main girder as the natural vibration mode, the results are presented for each target bridge in cases where non-structural members are not considered and in cases where every non-structural member except the RC railings is considered (with joints or without joints). From the results of T10 and S10, the natural frequency is about  $40 L_b^{-0.8}$  when non-structural members are not considered, while it is  $80 L_b^{-0.8}$  when all non-structural members are considered, indicating that the natural frequency has increased about twofold due to the influence of non-structural members. In the case of SRC22, the natural frequency increases by approximately



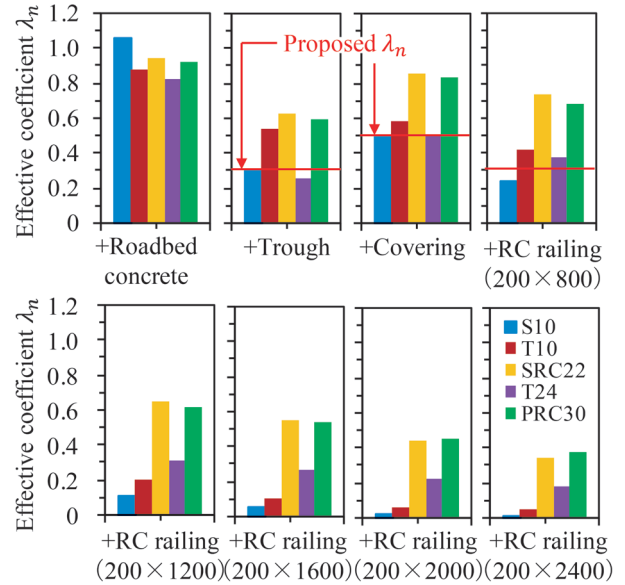
**Fig. 8 Relationship between natural frequency and span**

+42% from 3.91 Hz to 5.57 Hz due to the influence of non-structural members. In the case of PRC30, it increases by approximately +43% from 2.77 Hz to 3.95 Hz.

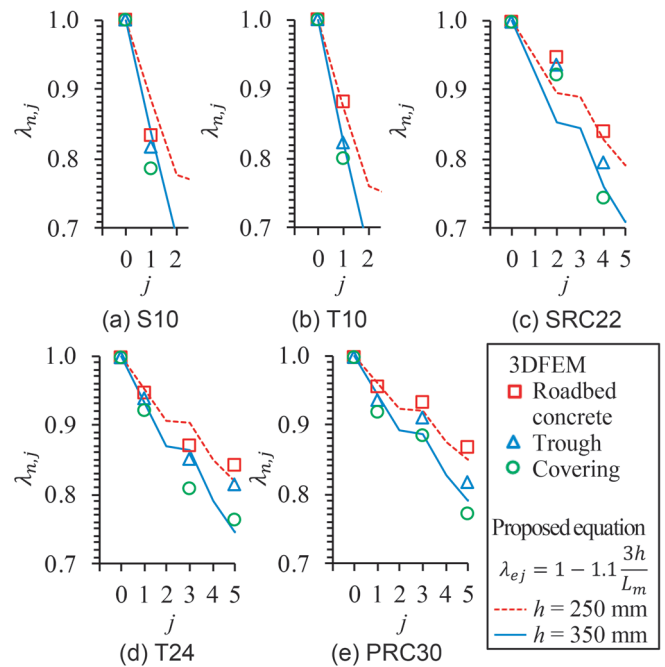
The cross-sectional stiffness is converted from the natural frequency obtained by 3D FEM using the following procedure. The main structure is expressed by the subscript  $m$  (main structure), the non-structural member is expressed by the subscript  $n$  (non-structural member). The bending stiffness when the main structure and the non-structural member with the number of joints in the track direction  $j$  are considered simultaneously is  $EI_{m+n,j}^{FEM}$ , and the bending stiffness when considering only the main structure is  $EI_m^{FEM}$ , then the bending stiffness increment  $\Delta EI_{n,j}^{FEM}$  due to non-structural members can be calculated as  $EI_{m+n,j}^{FEM} - EI_m^{FEM}$ . Furthermore, as an index to evaluate the effectiveness of the Bernoulli-Euler hypothesis when considering non-structural members, the coefficient  $\lambda_n$  is calculated by the ratio of the above  $\Delta EI_{n,j}^{FEM}$  to  $\Delta EI_n^{beam}$  which is the increase in bending stiffness due to non-structural members.

Figure 9 shows the coefficient  $\lambda_n$  for each type of non-structural member [8]. When  $\lambda_n = 1$ , it means that the non-structural members and the main structure are rigidly connected, and Bernoulli-Euler hypothesis is completely achieved. In contrast, when  $\lambda_n = 0$ , it means that the non-structural members have no contribution to the stiffness of the girder. From the figure, it can be seen that the evaluation is generally on the safe side by considering a coefficient  $\lambda_n$  of 0.9 for roadbed concrete, 0.3 for trough, and 0.5 for ground covering. Similarly, although the results are not shown, a coefficient  $\lambda_n$  of 1 for drainage slope concrete, 0.5 for CA mortar, 0.5 for track slab, and 0.5 for rail was obtained as a value that gives a safe evaluation. However, there is little merit in considering them in actual design because their cross-sectional area is small, and because drainage slope concrete is close to the neutral axis, which generally results in little effect on the stiffness of the main structure. It can be seen that the effective coefficient  $\lambda_n$  of RC railings tends to decrease as the height increases, and is generally in the range of  $\lambda_n = 0$  to 0.8, and  $\lambda_n > 0.3$  is generally satisfied when the height is up to 800 mm.

Next, we consider the decrease in growth of stiffness due to expansion joints in non-structural members. This decrease is due to a local decrease in bending stiffness at the joint, which reduces the effective bending stiffness. The effective coefficient  $\lambda_{n,j}$  of bending stiffness when there is an expansion joint is calculated by  $\Delta EI_{n,j}^{FEM} / \Delta EI_{n,0}^{FEM}$ . Here,  $\Delta EI_{n,0}^{FEM}$  is the increase in bending stiffness when considering each non-structural member without expansion joints and  $\Delta EI_{n,j}^{FEM}$  represents the increase in bending stiffness when considering each non-structural member with  $j$  expansion joints. When  $\lambda_{n,j} =$



**Fig. 9 Effective coefficient  $\lambda_n$  for each type of non-structural member**



**Fig. 10 Effect of number of expansion joints on effective coefficient of bending stiffness**

1, it means that there is no decrease in stiffness due to expansion joints.

Figure 10 shows the influence of the number of expansion joints on the non-structural members of roadbed concrete, trough, and ground cover on the effective coefficient of bending stiffness  $\lambda_{n,j}$ . The horizontal axis is the number of expansion joints  $j$ , which are basically spaced at 5 m intervals, so that only one joint is placed for girders with short spans of about 10 m. The estimation formula  $\lambda_{e,j}$  in the figure is a simple approximation formula calculated theoretically based on the modal stiffness of a beam of variable cross-section that takes into account the distribution of stress in the track direction of non-structural members. Where,  $h$  is the height of

the non-structural member, and  $L_m$  is the joint spacing, with a typical value of 5 m.

From the figure, it can be seen that  $\lambda_{n,j}$  tends to decrease as the number of joints increases for all non-structural members. It can be seen that the amount of decrease in roadbed concrete is small compared to the trough and ground cover. This is thought to be because as the height increases, the area of non-structural members that do not bear stress increases relatively near the expansion joint. Here, the height  $h$  of the roadbed concrete is 250 mm, while the height  $h$  of the trough and ground covering is 350 mm. When the maximum number of joints is installed in each girder,  $\lambda_{n,j}$  is approximately 0.75 to 0.85, which indicates that the contribution to the main structure stiffness decreases by approximately 15 to 25% due to the influence of expansion joints.

#### 4. Method for estimating reloaded bending stiffness of concrete girder during train passage

##### 4.1 Determination of zone of significant increase in response

Based on the above study results, we propose a method for evaluating the reloaded bending stiffness of concrete girders during train passage. As in the previous design standard, the entire cross-sectional stiffness (hereinafter referred to as the “conventional method”) can be used for calculation of the bending stiffness of general RC girders and PC girders. As for RC girders, although a decrease in stiffness due to bending cracks is observed, the decrease is small at the load level expected in actual structures, and the decrease can be offset by the increase due to the stiffness contribution of non-structural members, which implies that the entire cross section theory can be used. For PRC girders, on the other hand, the applicability of the conventional method is determined by considering the condition of a significant response increase due to resonance, assuming a decrease in stiffness due to bending cracks. If there is a concern about significant response increase due to resonance, the effective reloaded stiffness should be calculated by taking into account the stiffness reduction due to bending cracks and the contribution of non-structural members (hereinafter referred to as the proposed method).

Figure 11 shows an overview of the method for determining the significant response increase condition. The dynamic factor can be obtained from the analysis results given for  $L_b/L_v$  ( $L_v$  is the vehicle length) as a function of the speed parameter  $\alpha$  expressed by equation (3).

$$\alpha = \frac{v}{2fL_b} \quad (3)$$

Where,  $v$  is the train speed and  $f$  is the natural frequency.

From the figure, it can be seen that in this case, the dynamic factor significantly increases in the region of  $\alpha = 0.4$  and  $\alpha = 0.6$ . In this region, third-order resonance and second-order resonance occur ( $fL_v/v = 3, 2$ ), respectively, and the response significantly increases, as the excitation period due to the train load coincides with the natural frequency of the member. When designing a member under these calculated conditions, precise evaluation of the stiffness of the members is inevitable because the dynamic factor varies greatly depending on the stiffness. In contrast, in other regions, the dynamic factor becomes insensitive to  $\alpha$ .

The significant response increase condition is determined by the following procedure:

A: Calculate the dynamic factor  $i_{\alpha_0}$  ( $\alpha = \alpha_0$ ) based on the entire

cross-sectional theory  $EI_g$ .

B: Calculate the dynamic factor  $i_{\alpha_1}$  ( $\alpha = 1.25\alpha_0$ ) assuming a stiffness reduction rate of 0.65.

C1:  $i_{\alpha_1} - i_{\alpha_0} < 0.25\alpha_0$  or  $i_{\alpha_1} < 2\alpha_1 (= 1.25\alpha_0)$ : It is outside the response increase condition and the conventional method can be applied to the calculation.

C2:  $i_{\alpha_1} - i_{\alpha_0} \geq 0.25\alpha_0$  and  $i_{\alpha_1} \geq 2\alpha_1 (= 1.25\alpha_0)$ : It is within the response increase condition and the proposed method is required for the calculation.

In B above, a stiffness reduction rate of 0.65 is assumed as the smallest observed values. In C1 and C2, the increase in the dynamic factor when the bending stiffness decreases, is determined by the trial calculation.

##### 4.2 Method for estimating effective reloaded stiffness

The type and shape of non-structural members varies depending on the presence or absence of cracks in concrete or composite main girders, etc. We propose a method to calculate these differences in non-structural members through simple cross-sectional calculations using a unified index called the effective coefficient which represents the integrity with the main structure.

Figure 12 shows an overview of the calculation of the equivalent stiffness  $EI_{egr}$  during reloading. The effective reloaded stiffness  $EI_{egr}$  is calculated by taking into account the occurrence of cracks, the decrease in stiffness due to repeated loading, and the stiffness contribution of non-structural members. Specifically,  $EI_{egr}$  is calculated using equation (4) based on the Bernoulli-Euler hypothesis, taking into account simplicity in design. However, the moment of

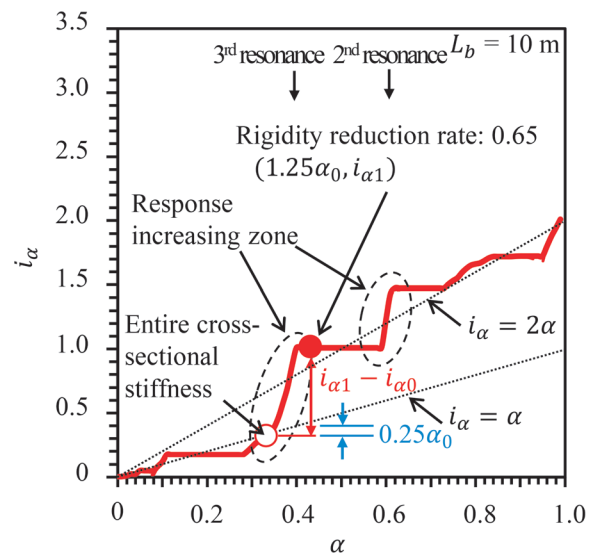


Fig. 11 Method for determining significant response increase condition

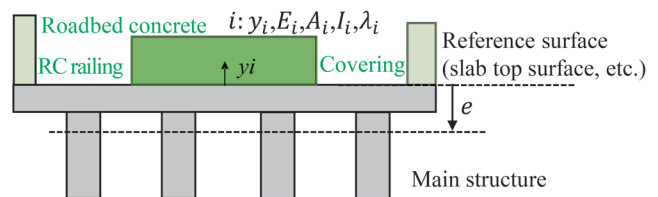


Fig. 12 Calculation overview of effective stiffness during reloading  $EI_{egr}$

inertia is reduced by the effective coefficient  $\lambda_p$ , taking into account the effects of cracks and expansion joints that exist in each element  $i$  that makes up the cross section.

$$EI_{eqr} = \sum_i E_i \lambda_i \{I_i + A_i (y_i - e)^2\} \quad (4)$$

$$e = \frac{\sum_i \lambda_i E_i y_i A_i}{\sum_i \lambda_i E_i A_i} \quad (5)$$

Where,  $E_i$  is a design Young's modulus of each cross-sectional component,  $A_i$  is a cross-sectional area of each component,  $I_i$  is a moment of inertia of each member around the centroid axis,  $y_i$  is a distance from the top surface of the slab to the centroid of each component and  $e$  is an average centroid position when considering cracks and non-structural members.

When a stiffness decrease may be expected due to the occurrence of bending cracks in the main structure of RC or PRC members, the effective coefficient  $\lambda (= I_{eqr}/I_g)$  is calculated using equation (2), which is the proposed empirical formula that roughly indicates the lower limit of the experimental results. Since  $M_{dmax}$  in equation (2) is originally a function of the dynamic factor, which requires repeated calculations and is complicated, in practical design, it can be assumed that  $M_{dmax} = 0.8M_y$ . In this case, the assumption gives  $I_{eqr} \approx 0.1I_g + 0.9I_{cr}$ . If there is no decrease in the stiffness of the main structure, such as with PC members or steel members,  $I_{eqr}$  can be determined as  $I_g$ .

Non-structural members can be expected as the effective cross section if the structural details are established to ensure integrity with the main structure over the service life. The concrete roadbed and track slabs are members that contribute greatly to the stiffness of the main structure; therefore, it is reasonable to consider them in the design: where the effective coefficient  $\lambda$  must be taken into account depending on the type of non-structural member. For concrete roadbeds without expansion joints that are not cast integrally with the main structure,  $\lambda$  is 0.9; however, the value is multiplied by 0.8 to give a general value  $\lambda = 0.9 \times 0.8 \approx 0.7$  because the contribution to the stiffness of the main structure decreases by about 15 to 25% due to the influence of the expansion joints. The track slab is assumed to be  $\lambda = 0.5$ . In general, other non-structural members such as rails, drainage slope concrete, and low ground cover may be considered; however, since their cross sections are small and their contribution is small, it is reasonable to ignore them in the calculations.

#### 4.3 Validation of proposed method

Table 2 shows the validity of the proposed method for evaluating the equivalent reloaded stiffness  $EI_{eqr}$ . Here, trial calculations are carried out on a PRC girder ( $L_b = 29.2$  m) [1], where a significant resonance phenomenon occurred, to verify the validity of the proposed method. For non-structural member in consideration of expansion joints, the specification close to the field test are as follows:

**Table 2 Validity of proposed method**

	Measured		Estimated			
	max	min	Full cross section	Proposed		
Non-structural member	existing	existing	–	considering	–	considering
Bending crack	–	existing	–	–	considering	considering
$f$ (Hz)	4.5	<b>2.42</b>	2.92	3.29	2.00	<b>2.38</b>
$EI_{eqr} / EI_g$	2.37	<b>0.69</b>	1.00	1.27	0.47	<b>0.67</b>

the roadbed concrete is 2,420 mm (width)  $\times$  100 mm (height) ( $\lambda_n = 0.9 \times 0.8$ ), the trough is 250 mm  $\times$  350 mm ( $\lambda_n = 0.3 \times 0.8$ ), and the ground cover is 250 mm  $\times$  350 mm ( $\lambda_n = 0.5 \times 0.8$ ), the drainage slope concrete is 2,500 mm  $\times$  500 mm ( $\lambda_n = 1.0$ ), the CA mortar is 2,340 mm  $\times$  50 mm ( $\lambda_n = 0.5$ ), the track slab is 2,340 mm  $\times$  190 mm ( $\lambda_n = 0.5$ ), the rail is 60 kg rail ( $\lambda_n = 0.2$ ). The actual measurement results are in the range of approximately 2.42 to 4.5 Hz, which represents the range of many actual measurement results of approximately 10 bridges with the same standard design. At a train speed of 260 km/h, primary resonance occurs at 2.89 Hz.

From the table, the actual measured value of the ratio of the equivalent reloaded stiffness  $EI_{eqr}$  to the entire cross-sectional stiffness  $EI_g$  is about 0.7 at the minimum. In contrast to this, the proposed method provides an appropriately similar value of minimum natural frequency and  $EI_{eqr}/EI_g$  by considering non-structural members and cracks respectively. The actual measured value of  $EI_{eqr}/EI_g$  is about 2.4 at maximum, which is larger than 1.27 when only non-structural members are considered in the proposed method. This is thought to be largely influenced by the fact that the Young's modulus of the concrete material and the thickness of the roadbed concrete differ from one bridge to another. Assuming that the Young's modulus of the main structure is 1.3 times, and the thickness of the concrete roadbed is 300 mm, the frequency is calculated to be 4.2 Hz, which is close to the actual high-stiffness example.

#### 5. Conclusion

This paper presents the results of a study on a method for estimating the bending stiffness of concrete girders when calculating dynamic factors and deflections in bridge design.

- Based on the results of static loading tests and fatigue tests on concrete members, an estimation empirical formula is proposed which takes into account the propagation of cracks and the decrease in bending stiffness due to increased repetitive loading.
- The contribution of non-structural members to girder stiffness is quantified using finite element analysis and other methods on a variety of girder structures.
- A simple method is proposed for estimating the equivalent bending stiffness of girders, taking into account the decrease in stiffness due to bending cracks in concrete members and the stiffness contribution of non-structural members.

#### References

- [1] Tokunaga, M. and Ikeda, M., "Reproduction Analysis of Dynamic Response Increase due to Crack Propagation Caused by Simultaneous Loading of Multiple Lines of Railway PRC Girder," *Journal of Japan Society of Civil Engineers*, Ser. A2 (Applied Mechanics (AM)), 77(2), I\_467-I\_476, 2021 (in Japanese).
- [2] Railway Technical Research Institute, *Design Standards for Railway Structures and Commentary (Concrete Structures)*, Maruzen Co., Ltd., Tokyo, 2004 (in Japanese).
- [3] Railway Technical Research Institute, *Design Standards for Railway Structures and Commentary (Concrete Structures)*, Maruzen Co., Ltd., Tokyo, 2022 (in Japanese).
- [4] Tokunaga, M., "Evaluation of vibration characteristics of RC and PPC beam members under cyclic train loading," *EURO-DYN 2020 XI International Conference on Structural Dynamics*, Athens, Greece, 2020.

- [5] Wakui, H., Matsumoto, N. and Watanabe, T., “An evaluation method of flexural rigidity of reinforced concrete girders for computing deflection,” *RTRI report*, 5(11), pp. 55-62, 1991.
- [6] Branson, D. E., *Deformation of Concrete Structures*, McGraw-Hill, New York, 1977.
- [7] Tokunaga, M., Yagi, H., Ikeda, M. and Sogabe, M., “Influence of non-structural member and its expansion joint on vibration characteristics of railway bridge,” *Journal of Japan Society of Civil Engineers, Ser. A2 (Applied Mechanics (AM))*, 75(2), I\_145-I\_153, 2019 (in Japanese).
- [8] Tokunaga, M. and Ikeda, M., “Evaluation method of vibration characteristics of main structure of railway bridge considering non-structural members,” *Journal of civil engineering, JSCE, Division A1*, Vol. 76, No. 3, pp. 580-596, 2020.

## Authors



*Munemasa TOKUNAGA*, Dr.Eng.  
Senior Researcher of Structural Mechanics  
Laboratory, Railway Dynamics Division  
Research Areas: Bridge Mechanics, Seismic  
Design, Bridge Vehicle Interaction



*Manabu IKEDA*, Dr.Eng.  
Senior Chief Researcher, Head of Structural  
Mechanics Laboratory, Railway Dynamics  
Division  
Research Areas: Bridge Design, Steel and  
Hybrid Structure

# Crossing Rod Breakage Detection Method Using Surveillance Camera Images

Ryo KAGEYAMA

Nozomi NAGAMINE

Image Analysis Laboratory, Information and Communication Technology Division

*For early and automatic detection of crossing rod breakage caused by vehicles forcibly entering in level crossing, we developed a method for detecting crossing rod breakage using surveillance camera images. The proposed method determines the presence or absence of stripes peculiar to level crossing by extracting the color components from images and identifying the spatial frequency of the waveforms converted from the extracted color components. This paper describes the details of the proposed method and the results of performance evaluation tests.*

**Key words:** crossing rod breakage, surveillance camera, image processing, Hilbert-Huang transform

## 1. Introduction

At Class 1 level crossings, which account for about 90% of all level crossings in Japan [1], crossing rods separate between road and railroad when a train approaches. These crossing rods are sometimes broken by the forceful entry or exit of vehicles or other vehicles. In such cases, the crossing rod is necessary to be replaced. Until the replacement is completed, it is maybe required to slow down trains or deploy monitoring personnel. Therefore, it is desirable to be able to detect occurrence of a breakage as early as possible to shorten the recovery time.

Under this background, several methods have been developed to automatically detect the breakage of crossing rod. For example, a method has been proposed to detect breakage by the reflectance of ultrasonic waves emitted by a sensor attached to the root of crossing rod [2] or by changes in the value of the operating current measured by a sensor attached to the crossing gate [3]. Such a method requires at least one sensor for each crossing gate or crossing rod, so that the cost of installation and maintenance becomes high.

Therefore, we developed a method for detecting a breakage of a crossing rod by using a level crossing monitoring camera, which has been installed by several railroad operators in recent years [4]. Figure 1 shows the system configuration of the developed method. As shown in Fig.1, the proposed method uses images transferred from existing surveillance cameras to the signal dispatcher through an external cloud or data server. Therefore, the method can be implemented without additional construction if surveillance cameras are already implemented. This paper provides an overview of the proposed method and the results of performance evaluation tests.

## 2. Crossing rod breakage detection method using image processing and Hilbert-Huang transform

### 2.1 Overview of proposed method

Figure 2 shows the detection algorithm of the crossing rod breakage used in the proposed method. First, a “detection area” is set up around the crossing rod in the whole image of the surveillance camera. Secondly, the color components specific to the stripe pattern of the crossing rod are extracted from the image of the detection area, and the intensity of the color components is converted into a 1-dimensional (1D) waveform. Finally, Hilbert-Huang transform (a kind of spatial frequency analysis) is applied to the 1D waveform, and the breakage is determined from the results. Details of each

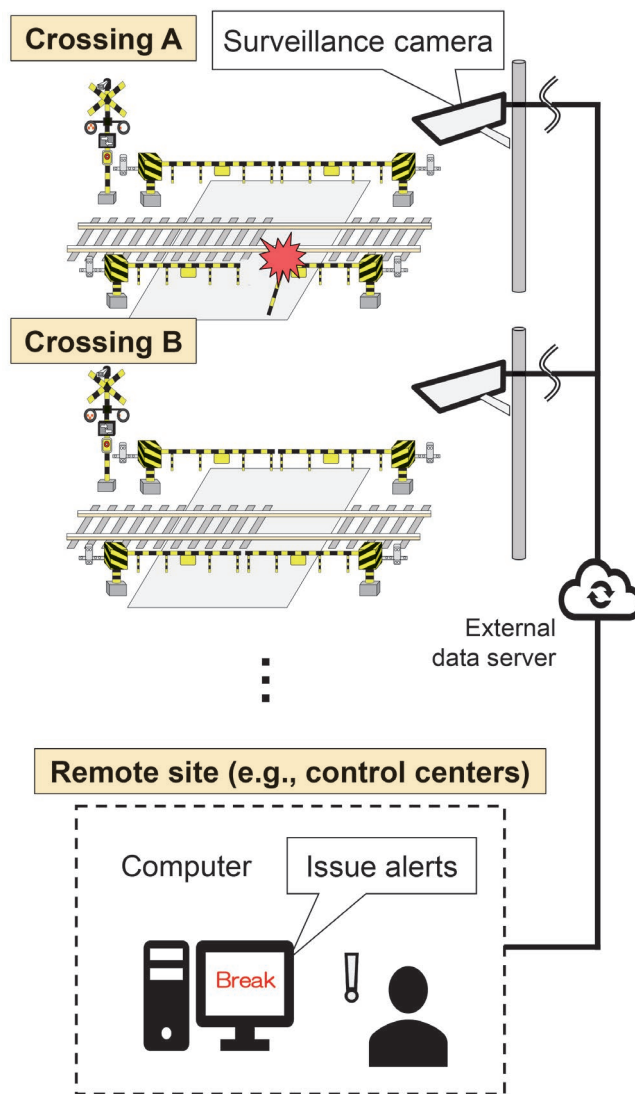


Fig. 1 System configuration

method shown in Fig.1 are described in the next section.

#### 2.1.1 Setting of the detection area

Generally, level crossing surveillance cameras record images

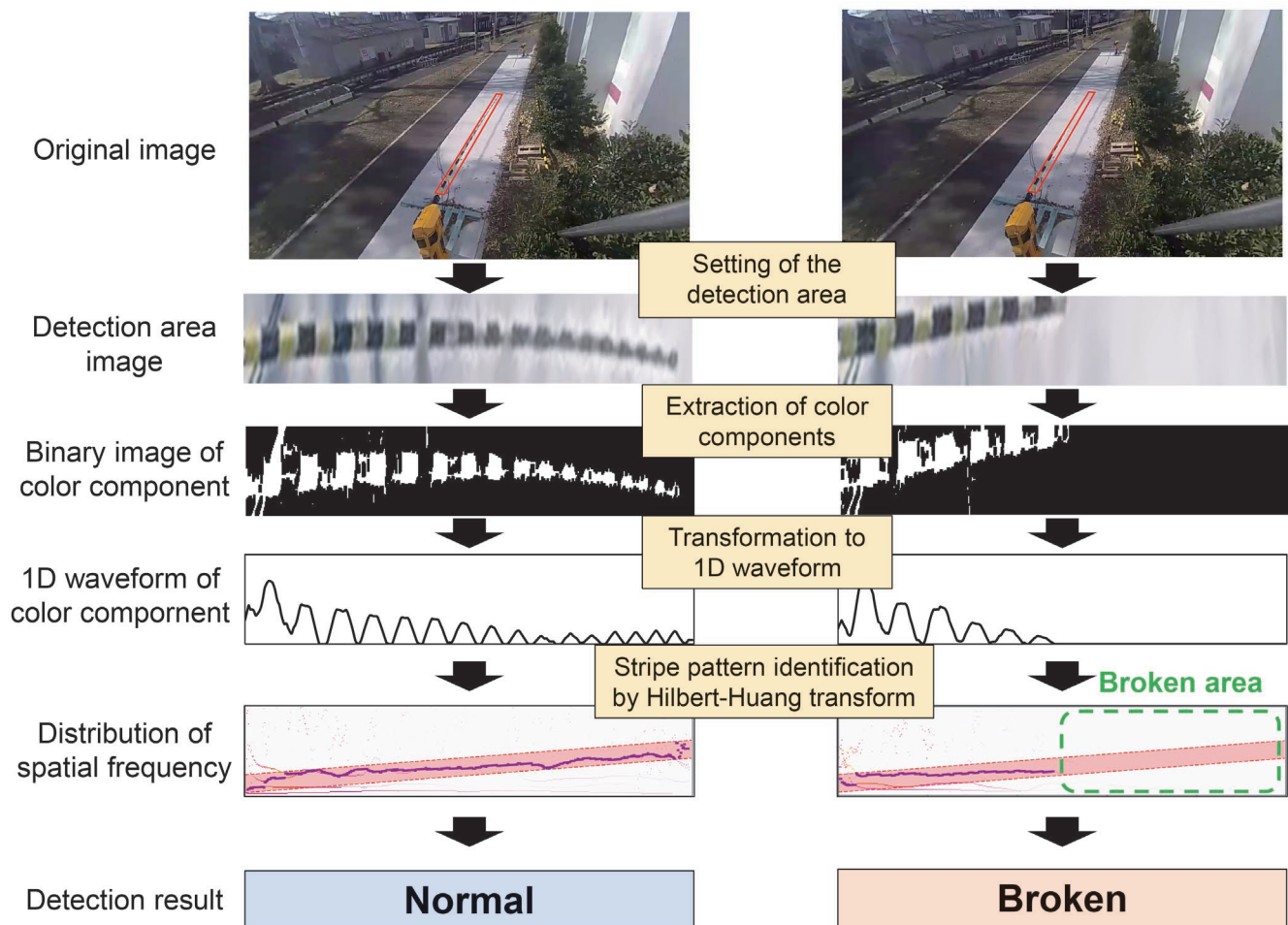


Fig. 2 Breakage detection algorithm using surveillance camera images

showing the entire level crossing. In order to focus on the part of the crossing rod in this image, the detection area formed by four points around the crossing rod specified by users is set. Subsequent processing is performed only within the detection area set for each crossing rod. The detection area tapers from the front to the back of the camera. To make the thickness of the crossing rod appear as even as possible, a projective transformation is applied to the detection area to transform the image as if it were viewed from directly above.

### 2.1.2 Extraction of color components and transformation to 1-dimensional waveform

Crossing rods are generally painted with yellow / black or red / white stripes. The proposed method extracts the color components that make up the stripe pattern of the crossing rod from the detection area image. To extract the color components, the image is represented in HSV color space. The color components to be selected, and the setting of the value range in the HSV color space, are selected by the user to be as far away as possible from the color components in the background of the crossing rod in the detection area image. Next, as shown in the top of Fig. 3, a binary image is generated with pixel value 255 for the area containing the selected color component and pixel value 0 for the rest. Then, the average of the pixel values is calculated sequentially at each column of the binary image. The result becomes a 1D waveform representing the presence of color components in the detection area, as shown in the bottom of Fig. 3.

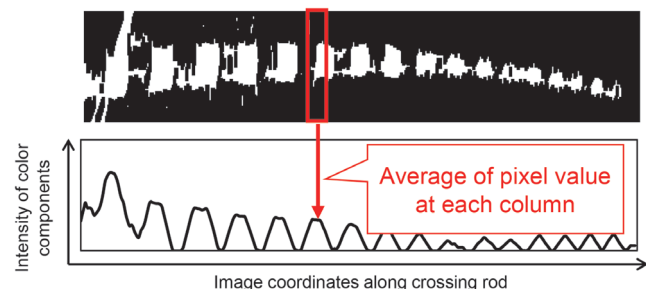
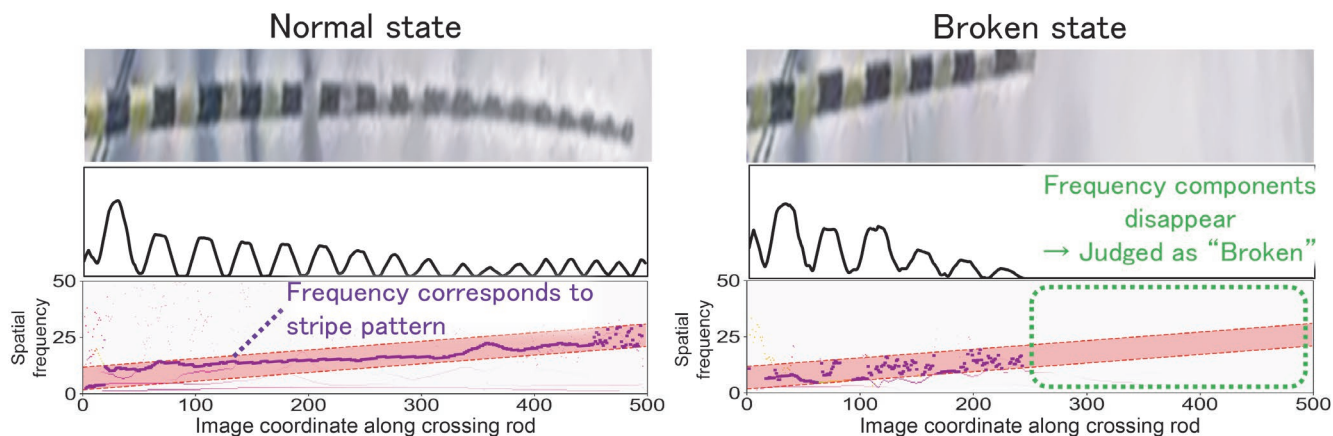


Fig. 3 The image of transformation from binary image (top) to 1-dimensional waveform (bottom)

### 2.1.3 Stripe pattern identification by Hilbert-Huang transform

The 1D waveform obtained by the procedure in the previous section has periodic peaks at the locations of the extracted color components. If this periodicity can be captured, the presence of a crossing rod in the detection area can be determined. Therefore, frequency analysis is applied to the 1D waveform. As the frequency analysis method, we adopted the Hilbert-Huang transform (HHT) [5], which is a suitable method for finding periodicity in complex waveforms whose amplitude and period vary with time / space. The HHT first decomposes the original waveform into multiple Intrinsic Mode Functions (IMFs) using an algorithm called Empirical Mode



**Fig. 4 Hilbert spectrum in normal state (left) and broken state (right)**

Decomposition (EMD). From the original waveform  $w(u)$  ( $u$  is the image coordinate axis in the longitudinal direction of the crossing rod), IMFs  $x_i(u)$  ( $i = 1, 2, 3, \dots$ ) are iteratively calculated by the EMD until the residual  $r$  increases or decreases monotonically.

$$w(u) = \sum_{i=1}^N x_i(u) + r \quad (1)$$

The number of IMFs  $N$  corresponds to the number of iterations of the EMD. Each EMD is represented by a single trigonometric function whose amplitude  $A_i$  and phase  $\theta_i$  vary with  $u$ .

$$x_i(u) = A_i(u) \cos(\theta_i(u)) \quad (2)$$

The Hilbert transform is applied to (2) to obtain the spatial frequency shown in (3).

$$f_i(u) = \frac{1}{2\pi} \frac{d\theta_i(u)}{du} \quad (3)$$

The Hilbert transform is applied to (3) to obtain the spatial frequency as follows. By superimposing the  $f_i(u)$  calculated for each IMF, a spatial frequency distribution (Hilbert spectrum) is obtained, where the vertical axis corresponds to the spatial frequency and the horizontal axis corresponds to the image coordinates of the detection area  $u$ . As shown in left of Fig. 4, If the crossing rod is not broken, the peaks of 1D waveforms appear periodically throughout the space, so that a frequency distribution above a certain level can be continuously observed in a specific frequency band of the Hilbert spectrum. Hereinafter, we define this frequency band as the normal frequency band. On the other hand, as shown in right of Fig. 4, when the crossing rod is broken, peaks of the waveform disappear after the broken part, so that no spatial frequency distribution is seen within the normal frequency band of the Hilbert spectrum. Based on this trend, we judge breakage when the frequency distribution disappears continuously for a certain length (approximately the length of one period of stripes) in the normal frequency band of the Hilbert spectrum, which is set by the user from the stripe pattern interval.

### 3. Performance evaluation experiment of proposed method

Performance evaluation experiments of the proposed method were conducted at the Railway Research Institute and at training facilities owned by railroad operators. This chapter presents an overview and results of each experiment.

## 3.1 Experiments in a test environment

### 3.1.1 Overview of experiment

We constructed a simulated level crossing environment (hereinafter referred to as test environment) and evaluation experiments were conducted in the test environment. The configuration of the test environment is shown in Fig. 5. The test environment consisted of two sets of level crossing gates, a surveillance camera, a level crossing light, and an apparatus box. The raising and lowering of the crossing gates can be performed automatically and continuously by a controller in the apparatus box. In the area where the crossing gate is installed, bolt holes are provided at regular intervals to fix the crossing gate to the ground, allowing the position of the crossing gate to be changed as desired. Surveillance camera and light was installed at a height of about 3 meters from the ground using poles erected beside the crossing gates. Figure 6 shows the appearance of the surveillance camera and Table 1 shows its main specifications. We used the surveillance camera that is used in the “Smart Unisite” [6] cloud-based video monitoring service introduced by railroad operators in the Tokyo and the Kansai area. The level crossing light was those that meet the illumination standard used by several railroad operators (30 lx or more at level crossings with a sight distance of 400 m and traffic volume of 500 vehicles/h or more). The crossing rod consists of five 1.5 m long parts (C1, C2, C3, C4, and C5 from the tip) shown in Fig. 7.

In order to confirm the basic performance of the proposed method, we conducted the evaluation experiment at the test environment, limiting the target broken condition to one, and was continuously filmed from 10:30 to 19:00, alternately reproducing the normal condition and the condition in which the middle part (C1 to C3) was missing about every hour. Since it is thought that the crossing rod is basically broken when it is descending, the crossing rod was always in a descending position during the filming. The light was turned on at 16:17, about 30 minutes before sunset.

### 3.1.2 Result of experiment

Surveillance camera images were acquired every 10 seconds, and detection processing was performed using the proposed method. The detection performance was evaluated by totaling the results of the processing for all frames and comparing them with the true state of the crossing rod that was visually confirmed. The detection rate was the ratio of the number of frames in which the breakage was

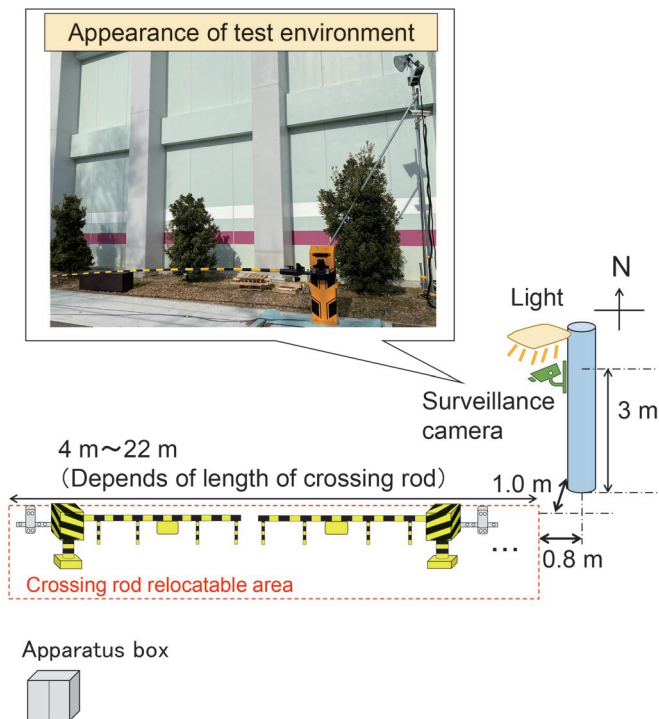


Fig. 5 Overview of test environment.



Fig. 6 Appearance of surveillance camera used in the experiment.

Table 1 Specifications of surveillance camera.

Resolution	Horizontal: 1,280px Vertical: 720px
Field of view	Horizontal: 131° Vertical: 70°
Frame rate	5 frame per second

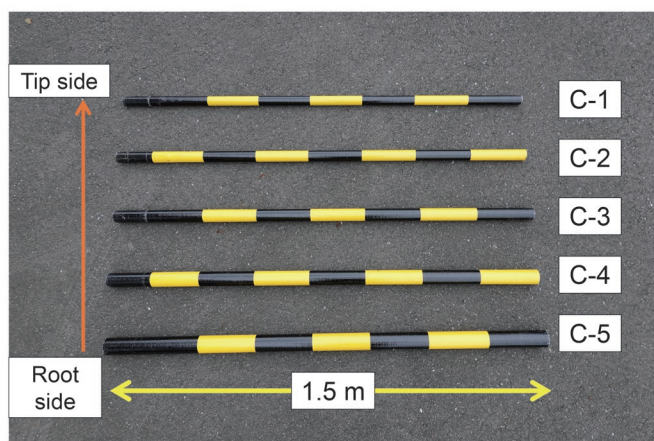
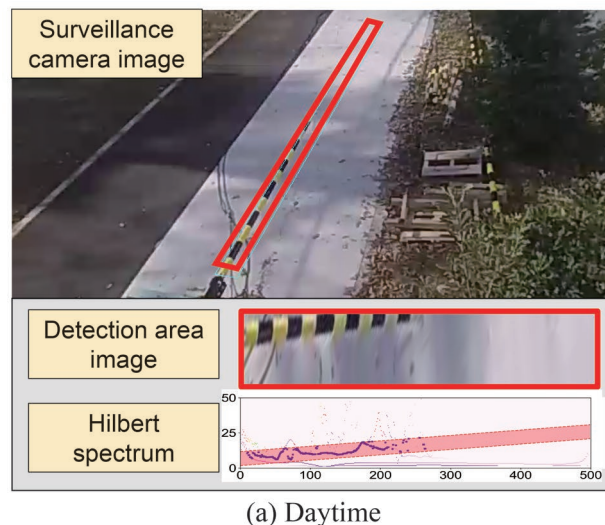
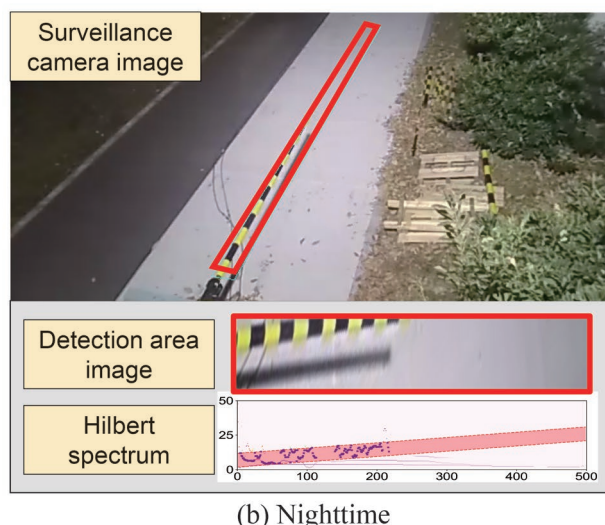


Fig. 7 Crossing rods used in the experiment.



(a) Daytime



(b) Nighttime

Fig. 8 Examples of breakage detection result at test environment in (a) daytime and (b) nighttime

detected correctly to the correct value of all images in which the breakage was shown. Figure 8 shows examples of detection results during the daytime (11:00) and nighttime (18:00). As shown in the figure, even if the background color in the image changes with time, it was confirmed that the loss of stripes in the detection area due to breakage was correctly captured. Table 2 shows the detection rate during the test period(10:00~19:00) divided into each time zone (10:30-12:59, 13:00-15:59, and 16:00-18:59). The detection rate was 100% for all time zones, indicating that under the environment of this test, the loss up to the middle part of the crossing rod can be detected reliably regardless of the time zone.

### 3.2 Performance evaluation experiment in actual environment

#### 3.2.1 Overview of experiment

To verify the effectiveness of the proposed method in the environment of an actual level crossing environment, we acquired images by surveillance cameras at three level crossings in a different training facilities owned by a railroad operator.

Table 3 shows the condition in experiments. We recorded images for two days (4-6 hours per day) at each crossing. As shown in

**Table 2 Detection rate in each timezone.**

Time zone	Number of frames	Detection rate [%]
10:30 – 12:59	378	100
13:00 – 15:59	557	100
16:00 – 18:59	546	100

**Table 3 Condition in experiments in actual environments.**

		Weather	Time zone
Crossing 1	Day 1	Sunny	14:00-18:15
	Day 2	Sunny	11:00-15:30
Crossing 2	Day 1	Rainy	12:00-17:50
	Day 2	Sunny	10:40-16:10
Crossing 3	Day 1	Cloudy	11:30-17:00
	Day 2	Sunny	10:30-15:30



**Fig. 9 Temporary installation of cameras at level crossing in training facilities**

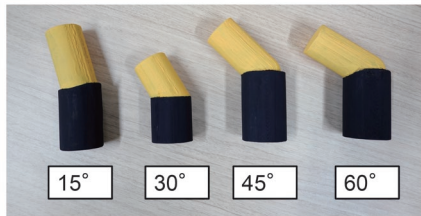


**Fig. 10 Adapter to reproduce bending state**

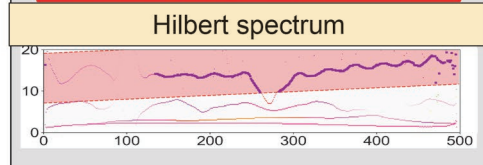
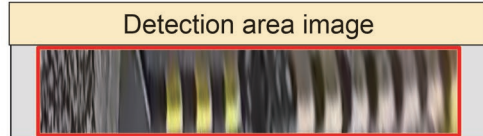
Fig. 9, an aluminum frame was temporarily erected beside the railroad crossing, and a surveillance camera was installed at a height of 3 meters from rail during the experiments. The eight breakage conditions listed below were repeatedly reproduced and the surveillance camera photographed crossing rod every 5 minutes.

- (A) Approximately 20% of the apical side is missing.
- (B) Approximately 40% of the apical side is missing.
- (C) Approximately 60% of the apical side is missing.
- (D) Missing all parts.
- (E) Tip part bent down at a 15° angle.
- (F) Tip part bent down at a 30° angle.
- (G) Tip part bent down at a 45° angle.
- (H) Tip part bent down at a 60° angle.

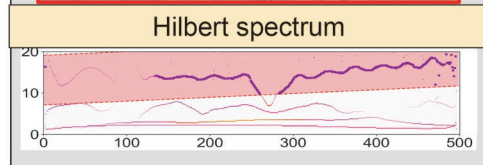
The bending state was reproduced using the adapter shown in Fig. 10.

### 3.2.2 Result of experiment

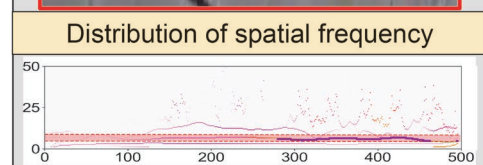
Figure 11 shows an example of the breakage detection result



(a) Crossing 1



(b) Crossing 2



(c) Crossing 3

**Fig. 11 Examples of breakage detection result at each level crossing.**

**Table 4 Detection rate in each broken state.**

Broken state	Number of frames	Detection rate [%]
(A)	4,863	96.9
(B)	3,696	98.2
(C)	769	100
(D)	3,923	97.7
(E)	3,362	90.5
(F)	3,631	97.6
(G)	3,400	97.6
(H)	3,230	97.3

using the proposed method at each crossing. We have confirmed that when the parameters are adjusted according to changes in the conditions, it is possible for the proposed method to correctly detect the breakage of the crossing rod. For the surveillance camera images acquired in the experiment (26,874 frames in total), we calculated the detection rate as the percentage of correctly detected breakages. As shown in Table 4, the detection rate through the test became more than 90% for all the breakage conditions.

#### 4. Conclusions

In order to detect broken crossing rods at an early stage, we have developed a method to determine whether the crossing rod is broken or not by identifying the presence or absence of stripes on the rods from images captured by surveillance cameras. The results

of performance evaluation experiments at several level crossings confirmed that the proposed method can correctly detect breakages with a detection rate of more than 90%, even when environmental conditions change. In the future, we plan to further improve the detection performance of the proposed method by examining the angle of view of the camera and the shape / material of the crossing rod suitable for detection toward practical use.

#### References

- [1] MLIT Railway Bureau, *Information on Safety in Rail Transportation (FY2019)*, 2020 (in Japanese).
- [2] Sugimoto, J., and Ichikura, T., "Research and development of crossing rod breakage failure," *JR EAST Technical Review*, No. 17, pp. 49-53, 2007 (in Japanese).
- [3] Ozaki, N., "About the detection method for crossing rod breakage detection using operating current of crossing gate," *Railroad and electrical technology*, Vol. 20, No. 12, pp. 36-39, 2009 (in Japanese).
- [4] Kageyama, R., and Nagamine, N., "Study of breakage detection method in crossing rod using monitoring camera image," *The papers of Technical Meeting on TER*, TER-21-066, 2021 (in Japanese).
- [5] Huang, N. Eh., "Hilbert-Huang transform and its applications," World scientific, Vol. 16, 2014.
- [6] Yamada, Y., "Smart unisite: Cloud-based video surveillance service," *Unisys Technology Review Extra Edition*, No. 135, pp. 19-27, 2019 (in Japanese).

#### Authors



*Ryo KAGEYAMA*  
 Researcher, Image Analysis Laboratory,  
 Information and Communication Technology  
 Division  
 Research Areas: Computer Vision, Image  
 Processing, 3D Point Cloud Processing



*Nozomi NAGAMINE*, Ph.D.  
 Senior Chief Researcher, Head of Image  
 Analysis Laboratory, Information and  
 Communication Technology Division  
 Research Areas: Computer Vision, Image  
 Processing, Signalling Systems

# Quantitative Evaluation Method of Measures for Prolonging Lifetime of Electronic Signalling Equipment

Hitoyuki FUJITA

Signalling Systems Laboratory, Signalling and Operation Systems Technology Division

Ken TAKASAKI

Takuro SHINDO

Signalling Systems Laboratory, Signalling and Operation Systems Technology Division

Tsuyoshi KAMIYA

*There is a strong need for prolonging the lifetime of electronic signalling equipment to reduce replacement costs. On the other hand, availability of equipment has become an issue due to the recent shortage of semiconductors. Since the actual lifetime of electronic signalling equipment depends on the lifetime of electronic components and solder joints with substrates, it is possible to prolong this lifetime by selecting suitable electronic components and improving the environment of use. In this paper, a method for quantitatively evaluating the effect of measures for prolonging lifetime was investigated utilizing a method developed to evaluate the lifetime of electronic signalling equipment.*

**Key words:** *electronic signalling equipment, electronic component, lifetime prolonging measures, lifetime estimation, quantitative evaluation method*

## 1. Introduction

Railway signalling equipment has been widely installed along railway lines to ensure safe and stable train operation. Recent years have seen the replacement of relay equipment with electronic devices in railway signalling systems, in order to reduce the size and improve the performance of the relay equipment. However, since it is often difficult to grasp how these electronic devices deteriorate, it is difficult to determine the correct intervals for replacing relays with electronic equipment. More recently in particular, in addition to the cost reduction of replacing relays with electronic equipment, there has been a growing need to extend the lifetime of electronic equipment as one of the measures to deal with the shortage of semiconductors.

In a previous study, the authors proposed a lifetime evaluation method for electronic signalling equipment installed in sheltered wayside environments or in equipment boxes [1][2]. The proposed lifetime evaluation method showed that the useful lifetime of electronic signalling equipment depended on the lifetime of its constituent electronic components and the solder joints with the substrates. Based on the results, it is considered that it is possible to prolong the life of electronic components by selecting them suitably and improving the environment of use that affects the life of components.

Therefore, the authors investigated a method for quantifying the effect of lifetime prolonging measures utilizing a method developed to evaluate the lifetime of electronic signalling equipment. In addition to an overview of the lifetime evaluation method, this paper describes the possible lifetime prolonging measures and methods for quantifying the effectiveness of the measures along with the results of a case study.

## 2. Lifetime evaluation method for electronic signalling equipment

This chapter describes an overview of the lifetime evaluation method for electronic signalling equipment that the authors have developed to date.

### 2.1 Concept of lifetime evaluation method

Electronic equipment is normally composed of multiple substrates on which electronic components are soldered. Therefore, failures which disrupt the operation of an entire piece of electronic equipment can be broadly divided into electronic component failures, printed circuit board failures and solder joint failures. From the results of past examinations of products collected from wayside signalling equipment, although no rust or cracks were found on the printed circuit boards, cracks were found in solder joints. Therefore, the influence of stress factors on solder joints was considered to be relatively greater than that on printed circuit boards. Thus, the authors excluded printed circuit board failures as targets for lifetime evaluation [1].

In addition, the results of a survey of removed equipment and a field survey of the usage environment showed that temperature and humidity were the dominant environmental stresses that affect the lifetime of wayside signalling equipment.

Therefore, as shown in Fig. 1, it was decided to use a dual approach to evaluate the lifetime of wayside electronic equipment: estimating the lifetime of electronic components (electronic component evaluation) and estimating the lifetime of solder joints (solder joint evaluation). Section 2.2 below describes the lifetime evaluation method for electronic components.

### 2.2 Lifetime evaluation method for electronic components (electronic component evaluation)

This section describes overview of the lifetime evaluation method for electronic components shown in Fig. 1, in three stages: extraction of electronic components affecting overall function, acquisition of reliability test data, and acceleration calculation based on usage environment conditions.

#### 2.2.1 Extraction of electronic components affecting overall function

The authors analyzed the degree of influence on overall function of electronic equipment when a specific electronic component

failed. The degree of influence was defined according to a five-point scale: level 0: no effect, level 1: unstable operation, level 2: partial function stop, level 3: unit stop, level 4: device function stop. Among the extracted electronic components on level 2 or above, the authors selected the parts which are generally considered to have a limited lifetime, such as aluminum electrolytic capacitors or parts which generate a large amount of heat when switched on.

### 2.2.2 Acquisition of reliability test data

The authors acquired the manufacturers' reliability test data (number of samples, accelerated environmental conditions, test time, number of failures) for the extracted electronic components. Note in order to derive the ageing change of the cumulative failure probability, which will be described later, it is desirable to acquire reliability determination test data which has been tested up to the lifetime of the component. However, in general, there are many components which only have reliability compliance test data based on public standards [3]. In any case, using the reliability test data conducted by the manufacturer eliminates the need for additional accelerated testing.

### 2.2.3 Acceleration calculation based on usage environment conditions

In order to match the reliability test data with the actual usage environment, an acceleration model is used to calculate the failure time  $L_1$  under the usage environment (obtain the acceleration factor  $AF$  and multiply it by the verification time  $L_0$ ). At this time, if multiple failure mechanisms are assumed, the shortest time failure time is adopted as the failure time, among the failure times calculated individually in parallel using the corresponding acceleration models. The acceleration model should be selected from models related to stress factors under the equipment operation. If the model is different for each component manufacturer, the authors select the model according to the manufacturer of the target component. Here, two typical acceleration models are shown. Equation (1) is a 10°C double rule (approximation of the Arrhenius equation) which expresses the decrease in capacitance accompanying electrolyte evaporation in an aluminum electrolytic capacitor. On the other hand, (2) is the Black model which expresses the brightness reduction of built-in LEDs in a photocoupler.

$$L_1 = L_0 \cdot 2^{\left(\frac{T_0 - T_1}{10}\right)} \quad (1)$$

$$L_1 = L_0 \cdot \left(\frac{J_0}{J_1}\right)^n \cdot \exp\left[\frac{E_a}{k} \cdot \left(\frac{1}{T_1} - \frac{1}{T_0}\right)\right] \quad (2)$$

Where  $E_a$  is the activation energy,  $k$  is the Boltzmann constant,  $J$  is the current density,  $T$  is the absolute temperature,  $n$  is the coefficient. The subscript 1 indicates the usage environmental conditions, while 0 indicates the test environmental conditions. In order to estimate under fixed environmental conditions, preset values are substituted for the current density and absolute temperature in (1) and (2).

In addition, the verification area is specified from the reliability test data of electronic components. For components which have undergone reliability determination tests, the authors use the defined failure time. On the other hand, for components which have only undergone reliability compliance tests, the value of the cumulative failure probability ( $F(t)$ ) specified by the number of samples ( $n$ ) at the confidence level ( $CL$ ) is obtained from (3) [3].

$$F(t) = 1 - (1 - C_L)^{\frac{1}{n}} \quad (3)$$

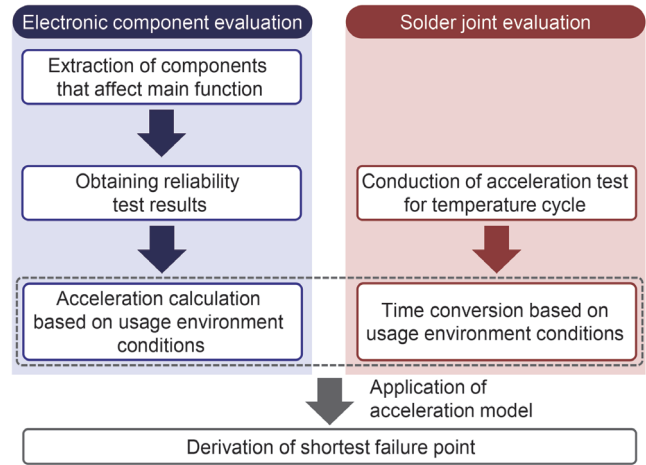


Fig. 1 Outline of lifetime estimation method for wayside signalling system electronic equipment

Figure 2 shows a method for estimating the cumulative failure probability over time based on reliability compliance test results. For example, the verifiable area with the test results of 22 samples, 90% confidence level, and 0 failures is the area indicated by A in Fig. 3 from (3) ( $F(t) = 10\%$ ). If this area is expanded to the failure time under the usage environment using the acceleration model, it becomes area B.

Furthermore, by empirically determining the shape parameter ( $m$ ) of the failure distribution on the Weibull plot as shown in Fig. 2 and estimating the area where the cumulative failure probability is low, the verification area can be expanded to C. This is an expanded verification area obtained by determining the minimum shape parameter value for each electronic component (safety side in empirical values) assuming that the first failure occurs in B. In this way, when the relationship in Fig. 2 is obtained, it is possible to estimate the time until an arbitrary cumulative failure probability reaches, making it possible to determine the useful life of the target component.

## 3. Measures for prolonging lifetime of electronic signalling equipment

### 3.1 Concept of measures for prolonging lifetime

Measures for prolonging lifetime of electronic signalling equipment are classified into two types: reviewing the design of target equipment and improvement of usage environment [4]. The former includes the selection of electronic components and circuit configuration, and the latter includes improvement of temperature and humidity environment which are dominant factors in determining the lifetime of the equipment. Sections 3.2 and 3.3 describe each specific method.

### 3.2 Measures based on reviewing design of target equipment

The measures described in this section mainly focus on reviewing the selection of electronic components and circuit configuration. Among the electronic components composing the target equipment, the lifetime evaluation methods are used to extract the components that have a short time to failure. Measures for prolonging lifetime are taken for the extracted components. There are three measures to

be considered: change of the parts themselves to longer-life products, change to parts that meet stricter reliability test conditions, and increase of the derating by reviewing the circuit configuration. Table 1 shows the specific measures for each. On the other hand, measures such as reviewing board design to alleviate stress are also considered for solder joints. Note that since these measures require design change, they are unlikely to be applied to prolong the lifetime of the existing product. However, the authors consider that these measures are effective in case of new designs and overhauls.

### 3.3 Measures based on reviewing usage environment

The measures described in this section mainly focus on reviewing the temperature and humidity environment, which is the dominant factor in the lifetime of target equipment. Various efforts, so far, have been made by railway operators and equipment manufacturers to review the temperature and humidity environment. A typical example is the installation of shielding plates in equipment boxes to prevent temperature from rising due to direct sunlight. It has been shown that as an effect of the installation of the shielding plate, the temperature change inside the equipment box is slow, the daily temperature range (the difference between the highest and lowest tem-

peratures) is small, and the average temperature is also slightly lowered. Considering the lifetime evaluation method, the difference between the reliability test conditions and the usage environment conditions increases due to improvement of the usage environment as shown in the example above, so that the measure effect can be expected with an increase in the acceleration coefficient. Since these measures are not the measure for the target equipment itself, but rather a measure against the usage environment, they are also effective as measures to prolong the lifetime of existing products. Sections 3.3.1 and 3.3.2 show the results of comparative verification tests conducted at the Railway Technical Research Institute for specific measures when the usage environment is divided according to temperature and humidity.

#### 3.3.1 Measures for reducing temperature and temperature difference

This section describes the results of the comparison and verification of measures such as applying functional paint to the surface of the equipment box to reduce the temperature and temperature difference inside the equipment box [5].

##### (1) Verification test method

The test specimen was an equipment box for the train detection device at level crossings which is a common piece of wayside electronic equipment, and the measures shown in Table 2 were implemented. The equipment box used as the specimen had shielding plates attached to the main body of the box, except for the door surface and the bottom. The authors tested two types of measures: high solar reflectance paint with the property of reflecting light in the near-infrared region at a high level as standardized by high solar reflectance paint for roofs (JIS K 5675), and paint and films which cause a radiation cooling phenomenon. These paints and films were applied to surfaces exposed to direct sunlight. The radiation cooling paint and film have the effect of emitting not only the heat due to direct sunlight but also the heat inside the storage box. Therefore, the authors prepared the equipment box for comparison in which the radiation cooling paint and film were also applied to the box itself. In order to verify the effect of paint in reducing the temperature rise inside the equipment box due to solar radiation, the temperature/humidity logger (TR-72wf-S, T&D) was installed inside the box to measure the temperature of the space inside. The measurement period was 6 days from September 29 to October 4, 2022, at the Railway Technical Research Institute (Kokubunji city, Tokyo). Additionally, temperature and illuminance loggers (TR-74Ui, T&D) were installed in the ventilated case for meteorological instruments to measure outside air temperature and illuminance. To equalize the environment in which the specimens were installed and to simulate the local environment, the storage boxes were placed on well-ventilated cases with their doors facing south as shown in Fig. 3. Furthermore, they were placed at intervals to prevent them casting shadow on each other.

##### (2) Verification results

Figure 4 shows the temperature measurement results on October 3, a sunny day, as a representative result during the test period. The temperature inside the box followed the change in illuminance, and the temperature inside the equipment box without measures was up to 7°C higher than the outside temperature. Based on the equipment box without measures, the maximum temperature reduction effect that leads to a reduction in temperature difference was the greatest for the radiation cooling film (No. 6: -6.4°C, No. 5: -5.7°C),

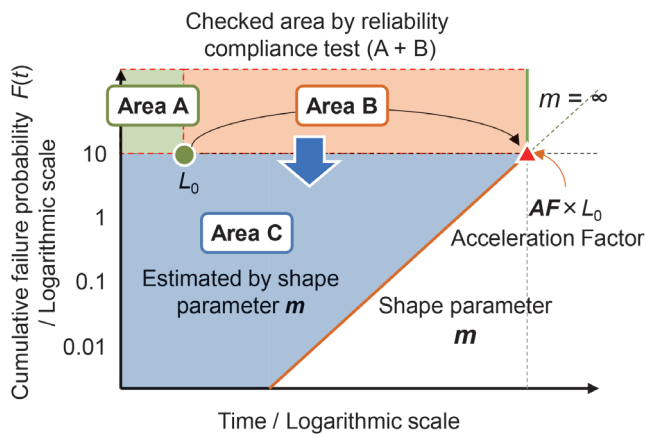


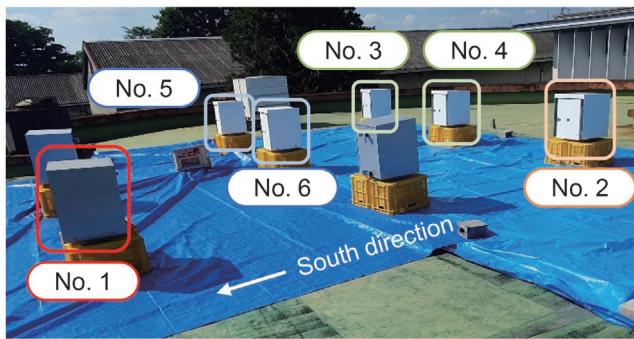
Fig. 2 Estimation method of cumulative failure probability over time based on reliability compliance test

Table 1 Specific measures by reviewing design of target equipment

Category	Measures	Example
Selection of electronic components	Change of components to Longer-life products	<b>Selecting components with long verification time <math>L_0</math></b> Verification time $L_0 = 1000$ h to 5000 h
	Change of components that meet stricter reliability test conditions	<b>Selecting components with strict verification temperature, voltage, and current conditions, or with large number of samples</b> Verification temperature $T_0 = 105^\circ\text{C}$ to $125^\circ\text{C}$ Verification voltage $V_0 = 5$ V to 6 V Number of samples $n = 10$ to 22
Circuit configuration	Increase of derating by reviewing circuit configuration	<b>Improving usage conditions with reviewing circuit configuration</b> Usage Voltage $V_1 = 6$ V to 5 V Usage current $I_1 = 20$ mA to 10 mA Failure judgement threshold Initial value -20% to -30%

**Table 2 Test conditions for temperature/ temperature difference reduction measures**

No.	Measures	Applied points	Solar reflectance [%]	Radiant emittance [W/m <sup>2</sup> ]
1	Without measures (reference)	—	—	—
2	High solar reflectance paint	Door + shielding plate	88	—
3	Radiation cooling paint	Door + shielding plate	86	100
4	Radiation cooling paint	Box + shielding plate	86	100
5	Radiation cooling film	Door + shielding plate	83	110
6	Radiation cooling film	Box + shielding plate	83	110



**Fig. 3 Estimation method of cumulative failure probability over time based on reliability compliance test**

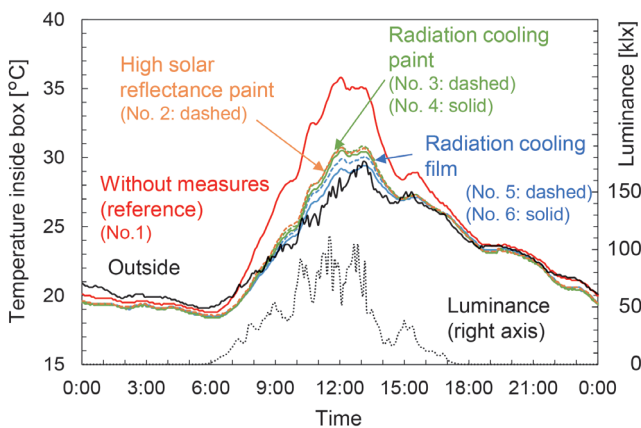


**Fig. 4 Results of temperature measurements (October 3, 2022)**

and for the radiation cooling paint (No. 6: -6.4°C, No. 5: -5.7°C). A suppression effect of about 5°C was also obtained for No. 4: -5.3°C, No. 3: -5.0°C) and high solar reflectance paint (No. 2: -5.1°C). In addition, regarding differences depending on the location of measures, the test specimen in which measures were applied to the box itself had greater suppression effect, although the maximum temperature was less than 1°C. In other words, it can be said that it is effective in dissipating not only heat due to direct sunlight but also heat inside the equipment box. On the other hand, regarding the average temperature, the temperature inside the equipment box in

the early morning and at night, when there is no influence of solar radiation, was almost the same as the outside temperature. Therefore, although the reduction effect was not as great as the maximum temperature, a reduction effect for average temperatures of about 2°C to 3°C was obtained.

### 3.3.2 Measures for reducing humidity

This section describes the results of the verification of measures such as installing the humidity control material to reduce the humidity inside the equipment box [6].

#### (1) Verification method

This verification used the same test specimen equipment boxes as those used for verifying measures to reduce temperature and temperature differences. In order to verify the effect of reducing the relative humidity inside the equipment box with or without the humidity control material, humidity control material (G-breath, NTT AT) was installed inside the equipment box door as shown in Fig. 5. In addition, the wooden board (lauan plywood) usually used to partition the inside of equipment boxes was considered to have a humidity controlling effect. Therefore, in order to isolate the humidity control effect of the wooden board, the authors also conducted tests without the wooden board for reference. In all tests, the inside of the equipment box was sealed. The measurements were taken over a total of 6 days from September 2 to 5 and September 10 to 11, 2022. The measurement conditions were the same as those used for verifying measures to reduce temperature and temperature differences.

#### (2) Verification results

As a representative example of the test results, Fig. 6 shows the humidity measurement results on September 4 when the weather was clear, and the temperature was at its highest for the period. While the humidity of the outside air and that in the boxes without the wooden boards changed in almost the same way, the relative humidity appeared to decrease as the outside temperature rose during the day. The reason is considered to be that in spite of an almost constant amount of water vapor in the air, the apparent relative humidity decreased because of a rise in temperature in the air outside or without the wooden boards. On the other hand, where only the wooden board or a combination of the wooden board and the humidity control material was used, the relative humidity remained almost constant throughout the day. It is thought that the relative humidity remained constant because the wooden boards and the humidity control material had a humidity controlling effect under similar conditions. Furthermore, when comparing the humidity control effect in terms of daily average relative humidity, the higher humidity control effect (5 to 7% lower) was confirmed under conditions where the humidity control materials were installed compared to where wooden boards alone were used, as shown in Fig. 7.

## 4. Method for quantifying effect of measures for prolonging lifetime

### 4.1 Quantification of prolonged lifetime

In order to evaluate quantitatively the implementation effects of measures to prolong the lifetime of equipment, as described in Chapter 3, the effects of the measures are converted into prolonged lifetime. Then, since the implementation effects of each measure can be compared using the same evaluation axis of prolonged lifetime,

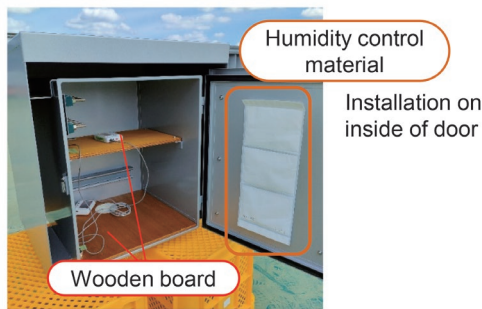


**Fig. 5 Photo of measurement setup of test specimens (humidity)**

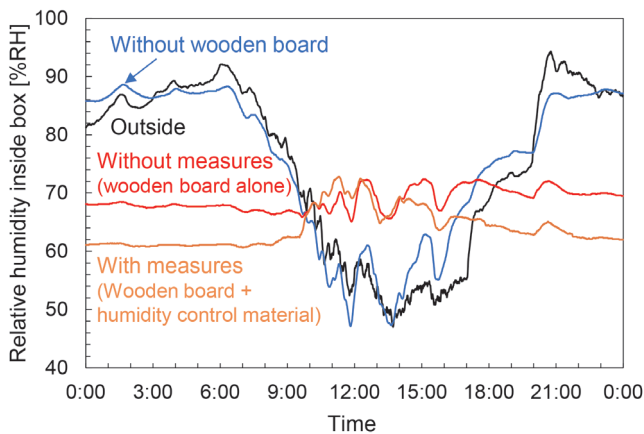


**Fig. 6 Results of relative humidity measurements (September 4, 2022)**

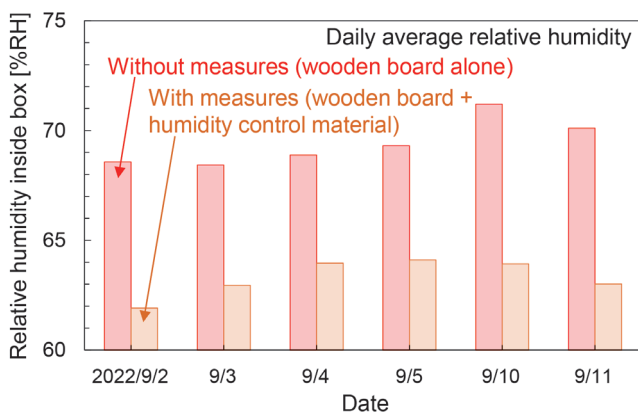


**Fig. 7 Results of relative humidity measurements (daily average relative humidity)**

it becomes easier to evaluate the cost-effectiveness of the measures.

To quantify the prolonged lifetime, the lifetime evaluation method described in Chapter 2 is used. In the measures taken by changing the design of target equipment, the reliability test conditions (test time, test temperature, number of samples, etc.) that serve as the basis for lifetime evaluation are changed in order to review the component selection. Therefore, comparing the lifetime evaluation results by using the reliability test conditions before and after review of electronic components, it is possible to derive the prolonged lifetime. In reviewing the circuit configuration, operating conditions such as the operating voltage and failure judgment

threshold are changed through derating. Then, using the operating conditions of electronic components before and after the review, the prolonged lifetime can be similarly derived in the same way as above. In addition, measures aimed at reviewing the usage environment involve changing usage conditions such as temperature and humidity, similar to reviewing the circuit configuration.

In other words, the effect of each measure to prolong lifetime can be converted into a prolonged lifetime by the increase in the acceleration coefficient due to the difference between the reliability (acceleration) test conditions and the usage environment conditions, and the increase in the verification time and number of samples under the test conditions. Based on Fig. 2, Fig. 8 shows the images of expanding the verification range according to the acceleration factor, verification time and number of samples. Note that Fig. 2 shows the method for estimating the secular change in cumulative failure probability from reliability compliance test results.

#### 4.2 Case study

This section describes the results of a case study in which the prolonged lifetime was estimated for each lifetime prolonging measure. Measures for prolonging lifetime include: (1) changing to longer-life products and components with strict reliability test conditions, (2) derating in reviewing circuit configuration, and (3) reducing temperature, humidity, and temperature difference. Table 3 shows the results of quantifying the effects of measures for prolonging lifetime. For electronic components other than solder joints, the time required to reach the cumulative failure probability of 1% (B1 life) was estimated.

In reviewing the component selection, the authors used aluminum electrolytic capacitors as an example of electronic components to calculate the prolonged lifetime when altering the test time, test temperature, and number of samples as reliability test conditions.

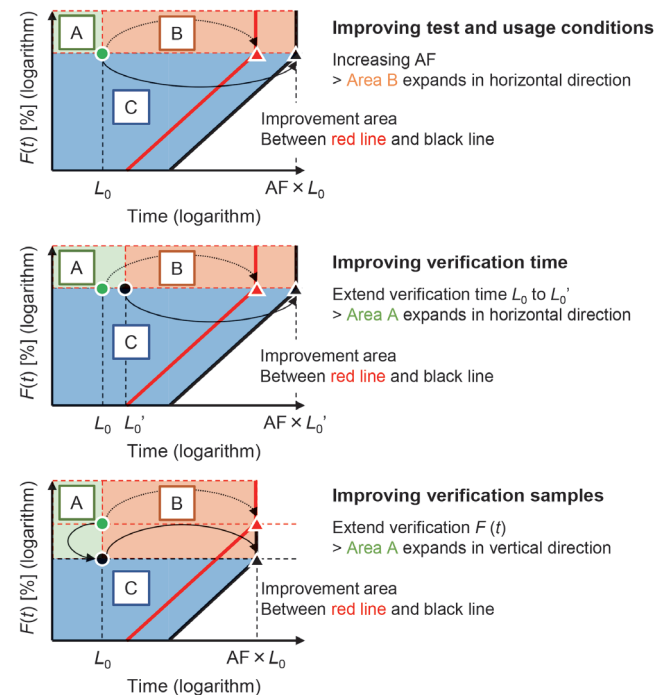


**Fig. 8 Images of expansion of verification range according to the acceleration factor, verification time and number of samples**

**Table 3 Results of quantifying the effect of lifetime prolonging measures (case study)**

Category	Measures	Evaluation condition*1	Applied point	Relational expression	Evaluation results	
					Prolonged lifetime [year] <sup>2</sup> (before·after)	Prolonged effect [times] <sup>3</sup>
Selection of electronic components	Changing components to longer-life products	<b>Aluminum Electrolytic Capacitor</b> $L_0 = 1000$ h, $T_0 = 105^\circ\text{C}$ , $n = 6$ , Self heating + $20^\circ\text{C}$ , Average temperature inside box + $5^\circ\text{C}$	$L_0 = 5000$ h	Eq. (1)	+ 14.2 (3.6·17.8)	5.0
	Changing to components that meet stricter reliability test conditions		$T_0 = 125^\circ\text{C}$	Eq. (1)	+ 10.6 (3.6·14.2)	4.0
			$n = 22$	Eq. (3)	+ 1.3 (3.6·4.9)	1.4
Circuit configuration	Increasing derating by reviewing circuit configuration	<b>Photocoupler</b> $L_0 = 50000$ h, $I_{F0} = 50$ mA, $T_0 = 40^\circ\text{C}$ , Self heating + $20^\circ\text{C}$ , Average temperature inside box + $5^\circ\text{C}$ , $I_{F1} = 20$ mA	$I_{F1} = 16$ mA	Eq. (2)	+ 6.1 (11.0·17.1)	1.6
Usage environment	Reducing temperature	<b>Aluminum Electrolytic Capacitor</b> $L_0 = 1000$ h, $T_0 = 105^\circ\text{C}$ , $n = 6$ , Self heating + $20^\circ\text{C}$ , Average temperature inside box + $5^\circ\text{C}$	Average temperature reduced by $3^\circ\text{C}$	Eq. (1)	+ 0.8 (3.6·4.4)	1.2
	Reducing temperature difference	<b>Solder joints</b> Testing cycle: 500 times, $T_{\text{max}} = 80^\circ\text{C}$ , $T_{\text{min}} = -20^\circ\text{C}$ , Average temperature inside box + $5^\circ\text{C}$ , Temperature difference without shielding plate + $10^\circ\text{C}$	Temperature difference reduced by $5^\circ\text{C}$	Eq. (4)	+ 28.1 (28.5·56.6)	2.0
	Reducing humidity	<b>Semiconductor (IC)</b> $L_0 = 1000$ h, $T_0 = 85^\circ\text{C}$ , $RH_0 = 85\%RH$ , $n = 22$	Average relative humidity reduced by $3^\circ\text{C}$	Eq. (5)	+ 69.5 (134.1·203.6)	1.5

\*1: Common evaluation conditions: Ambient temperature and humidity are based on values from the Japan Meteorological Agency Observatory (Tokyo)

\*2: Prolonged lifetime: B1 life without solder joints

\*3: Prolonging effect: Value calculated by dividing the evaluation lifetime after measure by that before measure.

For alteration of the test time and the test temperature, the  $10^\circ\text{C}$  double rule (1) was used as an acceleration model. On the other hand, for changes of the number of samples, (3) was used to quantify the prolonged lifetime. Especially, the significant effects of prolonging lifetime were obtained when selecting long-life products (1000 h to 5000 h product) and components with the higher temperature category ( $T_0$ ) ( $105^\circ\text{C}$  to  $125^\circ\text{C}$  product). In reviewing the circuit configuration, the authors used photocouplers as an example to calculate the prolonging lifetime when derating the input current  $I_F$  (from 20 mA to 16 mA) using the Black model (2) (replacing current density  $J$  with current  $I$ ). As a result of the calculations, it was confirmed that a lifetime prolonging effect corresponding to the acceleration model can be obtained. In improving the usage environment, the authors used the results obtained in the verification tests described in Section 3.3 as a reference. As an example, using the results, the authors estimated the prolonged lifetime due to reduction of the temperature using aluminum electrolytic capacitors (average temperature reduced by  $3^\circ\text{C}$ ), reduction of the temperature difference using solder joints (temperature difference reduced by  $5^\circ\text{C}$ ) and reduction of the humidity using semiconductors (average relative humidity reduced by 5%). For solder joints, the modified Coffin-Manson law shown in (4) was used as an acceleration model, and for semiconductors, the relative humidity model shown in (5) was used.

$$L_1 = L_0 \cdot \left(\frac{f_1}{f_0}\right)^m \cdot \left(\frac{\Delta T_0}{\Delta T_1}\right)^n \cdot \exp\left[\frac{E_a}{k} \cdot \left(\frac{1}{T_{1\text{max}}} - \frac{1}{T_{0\text{max}}}\right)\right] \quad (4)$$

$$L_1 = L_0 \cdot \left(\frac{RH_0}{RH_1}\right)^n \cdot \exp\left[\frac{E_a}{k} \cdot \left(\frac{1}{T_1} - \frac{1}{T_0}\right)\right] \quad (5)$$

Here,  $f$  is the number of temperature cycles per day;  $\Delta T$ : the temperature difference,  $T_{\text{max}}$ : the maximum temperature,  $RH$ : the relative humidity, subscript 1: the operating environment condition, and subscript 0: the test environment condition ( $m$  and  $n$  are coeffi-

cients), respectively. In both cases, the authors confirmed that improvements of the usage environment can have the effect of prolonging lifetime that corresponds to the accelerated model.

This case study showed that the effects of each measure for prolonging lifetime can be quantified as prolonged lifetime. It is believed that by using the proposed quantification method, it will be possible to make implementation decisions that take into account the cost and feasibility of each measure.

## 5. Conclusions

This paper described an overview of methods for evaluating lifetime of electric signalling equipment. This paper also reported on the possible measures for prolonging lifetime of electric signalling equipment and methods for quantifying the effectiveness of these measures along with the results of a case study.

In terms of measures for prolonging lifetime of electronic signalling equipment, the authors proposed suitable selection of electronic components used in target equipment, reviewing circuit configurations, and improving temperature and humidity conditions in the environment for use, as dominant factors determining lifetime. In order to quantitatively evaluate the implementation effects of the measures for prolonging lifetime, the effects of the measures were converted into a prolonged lifetime value. By making it possible to compare the implementation effects of each measure by using the same evaluation axis of prolonged lifetime, it is easier to evaluate the cost-effectiveness of each measure.

In the future, the authors aim to optimize the life cycle cost of electronic signalling equipment by utilizing lifetime estimation technology such as the proposed quantitative evaluation method in this paper and condition monitoring methods based on sensor measurements of the environment where the equipment is being used [7].

## References

- [1] Kunisaki, A., Fujita, H., Nomura, T., Ishii, T., “Lifetime Evaluation Method for Electronic Equipment of Wayside Signalling Systems,” *QR of RTRI*, Vol. 62, No. 2, pp. 110-117, May 2021.
- [2] Fujita, H., Niwa, J., Arai, H., “Development of Lifetime Evaluation Method for Electronic Interlocking Equipment in Consideration of Usage Environment,” *RTRI Report*, Vol. 32, No. 5, pp. 23-28, 2018 (in Japanese).
- [3] Matsuoka, T., “Reliability Test for Quality Assurance of the Electronic Component,” *Journal of the Adhesion Society of Japan*, Vol. 50, No. 10, pp. 318-325, 2014 (in Japanese).
- [4] Fujita, H., Takasaki, K., Shindo, T., Kamiya, T., “Quantitative Evaluation Method of Lifetime Prolonging Measures for Signalling Electronic Equipment,” *J-rail 2022*, S2-1-1, pp. 17-20, 2022 (in Japanese).
- [5] Shindo, T., Fujita, H., Takasaki, K., Isshiki, R., “A Study on Improving the Temperature Environment for Signalling Electronic Equipment,” *J-rail 2022*, S2-3-4, pp. 105-108, 2022 (in Japanese).
- [6] Kamiya, T., Fujita, H., Shindo, T., Takasaki, T., Isshiki, R., “Improvement of Humidity Environment for Signalling Electronic Equipment,” *J-rail 2022*, S2-3-3, pp. 101-104, 2022 (in Japanese).
- [7] Fujita, H., Tsubaki, K., Takasaki, K., Oko, N., “Lifetime Estimation of Electronic Signalling Equipment Based on Sensing Data from Usage Environment,” *QR of RTRI*, Vol. 64, No. 2, pp. 96-102, 2023.

## Authors



*Hiroyuki FUJITA*  
Senior Researcher, Signalling Systems Laboratory, Signalling and Operation Systems Technology Division  
Research Areas: Signalling Systems, Automatic Train Protection, Reliability



*Takuro SHINDO*  
Researcher, Signalling Systems Laboratory, Signalling and Operation Systems Technology Division  
Research Areas: Signalling Systems, Reliability



*Ken TAKASAKI*  
Researcher, Signalling Systems Laboratory, Signalling and Operation Systems Technology Division  
Research Areas: Signalling Systems, Reliability



*Tsuyoshi KAMIYA*  
Researcher, Signalling Systems Laboratory, Signalling and Operation Systems Technology Division  
Research Areas: Signalling Systems, Reliability

# Method for Evaluating Structural Design of Impedance Bond Molded with Resin

Shunsuke SHIOMI

Takuro SHINDO

Signalling Systems Laboratory, Signalling and Operation Systems Technology Division

Tsuyoshi KAMIYA

Terutaka SATO

Naoyuki OKO

Signalling Systems Laboratory, Signalling and Operation Systems Technology Division (Former)

*Thermal effects on trackside signalling devices, such as high air temperature, intense sunlight, and Joule heat generated by return currents, can be tested independently. However, it is difficult to evaluate the effects of multiple sources of heat. And yet, trackside signalling devices have occasionally failed due to heat, for example, deformation of the device structure because of heat. To reduce such failures, we developed a method for evaluating thermal effects on a resin-molded impedance bond using a computer simulation of heat-stress analysis. In this paper we also propose a method for evaluating thermal effects on impedance bonds through a combination of analytical and experimental methods.*

**Key words:** impedance bond, thermal stress analytics, return current, effect of temperature, testing method

## 1. Introduction

Since the 1990s, signalling devices for railways have been designed to be “maintenance-free” to reduce maintenance and eliminate the need for internal inspection, and replacement of internal parts and components. These signalling devices generally have no mechanical structures which allow them to be opened for maintenance, and so the status of internal components cannot be inspected and maintained. Consequently, such signalling devices and their internal components must be designed to remain sound until the end of their expected serviceable life.

The design of devices which will stand for several decades exposed to an outdoor environment, must be resilient to outdoor conditions, including mechanical vibrations and shocks, temperature changes and rain. Environmental tests regulated by JIS (Japan Industrial Standards) are used to evaluate the effect of these environmental conditions on the signalling devices. However, if the actual outdoor conditions are different to the standard, the actual reliability of a tested device will be different to the evaluation test outcome. Therefore, the resilience of signalling devices, especially “maintenance-free” devices, needs to be evaluated under conditions and methods that are closer to actual service conditions. Hence, it is important to understand the actual environmental conditions to which trackside signalling devices are exposed.

RTRI (Railway Technical Research Institute) has so far carried out research into the measurement of environmental conditions for signalling equipment and has developed methods for assessing the life and durability of equipment. We have proposed methods evaluating the life of signalling equipment in signalling huts [1] and field boxes [2] based on the results of studies of the relationship between temperature, humidity, and life of electronic components. In addition, we have also reported the results of field studies regarding vibrations affecting field signalling devices [3]. In this report, we describe the results of a study on the relationship between structural deformation of resin-molded impedance bonds, which are a part of track circuit equipment, and environmental conditions such as temperature and sunlight. Furthermore, we propose a method for evaluating the heat deformation of resin-molded impedance bond structures during the design and development stage.

## 2. Impedance bond and structure

### 2.1 Impedance bond

The impedance bond, which is installed at the boundary of track circuits, is a kind of transformer that has the function of separating return current and track circuit current. Figure 1 shows a typical impedance bond and its components. In the impedance bond, return current flows from rails, via primary sides of the connecting terminals and primary coil wire, to a terminal connected to the neutral point of the primary coil. Track circuit current from rails is transmitted from the primary coil to the secondary coil. By such a mechanism, a pair of impedance bonds performs the function of allowing return current to flow across the track circuits boundary, while allowing the track circuit current to flow independently through each track circuit.

In the impedance bond near the substation in DC electrified railways, large return current exceeding 1 kA flows through the impedance bond. Therefore, for stable operation and long service life for impedance bond, it is important to have a cooling method for Joule heat and a structural design that suppresses Joule heat. The Joule heat radiates from the primary coil, via fillings for electrical insulation or air, to the housing of the impedance bond. Although some types of impedance bond in use have no insulation fillings between coils and housings, all impedance bonds in Japan use insulation fillings such as oil, a kind of wax and resin. Previously, oil insulation had been used for all impedance bonds in Japan, but regular maintenance and replacement were required for oil insulation, which also posed a fire hazard. In addition, the heavy weight of oil-filled impedance bonds meant labor-intensive transportation and installation, especially in long tunnels and elevated sections. To solve these problems, wax-filled and resin-molded impedance bonds were developed and installed across in Japan from the 1990s.

### 2.2 Structure of resin-molded impedance bond

As shown in Fig. 1, the aluminum-molded housing of the resin-molded impedance bond contains the contents of the impedance bond such as the primary and the secondary coils, iron core, and

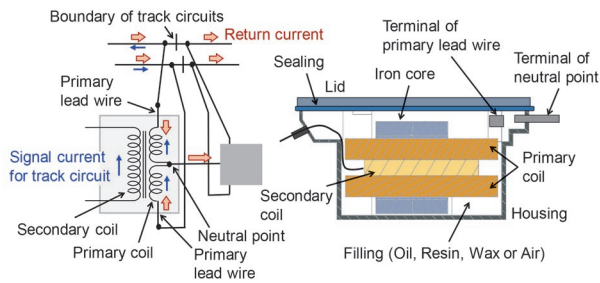


**Fig. 1 Typical impedance bond and its components**

electric wire connected to terminals. During manufacture, these contents are assembled in the housing, and then sealed before the housing and lid are bolted. The molten resin is then injected into the housing through an inlet on the lid. Since the coils, iron core, cables and terminals are sealed with resin during manufacture, there is no need to open the lid for maintenance and inspection. The interface between the housing and the lid is coated with a sealant to prevent water from entering the housing. The type, coating method, and thickness of the sealant varies depending on the type of impedance bond, and this selection is based on each manufacturer's experience.

### 2.3 Resin-molded impedance bond failure

The resin-molded impedance bond solved the problems of the previously used oil-insulated impedance bond such as fire hazard, maintenance, and heavy weight. However, some of the resin-molded impedance bonds experienced unexpected track circuit failure due to a reduction in insulation impedance, corrosion and terminal and cable breakages. Inside the resin-molded impedance bonds that were removed during the recovery work on failed track circuits, moisture and traces of water that had entered from the outside of the impedance bond were confirmed. However, no structural damage or cracks were found in the housing and lid of the failed impedance bonds. It is therefore assumed that moisture infiltrated the devices through the faying surfaces of the housing and the lid.

Whereas the location of corrosion and breakages in cases where moisture had entered the impedance bond and the inferred failure mechanisms varied depending on the type and model of impedance bond, one common feature in all the failed equipment was the presence of water or traces of water inside the sealed impedance bond.

### 2.4 Infiltration of water into impedance bonds

Impedance bonds, including resin-molded impedance bonds, are tested for waterproofness against showers in accordance with JIS E 3018 [4] (Japan Industrial Standards, Railway signalling equipment -Impedance bonds- Test methods) and JIS E 3017 [5] (Japan Industrial Standards, Parts for railway signalling -Waterproof test methods). Therefore, it can be considered that resin-molded impedance bonds are waterproof when exposed to rain. From this it is inferred that water infiltration occurs as a result of, a) use in an over specified atmosphere such as submersion of the joint surface due to heavy rain, b) loss or deterioration of the waterproofness of the impedance bond due to deformation of the housing and the lid or seal deterioration.

We therefore investigated the causes of water infiltration into resin-molded impedance bonds in service. Case a) possibility of submersion, was investigated by measuring the rise in water level

due to rain fall near the impedance bonds for approximately one year. For case b) the possibility of structural deformation, the housing and the lid of the resin-molded impedance bond was investigated. In particular, we tested and measured the relationship between the return current, Joule heat and temperature increase due to atmospheric temperature and intensity of sunlight. We also tested and analyzed the relationship between heat outside the impedance bond and deformation of the housing and lid.

## 3. Investigation of environmental impact on resin-molded impedance bonds

### 3.1 Water level around impedance bonds

To investigate the possibility of submersion of resin-molded impedance bond, which is not a requirement of the waterproofness test, we measured the water level rise due to rainfall near the impedance bonds including the previously failed impedance bonds. Figure 2 shows the measurement equipment and a resin-molded impedance bond. The water level was measured with a water level sensor capable of detecting water height as a change of resistance. The measured water level was periodically sent to the cloud storage via LTE. Measurements were taken between Mar. 2021 and Mar. 2022.

Figure 3 shows the results of water level measurements at a location where the highest water level among 12 measurement locations was confirmed. In addition to the water level, Fig. 3 also shows the hourly rainfall measured at the nearest observation location by the Japan Meteorological Agency. As shown in Fig. 3, heavy rainfall in excess of 41 mm/h during the measurement period was confirmed

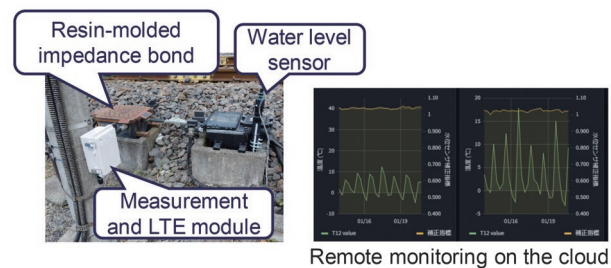


**Fig. 2 Water level measurement equipment and resin-molded impedance bond**

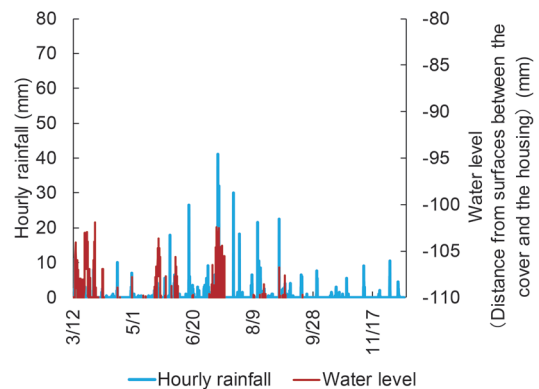


**Fig. 3 Measurement result of the water level and hourly rainfall**

on July 10, but the water level rising to height of the surface of the lid at -102.5 mm was not confirmed. Impedance bonds are sometimes installed at a lower level close to the ground to satisfy the clearance gauge of the railway. Even in this case, however, the risk of submersion due to normal rainfall was confirmed to be low within the scope of the measurement results.

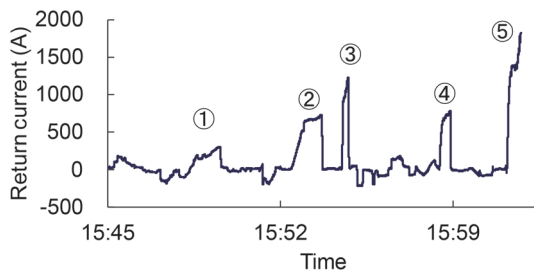
This investigation confirms the suitability of the waterproof test conditions. However, this investigation also revealed that water infiltrating impedance bonds is due to reasons other than water submersion, such as changes in operational conditions.

### 3.2 Effect of return current on temperature rise

The temperature of the impedance bonds rises due to the Joule heat by the return current to the primary coil. To confirm the effect of return current on increase in temperature during operation, current tests were carried out at the normal flowing time, interval, and amount of return current for test pieces.

To define the current test conditions for normal operation, we measured the return current on a resin-molded impedance bond with a rated current of 1000 A. The measurement location was near a DC electrified railway substation where electric multiple units (EMU) and electric locomotives (EL) run. Figure 4 shows the result of return current measured at the neutral point. It is noted that the rated current of the impedance bond is the rated current of the single rail. From Fig. 4, it is confirmed that the maximum current at the neutral point is 1240 A for an EMU, and in 1830 A for an EL, and the duration of the return current is 95 seconds for the EMU, and 46 seconds for the EL. As a result, test conditions were set to simulate normal train operation, with a current of 2000 A and a continuous energization time of 45 seconds or 135 seconds.

We then measured the temperature of the resin-molded impedance bonds while energizing the return current. The measurement items and testing conditions are shown in Table 1. Figure 5 shows results for the energizing current simulating periodic train running. It was found that the hourly temperature rise 9.2 degrees for 45 seconds energized and 75 minutes de-energized, and 11.7 degree for 135 seconds energized and 225 seconds de-energized. In addition, Figure 6 shows the results of continuous energizing tests. In test case-C using the same test conditions as for the high temperature test for impedance bonds as stipulated in JIS E 3018, the primary coil temperature rose to 94.4 degrees. Furthermore, it should be



	EMU Powering ①	EMU Powering ②	EMU Powering ③	EL Powering ④	EL Powering ⑤
Maximum (A)	313.8	732.0	1239.2	782.4	1830.4
Average (A)	158.4	491.7	837.9	610.6	1074.7
Duration (s)	95.6	81.6	19.0	28.5	46.2

Fig. 4 Measurement result of return current at neutral point (a trunk line, DC electrified)

Table 1 Measurement items and testing conditions

Testing circuit	Testing circuit for JIS E 3018:2001 temperature rise test	
Test piece	Resin-molded impedance bond for commercial frequency track circuit	
Measurement items	Rating current 1000 A DC (thermocouple built-in) Temperature of inner items (Coil, Iron core, inner of filling), and outer items (Housing, Cover)	
Test case-A	Current on neutral	1000 A and 2000 A
emulation of return current	Energizing duration (On/Off) (sec)	45/75, 45/195, 90/150, 135/225
Test case-B temperature rise and return current	1 hour energizing @ 3000 A + over 2 hours energizing @2000 A + 1 hour energizing (45 sec-on, 195 sec-off) @ 1000 A	
Test case-C JIS temperature rise test	1 hour energized @ 3000 A + over 2 hours energized @2000 A + 1 hour energized @ 3000 A	

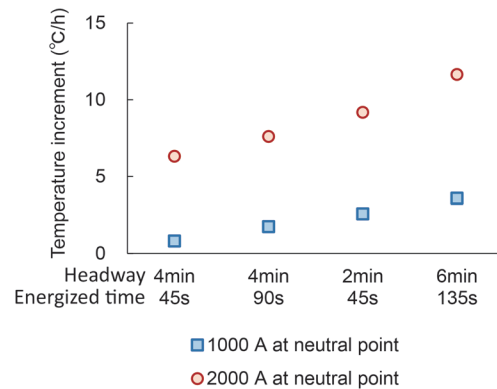


Fig. 5 Result of return current energizing test (simulating periodic train running)

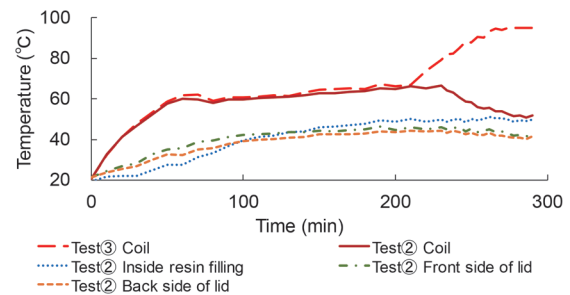


Fig. 6 Result of return current energizing test (continuous energizing)

noted that test case-C is a combination of the following sets of conditions: energized 1 hour at 150% of rated current, energized 2 hours at 100% of rated current and energized 1 hour at 150% of rated current.

From these tests, we confirmed that the effect of the return current is limited, since the temperature rise in severe conditions where a train frequency is every 2 minutes is only about 10 degrees per hour. In addition, the failures of resin-molded impedance bonds are also confirmed in small current conditions such as on track sections with low-frequency train operation and AC electrified railways. Therefore, the return current may affect the temperature rise of the internal of the impedance bond, but we do not think it is the main cause for the status change in operating equipment.

### 3.3 Effect of atmospheric heat and sunlight on temperature rise

Following the return current, the effect of atmospheric temperature and sunlight were investigated by testing as another cause of the impedance bond temperature rise. From the summer to the winter, 2022, we conducted a test on a resin-molded impedance bond installed outdoors in Tokyo without energization, measuring temperatures on the surface and the inside of the impedance bond and flux of solar radiation at the test site. Table 2 shows the testing conditions.

Figure 7 shows the temperatures of the impedance bond, atmospheric temperature, and flux of solar radiation over the test period. The surface temperature on the housing and other temperatures were affected by the rise in atmospheric temperature and increase in solar radiation, particularly on days with high daytime solar radiation. The maximum temperatures recorded throughout the test period were 53.4 degrees on the housing surface, 61.5 degrees on the lid surface, and 54.2 degrees in the primary coil. The temperature rise on rainy days was small however, within 10 degrees on the lid surface, and within 8 degrees at the coil. From this temperature measurement, we confirmed that the temperature of the impedance bond rises to around 60 degrees due to summer sunshine.

This test also revealed the relationship between temperatures and the deformation of the housing and the lid of resin-molded impedance bond. Figure 8 shows the temperatures and the relative displacement between the housing and the lid at point A shown in Figure 9, at a sunny and excessive heat day. The results of the relative displacement measurement shows that the gap between the lid and the housing of the tested resin-molded impedance bond reached 0.5 mm or more at noon, which is wide enough for water to infiltrate the device.

These field tests demonstrated the effect of the outdoor environment on water infiltration and demonstrated that the structure of resin-molded impedance bond could be deformed by increased temperature rise, or heat, of impedance bond.

**Table 2 Testing conditions of outdoor temperature measurement**

Test site	Greenhouse at RTRI, Kokubunji city, Tokyo
Testing duration	July 12, 2022 to Dec. 3, 2022
Test piece	Resin-molded impedance bond Rating current 1000 A DC (thermocouple built-in)
Measurement items	Temperature of greenhouse, Temperature of impedance bond (inner and outer), gap between housing and lid, flux of solar radiation
Maximum temperature	38.4°C At Fuchu AMeDAS measurement point, Aug. 2

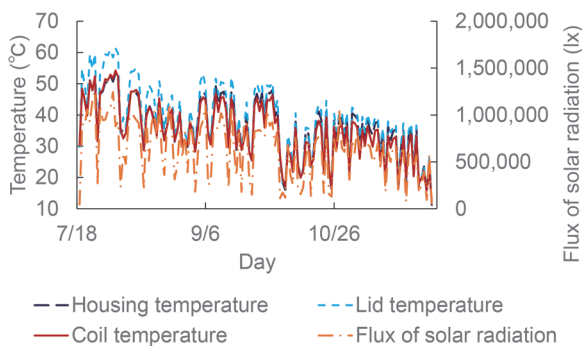


**Fig. 7 Maximum temperature and flux of solar radiation**

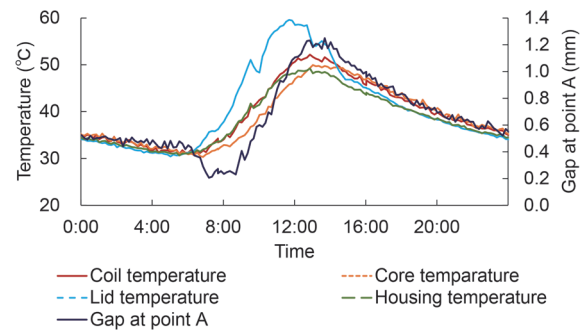


**Fig. 8 Temperature of the components of the resin-molded impedance bond and relative displacement at point A**

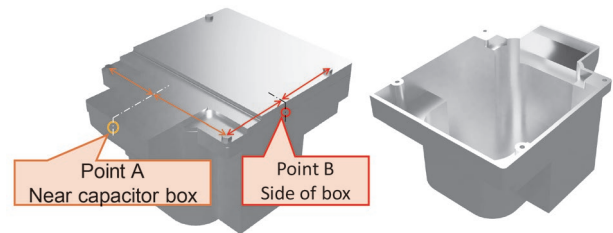


**Fig. 9 Displacement measurement points and analysis model (housing and lid)**

## 4. Effect of heat on structure of resin-molded impedance bond

### 4.1 Evaluation of structural deformation using the heat stress analysis

The effect of heat stress on the structure, including the degree of this effect, differs in the details of the structural design, or, the housing, the lid, the coils, the iron cores, and fillings, and the materials used. Therefore, it is necessary to develop a method for evaluating the heat stress and structural deformation capable of being used in the design and development process. In order to propose such a heat effect evaluation method, a model for the tested resin-molded impedance bond was developed. Using the developed model, the heat effects on deformation of the lid and housing were analyzed. In addition, the results of the analysis were compared with the results of the tests to evaluate the availability of the analytical method for the heat stress issues for trackside signalling equipment such as resin-molded impedance bonds.

### 4.2 Model and analysis conditions

The resin-molded impedance bond housing and lid with a shape similar to the tested impedance bond were modeled. Figure 9 shows the model. The model was composed of the housing made with aluminum casting, the lid, the coils made with copper, iron cores, cables, terminals, and epoxy resin for filling gaps. Ambient heat and sunlight heat were modeled as the surface temperature of the lid and the housing excluding the base and heat due to the return current was modeled as the coil surface temperature. Temperature distribution and heat stress were calculated for each analysis case shown in Table 3.

The effect of the material, in particular the coefficient of linear expansion of the epoxy resin, was also calculated. Table 4 shows the

**Table 3 Analysis conditions (Temperature Parameters)**

Analysis conditions	Temperature (°C)		
	Lid	Housing	Coil
Same temperature	20, 30, 40, ..., 80		
Coil temperature is high	0		80
	20		40, 60, 80
	40		60, 80
	60		80
Lid and housing temperature is high	40, 60, 80		20
	60, 80		40
	80		60
Lid temperature is different	40	30	
	80	70	
	20	70	

**Table 4 Analysis conditions (Parameters of materials and modeling)**

Material parameters	Items	Material	Coefficient of linear expansion (10 <sup>-6</sup> /°C)
	Material parameters	Lid and housing	Aluminum
Coil		Copper	16.7
Iron core		Steel	12.0
Terminals		Brass	20.5
Bolts		Stainless steel	10.4
Fillings		Epoxy resin	39.8
		Expandable resin	47.9
Software	Solver	Autodesk NASTRAN	
	Pre, post processing	Autodesk Fusion360	
Model	Mesh	Number of nodes	366,618
		Number of items	217,989

material parameters of the components used in the simulations. Two cases were used to calculate the effect of the expansion coefficient of resin: normal epoxy resin and resin with coefficient of 1.2 times that of normal resin.

A finite element analysis was performed using the Autodesk NASTRAN solver. The boundary conditions between the elements were defined as follows. The filling material, the internal coils and cores were bonded, and the outer components including the housing and the lids, and the filling were in contact. Contact between elements was handled using the penalty method.

**4.3 Analysis results**

Figure 10 shows an analyzed result of longitudinal deformation when each temperature of the housing, the lid and the coils is set to 80 degrees. The force due to the expansion of the resin fillings with a higher coefficient of linear expansion than aluminum used in the housing and the lid pushed out the housing and the lid. In particular, the center of the lid showed upward deformation. The deformation of the faying surface of the lid depended on location: deformation near the fixing bolts and the housing was small, and the deformation further away from the two adjacent fixing bolts was large. In addition,

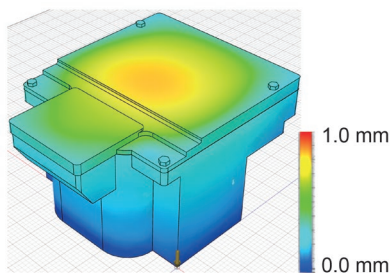


**Fig. 10 Analysis result (longitudinal deformation)**

**Table 5 Relational gap ratio of point A**

Analysis conditions	Temperature (°C)			Filling	RG ratio (%)
	Lid	Housing	Coil		
Same temperature	20			Normal resin	0.0
	30				11.4
	40				66.2
	50				100.0
	60				196.8
	70				326.4
	80				389.6
Coil temperature is high	0		80	Normal resin	813.7
	20	40			3.4
		60			19.7
		80			599.0
	40	60			111.1
		80			212.6
		80			270.0
Lid and housing temperature is high	40		20	Normal resin	14.5
	60				45.7
	80				140.3
	60	40			111.8
		80			234.3
		80			294.9
		80			28.6
Lid temperature is different	40	30		Expandable resin	273.7
	80	70			265.2
	20	70			265.2
Expandable filling	80			Expandable resin	841.1

tion, deformation of the lid near the capacitor box at the back was larger than elsewhere on the housing surface, causing a gap between the lid and the housing.

To confirm the effect of temperature on deformation of structure, the gaps between the housing and the lid at the point A (near the capacitor box) and the point B (the side face, midpoint of the bolts) shown in Fig. 9 were calculated by finite element analysis. To compare the results of the analysis, we calculated a value by dividing the gap at one point in each analysis result by the gap at the point A when the temperature setting is 50 degrees. In this paper, this value is called the relational gap ratio (hereinafter referred to as the RG ratio). Table 5 shows the RG ratio of the point A. As shown in Table 5, the RG ratio shows a tendency to increase with temperature. The RG ratios at the point B are 21.2% when the temperature is 50 degrees and 166.4% when the temperature is 80 degrees. Both the RG ratios at the point B are smaller than those at the point A. These results demonstrate that compared with the gap at point B, a large gap appeared between the lid and the housing due to the high temperature at point A. The linear expansion coefficient of the resin used to fill the resin-molded impedance bond also affects the gap width due to the rise in temperature.

**4.4 Factors influencing heat deformation**

Focusing on temperature conditions, we compared the analysis results with the test results. Figure 11 shows the RG ratio at the point A for the analysis results and the testing results. As shown in Fig. 11, The RG ratios of the analysis and those of the test show a similar tendency to the temperature rise. As shown in Fig. 8, the gap closed when the temperature of the coil was lower than the temperature of the housing and the lid. This tendency is also confirmed in the analysis result shown in Table 5.

These results show the deformation of the housing and the lid occur due to the rise in temperature caused by heat produced by the inner parts of the equipment and heat absorption by the outer parts

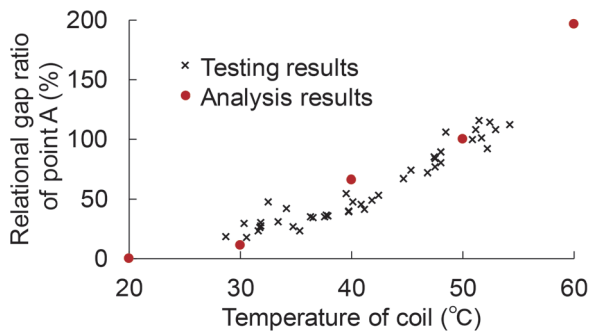


Fig. 11 Relational gap ratio of the point A

from the atmosphere. Deformation depends on the structure and materials of the equipment, so the elements affecting the deformation of resin-molded impedance bonds are complex. Therefore, it is difficult to obtain one temperature at which the deformation is at a maximum except through test and analysis. When testing and analyzing, it is necessary to consider the various temperature conditions; coil temperature due to the return current, temperature of the structure due to sunlight and atmospheric temperature, and these complex combinations.

### 5. Method for evaluating heat deformation in the design and development process

It is necessary to take appropriate measures against heat deformation in the design and development process of signalling devices used outdoors, since structural deformation affects its functionality and durability. The points which should be evaluated and the degree to which these need to be evaluated vary depending on each signalling device. However, in the case of the resin-molded impedance bond, where inspection of the inner parts to check for water infiltration is problematic, the point to focus on should be deformation and the formation of gaps between the housing and the lid, in order to avoid serious problems. This is because gaps allow water to infiltrate into the interior of the impedance bond, and this kind of problem is difficult to detect by visual inspection. The experimental and analytical results relating to gaps will enable evaluation of sealing performance during the design process. If the gap is smaller than sealing performance of adopted sealant, the sealing design can be evaluated as effective.

Figure 12 shows an evaluation flowchart of the sealing performance of the resin-molded impedance bond in the design and production process. As shown in Fig. 12, the thermal stress analysis

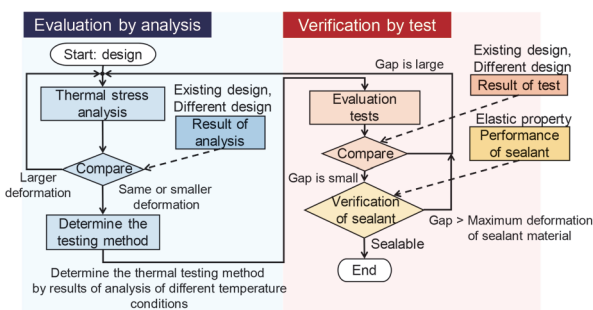


Fig. 12 Evaluation flowchart of the sealing performance of the resin-molded impedance bond

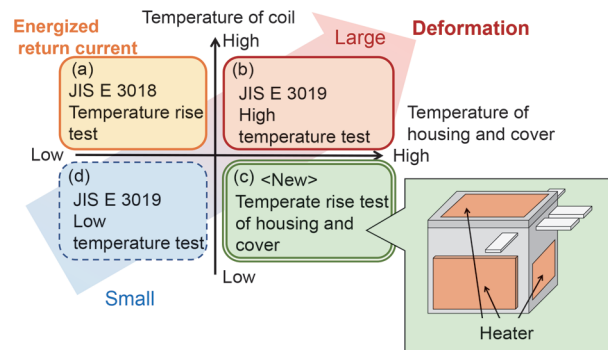


Fig. 13 Test method by thermal condition of the impedance bond

uses a combination of computer aided engineering (CAE) software and experimental testing. Thermal stress analysis is very useful in the design process. However, the absolute value of the analytical result will occasionally differ from the actual amount of physical deformation, since the result is affected by the boundary conditions and the modeling method. Therefore, in the design process, the thermal stress analysis result is used to compare different design plans with the existing design.

After completing the design review process, the design is evaluated based on test results using a real resin-molded impedance bond. In the experimental test, test conditions are important, especially the test temperature of each part mentioned in section 4.4. Figure 13 shows the thermal conditions of the coil temperature and structural temperature, i.e., the housing and lid, and the corresponding test methods. Since the existing test methods for impedance bonds defined in JIS E 3018 and JIS E 3019 [6] cover temperature conditions for most of the temperature conditions in operation, existing test methods defined in JIS can be adopted. If both coil and structural temperatures are high, the high temperature test defined in JIS E 3019 is applicable. JIS E 3018 is applicable if only the coil temperature is high. In the case of a high structural temperature and low coil temperature, as there is no existing test method, these thermal conditions can be replicated by heating of the surfaces using seat heaters. The thermal conditions to be tested as shown in Fig. 13 can be confirmed by the results of a pre-test thermal stress analysis.

### 6. Conclusions

In this paper we studied the relationship between structural deformation of resin-molded impedance bonds and environmental conditions such as temperature and sunlight. We proposed a method for evaluating the deformation of resin-molded impedance bond structures due to heat during the design and development stage. Moreover, we proposed a flowchart and testing methods to evaluate heat deformation using analytical and experimental methods. The proposed methods will be applied to the evaluation of sealing methods and design verification.

### Acknowledgment

The authors thank the staff of the East Japan Railway Company and related companies for their indispensable work on field measurements and factory and experimental data.

## References

- [1] Fujita, H., Niwa, J., and Arai, H., "Development of Lifetime Evaluation Method for Electric Interlocking Equipment in Consideration of Usage Environment," *RTRI Report*, Vol. 32, No. 5, pp. 23-28, 2018 (in Japanese).
- [2] Kunisaki, A., Fujita, H., Nomura, T., and Ishii, T., "Lifetime Evaluation Method for Electric Equipment of Wayside Signalling Systems," *QR of RTRI*, Vol. 62, No. 2, pp. 110-117, 2021.
- [3] Oshimi, Y., Shiomi, S., Kamiya, T., and Isshiki, R., "Suggestion of Excitation Acceleration in Vibration Endurance Tests for Signaling Equipment," *RTRI Report*, Vol. 38, No. 5, pp. 11-16, 2024 (in Japanese).
- [4] "Railway signalling equipment -Impedance bonds- Test methods," Japan Industrial Standards JIS E 3018:2001, 2001 (in Japanese).
- [5] "Parts for railway signalling -Waterproof test methods," Japan Industrial Standards JIS E 3017:2007, 2007 (in Japanese).
- [6] "High and low temperature testing methods for parts of railway signalling," Japan Industrial Standards JIS E 3019:2018, 2018 (in Japanese).

## Authors



*Shunsuke SHIOMI*  
Senior Researcher, Signalling Systems Laboratory, Signalling and Operation Systems Technology Division  
Research Areas: Point Machine, Signalling Devices



*Terutaka SATO*  
Researcher, Signalling Systems Laboratory, Signalling and Operation Systems Technology Division (Former)  
Research Areas: Signalling Devices



*Takuro SHINDO*  
Researcher, Signalling Systems Laboratory, Signalling and Operation Systems Technology Division  
Research Areas: Signalling Devices



*Naoyuki OKO*  
Researcher, Signalling Systems Laboratory, Signalling and Operation Systems Technology Division (Former)  
Research Areas: Signalling Devices



*Tsuyoshi KAMIYA*  
Researcher, Signalling Systems Laboratory, Signalling and Operation Systems Technology Division (Former)  
Research Areas: Signalling Devices

# Typology of Train Evacuations from the Viewpoint of Information Provision and Context

**Ayano SAITO**

Ergonomics Laboratory, Human Science Division

**Takayuki MASUDA**

Safety Psychology Laboratory, Human Science Division

**Hiroaki SUZUKI**

Human Science Division

**Tadashi TAKAI**

East Japan Railway Company

**Kana YAMAUCHI**

Safety Psychology Laboratory, Human Science Division (Former).

*As a baseline study on the provision of information to enable prompt evacuation from a train, different types of evacuation were grouped into three categories: immediate evacuation with passengers only, evacuation by remote instruction and evacuation by Staff Guidance. A web-based survey showed that there is a certain degree of role awareness in fellow passengers helping each other during escape, and that cooperative behavior can be expected. It also showed that those who understood instructions more clearly tended to act more immediately. Thus, it is considered important to inform passengers about their expected role, the flow of action to be taken, and the overall evacuation process.*

**Key words:** *stopping between stations, evacuation, information provision, unmanned operation*

## 1. Introduction

Various preparative measures have been taken to shorten passenger evacuation times from trains stopped between stations due to internal or external factors such as earthquakes or train fires. These include evacuation guidance training, installation of evacuation equipment, deployment of staff for guidance, and examination of ways people can get out of trains. The present survey research described in this paper focuses on provision of information to passengers on trains stopped between stations.

Conveying information to passengers in a prompt yet easy-to-understand manner is important for rapid evacuation. For this reason, clarifying what information to communicate to passengers and how to do so are key issues. However, what type of information and how it should be delivered depends on context, such as type of emergency, what kind of emergency equipment is on the train, and whether staff are or are not present. We first grouped the various evacuation contexts into three types from the perspective of information provision (Section 3). The content and method for communicating the information must be determined considering the psychological and behavioral characteristics of passengers. Therefore, we conducted an online survey that assumes evacuation from a train stopped between stations in order to understand passengers' behavioral intentions in such a situation, as well as the role awareness that governs those behaviors (Section 4). These were used as a basis to determine points which needed to be considered in the communication of information (Section 5). To include the prospect of unmanned operations in the future (GoA4.0 [1]), this paper also examined one of the most difficult sets of conditions for providing passenger guidance, which is evacuation from a train with no crew. In this paper, on-board staff, such as the driver and conductor, are referred to collectively as "crew members," to distinguish them from staff outside the train, such as dispatchers and station

staff. The generic term "staff member" used in this paper, refers to all staff, both on and outside the train.

## 2. Previous studies regarding evacuation of trains stopped between stations

Various studies regarding guidance for evacuation from trains stopped between stations have been conducted. These include the creation of systems for responding to abnormalities and evacuation drills. In addition, issues in recent years such as the Great East Japan Earthquake, Northern Osaka Earthquake, and long-term stoppages due to power outages have led to a review of issues, and recommendations. These reports contain a variety of measures, such as fostering a strong sense of cooperation to enable faster disembarkation and evacuation, and it is expected that passengers will cooperate with guidance on disembarkation and mutual assistance.

## 3. Typology of evacuation from the perspective of information provision

### 3.1 Typology of evacuation

Before examining what information should be provided to passengers it is necessary to generalize and sort various evacuation contexts. We categorized the possible evacuation scenarios where no crew are present and evacuation onto the tracks is required. This is considered to be the most difficult situation for providing evacuation guidance, as shown in Fig. 1. The blue text in Fig. 1 describes typical abnormal events. These event descriptions are given to facilitate visualization of each type of scenario. The same event may be

classified into different types of scenarios depending on the train consist, track characteristics, distance between stations, scale of the event, location of staff members, and other factors. Each grey shaded box in the figure contains examples of elements that may influence the decisions to be taken and described in the lozenge-shaped box directly above it.

The first step in the flow chart, is when an abnormal event occurs. The type of scenario which follows depends on whether the train is stopping between stations or able to continue running to the station. If the train can advance to the station, no evacuation onto the tracks is required, so this is excluded from the present study. Cases where a train stops between stations are then further divided between urgent situations where immediate evacuation is required, and cases where there is less urgency. An example of an urgent case is when a life-threatening situation occurs on the train such as arson with a large fire source. These events are classified as evacuation type I. There is not enough time for staff members to arrive at the scene, so passengers must evacuate by themselves. Cases in which external communication is interrupted or when there is no evacuation order from a dispatcher, such as a dispatcher being unable to detect an abnormality in the train, may require the passengers to decide on their own whether evacuation is necessary.

Cases where there is no need for immediate evacuation and where operations can be expected to resume in a relatively short period of time, or if the train is connected to a relief train which then transfers them to the station, do not require evacuation onto the tracks, and are thus excluded from the present study. If it is judged that passengers would need to disembark because resumption of operations would take too long, then staff members will be dispatched to guide the evacuation. However, there are times when there is not enough time to wait for staff to arrive, such as when there is a risk of flooding at the stopping point. Such cases, where external communication is not interrupted and in-train announcements can be made, are classified as a type II evacuation where only remote instructions are provided by a dispatcher.

The last type of case is where passengers can wait for staff to arrive, and if evacuation is possible, they are guided directly by staff. This is classified as evacuation type III.

Nevertheless, even if staff reach the train, passengers may be unable to disembark due to heavy snow or other reasons, and they may have to wait inside the train. This will eventually lead to the resumption of operations or an evacuation type III.

As shown above, evacuation onto the tracks can be broadly divided into three types of scenario: immediate evacuation without the help from staff (type I), evacuation guided only through remote instructions provided by a dispatcher (type II), and evacuation with the help of staff (type III).

### 3.2 Anticipated action from passengers

The essential elements of an evacuation are the detection of abnormalities, a need to make a judgment of whether evacuation is necessary or not, information on how to evacuate, and actual execution of the evacuation. If an abnormality occurs on a train with no crew present, then it is thought that the abnormality will be detected by automatic or remote confirmation of the situation or is reported by a passenger, for example over an emergency intercom system; the need for evacuation will be judged automatically or remotely, and evacuation then proceeds under the guidance of staff dispatched on site or by remote instruction.

Regardless of whether or not crew members are present, passengers will cooperate in an evacuation by reporting a detected abnormality, following instructions to wait on the train or evacuate, and by helping each other.

The far-left hand column in Table 1 gives specific examples of elements required for rapid evacuation when no crew member is present. The other columns give situations where these basic elements may be disrupted, by evacuation type. Type I, which is the most severe evacuation context, assumes a situation where not only is there no dispatcher, but also there are no means of communication

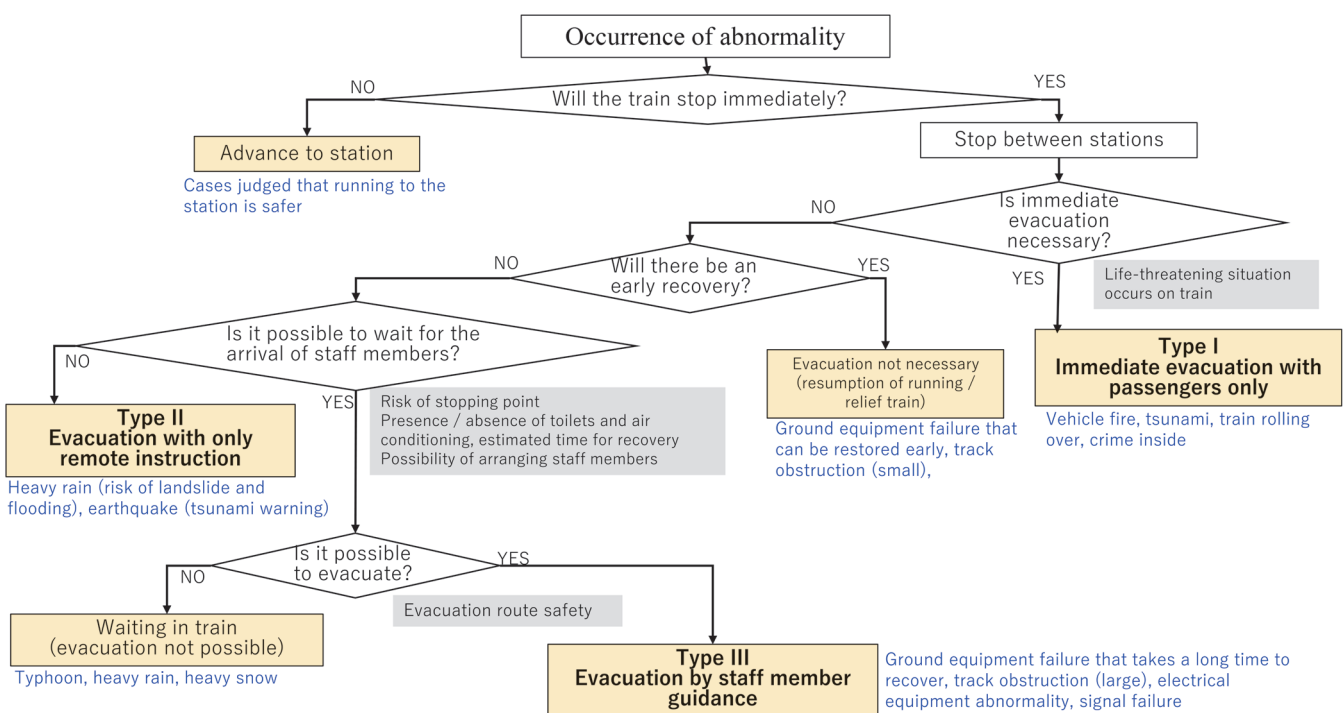


Fig. 1 Classification of evacuation (when no staff members are inside train)

and no evacuation instructions or external guidance. The items accompanied by an arrow ( $\Rightarrow$ ) in the table indicate that they can also occur in the type of scenario in the column to the right.

The “Knowing the need for evacuation” in the “Specific examples of elements required for rapid evacuation” in the far lefthand column of Table 1 means recognizing that the situation requires evacuation and a decision to evacuate. In Types II and III, passengers can rely on evacuation instructions, but in Type I, the passengers themselves must detect the abnormality and judge whether evacuation is necessary. Possible situations arising in Type I scenarios include passengers thinking that “there are instructions when evacuation is necessary” and waiting for evacuation instructions, thereby missing the opportunity to escape, or disembarking even when it is more dangerous outside of the train. Disembarking from a train unnecessarily can also occur in situation Types II and III. In Type II, the confirmation of the situation inside the train is done remotely using information from surveillance cameras and sensors, or by communication between passengers and dispatchers. However, given that this is not face-to-face communication, and passengers may be reluctant to use the passenger emergency intercom system [2], there is the possibility that the information which serves as the basis for giving evacuation instructions is insufficient because it is not communicated from the passenger to the dispatchers. Another possible issue is that even if an instruction to remain in the train is issued from the dispatcher, the passenger may not follow the instructions and disembark. In Type III, example situations include evacuating without waiting for the arrival of staff members, and instructions not reaching railcars that are far away from staff members.

“Knowing where to get out,” “being able to open emergency exits and get out of the train,” “knowing which way to go,” and “being able to get away from the train” are information and actions related to evacuation. Possible situations include making evacuation slower because passengers do not know where emergency exits are located or how to open them, and then accidentally doing something dangerously (e.g., safety device that only operates in conjunction with emergency exit will not work if escaping via a location other than the emergency exit); and taking more time even when knowing how to evacuate due to difficulties such as steps and darkness. To know the location of emergency exits and how to operate them in Type I scenarios, passengers need to rely on in-situ readily available information or previous knowledge to deal with the situation. In Type II and III scenarios, instructions are provided by staff, but Type II situation involves remote communication, and Type III context may involve passengers in railcars far away from staff members, so there is a possibility that more time is needed for the instructions to be conveyed to all passengers. These situations can be compensated to some extent by cooperative action such as knowledgeable people communicating with or providing assistance to nearby passengers.

Information needs to be provided to enable evacuation in each type of scenario: in Type I situations, to enable passengers to make judgements and take action based only on information displayed at the scene and their existing knowledge; in Type II scenarios, based on remote communication of instructions; and in Type III situations, with guidance from staff.

**Table 1 Specific examples of elements required for rapid evacuation and examples of possible situations by evacuation type**

Specific examples of elements required for rapid evacuation	Evacuation type		
	I. Evacuation with passengers only	II. Evacuation with only remote instruction	III. Evacuation by staff member guidance
Knowing it is necessary to evacuate (evacuation instruction, detection of abnormality and judgment of extent of emergency)	<ul style="list-style-type: none"> <li>Evacuation delayed waiting for instruction</li> <li>Disembarking even when unnecessary<math>\Rightarrow</math></li> </ul>	<ul style="list-style-type: none"> <li>No evacuation instruction because passengers did not report the abnormality</li> <li>Instructions are unknown <math>\Rightarrow</math></li> <li>Not following instructions<math>\Rightarrow</math></li> </ul>	<ul style="list-style-type: none"> <li>Evacuation without waiting for staff members</li> <li>Not conveyed to railcar far away from staff member</li> </ul>
Knowing where to get out of the train	<ul style="list-style-type: none"> <li>Not knowing where the emergency exit is located (on lines where evacuation through passenger doors is not possible)<math>\Rightarrow</math></li> </ul>	<ul style="list-style-type: none"> <li>Instructions are unknown <math>\Rightarrow</math></li> </ul>	<ul style="list-style-type: none"> <li>Not conveyed to railcar far away from staff member</li> </ul>
Being able to open emergency exits and get out of the train	<ul style="list-style-type: none"> <li>Unable to open emergency exit<math>\Rightarrow</math></li> <li>Evacuate using means other than emergency exit<math>\Rightarrow</math></li> <li>Unable to install ladder<math>\Rightarrow</math></li> <li>Safety device does not work due to incorrect use<math>\Rightarrow</math></li> <li>People with reduced mobility unable to evacuate<math>\Rightarrow</math></li> <li>Footing is dark preventing disembarkation <math>\Rightarrow</math></li> </ul>	<ul style="list-style-type: none"> <li>Instructions are unknown <math>\Rightarrow</math></li> </ul>	<ul style="list-style-type: none"> <li>Unable to open since railcar is too far away from staff members</li> </ul>
Knowing which way to go Knowing the dangers of being on the tracks	<ul style="list-style-type: none"> <li>Going in the wrong direction<math>\Rightarrow</math></li> <li>Contact with oncoming trains, electrocution<math>\Rightarrow</math></li> </ul>	<ul style="list-style-type: none"> <li>Instructions are unknown<math>\Rightarrow</math></li> <li>Instructions fail to reach passengers outside the train</li> </ul>	<ul style="list-style-type: none"> <li>Straying from staff member guidance</li> </ul>
Being able to get away from the train	<ul style="list-style-type: none"> <li>People in train unable to disembark due to pile-up<math>\Rightarrow</math></li> </ul>	<ul style="list-style-type: none"> <li>Instruction content is unknown<math>\Rightarrow</math></li> </ul>	<ul style="list-style-type: none"> <li>Getting separated from staff member guidance</li> </ul>

\*:  $\Rightarrow$  indicates that this can also occur in the type to the right

#### 4. Online survey regarding role awareness, etc.

##### 4.1 Overview of survey

To ensure rapid evacuation in the event of an emergency, it is essential for passengers to follow evacuation instructions and cooperate. We conducted an online survey to gather passenger responses, in the context of the current railway system with crew members present, to gain insight about the following aspects: how aware are passengers about the type of “behaviors that may be expected during evacuation” (“role awareness”)?; to what extent do passengers cooperate with evacuation instructions (“cooperation intention”)?; and what kind of information is desired during evacuation or during periods of normal operation? The survey was conducted in December 2021, targeting railway users living in the Tokyo metropolitan area, and 4,394 responses collected. The survey was conducted using the scenario method. Respondents were asked to imagine they were on their most frequently used route, at the time they usually travel, and that the train had stopped between stations.

The following three situations were set as requiring evacuation out of the train during stopping between stations: long-term power outage due to a substation fire (“power outage”), railroad crossing obstruction caused by trucks (omitted in this report), and earthquakes in areas where there is a tsunami risk (“earthquakes”). Respondents were then asked questions to investigate their level of understanding about evacuation instructions and the behavior they would adopt in response to instructions (responding to evacuation instructions). Power outages and earthquakes were set as having different levels of evacuation urgency, and if there are no crew members, then they correspond to Type III and II in Fig. 1, respectively.

Evacuation instructions were provided in written form, for example, instructing passengers to move to the head of the train to disembark in the event of a power outage or railroad crossing obstruction, or instructing passengers that they should disembark through the doors since they will open in the event of an earthquake. Respondents were asked to respond to the level of understanding of the instruction content on a four-point scale.

For items investigating responding to evacuation instructions and cooperative behavior, respondents were asked about whether they were likely to implement the behavior shown in Table 2 on a six-point scale. Responses of “4: Slightly likely to do it” and higher were set as “intention to adopt this behavior.”

Additionally, regarding the six types of cooperative behavior that passengers may adopt (including behaviors that railway operators may not expect), respondents were asked to indicate how much they think railway operators expect them to perform these behaviors in the event of an earthquake on a seven-point scale. Responses of “4: Somewhat expected” and higher were set as “presence of role awareness,” and its percentage was calculated.

Respondents were also asked to describe in an open question “what they would like to know about emergency equipment on the train, what behavior to take in an emergency, etc.” during normal periods of operation.

#### 4.2 Results and discussion

##### 4.2.1 Role awareness and behavioral intention

Figure 2 shows the results for responses to determine the degree to which respondents thought that each behavior is expected by the railway operators. The percentages of people with role aware-

**Table 2 Intended behaviors**

Behavior and “abbreviation”	
Responding to evacuation instruction	Taking the initiative when moving / disembarking: “Initiative”
	Following people after several have begun to move: “Following movement”
	Acting after most people have moved: “Following majority”
	Staying in place until staff member comes: “Wait for staff”
Cooperative behavior	Calling out to people who do not understand the situation, such as children or foreigners: “Verbal assistance (explaining)”
	Helping elderly passengers move / assisting elderly passengers who are struggling with disembarkation: “Assisting the elderly”
	Calling out to encourage cooperative behavior (let’s go, it’s this way): “Leadership (promoting)”
	Warning against unhelpful action (don’t push, don’t take pictures): “Warning”
	Cooperating with people who call out: “Cooperating”

ness (sum of people who selected 4: Somewhat expected–6: Expected very much) were relatively high for “Helping people nearby disembark” (79.0%) and “Offering verbal assistance to people who do not seem to understand the situation” (72.6%). For “Checking for people left behind,” “Warning people taking pictures,” and “Convincing people who are not moving to move,” the percentages of those who felt that there were expectations and those who felt that there were no expectations were similar.

Figure 3 shows the percentage of respondents showing an intention to cooperate regarding behaviors in the specific scenario of a power outage or earthquake. For “Cooperating” and “Assistance to elderly,” the percentages of people showing an intention to cooperate were both around 70%. For “Leadership” and “Verbal assistance,” the percentages of people showing an intention to cooperate were 55–61%. For “Warning,” the percentages were 33–35%, showing a greater number of responses with no intention to cooperate.

##### 4.2.2 Level of understanding and response to evacuation instruction

The level of understanding of evacuation instruction for power outages and earthquakes, respectively, was as follows: “Understand well,” 46.7%, 36.8%; “Generally understand,” 45.0%, 49.0%; “Do not understand much,” 6.1%, 10.8%; and “Not understand at all,” 2.2%, 3.4%. There were fewer responses with “Understand well” and more responses with “Do not understand much” during an earthquake compared to a power outage scenario, which was thought to be due to the fact that there were relatively fewer people who could imagine the action expected with the instruction (disembarking to the ground from the passenger door).

The percentages of people with the intention of reacting to evacuation instructions (Table 2) during a power outage or earthquake, respectively, were as follows: “initiative,” 75.0%, 75.9%; “following movement,” 80.7%, 77.9%; “following majority,” 47.5%, 43.9%; and “wait for staff,” 22.6%, 19.8%. The percentages for “following movement” were the highest.

Figure 4 shows the reactions to evacuation instructions according to their understanding. People responding to evacuation instruc-

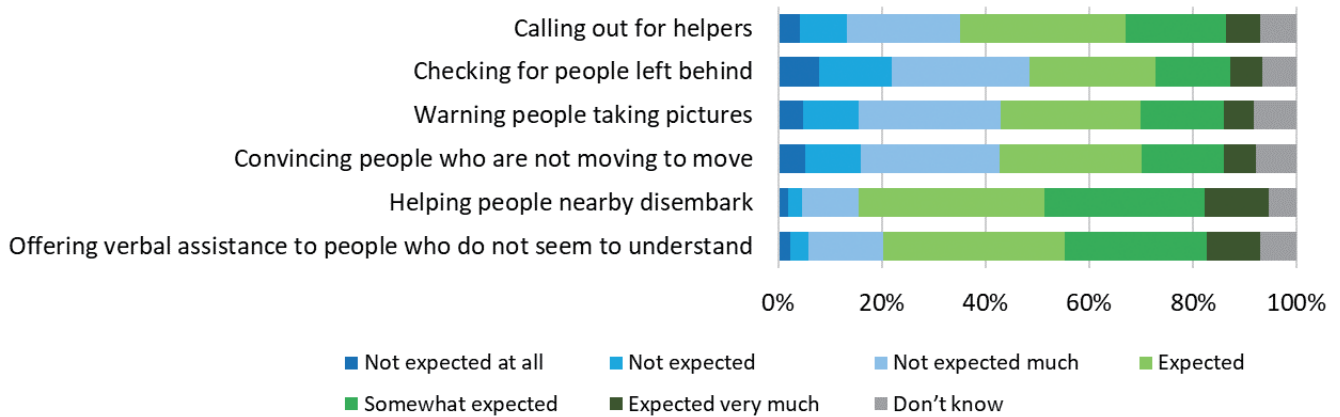


**Fig. 2 Extent to which passengers think operators have expectations**

tions with “Understand well” had high intentions for “initiative” (power outage: 84.2%, earthquake: 85.0%) and low intentions for “following majority” (41.2%, 36.3%). People responding with “Generally understand” had the highest intentions for “following movement” (83.5%, 82.5%). People who chose “do not understand” had the highest intentions for “following movement,” but a majority also had intentions for “following majority” (59.2%, 57.1%). People with higher levels of understanding about evacuation instructions tended to have higher intentions for “initiative.” Though a causal relationship cannot be stated from this survey, there is a tendency for people to act in a similar way to others in uncertain situations, so there is the possibility that more people would take the initiative if they had easier-to-understand evacuation instructions. Confirming this requires experiments in which the wording of evacuation instructions is manipulated. In the present study, the evacuation instructions were presented as text, but it would be desirable to present it aurally, similar to onboard train announcements.

#### 4.2.3 Requests for information provision

The most frequently mentioned response to questions about what information respondents wanted to know during evacuation or during periods of normal operation was the “series of steps on what to do” (approximately 1,600 responses, 36% of respondents), and when combined with responses for public awareness for specific behaviors, such as safety videos shown in passenger planes (approximately 400 responses), the total number was approximately 2,000 responses (46% of respondents). There were approximately 830 responses (19%) on the location of emergency equipment and instructions on use, approximately 460 responses (10%) requesting frequent announcements, and approximately 230 responses requesting the display of criteria to consider when judging the level of emergency of a situation, which shows when and in what situations the passenger emergency intercom should be used or when evacuation is necessary. There were approximately 120 responses requesting pointers on what not to do and precautions. There were approximately 70 responses with the opinion of wanting to know about the staff member response, such as knowing about whether there will be instructions during an emergency or whether staff members will do something; and approximately 60 responses indicating a desire to know what behaviors are expected of passengers and to what extent they are expected. Examples included descriptions such as “should I lend a hand to the elderly, or not go out of my way to help?” and “I hesitate because I am concerned that this action may hinder the work of the railway operator,” suggesting the possibility that con-

cerns about whether a passenger should act is hindering cooperative behavior.

#### 4.3 Summary of passenger survey

The following was shown by a scenario method study that targeted train lines with crew members in the Tokyo metropolitan area.

- The percentage of people who felt that railway operators expected them to help those such as the elderly get off trains in the event of an earthquake was 79.0%.
- The percentage of people who took the initiative in moving after evacuation instructions were given in the event of an earthquake was 75.9% overall, but the value was high among those with a high level of understanding of evacuation instructions (85.0%) and low among those who did not understand the evacuation instructions (55.9%).
- Regarding the type of information desired, many respondents mentioned the series of steps for what to do. There were also a certain number of respondents who stated that they would like to know where emergency equipment is located, and how and when to use it, as well as staff member responses and the expected behavior of passengers.

#### 5. Discussion on content that should be communicated

Over 70% of the respondents felt that they were expected by railway operators to help elderly people disembark from trains or offer verbal assistance to some extent when evacuating from a train stopped between stations, and the percentage of those who said they would try to help in disembarkation or offer verbal assistance in an evacuation scenario assuming a power outage or earthquake was around 70%, which indicates that passengers have a certain level of role awareness regarding cooperation. Meanwhile, it was suggested that the concern of “is it better to not go out of my way to help?” may hinder cooperative behavior. There were many direct descriptions of wanting to know the cooperative behavior expected from railway operators as well as opinions of wanting to know what to do, so there is a desire for the behaviors expected by passengers to be clarified. In a survey of passengers who experienced stoppage between stations during the Northern Osaka Earthquake [3], 97% of passengers showed an intention of responding to cooperation requests from crew members in the future, whereas 15% of people conducted assistive behaviors themselves. A trigger was needed for assistive behavior, suggesting the importance of requests for action

through in-train announcements [3].

One example of information that was requested by passengers was the series of steps or an overall picture of the response during an emergency, including that of evacuation. The overall picture includes not only the presence or absence of evacuation instructions and how staff members respond, but also the larger framework, such as showing cases where the train runs to the station at low speed and cases where passengers disembark in response to a train stopping between stations. People’s information processing ability generally decreases in the event of an emergency. If public awareness campaigns lead to only partial passenger knowledge, for example, “how to open the door,” even if a train can move to the nearest station at low speed, it is also possible that passengers may not be able to think of any other action than “open the door and disembark.” It is desirable therefore to also raise awareness about the possibility that it may be better to remain on a train as it may be able to move to the next station.

Many respondents also requested that they wanted to know how to use individual emergency equipment. A separate study has been conducted on this aspect, where it was confirmed that the evacuation ladder assembly time could be shortened by providing support such as showing a video in advance [4].

More people understanding evacuation instructions well increased intentions to take the initiative. Creating situations where it is easier to understand evacuation instructions at the right time through public awareness during periods of normal operation and reviewing written instructions during evacuation guidance is thought to be an effective way to ensure faster evacuation. Even if only some people take the initiative to follow instructions, those who do not know what to do can follow those people taking the initiative, which is expected to reduce the amount of time before evacuation begins.

“Sharing a social reality” and “improving trust in the system” can be considered as necessary elements in cooperation and collaboration between users and risk managers, such as passengers and railway operators [5]. “Sharing a social reality” means, for example, that passengers are aware that off-train evacuation may be necessary, and that by conducting the appropriate behaviors, they can mitigate damage. “Trust in the system” is trust in railway operators, which combines trust in the railway staff members and a sense of security regarding the railway system. The Railway Technical Research Institute is also examining measures for increasing trust in the system, where they have shown that educational videos on how to respond in the event of an abnormality are useful in increasing trust in railway operators [6].

It is also thought that passengers discovering and reporting problems plays a large part in the detection of abnormalities, which is a prerequisite for evacuation. However, it has been reported that even among passengers who are aware that a problem should be reported, there is a reluctance to use the passenger emergency intercom to report a problem [2]. Separate studies are being conducted on measures to encourage problem-reporting behavior [7].

## 6. Summary

This study was a basic investigation about providing information that enables rapid evacuation from a train. We summarized the evacuation situations where no crew is present into the following three types: immediate evacuation by passengers alone (type I), evacuation of passengers following remote instructions (type II), and evacuation of passengers with staff guidance (type III). An on-

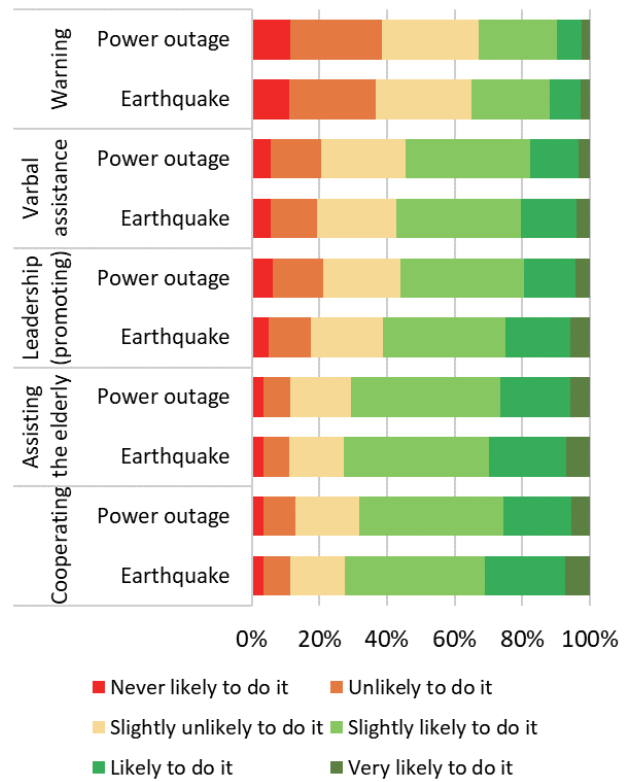
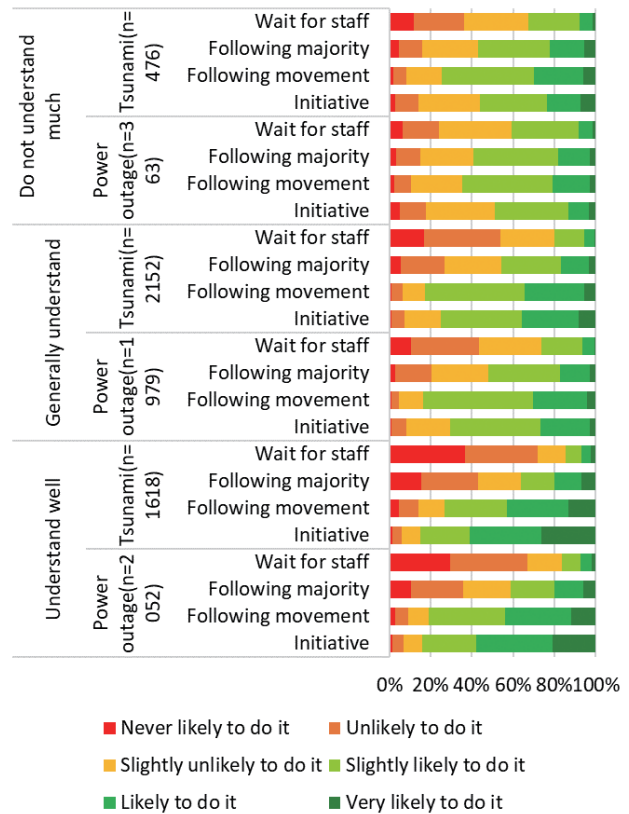


Fig. 3 Cooperation intention



“Do not understand much” and “Not understand at all” are shown together.

Fig. 4 Reaction to instruction according to level of understanding of evacuation instruction

line survey based on a scenario that a train had stopped between stations showed that there was a certain level of role awareness regarding passengers helping each other when disembarking, and that cooperative behavior can also be expected. People with better understanding of evacuation instructions tended to take the initiative in evacuation, and it was thought in this respect as well that it is important to make evacuation instructions easy to understand. It is thought that informing passengers about the behaviors they are expected to adopt, the series of steps involved in an evacuation, and providing an overall picture of how an evacuation is carried out, is important to ensure rapid evacuations.

This study was published in RTRI Report (in Japanese) in 2023 [8].

## References

- [1] JIS E3802:Automated urban guided transport(AUGT)-safety requirements, 2012.
- [2] Omichi, T., Takasu, H., Horishita, T., Fujino, H., "Research on effective requests for cooperation and ways to encourage customers," *Annken*, Vol. 3, pp. 26-31, 2010 (in Japanese).
- [3] West Japan railway company, "Survey report on customer response in abnormal times-Looking back on the 2018 Northern Osaka Earthquake," 2021 (in Japanese).
- [4] Yamauchi, K., Onoma, N., Masuda, T., Ishizuki, M., Tsushima, G., Kitamura, Y., Sato, A., Kikuchi, F., "A basic study on support for the installation of emergency ladders for autonomous trains," *The 84th annual convention of the Japanese psychological association*, 2020 (in Japanese).
- [5] Ikeda, K., "Structure of Institutional Trust in Government," *Annual Report of Political Science*, 010-1, pp. 11-30, 2010 (in Japanese).
- [6] Yamauchi, K., Masuda, T., "A basic study on the effects of watching safety awareness videos on trains," *The 85th annual convention of the Japanese psychological association*, 2021 (in Japanese).
- [7] Masuda, T., Saito, A., "Promoting/Inhibiting Factors of Passenger Call Button Use: A Study of the Effects of Awareness-Raising Messages," *Japan human factors and ergonomics society 63th annual meeting*, 2022 (in Japanese).
- [8] Saito, A., Masuda, T., Suzuki, H., Takai, T., Yamauchi, K., "Typology of off-train Evaluation from the Viewpoint of Information Provision and Sorting out Issues," *RTRI Report*, Vol. 37, No. 9, pp. 41-47. 2023 (in Japanese).

## Authors



*Ayano SAITO*, Ph.D.  
Senior Chief Researcher, Head of Ergonomics Laboratory, Human Science Division  
Research Areas: Ergonomics



*Tadashi TAKAI*  
Deputy Chief, East Japan Railway Company  
Research Areas: Innovation of Transportation System



*Takayuki MASUDA*, Ph.D. (psychology)  
Senior Researcher, Safety Psychology Laboratory, Human Science Division  
Research Areas: Traffic Psychology



*Kana YAMAUCHI*, Ph.D.  
Safety Psychology Laboratory, Human Science Division (Former)  
Research Areas: Psychometrics, Social Psychology



*Hiroaki SUZUKI*, Ph.D.  
Principal Researcher, Human Science Division  
Research Areas: Ergonomics

## Summaries of Papers in RTRI REPORT (in Japanese)

### Obstacle Detection Method Using Cameras and Sensors for Train Forward Surveillance

Ryo KAGEYAMA, Nozomi NAGAMINE, Junki YOSHINO  
(Vol.38, No.2, 1-7, 2024.2)

In train forward surveillance, it is important to establish sensing technology to reliably detect distant obstacles in front of trains. Therefore, we have developed a method for detecting obstacle in front of trains using cameras and sensors. The developed method detects obstacles such as people and vehicles by combining multiple sensors within the detection area around the railroad tracks. In this paper, we report on the results of a study of sensor configurations suitable for obstacle detection, the detail of detection algorithm using cameras and LiDARs or a stereo camera. In addition to these, the relationship between distance to obstacles and detection performance is also reported.

### Calculation Equation for Deformation Performance of RC Members with High-Strength Rebar

Yuki NAKATA, Yuko SATO, Toshiya TADOKORO, Ken WATANABE  
(Vol.38, No.2, 9-15, 2024.2)

A positive and negative alternating loading experiment for full-scale reinforced concrete (RC) column specimen with SD490 as longitudinal bar or SD1275 equivalent as ties was conducted to verify the damage properties and deformation capacity. All specimens showed flexural failure with buckling of the longitudinal bars. When SD490 was used for the longitudinal bars, the increased compressive strength of the concrete tended to suppress the damage to the core concrete and improve the deformation capacity. When SD1275 equivalent was used for the ties, the ties did not yield and did not exhibit the deformation performance equivalent to the yield strength. The results of these experiments clarify the conditions under which calculation equation for deformation capacity can be applied.

### Reduction Effect of Ground Vibration and Rail Corrugation by Floating Track with Under Sleeper Pads

Shota FUCHIGAMI, Tsutomu WATANABE, Hirofumi TANAKA, Takatada TAKAHASHI  
(Vol.38, No.2, 17-23, 2024.2)

Various types of vibration-reducing tracks have been developed to reduce noise and vibration during train running. Of these vibration-reducing tracks, although floating track with coil-spring units installed on conventional lines has shown excellent effects of reducing ground vibration, rail corrugation on the high rail has been observed in some sharp curve sections. Therefore, we have proposed a floating track with under sleeper pads in order to reduce the occurrence of rail corrugation on the high rail in floating track with coil-spring units. In this paper, we introduced the proposed floating track with under sleeper pads and evaluated its effectiveness in reducing ground vibration and rail corrugation by analytical methods.

### A Method for Monitoring Running Condition of a Bogie by Using an Axle Spring Isolation Rubber with a Built-in Piezoelectric Element

Shogo MAMADA, Tatsuya OTA, Shinichi SAGA, Kazuhiro YOSHIKAWA  
(Vol.38, No.3, 1-7, 2024.3)

Axle spring isolation rubber installed on an axle box is subjected to loads equivalent to the wheel loads during running. Therefore, to investigate a method for monitoring running conditions of a bogie, as first step in the research in this paper, we fabricated an axle spring isolation rubber with a

built-in piezoelectric element (AIBP). Since an AIBP can generate an electric charge in response to the load, it may be effective as a method for monitoring the running condition of the bogie. Then, running test with AIBP installed on the bogie was conducted to obtain wheel loads by calculated by converting the electric charge generated from the AIBP into a load. The test result of running tests showed that the calculated rubber load correlates with the wheel load, so that the time waveform of the rubber load could be used to monitor the running condition of the wheel.

### Numerical Flow Simulation of Mechanism of Increase and Method for Suppressing Increase in Lift Force of Pantograph Head of Conventional Line Pantograph under Crosswind

Takumi ABE, Koji NAKADE, Takeshi MITSUMOJI  
(Vol.38, No.3, 9-15, 2024.3)

We numerically investigated the aerodynamic characteristics of a conventional line pantograph in a crosswind by using large-eddy simulations (LESs). Although previous experimental study revealed that the lift force increases significantly under crosswind conditions, the mechanism of the phenomenon has not been clarified. Therefore, the flow fields around the pantograph head were carefully investigated by LESs. It was found that there are two main mechanisms: one is a stationary large-scale vortex generated on the upper surface of the pantograph head, and the other is a pressure increment on the lower surface of the pantograph head. In addition, LESs were conducted using modified pantograph head shapes to investigate methods for reducing the lift force of the pantograph head taking account of the mechanisms above. As a result, maximum lift reduction rate reaches approximately 60%, indicating that effective lift force reduction method was proposed.

### Design Method for Seismic Control Devices Installed on Steel Railway Bridges

Kazunori WADA, Takuma KUSHIYA, Akihiro TOYOOKA  
(Vol.38, No.3, 17-24, 2024.3)

Some authors of this paper have proposed a damping device with a bridge collapse prevention function installable in narrow spaces. In this paper, we propose a method for the rough design of the proposed device. Specifically, we organized the results of the nonlinear response analysis of a single degree of freedom system and proposed a nomogram that can be used to calculate the displacement of the girders and the response ductility factor of the piers in accordance with equipment specifications. By using this result, it is possible to have a rough idea of the specifications to meet the required performance before detailed dynamic analysis is carried out, so it is expected to reduce the amount of work involved in the detailed calculations.

### Development of Nighttime Rail Temperature Prediction Method in Consideration of the Radiant Heat from Surrounding Geographical Features

Fumihiro URAKAWA, Tsutomu WATANABE  
(Vol.38, No.3, 25-33, 2024.3)

This study proposed a new method capable of predicting the rail temperature distribution in nighttime at intervals of about 1 m by modeling the radiant heat of rail in detail using digital surface model (DSM) and meteorological data. To verify its prediction accuracy, the distribution of rail temperature and radiant heat were measured on an actual track. As a result, the minimum rail temperature was about 2°C high at the measurement points near buildings compared with that at other points due to strong radiant heat. We also confirmed that the proposed method can accurately

reproduce the actual rail temperature distribution in nighttime.

### **Evaluation of Impact of Volcanic Ash on Railway Electric and Signal Equipment and Proposal of Utilizing Information on Ash Fall**

Yuichiro NISHIKANE, Natsuki TERADA, Takeshi KONISHI, Takuya URAKOSHI, Shoichi KAWAMURA (Vol.38, No.3, 35-42, 2024.3)

Ash fall could have critical impacts on railway such as the failure of shunting of the track circuit and the decrease in insulation performance of insulator. In this study, we experimentally investigated conditions that cause these impacts of volcanic ash. Then, we clarified that over 0.05 mm thick volcanic ash causes the malfunction of shunting and that 1.2 mm thick volcanic ash containing saltwater causes the insulator flashover. Based on the results, we propose prevention actions against ash fall for railway companies to mitigate the impacts, using public information on eruption.

### **Operation Risk Assessment Method based on Information on Wayside and Vehicle Conditions for Autonomous Train Operation**

Yuki OTA, Akihiro GION, Sho NISHIMOTO, Yuki SAKURAI (Vol.38, No.3, 43-48, 2024.3)

We have been developing an autonomous train operation system that allows trains to be operated automatically while controlling wayside equipment based on the conditions of a vehicle and wayside. Autonomous train operation not only controls the acceleration and deceleration of a train, which is achieved by automatic operation, but also automatically makes operational decisions on board. We have developed a railway dynamic map as an information infrastructure for collecting and sharing necessary on-board and wayside condition information for making operational decisions and for risk assessment. This paper provides an overview of condition information management and risk assessment using railway dynamic map.

### **Development of an On-board Autonomous Train Control System**

Takayasu KITANO, Kazumasa KUMAZAWA, Hiroyuki FUJITA, Yoichi SUGIYAMA (Vol.38, No.3, 49-55, 2024.3)

As a basic technology for realizing autonomous train operation, we propose two functions: a function to create a running profile on board a train and a function to directly control wayside equipment from a train. The function to create a running profile onboard a train generates a running pattern to recover from delays caused by abnormalities, based on information such as timetables that is acquired and held by the onboard train. On the other hand, the function to directly control ground equipment from the vehicle is to set the train's path by the on-board equipment, switch the necessary turntable machines, and control level crossing warning.

### **Countermeasures to Prevent Dewirement Incident of Conventional Railway Pantographs Based on Lift Force Characteristics Under Crosswind**

Takeshi MITSUMOJI, Yuki AMANO, Takumi ABE, Shigeyuki KOBAYASHI, Koji NAKADE, Yuhei NOGUCHI (Vol.38, No.4, 1-7, 2024.4)

Wind-induced pantograph dewirement, which occurs only occasionally, causes transport disruption. It has been considered that the increase in pantograph lift force due to crosswinds results in the dewirement, but the mechanism by which the dewirement occurs is not completely understood. In this study, we focused on the increase in pantograph lift force due to crosswinds, and analytically identified the causal relationship between the dewirement incident and the lift force increase. We then experimentally

confirmed the amount of the lift force increase when pantographs are exposed to crosswinds. In addition, we used numerical simulations to identify the fluid-dynamic causes of the lift force increase and proposed countermeasures to prevent the lift force increase.

### **Experiments on Damage to Track Components due to Repeated Passage of Vehicles on Rail Gaps**

Katsutoshi SHIOTA, Yuki NISHINOMIYA (Vol.38, No.4, 9-17, 2024.4)

In railways where wireless train control systems are employed, track circuits may be removed, so that it is difficult to detect rail broken in such cases. In railways without track circuit, vehicles are assumed to run repeatedly on rail gaps until rail broken is found by rail inspection or other means. Therefore, in order to evaluate the strength of track components due to repeated vehicle passage, we conducted a falling weight test in the laboratory, in which impact loads during vehicle passage were applied to the rail simulating the damage. This test clarified the plastic deformation of the rails and functional deterioration of the rail fastenings system in response to the impact loads.

### **Construction of Method for Creating Energy-saving Rescheduling Timetable for Small-scale Delays**

Aiko KUNISAKI, Yoko TAKEUCHI (Vol.38, No.4, 19-25, 2024.4)

We constructed a method for creating energy-saving rescheduling timetables for small-scale delays using mathematical optimization. In the constructed algorithm, the rescheduling timetable is converted into an energy-saving rescheduling timetable by reducing the powering energy and increasing the regenerative energy. We considered passenger convenience under the condition that the total time from the starting station to the terminal station of each train does not change. This paper describes the details of the method for creating energy-saving rescheduling timetables and reports the results of a case study using real line data.

### **Wind Tunnel Test Results of Railway Vehicles under Cross Winds in Half-bank Half-cut Line Sections**

Tatsushi OTOBE, Minoru SUZUKI (Vol.38, No.4, 27-31, 2024.4)

The evaluation of the running safety of railway vehicles in high cross winds is carried out using an aerodynamic coefficient obtained from wind-tunnel tests. In a previous study, wind tunnel tests were carried out on commuter-type vehicles in a half-bank half-cut section, to obtain aerodynamic coefficients. However, studies have not been carried out on the influence of different vehicle shapes on the aerodynamic coefficients. Therefore, wind tunnel tests were carried out on double-decker-type vehicles and freight-type vehicles as a follow-up to the previous study.

## Editorial Board

Chairperson: Kimitoshi ASHIYA

Co-Chairperson: Hisayo DOI

Editors: Ryohei IKEDA, Masateru IKEHATA, Fumiko MORIMOTO, Nozomi NAGAMINE, Erimitsu SUZUKI, Tadao TAKIGAMI, Munemasa TOKUNAGA, Fumihiro URAKAWA, Kazuhide YASHIRO

---

## QUARTERLY REPORT of RTRI

第 65 卷 第 2 号

Vol. 65, No. 2

2024 年 5 月 1 日 発行

Published date: 1 May 2024

監修・発行所：公益財団法人鉄道総合技術研究所

Supervision/Publisher: Railway Technical Research Institute

〒 185-8540 東京都国分寺市光町 2-8-38

Address: 2-8-38 Hikari-cho, Kokubunji-shi, Tokyo 185-8540, Japan

発行人：芦谷公稔

Issuer: Dr. Kimitoshi ASHIYA

問い合わせ：鉄道総研広報

Contact us: Public Relations, Railway Technical Research Institute

Mail Address: rtripr@rtri.or.jp

**Q**UARTERLY  
**R**EPORT of  
**RTRI**